Hydrothermal monazite : the unavoidable accessory

Alexis Grand'Homme

UNIVERSITÉ GRENOBLE ALPES

THÈSE

Pour obtenir le grade de

DOCTEUR DE L'UNIVERSITÉ GRENOBLE ALPES

Spécialité : **Sciences de la Terre, de l'Univers et de l'Environnement**
Arrêté ministériel : 7 août 2006

Présentée par

Alexis GRAND'HOMME

Thèse dirigée par **Émilie Janots** et
codirigée par **Anne-Magali Seydoux-Guillaume**

préparée au sein de **l'Institut des Sciences de la Terre**
dans **l'École Doctorale Terre, Univers, Environnement**

Étude de la monazite comme chronomètre et traceur géochimique des minéralisations hydrothermales : Approche expérimentale et analyses de monazites de veines alpines

Thèse dont la soutenance est prévue le **« 4 Mars 2016 »**,
devant le jury composé de :

Jean-Marc MONTEL
Professeur, ENSG, Nancy, Rapporteur
Edwin GNOS
Professeur, Muséum d'histoire naturelle, Genève, Rapporteur
Julia DE SIGOYER
Professeur, ISTerre, Grenoble, Présidente du jury
Bernard BINGEN
Senior Geologist, NGU, Trondheim, Examinateur
Émilie JANOTS
Maître de conférences, ISTerre, Grenoble, Directrice de thèse
Anne-Magali SEYDOUX-GUILLAUME
Chargée de Recherche, LMV, Saint-Étienne, Co-Directrice de thèse
Magali ROSSI
Maître de conférences, EDYTEM, Chambéry, Invitée

« Je remercie les singes du passé,
Je remercie les singes qui m´ont précédé »

Andréas et Nicolas

Remerciements

Tout d'abord, je tiens à remercier mes directrices de thèse, Émilie Janots et Anne-Magali Seydoux-Guillaume, pour leur confiance et pour m'avoir lancé sur les sentiers de la monazite. Leur disponibilité, leur patience et leurs encouragements ont plus que grandement contribué à l'aboutissement de ce travail. Leur passion pour la minéralogie (et les belles images de minéraux exotiques) a été très communicative et je leur en suis vraiment reconnaissant. Grâce à vous, j'ai pu améliorer mes compétences et m'initier à un très grand nombre de techniques analytiques. Ce fût une réelle chance et une grande source de motivation au cours de ce travail.

Je remercie également le jury de thèse qui a accepté de relire et d'évaluer ce travail: Jean-Marc Montel, Edwin Gnos, Julia de Sigoyer, Bernard Bingen et Magali Rossi. Les publications issues de ce manuscrit ont grandement bénéficié de leurs commentaires et précieux conseils.

Ce travail de thèse n'aurait pas non plus été possible sans de nombreuses collaborations. Un grand merci, donc, à toutes les personnes qui m'ont accueilli et/ou avec qui j'ai eu la chance de travailler. Je remercie particulièrement Damien Guillaume (au GET à Toulouse au moment de ma thèse) pour son enthousiasme avec les expériences et Valérie Bosse (au LMV à Clermont-Ferrand) pour sa gentillesse et sa patience lors de mes séjours (ainsi que pour ses conseils dans la gestion des jumeaux…). Je remercie également Matthias Bernet, Marie-Christine Boiron, Jörn Hövelmann et Carmen Höschen d'avoir contribué à ce travail avec enthousiasme. Je remercie l'ensemble des personnes du laboratoire ISTerre qui m'ont, de près ou de loin, aidé dans le travail de préparation ou les analyses présentées dans ce manuscrit. Merci aussi à vous, Valérie, Martine et Nathaniel pour votre aide pendant ces heures passées à la microsonde, au MEB ou en salle de chimie. Ce fût toujours un réel plaisir.

Un grand Merci aussi, Roger, pour les sorties Alpines à la recherche de la monazite (ou autre). Ta passion et ton investissement au cours de ces trois années de thèse m'ont été d'une très grande aide. Et quand tu veux, on retourne à la cueillette de cristaux.

Il est temps de remercier tous mes collègues et amis du laboratoire et d'ailleurs avec qui j'ai passé beaucoup de temps (pas forcement au laboratoire…).

Merci à tous ceux croisés et re-croisés (Arnaud et les Orléanais, Oscar et Amélie) au détour de conférences et avec qui ce fût toujours un immense plaisir de passer du temps. Bonne chance pour la suite.

À Toulouse, je remercie Marieke, Michel et Philippe qui m'ont envoyé chercher des pegmatites (déjà de beaux minéraux…) au Cap de Creus ou des péridotites dans les Pyrénées dès le Master. C'est vous qui m'avez donné envie de continuer. Je remercie également tous les thésards Toulousains qui m'ont toujours accueilli avec enthousiasme lors de mes visites régulières et qui m'ont toujours gardé un petit coin de bureau pour travailler (ou de comptoir pour …). Un ENORME Merci à Arnaud et Damien (et bien sûr Emilie, Marion et vos familles) pour votre amitié depuis mon arrivée en Haute-Garonne, pour m'avoir accueilli et supporté à chacune de mes visites. C'était burné. Arnaud, on ouvrira notre bar à Ricard-Suze-Tripoux, ça va cartonner, j'en suis sûr, et Damien quand tu veux on fait la course en moissonneuse.

À Grenoble, Merci Julien, Schwartz et Jérôme d'avoir égayé mes journées par des poses obligatoires et régulières (ainsi que pour avoir accepté de partager certains de vos coins à champignons). Merci German pour ton intérêt pour ce qui se passait dans le bureau d'en face et les petites blagues. Merci Mélanie, Francis et François pour le café du matin et Sylvain pour les apéros et pour m'avoir appris plein de choses sur les abeilles (ce n'est pas fini, j'espère). Merci aux « anciens » d'ISTerre: Benjamin, Romain, Karim et Mélanie ainsi qu'aux moins anciens qui ont partagés ces trois années avec moi. Je garde une place de choix pour ceux qui ont partagés mon bureau (re-Romain, Cécile, Cyril et Chloé) et mon barbecue. Revenez quand vous voulez passer le weekend à la maison et si vous êtes sages, vous pourrez peut-être conduire le Lada.

Enfin, une place toute particulière pour mes compères du troisième: Hélène (prononcez « delavÔlte »), Baptiste (mon Fréro Delavega) et Anthony (aka Pinus) sans qui tout cela n'aurait pas été possible. J'y ajoute évidement et respectivement, Bruno, Julie et Simone, vos moitiés bien courageuses ! Un grand Merci. Hélène, pour ton enthousiasme, tes petits plats (préparer un brunch sans dormir pour 10: c'est balèze), tes cocktails et ton amour invétéré pour Clamecy (même si bon, hein…). Baptiste, pour avoir été là dans les moments de doute et de joie, et pour pouvoir parler de marques de couches bébé et du dernier album de Motörhead (RIP…) dans la même phrase. Ça n'a pas de prix. Anthony, pour avoir été là jusqu'au bout de ma thèse, les matchs de rugby et de hockey et les apéros/bouffes fougueux. La bise à tous les trois.

Un très grand MERCI à ma famille (et belle-famille) et notamment mes parents qui m'ont soutenus, laissé libre et fait confiance dans tous mes choix. Merci pour votre soutien.

Enfin, le plus grand MERCI revient à Marion, sans qui tout cela aurait été bien plus difficile… Merci pour ta patience, ton aide et ta confiance qui m'ont permis de réaliser ce travail. Avec les deux sauterelles (Lola et Célina) qui nous ont rejoints pendant la thèse, les journées étaient bien chargées et tu as largement assumé ma part du travail pendant plusieurs mois pour permettre l'aboutissement de ce doctorat. Tu mérites ta part du gâteau. Encore merci !

Bonne lecture, et n'oubliez pas :

SOMMAIRE

Résumé

La monazite est présente comme minéral accessoire dans la plupart des environnements géologiques. Elle est souvent riche en U et Th, n'incorpore pas (ou peu) de Pb initial et son système isotopique (U-Th-Pb) est résistant à la diffusion dans la majorité des conditions crustales, ce qui en fait un chronomètre très attractif. De plus, elle constitue la principale source de Th et une des principales sources de terres rares (REE) contenus dans la croûte terrestre. En présence de fluide, la monazite peut recristalliser par un processus de dissolution-précipitation couplée, avec une composition chimique et/ou isotopique différente de la monazite initiale. Ces recristallisations impliquent alors une redistribution des éléments contenus par la monazite (REE, Th, U, Pb) et la compréhension de la mobilité de ces éléments stratégiques est cruciale pour leurs aspects économiques (ressources en lanthanides et actinides) et environnementaux (contexte de stockage des déchets).

Cette thèse vise à étudier le comportement de la monazite lors des interactions fluide-monazite et son potentiel comme traceur chronomètre et traceur géochimique des minéralisations hydrothermales. Pour cela une approche pluridisciplinaire a été adoptée, combinant minéralogie, pétrologie expérimentale, géochronologie, et tectonique. Les travaux présentés s'organisent en deux parties: l'une concernant la datation de monazites hydrothermales de fentes alpines, et l'autre des expériences d'altérations hydrothermales en laboratoire.

Une quarantaine de cristaux de monazite et une dizaine de cristaux de xénotime ont été collectés dans des fentes alpines (veines hydrothermales se formant durant l'exhumation) des domaines externes (Argentera, Belledonne et Mont-Blanc) et internes (zone Briançonnaise). La datation U-Th-Pb in-situ par LA-ICP-MS a permis de mieux contraindre l'âge et la durée des circulations hydrothermales pendant les épisodes de déformation tardifs liés à l'exhumation des Alpes occidentales. Les analyses d'inclusions fluides dans la monazite couplées à des âges traces de fission sur zircons ont apporté de nouvelles contraintes sur le gradient géothermique induit par les circulations fluides dans les veines hydrothermales. L'analyse systématique des produits expérimentaux (monazite et fluide) de 18 expériences hydrothermales a permis de confirmer la mobilité des éléments comme l'uranium ou les terres rares lourdes lors des réactions hydrothermales. L'étude à l'échelle nanométrique des domaines de monazite recristallisée a mis en évidence un nouveau mécanisme de remplacement caractérisé par la propagation du front de réaction à l'aide de nano-pores et nano-fractures. Ce mécanisme conduit à un remplacement anisotrope et à un mélange de nano-domaines de monazite primaire et recristallisée. Ces observations ont des implications majeures pour le stockage des déchets radioactifs ou en géochronologie pour expliquer les perturbations des âges monazites ayant réagi avec un fluide dans les milieux hydrothermaux ou métamorphiques.

Abstract

Monazite is commonly found in most of geological environments. Monazite can be rich in uranium and thorium, does not incorporate lead, and its isotopic (U-Th-Pb) system is very robust to diffusion in most of crustal conditions, which makes it a very attractive chronometer. In addition, it represents the main source of thorium and a major source of rare earth elements (REE), in the crust. During fluid-monazite interaction, monazite can recrystallize by a coupled dissolution-precipitation process, with a chemical/isotopic composition different from the initial monazite. These recrystallizations involve a redistribution of the elements contained in monazite (REE, Th, U, Pb) and understanding of the mobility of these strategic elements is crucial for their economic (lanthanides resources and actinides) and environmental (storage of radioactive waste) aspects.

The aim of this thesis is to investigate the behaviour of monazite during fluid-monazite interactions and its potential as chronometer and geochemical tracer of fluid mineralization, via a multi-disciplinary approach including mineralogy, experimental petrology, geochronology and tectonic. The work presented here is organized in two parts: one on Alpine hydrothermal monazite dating and the other on the results of hydrothermal alteration experiments in laboratory.

About forty monazite and ten xenotime crystals were collected in Alpine clefts (hydrothermal veins formed during exhumation) of the external (Argentera, Belledonne, Mont-Blanc) and the internal (Briançonnais Zone) domains. The LA-ICP-MS in-situ U-Th-Pb dating allowed to better constrain the age and duration of hydrothermal circulation during the late deformation stages related to the exhumation of the western Alps. The fluid inclusion analysis of monazite crystals coupled with zircon fission-track dating have brought new constrains on the geothermal gradient induced by fluid circulations in the hydrothermal veins. Systematic analysis of experimental products (monazite and fluid) of 18 experiments confirmed the mobility of elements such as uranium or heavy REE during hydrothermal reactions. The nanoscale study of monazite recrystallized domains showed a new replacement mechanism characterized by the propagation of the reaction front through nano-pores and nano-fractures. This mechanism leads to anisotropic replacement and a mixture of nano-domains of primary and recrystallized monazite. These observations have major implications for the storage of radioactive waste or in geochronology to explain the disturbances of monazite ages that have reacted with fluid in hydrothermal or metamorphic environments.

1. INTRODUCTION GENERALE

La monazite est un phosphate de terres rares légères ($LREEPO_4$) présent comme minéral accessoire des roches crustales dans une grande variété d'environnements géologiques et pouvant contenir de grandes quantités de Th et d'U (Overstreet, 1967 ; Bea, 1996). Ce minéral a été décrit pour la première fois par A.F. Breithaupt en 1829, du grec *μονάζω* («vivre seul»), en rapport à sa relative rareté. Grâce à ses propriétés physiques et chimiques intéressantes, la monazite trouve diverses applications (Clavier et al., 2011 et référence qui y sont citées) dans les domaines des matériaux, des émetteurs lumineux ou des conducteurs:

- *Comme revêtement et barrière de diffusion à haute température*. $LaPO_4$ est utilisé en tant que couche interfaciale dans les matériaux composites, grâce à son point de fusion élevé et sa résistance à la corrosion à haute température dans les environnements oxydants.
- *Comme luminophores et émetteurs laser*. Les propriétés d'émission lumineuse de cristaux dopés en $LaPO_4$ sont directement liées à l'enrichissement en éléments substitués dans sa structure comme Ce^{3+}, Eu^{3+}, Tb^{3+}, Yb^{3+}. La plupart des applications dépendent de la cristallographie entre la structure monoclinique de type monazite et la structure tétragonale de $LaVO_4$.
- *Comme conducteurs ioniques*. Des composés de la famille des phosphates et vanadates à structure de type monazite ont des applications spécifiques dans le domaine de conducteurs ioniques.

Mais, elle présente également un intérêt particulier dans les domaines des ressources énergétiques, du stockage des déchets radioactifs et de la géologie :

- *Comme source de terres rares et actinides*. Les métaux stratégiques comme les terres rares ou les actinides sont cruciaux dans les domaines de haute technologie comme par exemple les nanotechnologies, les énergies

renouvelables ou les ressources énergétiques. Les minéraux accessoires représentent 70 à 95% des lanthanides et actinides contenus dans la croûte terrestre (Bea, 1996) et la monazite constitue la principale source de Th et une des principales sources de terres rares (Smith et al., 1999), principalement exploitées dans des dépôts de sable (fossiles ou non).

- *Comme matrice pour le stockage des déchets radioactifs*. La monazite, riche en Th et U radioactifs et présentant une haute durabilité chimique et résistance à l'altération pendant les processus géologiques, est pressentie pour être utile dans le domaine de stockage de longue durée des déchets radioactifs (e.g. Boatner et al., 1980 ; Oelkers and Montel, 2008 ; Schlenz et al., 2013) . La monazite reste parfaitement cristallisée à l'état naturel bien que soumise à de forte doses d'irradiation liées à la désintégration α des chaines radioactives de l'U et du Th (e.g. Seydoux-Guillaume et al., 2004)
- *En géochronologie*. Les monazites naturelles étant souvent riches en Th et U, le Pb radiogénique issu des désintégrations α et β des chaines de désintégration de l'^{238}U, ^{235}U et ^{232}Th peut s'accumuler rapidement. En considérant que les systèmes isotopiques évoluent dans un système clos et que la monazite n'incorpore pas de Pb commun (Parrish, 1990), les mesures chimiques ou isotopiques simultanés d' U, Th et Pb peuvent permettre de déterminer des âges géologiques significatifs.

Le travail présenté dans cette thèse s'intéresse au comportement de la monazite en présence de fluides hydrothermaux. L'étude du fractionnement des terres rares entre la monazite et les fluides hydrothermaux a des implications cruciales pour comprendre la mobilité et les mécanismes de concentration des terres rares dans la croûte terrestre (e.g. Hetherington et al., 2010 ; Harlov et al., 2011). Dans le contexte du stockage des déchets nucléaires, la compréhension des comportements de l'U et du Th contenus dans la monazite en fonction des conditions hydrothermales ou de la nature des fluides

géologiques a des implications pour connaître la destinée des actinides dans les environnements géologiques (e.g. Mathieu et al., 2000). Enfin, la compréhension du comportement de la monazite dans les environnements hydrothermaux est cruciale pour reconstruire l'histoire des évènements métamorphiques ou tectoniques à l'origine des gisements hydrothermaux (e.g. Rasmussen et al., 2007 ; Kempe et al. 2008).

En géologie, au cours des dernières décennies de nombreuses études ont démontré le potentiel des minéraux accessoires comme la monazite pour reconstruire l'histoire géologique des roches. Ces études ont montré que la monazite était particulièrement utile comme chronomètre et traceur pétrogénétique des roches métamorphiques du faciès schiste vert au faciès granulite (Bingen et al., 1996 ; Spear and Pyle, 2002), mais aussi des roches magmatiques (Rapp and Watson, 1986), sédimentaires (Evans and Zalasiewicz, 1996) ou des environnements hydrothermaux (Janots et al., 2012). La composition chimique et isotopique de la monazite apporte de nombreuses informations sur son environnement de formation et sur les variations des paramètres physico-chimiques ayant affectés sa roche hôte.

Des études récentes ont également montré que la monazite n'était pas ou peu sensible à la diffusion du Pb dans les conditions crustales (Cherniak et al., 2004 ; Gardès et al., 2006, 2007) et que malgré sa richesse en actinides, elle était rarement amorphisée (état métamicte) dans le milieu naturel suite aux dégâts d'irradiations (Meldrum, 1997 ; Seydoux-Guillaume et al., 2002, 2004). De plus, les cristaux de monazite peuvent présenter des zonations chimiques et isotopiques pouvant enregistrer différents événements géologiques successifs, et qui peuvent être analysées séparément grâce aux techniques d'analyses in-situ (microsonde électronique, ablation laser, sonde ionique). Le développement de ces techniques ponctuelles au cours des dernières années a permis d'augmenter considérablement la résolution spatiale des analyses et les limites de quantification, permettant de contraindre les variations des concentrations élémentaires et isotopiques à l'échelle des grains de monazite. Ainsi, couplée à une étude pétrologique, l'analyse géochimique et géochronologique de la monazite s'intègre naturellement dans

les études intégrant pression-température-déformation-composition-temps (Hetherington and Dumond, 2013), en particulier dans les environnements ayant subi plusieurs épisodes métamorphiques (par exemple, Franz et al., 1996 ; Pyle and Spear, 2003 ; Janots et al., 2012 ; Kelly et al., 2012).

De nombreuses études sur des échantillons naturels (Poitrasson et al. 1996 ; Poitrasson et al. 2000 ; Mathieu et al. 2001 ; Janots et al., 2008, 2011 ; Bosse et al. 2009 ; Poujol et al. 2010 ; Tartese et al. 2012 ; Seydoux-Guillaume et al. 2012 ; Didier et al. 2013) ou expérimentaux (Teufel and Heinrich, 1997 ; Seydoux-Guillaume et al., 2002a ; Harlov and Hetherington, 2010 ; Hetherington et al., 2010 ; Harlov et al., 2011 ; Williams et al., 2011 ; Budzyń et al., 2011, 2015 ; Shazia et al., 2015) ont montré qu'en présence de fluide, la monazite pouvait recristalliser par un processus de dissolution-précipitation avec une composition chimique ou isotopique différente. Ces études ont également montré que les interactions fluide-monazite pouvaient avoir des conséquences sur le chronomètre U-Th-Pb de la monazite, perturber ou remettre à zéro les âges, et particulièrement à basse température (Bosse et al., 2009 ; Seydoux-Guillaume et al., 2012 ; Didier et al., 2013 ; Wawrzenitz et al., 2012).

Le fractionnement des terres rares et Y (REE+Y), U, Th, Pb entre fluide et monazite ou monazite et monazite (lors d'un épisode de remplacement par exemple) demeure inconnu selon les conditions hydrothermales (ou métamorphiques) et sa compréhension est cruciale pour reconstruire les environnements de précipitation des gisements ou des roches métamorphiques. La compréhension des paramètres (température, composition du fluide et de la monazite, etc.) affectant le géochronomètre est donc cruciale pour l'interprétation des âges enregistrés par la monazite.

Démarche scientifique et organisation du manuscrit

Le travail de recherche présenté dans ce mémoire a été effectué dans la cadre du projet ANR : La monazite hydrothermale : l'accessoire indispensable (Janots, 2012). Il s'intéresse particulièrement au comportement de la monazite lors des interactions fluide-monazite, à travers une approche pluridisciplinaire combinant minéralogie, pétrologie expérimentale, géochronologie, géologie structurale et tectonique. Les objectifs de cette étude sont doubles : 1. Obtenir et comprendre la signification des âges de monazites de veines alpines et les corréler avec la déformation et l'exhumation. 2. Comprendre les partitionnements élémentaires et isotopiques des terres rares, Th, U, Pb et O lors des interactions entre les monazites et les fluides hydrothermaux.

Le **chapitre 2** constitue un rappel sur la monazite en tant que chronomètre et traceur géochimique, le processus de dissolution-précipitation et la méthode de datation U-Th-Pb sur monazite.

Les chapitres suivants correspondent à des articles à différents stades d'avancement :

Les fentes à cristaux (fentes ou veines alpines), appelées aussi « fours » dans le massif du Mont-Blanc en raison de leur forme (cavités de sections ellipsoïdale et d'allongement horizontal), sont relativement fréquentes dans les massifs externes alpins. Ces veines sont de tailles variables, de quelques décimètres à décamétrique. Elles sont fréquemment entourées d'une zone d'altération, de quelques centimètres à quelques décimètres où le quartz de la roche encaissante est (partiellement à totalement) dissous et où d'autres transformations minéralogiques peuvent être observées. Ces fentes correspondent à des veines hydrothermales formées pendant la déformation dans des conditions métamorphiques rétrogrades ($T<450°C$), et dont les épontes sont minéralisées en quartz, albite, chlorite (± épidote) et parfois, en de nombreux minéraux accessoires

(monazite, apatite, xénotime, anatase, rutile). Les monazites de veines alpines permettent ainsi de dater l'hydrothermalisme tardif de ces massifs. Dans ces environnements, la monazite peut (re)cristalliser et chaque épisode de cristallisation peut être daté individuellement. Les différents épisodes de croissance se distinguent par des zonations en éléments traces (REE +Y, Th, U et Pb) dans la monazite. Cependant, la datation de minéralisations hydrothermales est délicate car la majorité des chronomètres souffrent de perturbation de leurs systèmes isotopiques en milieu ouvert (présence de fluides). Ainsi, la compréhension du comportement des chronomètres U-Pb et Th-Pb de la monazite est cruciale pour interpréter les âges des cristaux hydrothermaux. En parallèle, l'étude de monazites hydrothermales à l'échelle de l'arc alpin occidental est nécessaire pour faire le lien entre les âges monazites et les âges de déformation et d'exhumation des massifs. En effet, des études ont montré un lien entre les âges de monazites hydrothermales de veines alpines et les âges traces de fission sur zircons dans les massifs correspondants.

Des échantillons de monazites hydrothermales ont été collectés dans des veines des Massifs Cristallins Externes (Argentera, Belledonne, Mont-Blanc) ainsi que dans les domaines internes (zone Briançonnaise). Dans un premier temps, des échantillons ont été récupérés auprès de collectionneurs grâce à la collaboration avec R. De Ascenção Guedes (minéralogiste). Ensuite, un travail de terrain a été effectué afin de caractériser la roche hôte des veines hydrothermales, leur orientation structurale, et lorsque cela était possible, de ré-échantillonner les veines afin d'obtenir de nouveaux cristaux de monazite. Une trentaine de cristaux de monazites (et quelques xénotimes) provenant de onze veines hydrothermales ont été extraits, montés dans l'époxy et polis afin de pouvoir être analysés au microscope électronique à balayage (MEB) pour identifier d'éventuelles zonations compositionnelles, correspondant potentiellement à différents épisodes de croissance. Les compositions chimiques de ces domaines ont ensuite été analysées à la microsonde électronique (EPMA) au laboratoire ISTerre (Grenoble). Les datations des différents grains ont été effectuées par ablation laser (LA-ICP-MS) au LMV (Clermont-Ferrand) en collaboration avec V. Bosse. Parallèlement, des analyses d'éléments traces (Sr, Eu,

HREE+Y), également par LA-ICP-MS, ont été effectuées afin de corréler leurs concentrations avec les différents domaines d'âge des cristaux de monazite.

Ce travail a permis de discuter la comparaison et la signification des âges Th-Pb et U-Pb de monazites de veines alpines, ainsi que de ceux de xénotimes, et de mettre en évidence les perturbations de ces systèmes liées à leur environnement hydrothermal. Les âges déterminés montrent également des épisodes de croissance courts qui peuvent être reliés à l'échelle des massifs à des épisodes tectoniques intenses. Ces données mettent en évidence le lien entre circulations fluides, cristallisation de monazite et déformation/exhumation dans les Alpes occidentales.

Cette étude est présentée au **chapitre 3**, et correspond à un article soumis à *Mineralogy and Petrology*, qui nécessite des révisions pour sa publication définitive.

Le lien apparent entre les âges monazites et les âges traces de fission sur zircons semble indiquer des températures de cristallisation de monazite dans les veines hydrothermales autour de la température de remise à zéro des âges trace de fission sur zircons (240-280°C), et donc une cristallisation pendant le refroidissement lié à l'exhumation. Cependant, cette hypothèse est en contradiction avec les épisodes de croissances courts et liés à des épisodes tectoniques intenses. Ainsi, le travail suivant porte sur la détermination des conditions de température du fluide responsable de la cristallisation de monazite dans les veines et sur son influence sur le gradient thermique de la roche hôte. Pour cela, des échantillons de roches ont été prélevés à différentes distances (environ 0, 30 et 90m) d'une veine dont les monazites avaient été précédemment datées. Ces échantillons ont été broyés et les zircons séparés et triés. Les datations traces de fission ont été réalisées par M. Bernet à ISTerre (Grenoble). Parallèlement, d'autres cristaux de quartz et monazite ont été extraits de la veine, séparés et polis afin d'effectuer une étude microthermométrique au laboratoire G.E.T. (Toulouse) en collaboration avec D. Guillaume. Des tests de détermination de la composition du fluide, responsable de la cristallisation de monazite, ont été réalisés dans des cristaux de

quartz dont la croissance semblait contemporaine de celle de la monazite, par LA-ICP-MS en collaboration avec M.C. Boiron au laboratoire GéoRessources (Nancy).

Ce travail a permis de comparer les températures de cristallisation de monazite et des circulations de fluides associées avec les âges de refroidissement à l'échelle locale. L'influence des circulations fluides sur le gradient géothermique ainsi que la signification des âges monazite ont ainsi pu être discutées.

Cette étude est présentée au **chapitre 4**, et correspond à un article en préparation.

La seconde partie du travail réalisé au cours de cette thèse s'appuie sur une approche expérimentale pour étudier le fractionnement des REE+Y, U, Th, Pb entre fluide / monazite ou monazite / monazite, en fonction des paramètres physico-chimiques du fluide (température, fugacité en oxygène, composition, etc.), lors des épisodes d'altération hydrothermale. En effet, la compréhension du comportement de la monazite en présence de fluide est cruciale pour reconstruire l'histoire des évènements métamorphiques ou tectoniques à l'origine de sa cristallisation ou de ses différents épisodes de cristallisation. De plus, les compositions élémentaires (HREE+Y) ou isotopiques (^{18}O) dans la monazite peuvent renseigner sur les conditions de température au moment de sa cristallisation. Ces géothermomètres sont cependant mal contraints à basse température (<400 °C) et nécessitent de nouvelles calibrations.

Une vingtaine d'expériences hydrothermales ont été réalisées dans des autoclaves à joint froid simultanément dans les laboratoires ISTerre (Grenoble) et G.E.T. (Toulouse), en collaboration avec D. Guillaume. Le standard de monazite Manangotry, de composition chimique homogène, a été utilisé pour ces expériences. Les fractionnements monazite-monazite et fluides-monazite ont été étudiés à 2 kbar en fonction de différents paramètres incluant la température entre 300 et 600°C, la composition du fluide (H2O, NaCl 10wt.% et NaOH 1 ou 2 M), les rapports fluide/monazite et la fugacité d'oxygène. Des cristaux de quartz pré-fracturés ont été ajoutés dans les expériences pour piéger les fluides hydrothermaux lors des réactions d'altérations. Les fluides ont également été

dopés en ^{18}O afin de retracer les recristallisations éventuelles et d'étudier la répartition isotopique de l'oxygène entre la monazite et le quartz. Les produits solides expérimentaux ont été extraits, rincés et montés dans l'époxy avant d'être analysés au MEB pour identifier les domaines d'altération de la monazite et les éventuels minéraux secondaires. Ces zones ont ensuite été analysées à l'aide de nombreuses techniques analytiques incluant EPMA (Isterre, grenoble), microscope électronique à transmission (MET, Centre de micro-caractérisation Raimond Castaing, Toulouse), spectroscopie Raman (coll. J. Hövelmann, Institut für Mineralogie, Münster), Nano-SIMS (coll. C. Höschen, Technische Universität München, Munich), LA-ICP-MS (coll. V. Bosse, LMV, Clermont-Ferrand). Les cristaux de quartz ont été polis afin de pouvoir analyser les fluides piégés durant les expériences par LA-ICP-MS (coll. M.C. Boiron, GéoRessources, Nancy).

Les résultats de ces expériences ont permis de discuter les mécanismes intervenant lors des interactions entre les fluides hydrothermaux et la monazite, qui peuvent se traduire par du remplacement par dissolution-précipitation couplée ou des surcroissances par dissolution-précipitation non-couplée. L'étude MET a montré le rôle prépondérant de la porosité et de nano-fractures à l'interface de dissolution-précipitation pour la progression du front de réaction. Enfin le rôle de la composition du fluide pour le fractionnement élémentaire lors des interactions hydrothermales a pu être discuté. Les implications de ces travaux concernent notamment la compréhension de la mobilité et des mécanismes de concentration des terres rares (métaux stratégiques) et actinides dans la croûte terrestre, ainsi que le stockage des déchets radioactifs.

Cette étude est présentée au **chapitre 5**, et correspond à un article en préparation.

Les analyses chimiques (EPMA) et isotopiques (LA-ICP-MS) des domaines de monazite recristallisés aux cours des expériences hydrothermales ont montrés que le système chronométrique U-Th-Pb de la monazite souffrait de perturbation dues aux interactions fluide-monazite. Ces perturbations ont été mises en évidence par la mesure

(quasi-) systématique de Pb à la microsonde éléctronique dans les domaines recristallisés et sont dépendantes de la température de l'expérience. L'étude MET a permis de révéler un remplacement partiel à l'origine de mélange de domaines (primaire et recristallisé) à l'échelle nanométrique. Ce mécanisme a des implications importantes pour le chronomètre U-Th-Pb de la monazite, notamment lors des épisodes de dissolution-précipitation en présence de fluides hydrothermaux, et particulièrement à basse température. Les processus de remise à zéro (partielle ou totale) du chronomètre U-Th-Pb et l'incorporation du Pb par la monazite lors des réactions hydrothermales ont pu être discuté.

Ce travail est présenté au **chapitre 6**, et correspond à un article en voie de soumission à *Geology*.

2. LA MONAZITE

2.1. Structure cristallographique

La monazite est un phosphate de terres rares légères (LREE, Th, U)PO_4 (Fig. 2-1), présent comme minéral accessoire dans la majorité des roches magmatiques et métamorphiques crustales. Elle représente une des principales source de lanthanides et d'actinides dans la croûte (Bea, 1996; Smith et al., 1999) et contrôle le comportement et le budget de ces éléments dans les roches (e.g. Montel, 1993). Elle est communément présente en grains disséminés dans les roches cristallines ou dans les sables mais on l'observe aussi en masse grossièrement grenue ou en cristaux (Fig. 2-1A). Ceux-ci sont généralement micrométriques à millimétriques bien qu'ils puissent atteindre plusieurs centimètres dans les pegmatites ou les veines hydrothermales (Fig. 2-1B).

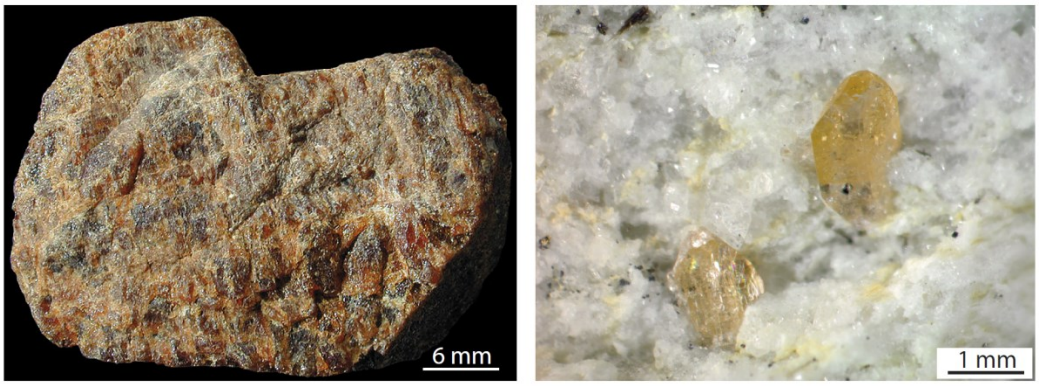

Figure 2-1 A. Monazite de Madagascar (44 mm). Collection César Novak. B. Cristaux de monazite hydrothermale sur quartz. Vallon d'Entre deux Roches, Celliers, Savoie.

La monazite cristallise avec une structure monoclinique dans le groupe d'espace $P2_1/n$ (Z = 4). Ses propriétés structurales ont été décrites précisément pour la première fois par Ni et al. (1995). Les paramètres de maille de la monazite sont de l'ordre de a = 6.823 (Å), b = 7.026 (Å), c = 6.499 (Å) et β = 103.79 (Å) pour un volume V = 302.60 (Å^3), pour le standard Moacyr par exemple (Seydoux-Guillaume et al., 2002c). Sa structure est basée sur deux types de sites présents en quantités égales avec les cations

métalliques, coordinés à neuf anions O^{2-} (Fig. 2-2A), formant des nonaèdres, et des tétraèdres contenant le phosphore (Ni et al., 1995). Les nonaèdres et les tétraèdres partagent une arrête formant des chaines (Fig. 2-2B) alignées selon l'axe *c* (direction [001]) qui sont reliées entre elles par les arrêtes des nonaèdres adjacents (Fig. 2-2C).

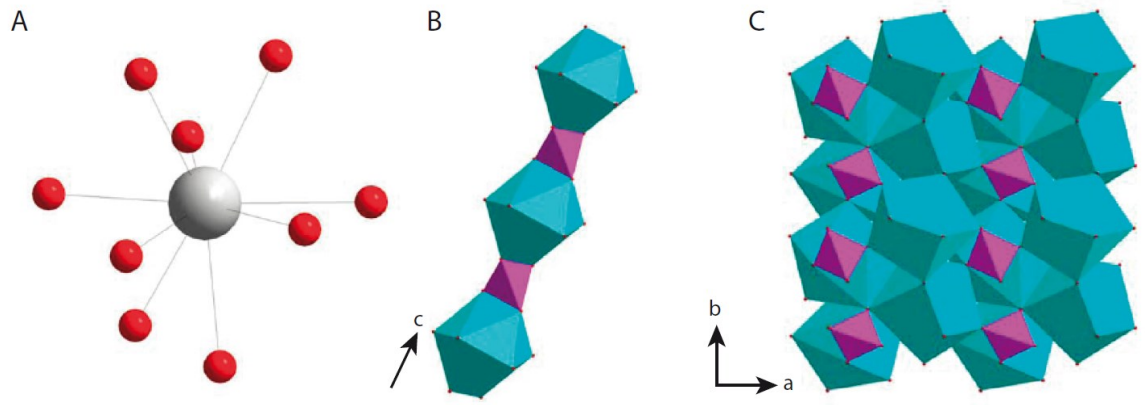

Figure 2-2 A. Coordination des terres rares (en blanc) avec l'oxygène (en rouge). B. Chaine de nonaèdres (contenant les terres rares) et tétraèdres (contenant le phosphore) selon l'axe c. C. Structure de la monazite. (extrait de Clavier et al., 2011)

Les monazites naturelles peuvent incorporer des terres rares lourdes (HREE) et de l'Y dans leur réseau cristallin par substitution des LREE, mais en faible quantité due à la taille importante des sites nonaèdriques. Le rayon ionique des HREE+Y étant plus faible que celui des LREE, la structure évolue vers celle du xénotime $(Y,HREE)PO_4$, tétragonale et identique à celle du zircon. Dans les monazites naturelles, les concentrations en Y et HREE individuelles n'excèdent généralement pas 0.1 et 0.02 cations pour quatre oxygènes, respectivement (Heinrich et al., 1997).

Les monazites peuvent également incorporer du Th et de l'U tétravalents grâce notamment à deux substitutions couplées (Van Emden et al., 1997) faisant intervenir du Ca et du Si :

$$(1)\ Si^{4+} + Th(U)^{4+} \Leftrightarrow REE^{3+} + P^{5+}\ \text{(huttonite)}$$

$$(2)\ Ca^{2+} + Th(U)^{4+} \Leftrightarrow 2REE^{3+}\ \text{(chéralite)}$$

Pour incorporer les actinides, les monazites naturelles forment en réalité une solution solide entre le pôle monazite $LREEPO_4$ et les pôles chéralite $CaTh(PO_4)_2$ et huttonite $ThSiO_4$ qui possèdent une structure de type monazite (Montel et al., 2002). La monazite incorpore préférentiellement le Th à l'U (Van Emden et al., 1997) et le rapport Th/U des monazites est généralement > 1.

Bien que le Pb initial ne soit pas (ou très peu) incorporé dans les monazites naturelles (Parrish, 1990, Montel et al., 1996) mais présent sous forme de Pb radiogénique, des brabantites de Pb ($PbCa(PO_4)_2$ ont déjà été synthétisées (Montel et al., 2002). D'autres cations comme le Sr ou l'As (sous sa forme pentavalente) peuvent également être incorporés dans les monazites naturelles (e.g. Janots et al., 2006, 2010 ; Gnos et al., 2015), tout comme S^{6+} (e.g. Jercinovic and Williams, 2005). De plus, une distance REE-O est légèrement supérieure aux huit autres, ce qui induit une distorsion des polyèdres $REEO_9$ (Boatner, 2002). Cette distorsion ainsi que la grande diversité de cations pouvant être incorporés (largement reportés dans Clavier et al. 2011) prodiguent à la monazite une grande flexibilité chimique qui se traduit par une stabilité sur une large gamme de pression-température.

2.2. Occurrences

De nombreuses études ont montré que la monazite pouvait se trouver dans une grande variété d'environnements géologiques, incluant les roches magmatiques et les roches de tous les grades du métamorphisme. Elles sont abondantes dans les métapélites et plus rares dans les roches de compositions mafiques ou calciques. Initialement, les monazites étaient considérées instables aux plus basses conditions métamorphiques (Overstreet, 1967) ou présentes sous forme de grains détritiques (Suzuki and Adachi 1991 ; Suzuki et al. 1994 ; Hawkins and Bowring 1999 ; Ferry 2000 ; Catlos et al. 2001 ; Rubatto et al. 2001 ; Wing et al. 2003 ; Krenn et al, 2008 ; Cottle et al., 2012). Cependant, des travaux ont démontré que la stabilité de ce minéral pouvait s'étendre au domaine diagénétique (Evans and Zalasiewicz, 1996 ; Evans et al., 2002 ; Allaz et al., 2013) ainsi qu'au métamorphisme de très bas degré (Ferry, 2000 ; Rasmussen, 2001 ; Cabella et al., 2001 ; Wing et al., 2003 ; Janots et al., 2006, 2008 ; Allaz et al., 2013) et aux auréoles métamorphiques de basse pression (Ferry, 2000 ; Wing et al., 2003).

En contexte métamorphique, la monazite s'observe dans les roches du faciès schiste vert (Franz, 1996 ; Townsend et al., 2000 ; Catlos et al., 2002 ; Rasmussen et al., 2007 ; Bollinger et Janots, 2006 ; Krenn and Finger, 2007 ; Janots et al., 2008, 2011), amphibolite (Bingen et al., 1996 ; Janots et al., 2008 ; Krenn et al., 2008 ; Nakano et al., 2015), granulite (Smith and Barreiro, 1990 ; Bingen et al., 1996 ; Hawkins and Bowring, 1997 ; Bea and Montero, 1999 ; Pyle et al., 2001). Bien que la présence de monazite ait été rapportée dans des pélites de ultra-haute pression (Terry et al., 2000), le comportement de la monazite est peu documenté (Krenn and Finger, 2004 ; Janots et al., 2006 ; Finger and Krenn, 2007) dans les environnements métamorphiques de haute pression (faciès schiste bleu à éclogite). Enfin, il a été démontré que la monazite était la principale phase porteuse de LREE, Th et U dans les migmatites (Bea, 1996) et fréquemment observée comme phase résiduelle des épisodes de fusion crustale ou anatexie (e.g. Schnetger, 1994). Ces observations ont été confirmées par des études

expérimentales qui ont montré que la monazite était peu soluble dans les liquides peralumineux (e.g. Montel, 1986, 1993 ; Rapp et al., 1987 ; Stepanov et al., 2012) et qu'elle y était moins soluble que dans les liquides peralcalins. D'autres études montrent une dépendance forte de la solubilité de la monazite dans les magmas avec la température (e.g. Rapp and Watson, 1986 ; Stepanov et al., 2012).

Les minéraux de terres rares principaux dans les roches métamorphiques sont la monazite (LREE,Th,U)PO_4, le xénotime (HREE,Th,U)PO_4 et l'allanite CaLREE(Fe)(Al, $Fe)_2(SiO_4)_3(OH)$ et plus rarement, la florencite $CaAl_3(PO4)_2(OH)_6$, les fluorocarbonates de terres rares : synchisite $Ca(Ce,La)(CO_3)_2F$, bastnaesite $LREE(CO_3)F$ et parisite $Ca(LREE)_2(CO_3)_3F_2$, la britholite $Ca_2REE_3(SiO_4)_3(OH, F)$ ou le rhabdophane $(LREE)PO_4,H_2O$. Le xénotime peut être présent dans la plupart des roches métamorphiques, tout comme la monazite. Cependant, il a tendance à disparaitre dans les roches riches en grenat qui incorporent également les HREE. Tous les minéraux cités précédemment peuvent être précurseurs de la monazite dans les roches métamorphiques. Les transitions de phases entre la monazite et l'allanite ont été les plus étudiées parmi ces minéraux. Dans certaines roches métamorphiques, l'allanite cristallise préférentiellement au dépend de la monazite dans les conditions inférieures à celle du faciès amphibolite (Overstreet 1967 ; Smith and Barreiro, 1990 ; Kingsbury et al.1993 ; Bingen et al. 1996 ; Harrison et al. 1997 ; Ferry, 2000 ; Rubatto et al. 2001 ; Pyle, 2001 ; Wing et al. 2003 ; Janots et al., 2006, 2008, 2011). Des études ont montré que les transitions de phase entre monazite et allanite sont influencées par la composition chimique de la roche hôte et particulièrement de sa teneur en Ca et Al (Janots et al., 2007 ; Spear, 2010), la croissance d'allanite étant favorisée dans le roches riches en Ca et pauvre en Al.

2.3. Textures et compositions

Les cristaux de monazites présentent fréquemment des zonations chimiques (Fig. 2-3) et/ou isotopiques dans les roches métamorphiques (e.g. Parrish, 1990 ; Zhu and O'Nions, 1999 ; Ayers et al., 1999 ; Townsend et al., 2000 ; Pyle et al., 2001 ; Pyle and Spear, 2003 ; Gibson et al., 2004 ; Finger et al., 2007 ; Janots et al., 2008, 2011 ; Didier et al., 2014, 2015 ; Janots and Rubatto, 2014), qui peuvent traduire l'évolution prograde et/ou rétrograde de leur roche hôte. Les réactions métamorphiques peuvent donner lieu à des textures complexes qui peuvent correspondre à plusieurs épisodes de croissance/dissolution pendant l'interaction avec les fluides métamorphiques (e.g. Pyle and Spear, 2003). Dans les roches magmatiques, ces zonations sont le plus souvent concentriques et reflètent l'évolution de la composition du magma pendant la cristallisation avec la composition d'équilibre de la monazite (Williams et al., 2007).

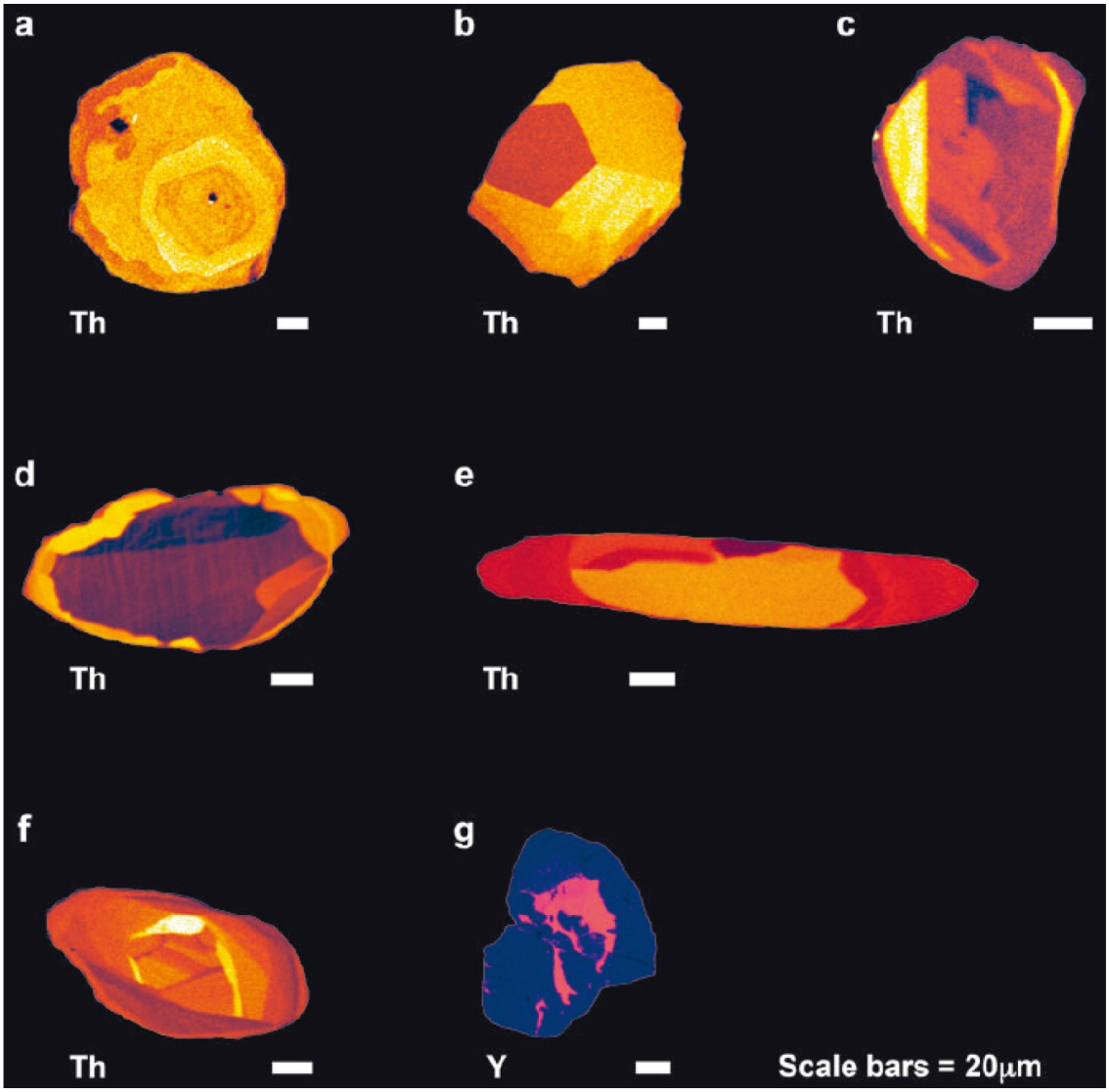

Figure 2-3 Exemples de zonation complexes dans la monazite (extrait de Williams et al., 2007)

Les images en électrons rétrodiffusées (BSE back-scattered electron) au microscope électronique à balayge (MEB) peuvent être utiles pour identifier les différents domaines de la monazite. Cependant, malgré la facilité d'utilisation de cette technique, les images font surtout ressortir les variations de compositions en éléments les plus lourds (Th par exemple). Des cartographies chimiques en U, Th, Y, Ca, Si et Pb à la microsonde électronique notamment, sont utiles pour délimiter les domaines de composition mais ces

éléments doivent être choisis en fonction de la pétrographie et de la géochimie de la roche hôte. Récemment, une étude a montré que la spectrométrie de masse à ionisation secondaire (Nano-SIMS) pouvait également être utilisée pour étudier la composition isotopique à l'échelle sub-micrométrique (Fig 2-4 ; Didier et al., 2015).

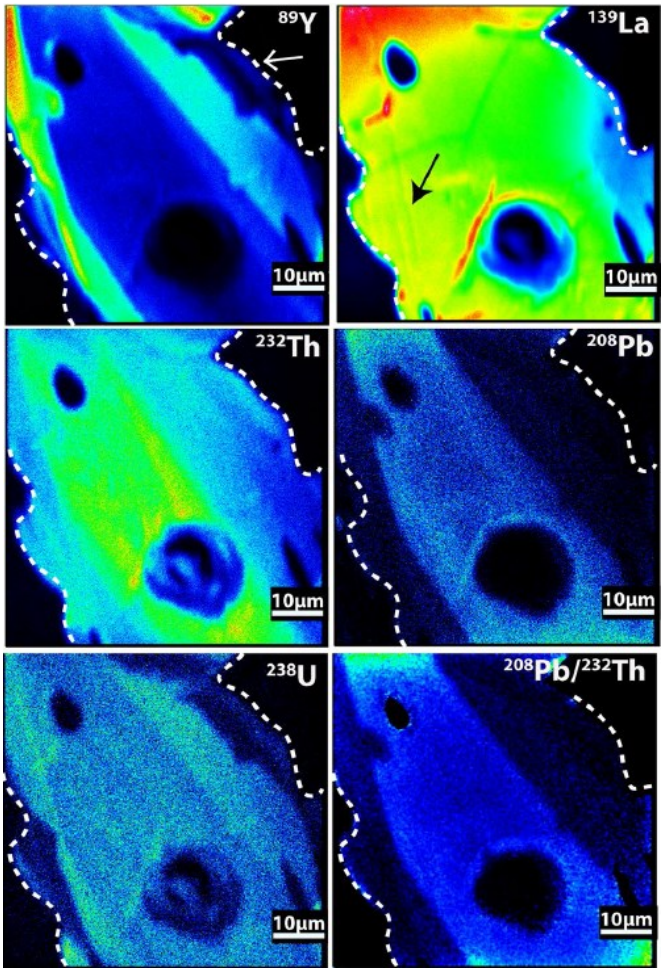

Figure 2-4 Exemple de cartographies isotopiques de monazite réalisées à la Nano-SIMS. Notez l'intérêt des cartographies $^{208}Pb/^{232}Th$ pour identifier les différents domaines d'âge de la monazite. (extrait de Didier et al., 2015)

Les monazites magmatiques sont caractérisées par des concentrations en Th importantes (Franz et al., 1996) sauf dans les carbonatites où les concentrations en Th sont plus faibles (e.g. Wall and Mariano, 1996). Dans les roches métamorphiques, des variations importantes de la concentration en thorium, au sein de différents domaines d'un grain de monazite, peuvent être contrôlées par le minéral précurseur de la monazite, les conditions de pression-température ou des interactions avec un fluide (Catlos et al., 2013). Cependant, il n'existe pas de relation claire entre la concentration en Th et le degré du métamorphisme. Seules les monazites diagénétiques contiennent généralement peu de Th (Cabella et al., 2001). Les monazites hydrothermales peuvent avoir des concentrations en ThO_2 quasi-nulle (~0.2 ppm, Kempe et al., 2008) ou, au contraire, de plusieurs pourcents (~4-5 wt.% ThO_2, e.g. Janots et al., 2012 ; Gnos et al., 2015). Les concentrations en U et Th de la monazite ont été étudiées par Janots et al. (2012) et son reportées Figure 2-5.

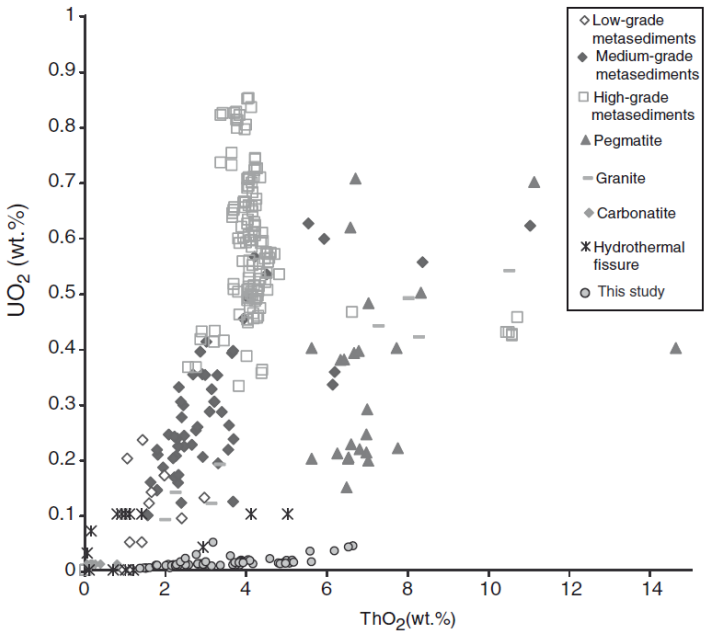

Figure 2-5 Concentrations en Th et U de monazites en fonction de leur environnement pétrologique. *This study* correspond à des monazites hydrothermales. Extrait de Janots et al. (2012)

Des études ont montrées que la concentration en Y (+HREE) dans la monazite, coexistant avec le xénotime, pouvait être reliée aux conditions de pression-temperature au moment de sa cristallisation et utilisée comme géothermomètre (Gratz and Heinrich 1997, 1998 ; Andrehs and Heinrich, 1998 ; Heinrich et al., 1997 ; Pyle et al. 2001 ; Seydoux-Guillaume et al., 2002b). Ainsi, les monazites formées dans un environnement de haut grade métamorphique peuvent présenter des concentrations en Y importantes (e.g. Krenn and Finger, 2010). Cependant, la concentration en Y de la monazite est variable et liée à différents paramètres tels que la stabilité des minéraux primaires et accessoires riches en Y (e.g. xenotime, allanite, grenat) au moment de sa cristallisation (e.g. Zhu and O'Nions, 1999b ; Spear and Pyle, 2010).

2.4. Le chronomètre U-Th-Pb de la monazite

2.4.1. Principe

La monazite est généralement riche en Th et U (Bea, 1996). Elle possède trois systèmes chronométriques issus de ses trois couples isotopiques : $^{238}U/^{206}Pb$, $^{235}U/^{207}Pb$, $^{232}Th/^{208}Pb$. La désintégration des isotopes pères (^{238}U, ^{235}U, ^{232}Th) en isotopes fils (^{206}Pb, ^{207}Pb, ^{208}Pb) stables, s'effectue au long de chaînes radioactives émettant des particules α ou β (Fig. 2-6). Ainsi, au cours du temps, les quantités de Th et d'U décroissent régulièrement alors que les quantités de Pb, issues de la désintégration radioactive, augmentent proportionnellement.

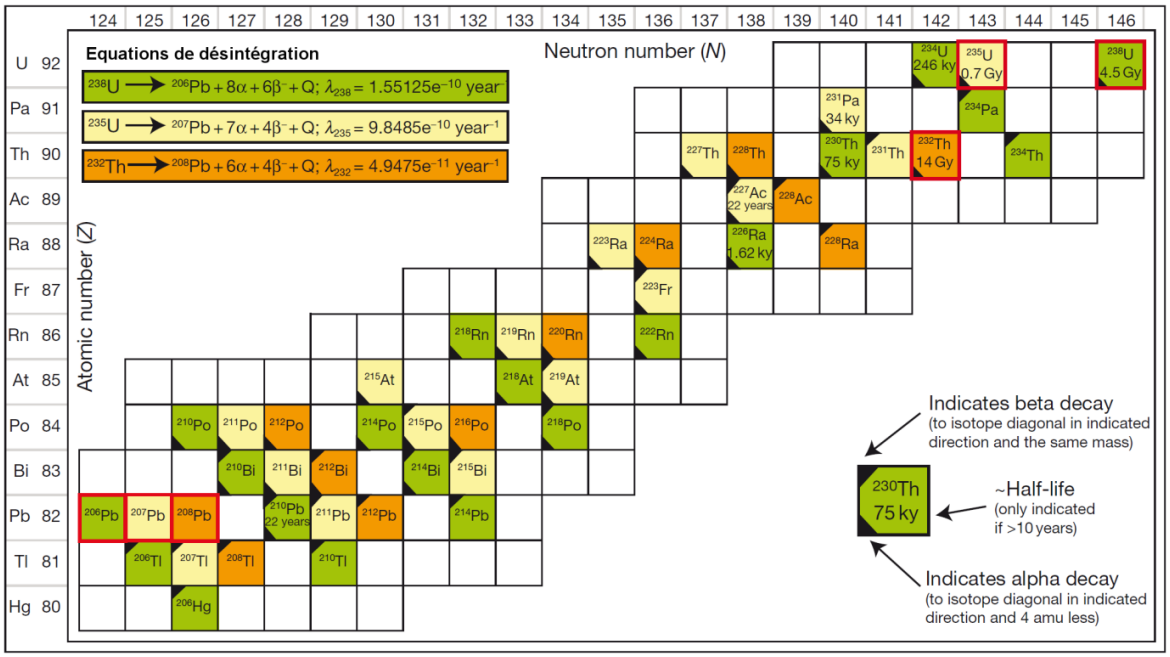

Figure 2-6 Représentation des chaînes de désintégration radioactive des systèmes U-Pb et Th-Pb. Les couleurs correspondent à chaque chaîne dont les équations sont données. α : émission d'une particule alpha ; β : émission d'une particule beta ; Q : énergie relâchée (extrait de Schoene, 2014)

La datation est possible pour les systèmes U-Pb et Th-Pb car l'équilibre séculaire est rapidement atteint, c'est-à-dire que la quantité d'isotopes fils produites est égale à la quantité d'isotopes pères désintégrée. En effet, les demi-vies de ^{238}U, ^{235}U et ^{232}Th sont beaucoup plus longues que les demi-vies de leurs radionucléides fils respectifs. On peut alors négliger les radionucléides intermédiaires et considérer que l'U et le Th se désintègre directement en Pb :

$$^{238}U \rightarrow {}^{206}Pb \ (t_{1/2} = 4.4688 \text{ Ga}, \lambda = 1.551 \times 10^{-10} \text{ a}^{-1})$$
$$^{235}U \rightarrow {}^{207}Pb \ (t_{1/2} = 0.7038 \text{ Ga}, \lambda = 9.849 \times 10^{-10} \text{ a}^{-1})$$
$$^{232}U \rightarrow {}^{208}Pb \ (t_{1/2} = 14.05 \text{ Ga}, \lambda = 4.933 \times 10^{-9} \text{ a}^{-1})$$

La datation isotopique de la monazite implique également qu'elle n'incorpore pas de Pb initial lors de sa cristallisation et évolue en système clos. Ainsi, on considère que la monazite incorpore peu (ou pas) de Pb dans sa structure lors de sa cristallisation (Parrish, 1990 ; Montel et al., 1996), le rayon ionique du Pb étant trop élevé. De plus, des études expérimentales récentes (Cherniak et al., 2004 ; Gardès et al., 2006 ; Gardès et al., 2007 ; Cherniak and Pyle, 2008) ont montré que la monazite était très robuste à la diffusion du Pb ou du Th dans la majorité des conditions crustales (températures < 800 °C).

Ainsi, la mesure des rapports isotopiques $^{206}Pb/^{238}U$, $^{207}Pb/^{235}U$, $^{208}Pb/^{232}Th$ permet de calculer trois âges à partir des équations suivantes, en considérant la teneur initiale en Pb radiogénique comme nulle (avec λ la constante de désintégration de l'U ou du Th) :

$$^{206}Pb = {}^{238}U\ (e^{\lambda_{238}t} - 1)$$

$$^{207}Pb = {}^{235}U\ (e^{\lambda_{235}t} - 1)$$

$$^{208}Pb = {}^{232}Th\ (e^{\lambda_{232}t} - 1)$$

Dans le cas des monazites de veines alpines jeunes (âges de quelques millions d'années) comme celles étudiées dans cette thèse, on discute préférentiellement les âges $^{232}Th/^{208}Pb$ car : 1. Les monazites hydrothermales ont des rapports Th/U fréquemment élevés (Poitrasson et al., 2000 ; Pyle, 2006 ; Janots et al., 2012 ; Seydoux-Guillaume et al. 2012) et peuvent être très pauvres en U; 2. La chaîne de désintégration de l'U peut être en déséquilibre dans les monazites jeunes (Scharer, 1984), résultant en une surestimation des âges $^{238}U/^{206}Pb$. En effet, la monazite peut incorporer préférentiellement du ^{230}Th, produit intermédiaire de la chaîne de désintégration radioactive du ^{238}U, lors de sa cristallisation, et induire un excès de ^{206}Pb (e.g. Janots et al., 2012) ; 3. La concentration en Th de la monazite étant généralement importante, le ^{232}Th est assez abondant pour considérer que

le ^{208}Pb issu du Pb initial est négligeable comparé au ^{208}Pb radiogénique (Bosse et al., 2009 ; Janots et al., 2012).

2.4.2. Diagramme Concordia et Tera-Wasserburg

Lorsque les systèmes ne contiennent initialement pas ou une quantité négligeable de Pb initial, on traite généralement les données U-Pb (ou U-Pb, Th-Pb) dans des diagrammes Concordia (Wetherill, 1956), dans lequel on reporte les rapports $^{206}Pb/^{238}U$ en fonction des rapports $^{207}Pb/^{235}U$ (ou $^{208}Pb/^{232}Th$). La courbe représentée dans ces diagrammes représente alors la courbe des âges « concordants » entre les deux systèmes étudiés (Fig. 2-8A). Si le système a été ouvert, les deux chronomètres donnent des âges différents qui se trouveront alors en dehors de la courbe Concordia. Si le système a subit une perte de Pb ou un gain d' U, les âges alors « discordants », se trouveront au-dessous de la Concordia. Dans le cas inverse, les points se trouveront au-dessus (Fig. 2-7A). Il arrive également que les âges s'alignent sur une droite, appelée alors Discordia, entre deux points de la courbe Concordia. Cette droite correspond, le plus souvent, au mélange d'âges entre deux domaines dont les âges correspondent à ceux des intersections entre les courbes Concordia et Discordia. Cependant, l'alignement des analyses sur la Discordia peut également correspondre à une perte en Pb, par diffusion suite à un évènement thermique ou dans le cas des minéraux métamictes (zircons par exemple) dont la structure a été fortement altérée. Dans le cas de perte en Pb par diffusion, l'intercept inférieur correspond à l'âge de l'évènement perturbateur et l'intercept supérieur à l'âge de cristallisation du minéral, et dans le cas des minéraux métamictes les âges s'alignent sur une droite passant par l'origine.

Si le système a incorporé du Pb initial (dont on ne peut estimer la quantité), au moment de la cristallisation de son minéral hôte, on utilise alors le diagramme Tera-Wasserburg (Fig. 2-7B, Tera and Wasserburg, 1972) dans lequel on reporte les rapports $^{207}Pb/^{206}Pb$ en fonction des rapports $^{238}U/^{206}Pb$. Dans le cas de présence de Pb initial la droite Discordia coupe la Concordia en deux points. L'intersection supérieure donne la composition du Pb initial au moment de la cristallisation du minéral, et l'intersection inférieure la composition du Pb radiogénique donc l'âge de fermeture du système isotopique.

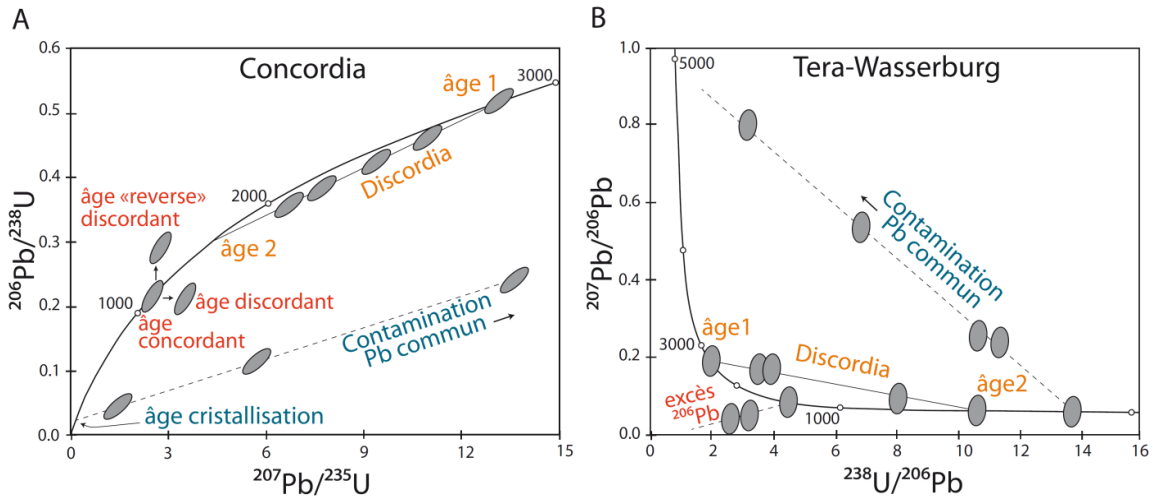

Figure 2-7 Diagrammes Concordia (A) et Tera-Wasserburg (B) dans lesquels sont reportés les principales perturbations des systèmes isotopiques (mélange entre différents domaines, contamination Pb commun, excès ^{206}Pb)

2.4.3. Les différentes techniques d'analyse ponctuelles

Les datations isotopiques in-situ peuvent être effectuées par ablation et ionisation par un faisceau d'ions primaires (SIMS) ou par ablation laser couplée à la spectrométrie de masse à source plasma (LA-ICP-MS) comme celles présentées dans cette étude (Chapite 3). L'intérêt de cette technique est de pouvoir analyser séparément chaques domaines

compositionnels de la monazite et éventuellement contraindre plusieurs épisodes de cristallisation.

L'autre technique de datation utilisée au cours de cette thèse est la datation chimique par microsonde électronique (EMP ou EPMA) développée par Suzuki et Adachi (1991, 1994) et Montel (1996). Le principe est d'obtenir un âge à partir des concentrations en U, Th et Pb de la monazite. Ainsi le Pb mesuré (Pb_{total}) correspond au Pb radiogénique produit par les trois systèmes isotopiques et au Pb commun (^{204}Pb). En utilisant les lois de désintégration de la monazite, on obtient :

$$Pb_{total} = \left[^{232}Th\left(e^{\lambda_{232}t} - 1\right)\right] + \left[^{238}U\left(e^{\lambda_{238}t} - 1\right)\right] + \left[^{235}U\left(e^{\lambda_{235}t} - 1\right)\right] + {}^{204}Pb$$

En considérant que la monazite n'intègre pas de Pb commun dans sa structure lors de sa cristallisation et que la composition isotopique de l'U dans la monazite correspond à celle de la croûte, on obtient :

$$Pb_{total} = \left[^{232}Th\left(e^{\lambda_{232}t} - 1\right)\right] + \left[^{238}U \times 0.9928\left(e^{\lambda_{238}t} - 1\right)\right] + \left[^{235}U \times 0.072\left(e^{\lambda_{235}t} - 1\right)\right]$$

L'âge peut alors être obtenu par itération à partir de l'équation précédente. Contrairement à la méthode isotopique qui permet de contrôler la concordance entre les systèmes, la méthode chimique implique que la monazite n'incorpore pas de Pb lors de sa cristallisation et que les teneurs en U, Th et Pb n'aient pas été modifiées au cours du temps (système clos) pour déterminer un âge significatif. On considère également que la quantité de Pb radiogénique produit par l'U et le Th dans la monazite, n'est suffisante

pour être analysée qu'au bout d'environ 100 Ma (Montel, 1996) et avec une erreur globale d'environ 20-30 Ma pour des monazites hercyniennes, par exemple. Ainsi, cette méthode n'a pas pu s'appliquer aux monazites alpines étudiées au cours de cette thèse (~30 Ma maximum). Cependant, la résolution spatiale (~1-2 μm) permet la datation de monazites présentant des textures complexes de manière rapide et non-destructive.

2.5. Altération hydrothermale

2.5.1. Le processus de dissolution-précipitation

Ce paragraphe s'appuie sur l'article de Ruiz-Agudo et al., 2014

Dès le début des années 1950, Goldsmith and Laves (1954) proposèrent que les transformations de feldspaths pouvaient résulter d'un mécanisme de dissolution du minéral parent et de précipitation d'une phase qui le remplace, en conditions hydrothermales, contrairement au mécanisme de diffusion à l'état solide à plus haute température et sans eau. En 1967, O'Neil and Taylor suggérèrent la présence d'un mécanisme de dissolution-précipitation interfacial pour expliquer le remplacement de feldspath potassique par du feldspath sodique. Ils affirment également que le front de réaction est associé à la présence d'une fine couche de fluide à l'interface de remplacement. Plus récemment, des études ont démontré le couplage entre les processus de dissolution-précipitation à l'interface de réaction à l'origine des remplacements pseudomorphiques et étudié les conditions nécessaires au développement de porosité dans le minéral parent (Puntis, 2002, 2009 ; Putnis and Putnis, 2007).

Le principe du processus de dissolution-précipitation couplée repose sur la formation d'un film de fluide interfacial sursaturé (vis-à-vis d'une ou plusieurs phases stables) lors de la dissolution d'un minéral par un fluide avec lequel il n'est pas à l'équilibre (Fig. 2-8A). Une ou plusieurs de ces phases peuvent alors précipiter à la surface du minéral parent (Fig. 2-8B) initiant une réaction autoentretenue grâce au couplage des taux de dissolution et de précipitation. De cette façon, le minéral parent peut transmettre ses informations cristallographiques au minéral qui le remplace si des critères d'épitaxie existent entre ces deux minéraux. La propagation du front de réaction continue tant que le fluide interfacial est relié à un réservoir de fluide (Fig. 2-8B,G). Cette connexion est possible grâce notamment à la présence de porosité induite par un changement de volume molaire entre parent et produit ainsi que par les différences de solubilités des phases au niveau du fluide interfaciale (Pollock et al., 2011, Raufaste et al., 2011).

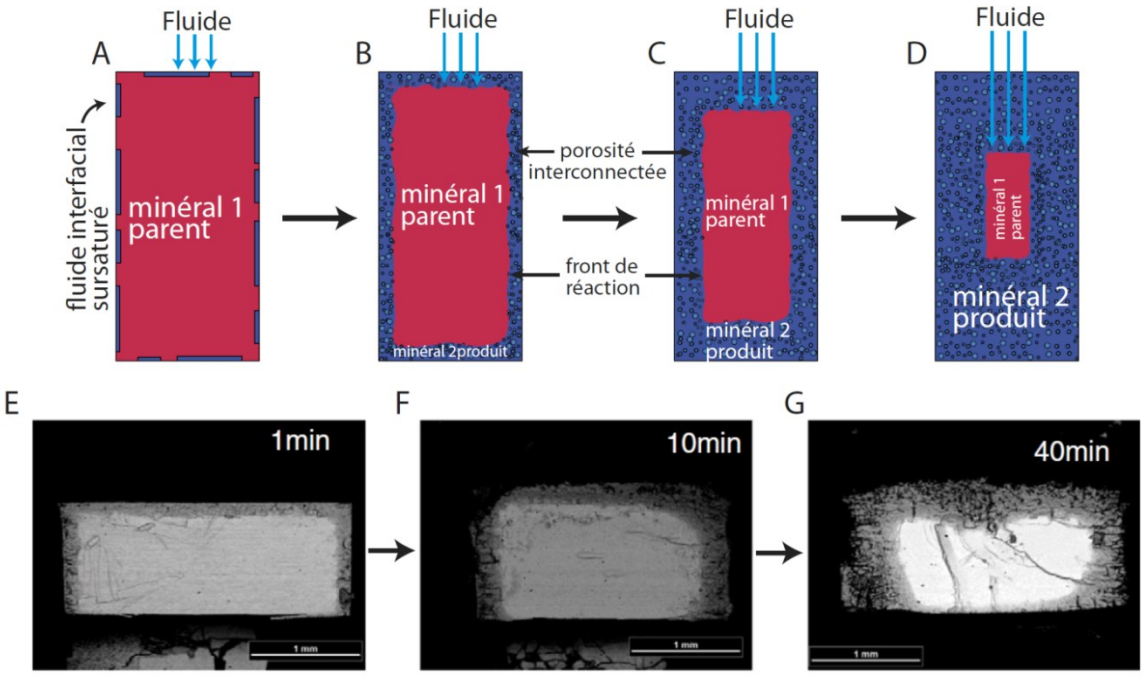

Figure 2-8 Schéma de remplacement pseudomorphique par dissolution-précipitation couplée à l'interface (A-D). Expérience de remplacement pseudomorphique de KBr par KCl avec développement de porosité (E-G). (modifié à partir de Ruiz-Agudo et al., 2014)

Dans le cas de différences de volumes molaires importantes entre le parent et le produit, les contraintes générées peuvent induire de la facturation permettant également de propager le front de réaction (Fig. 2-9). C'est le cas, par exemple, lors de remplacement de leucite par analcime (Putnis et al., 2007; Jamtveit et al., 2009), d'ilménite par rutile (Janssen et al., 2010), d'aragonite par calcite (Perdikouri et al., 2011) ou de scolecite par tobermorite (Dunkel and Putnis, 2014). Un autre exemple de fracturation a lieu pendant les processus de serpentinisation (Plümper et al., 2012) et est attribuée à des contraintes générées par la croissance et la transformation d'une phase de proto-serpentine amorphe métastable dans des pores de dissolution.

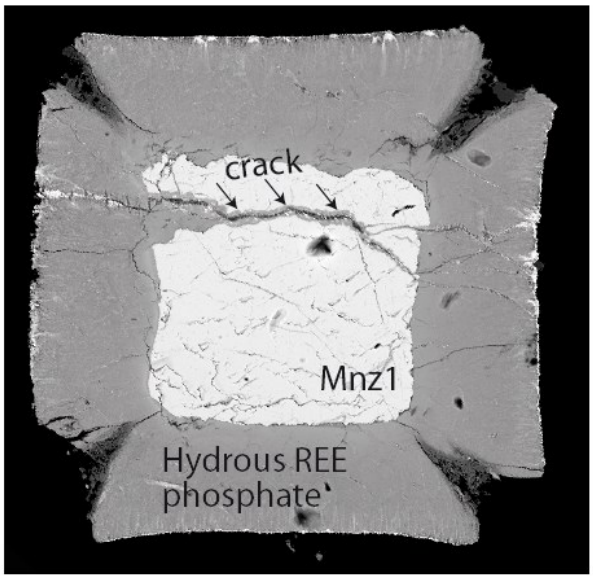

Figure 2-9 Image en électron rétrodiffusés (BSE) au microscope électronique à balayage (MEB) de remplacement de monazite primaire (mnz1) à 600°C, 200MPa en présence de NaOH, par un phosphate de terres rares hydraté (Hydrous REE phosphate) réalisé au cours de cette thèse. Notez la différence de volume importante entre la monazite parent et le minéral secondaire ainsi que la fracturation (crack) induite par ce changement de volume. Taille de l'image 1,2 mm

2.5.2. Dissolution-précipitation de monazite

Dans le cas de dissolution-précipitation de monazite naturelle, la monazite primaire (parent) peut être remplacée par une monazite avec une composition chimique différente ou par un minéral secondaire (produit) incorporant les éléments de la monazite (Fig. 2-10). On reporte par exemple, les cas de remplacement de monazite par monazite, apatite, allanite, thorite, thorianite, uraninite, rhabdophane, bastnäesite ou synchysite (e.g. Finger et al., 1998 ; Poitrasson et al., 2000; Broska, 2005 ; Harlov et al., 2007 ; Berger et al., 2008 ; Hetherington and Harlov, 2008 ; Bosse et al., 2009 ; Budzyn et al., 2010 ; Didier et al., 2013, 2015; Janots et al., 2011, 2012 ; Petrik and Konečný, 2011 ; Gasser et al., 2012 ; Ondrejka et al., 2012 ; Seydoux-Guillaume et al., 2012).

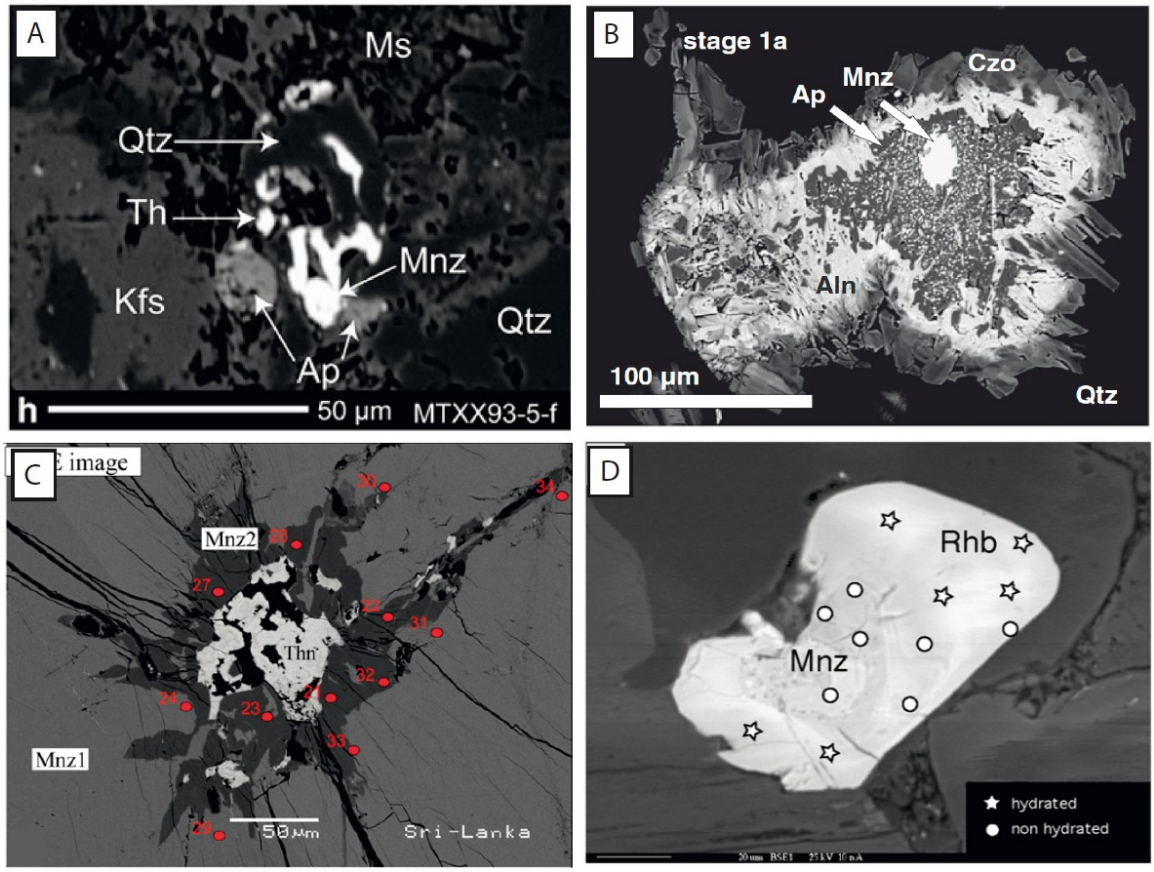

Figure 2-10 Exemples naturels de remplacement de monazite par dissolution-precipitation en image BSE. A : monazite altérée (Mnz) et minéraux secondaires (Ap : apatite ; Th : silicate de thorium) du granite de Montasset (Didier et al., 2013). B : Cœur relique de monazite (Mnz) entouré d'apatite (Ap) et thorite avec une couronne externe composée d'allanite (Aln) et clinozoïsite (Czo) ; Ondrejka et al., 2012. C : Zone d'altération d'une monazite primaire (Mnz1) en monazite secondaire (Mnz2) et thorianite (Thn) ; Seydoux-Guillaume et al., 2012. D : Remplacement pseudomorphique de monazite par rhabdophane (Rhb) ; Berger et al., 2008.

Dans les environnements métamorphiques ou magmatiques, de nombreuses études sur les monazites naturelles (e.g. Poitrasson et al. 1996 ; Poitrasson et al. 2000 ; Mathieu et al. 2001 ; Berger et al., 2008 ; Hetherington and Harlov, 2008 ; Bosse et al. 2009 ; Poujol et al. 2010 ; Tartese et al. 2012 ; Seydoux-Guillaume et al. 2012 ; Didier et al. 2013) ont montré que la monazite pouvait réagir en présence de fluide et ce, même à basse température, par un processus de dissolution-précipitation. Ces réactions peuvent se

traduire par la cristallisation de domaines de différentes concentrations chimiques et/ou isotopiques, en U, Th, et REE+Y, au sein des grains de monazite. Les monazites altérées présentent régulièrement des domaines enrichis ou appauvris en Th (le plus visible) ou en un autre élément (e.g. Hawkins and Bowring, 1997; Bingen and van Breemen, 1998 ; Ayers et al. 1999 ; Cocherie et al. 2005 ; Pyle et al. 2005 ; Rasmussen and Muhling, 2007 ; Bosse et al., 2009 ; Seydoux-Guillaume et al., 2012 ; Didier et al., 2013).

Enfin, des travaux ont montré que la monazite pouvait être utile pour dater la déformation dans les zones de cisaillement. Dans ce cas, la monazite va recristalliser sous forme de grains néoformés alignés ou de surcroissances dans les ombres de pression (Dumond et al., 2008 ; Wawrzenitz et al., 2012) par dissolution-précipitation, qu'il est alors possible d'analyser pour dater la déformation.

2.5.3. Approche expérimentale

Des expériences ont été réalisées dans le but d'étudier la solubilité et les cinétiques de dissolution de monazite naturelle (Ayers and Watson, 1991 ; Oelkers and Poitrasson, 2002 ; Schmidt et al., 2007) ou de pôles synthétiques (e.g. Liu and Byrne, 1997 ; Devidal et al., 1998 ; Poitrasson et al., 2004 ; Cetiner et al., 2005 ; Schmidt et al., 2007 ; Pourtier et al., 2010 ; Tropper et al., 2011, 2013). Ces études ont montré que la monazite était très peu soluble dans l'eau pure et que sa solubilité augmentait avec l'augmentation ou la diminution du pH et était dépendante de la nature des ligands en solutions (F^-, OH^-, Cl^-, CO_2^-, SO_4^{2-}). Un tableau synthétique des expériences de solubilité est présenté Table 2-1.

D'autres études se sont intéressées au comportement du chronomètre de la monazite (U-Pb et Th-Pb) en présence de fluide (Teufel and Heinrich, 1997 ; Seydoux-Guillaume et al., 2002a). Ces premiers travaux expérimentaux ont montré que le processus de dissolution-précipitation était plus efficace que la diffusion volumique pour remettre à zéro le chronomètre de la monazite. Ils ont initié une série d'études (Fig. 2-11) s'intéressant à la stabilité de la monazite en présence de fluide (Seydoux-Guillaume et al.,

2002a ; Harlov et al., 2007 ; Hetherington et al., 2010 Harlov et al., 2010 ; Williams et al., 2011 ; Harlov et al., 2011 ; Budzyń et al., 2011, 2015 ; Richard et al., 2015 ; Shazia et al., 2015), et dont les conditions expérimentales et les résultats principaux sont résumés dans la Table 2-2. Ces études ont montré que la composition du fluide jouait un rôle prépondérant dans le contrôle de la stabilité de la monazite, les fluides alcalins (riches en NaOH, KOH ou $Na_2Si_2O_5$) étant les plus efficaces pour reproduire expérimentalement par dissolution-précipitation les textures complexes observées dans les monazites naturelles contrairement aux saumures (NaCl, KCl) avec lesquelles seuls quelques pores de dissolution sont observés (Richard et al., 2015). Bien que la température ait un contrôle limité sur le processus de dissolution-précipitation (Budzyń et al., 2011), les résultats expérimentaux indiquent néanmoins une augmentation du volume de monazite remplacée avec l'augmentation de la température.

Table 2-1 Experimental background on monazite solubility experiments

Reference	T (°C)	P (MPa)	Duration (hours)	Fluid composition	pH	Starting Mnz	Selected results	Methods
Tropper et al., 2013	800	1000	12	H_2O-NaF	near neutral	pure $CePO_4$	monazite solubility greater in NaF than in NaCl	weight-loss
Tropper et al., 2011	800	1000	90	H_2O	near neutral	pure $CePO_4$	low solubility in pure H_2O	weight-loss
			12-90	H_2O-NaCl		pure $CePO_4$	solubility increase with NaCl concentration	
			12	H_2O-NaCl		[1]North Carolina		
*Pourtier et al., 2010	350-800	200	72-360	H_2O	1-8	pure $NdPO_4$	$Nd(OH)3^0$ main species at 650 °C and 2000 bars (pH from 4 to 6)	weight-loss and ID-TIMS
	300-800			H_2O-NaCl		pure $NdPO_4$	$Nd(OH)^{2+}$ in acidic conditions, $Nd(OH)_2^+$ in neutral conditions and $Nd(OH)_3^0$ in alkaline solution at 300 °C and 2000 bars.	
Schmidt et al., 2007	25-800	0.1-2000	0.8-11	H_2O+HCl±NaCl	-0.5-1	pure $LaPO_4$	lower mobility of Y, Gd, and Th compared to that of the LREE	in situ SR-XRF
				H_2O+HCl		[2]Kakola monazite	strong enrichment of Th relative to the LREE and Pb in monazite	
Cetiner et al., 2005	23 and 50	-	20 (days)	H_2O+HCl±NaCl	1-1.2	pure $LaPO_4$	retrograde monazite solubility from 23 to 150 °C	ICP-AES ICP-MS (solution)
						pure $SmPO_4$	low solubility up to 300°C, even at low pH and high chloride concnentrations	
	23, 50 and 150	1-1.4				pure $NdPO_4$		
Poitrasson et al., 2004	21, 70, 200, 300	-	0-296 (days)	H_2O+HCl	2	pure $NdPO_4$	retrograde solubility under acidic conditions from 70 to 300 °C	ICP-MS (solution)
	21					pure $GdPO_4$		
Oelkers and Poitrasson, 2002	50-230	-	0-14 (days)	H_2O±HCl±NaOH ±(NH_4OH+NH_4Cl)	1.5-10	[3]Manangotry	low solubilty at 70°C, near neutral pH solubility increase with pH increase (10) or decrease (2)	ICP-MS (solution)
Liu and Byrne, 1997	25	-	2days-5months	$HClO_4$ (0.1m)	1	Pure $REEPO_4$	HREE+Y solubility higher than LREE solubility	spectrophotometry (P)
Ayers and Watson, 1991	800-1100	1000-2800	24	H_2O, HCl (1M), NaCl(1M)	neutral to acidic	-	same solubility with NaCl and H_2O decrease the pH increase solubility	weight-loss

[1]Heavy mineral sand deposit located in Cleveland County, North Carolina (UCLA, Department of Geology mineral collection catalog number MS-1762); see Williams et al., 2011

[2]natural monazite from Kakola, Turku, Finland (Suominen, 1991)

[3]Manangotry monazite from Anosyan granite, Madagascar; see e.g. Montel et al., 1996, Seydoux-Guillaumet et al., 2004

*Extend of previous data obtained by Gibert and Montel, 1996 and Devidal et al., 1998

La compréhension des réactions de dissolution-précipitation de la monazite est fondamentale en géochronologie. En effet, des travaux sur des échantillons naturels ont montré que les interactions fluide-monazite pouvaient avoir des conséquences sur le chronomètre U-Th-Pb de la monazite, et perturber les âges, et particulièrement à basse température (Bosse et al., 2009 ; Seydoux-Guillaume et al., 2012 ; Didier et al., 2013 ; Wawrzenitz et al., 2012). Expérimentalement, des études montrent que du Pb peut être mesuré dans les domaines recristallisés par dissolution-précipitation (e.g. Harlov et al., 2011 ; Budzyń et al., 2015 ; Shazia et al., 2015), ou non (Williams et al., 2011). L'impact du mécanisme de remplacement sur l'incorporation du Pb dans la monazite ainsi que sur la signification géologique des domaines de remplacement est toujours controversée.

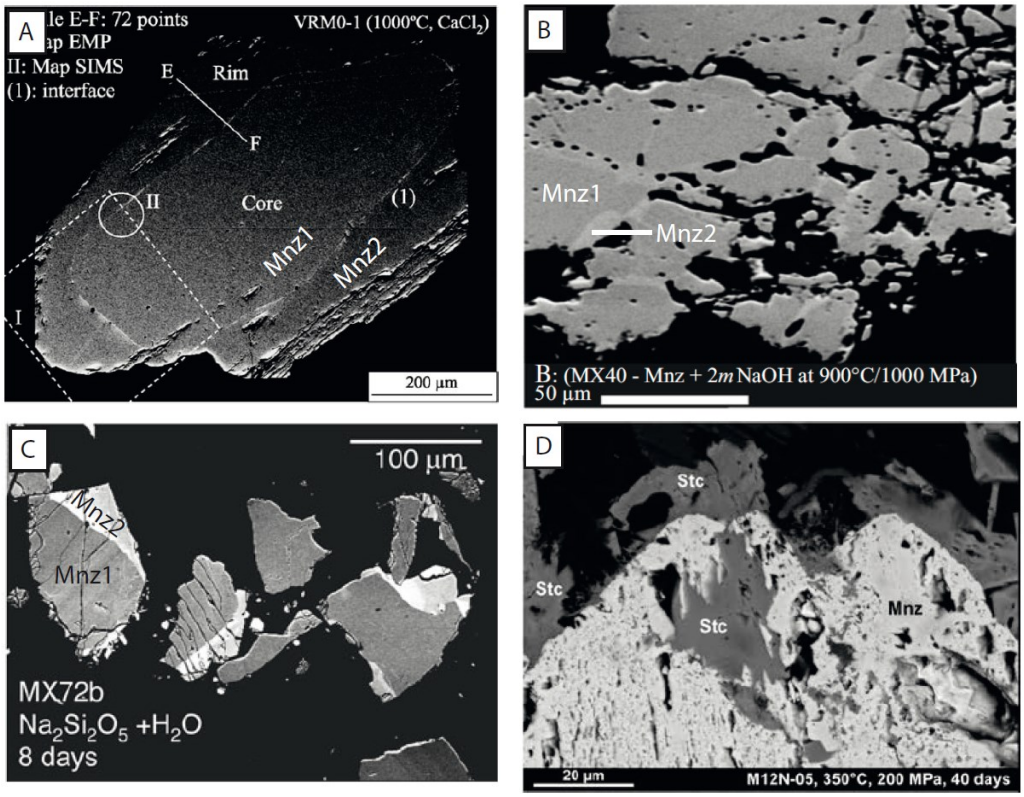

Figure 2-11 Exemples d'expériences d'altération hydrothermale de monazite par dissolution-précipitation en présence de $CaCl_2$ (A), NaOH (B) et $Na_2Si_2O_5$ (C-D). Mnz1 : monzaite primaire ; Mnz2 : monazite secondaire ; Stc : Steacyite (silicate avec Th). A. Seydoux-Guillaume et al., 2002a ; B. Hetherington and Harlov, 2010 ; C. Harlov et al., 2011 ; D. Budzyń et al., 2015.

Légende de la Table 2-2 (page suivante):

[1]Pegmatite in Burnet County, Texas, USA (see Budzyń et al., 2015)

[2]Ruschel et al., 2012

[3]Heavy mineral sand deposit located in Cleveland County, North Carolina (UCLA, Department of Geology mineral collection catalog number MS-1762); see Williams et al., 2011

[4]Heavy mineral sands deposit at Cumuruxatiba, Bahia State, Brazil.; highly suspected to be the same monazite than 3

[5]Moacyr standar monazite from Itambe pegmatite district (Brazil, Cruz et al., 1998)

[6]Monazite from a lower amphibolite-facies metapelite from NE, Bavaria, Germany; also described in Heinrich et al., 1996

F/M ratio: Fluid/Monazite (mg); Mnz: monazite; Mnz2: secondary monazite; n.a.: not analizyed; Ab: albite; Kfs: K feldspar; Bt: biotite; Ms:muscovite; Stc: Steacyite; Ap: Apatite; Amph: amphibole; Brit: britholite; Trk: turkestanite

Reference	T (°C)	P (MPa)	Duration (days)	Fluid composition	Starting solid assemblage	Starting Mnz	F/M ratio	Mnz size (µm)	Mnz1 compo. (wt.%)		
									ThO_2	UO_2	PbO
Budzyń et al., 2015	250	200	40	$Na_2Si_2O_5+H_20$	Mnz+Ab+Kfs+Bt+Ms+SiO_2	[1]Burnet	1.9	50-250 crushed grains	9.4-17	0.3-0.4	0.51-0.68
	350	200	40				1.9				
	350	400	20				2				
Shazia et al., 2015	800	200	19	H_20	Mnz+Kfs+SiO_2	[3]North Carolina	2	50-200 crushed grains	7.3-8.2	0.4-0.6	0.13-0.14
Budzyń et al., 2011	450	450	16	$Na_2Si_2O_5+H_20$	Mnz+Ab+Ms+SiO_2+CaF_2	North Carolina	2	50-100 crushed grains	7.3-8.4	0.3-0.7	0.09-0.14
	500	450	16		Mnz+Ab+Kfs+Ms+Bt+SiO_2+CaF_2		2				
Harlov et al., 2011	900	1000	25	NaOH 2N	Mnz+SiO_2+Al_2O_3	[4]Brazil heavy sand deposit	3	5-200 crushed grains	6.3-8.1	0.2-0.5	0.11-0.17
	900	1000	8	$Na_2Si_2O_5+H_20$	Mnz		2				
	900	1000	2	$Na_2Si_2O_5+H_20$	Mnz		2.1				
	900	1000	8	$Na_2Si_2O_5+H_20$	Mnz+Al_2O_3		2.1				
	900	1000	7	KOH 2N	Mnz+SiO_2		1.3				
	900	1000	8	KOH 2N	Mnz+SiO_2+Al_2O_3		2.3				
	600	1000	49	KOH 2N	Mnz+SiO_2+Al_2O_3		1.7				
	600	1000	23	NaOH 2N	Mnz+SiO_2+Al_2O_3+$ThSiO_4$		1.3				
	600	1000	23	$Na_2Si_2O_5+H_20$	Mnz+SiO_2+Al_2O_3+$ThSiO_4$		2.1				
	900	1000	25	KOH 2N	Mnz+SiO_2+Al_2O_3		3.3				
	900	1000	2	$Na_2Si_2O_5+H_20$	Mnz+Al_2O_3		2				
Williams et al., 2011	450	450	16	$Na_2Si_2O_5+H_20$	Mnz+Ab+Ms+CaF_2	North Carolina	2	50-300 crushed grains	7.1-8.8	0.4-0.6	0.14-0.16
Harlov and Hetherington, 2010	900	1000	8	$Na_2Si_2O_5+H_20$	Mnz	Brazil heavy sand deposit	2	50-200 crushed grains	7-8	0.4-0.5	0.12-0.13
Hetherington et al., 2010	900	1000	8	NaOH 2N	Mnz	Brazil heavy sand deposit	0.2	100-500 crushed grains	7.8±0.2	0.6±0.1	n.a.
	900	1000	8	$Na_2Si_2O_5+H_20$	Mnz		0.1				
Seydoux-Guillaume et al., 2002	1000	1000	21	$CaCl_2$ 10 wt.% + SiO_2	Mnz	Brazil Itambe pegmatite (Moacyr)	5.2	200-400 rounded grains	6.92	0.13	0.16
	1000	1000	14	HNO_3+Pb(std)+SiO_2	Mnz		11.2				
Teufel and Heinrich, 1997	400	300	28	H_2O	Mnz	[6]Metapelite, Bavaria	2	<1-15 sharp edges	-	0.09	0.09
	650	300	28								
	750	300	28								

Table 2-2 (1/2) Synthèse des expériences hydrothermales de remplacement de monazite

Secondary minerals	Observations			Pb in Mnz2
	Textures	Mnz2 compositions /Mnz1	Mnz2 Th-U-Pb compositions	
Stc+Mnz2 REE-Ap+Stc+Amph+Mnz2 REE-Ap+Stc+Amph+Mnz2	strong dissolution with porosity, internal zoning (patchy	LREE enrichment HREE+Y depletion increase of LREE/HREE+Y	ThO_2 (4-5 wt. %), UO_2 (0.5-0.1 wt.%) and PbO (0.06 to 0.14 wt. %) depletion	yes
Mnz2	internal sector zoning, no porosity	no REE significant variation slight Si increase and Ca decrease with Th increase	Th enrichment or constant; Pb concentration increases with Th or constant between Mnz1 and Mnz2	no
Mnz2+F-Ap+Brit+Trk	strong dissolution with porosity, internal zoning (patchy)	LREE enrichment HREE+Y, Ca depletion increase of LREE/HREE+Y	strong Th and U depletion, Pb below detection limit	no
Mnz2 (± britholite nano-inclusions)	Extensive ThSiO4-enriched textures on monazite rim	LREE, Si enrichment HREE+Y, Ca depletion increase of LREE/HREE+Y	Systematic Th enrichment, no significant U variations, Significant Pb depletion in only one experiment	yes yes yes n.a.
	ThSiO4-enriched texture along the rim of some Mnz grain	no significant variation		yes yes
	ThSiO4-enriched texture along the rim of one Mnz grain	LREE, Si enrich.; HREE, Ca depl.		yes yes
	Faint reaction rim	no significant variation		n.a. yes n.a.
Mnz2 + inclusions (?)	Lobate reaction front at the edges of the original grain or arround inclusions and fractures	LREE, Si enrichment HREE+Y, Ca depletion increase of LREE/HREE	ThO_2 depletion (1-2 wt.%), UO_2 almost absent (0-0.2 wt.%), PbO almost absent (between 0-40 ppm)	no
Mnz2	Extensive ThSiO4-enriched textures on monazite rim, no porosity	No significant variation	ThO_2 enrich. (11-16 wt.%), UO_2 slight depletion (0.2 wt.%), No PbO in Mnz2	no
Mnz2	prononced porosity and dissolution channels with Mnz2 domains around	No significant variation of REE	No significant variation of Th, U	n.a.
	limited pore development, unclear internal zoning or sharp Mnz2 domain along Mnz1 rim	heterogeneous variation of REE	ThO_2 slight enrich. (9 wt.%), UO_2 slight depletion (0.2 wt.%)	n.a.
Mnz2	significant overgrowth	(HREE+Y) depletion	Th enrichment at the interface and in Mnz2 U depletion, no Pb in Mnz2	no
	significant overgrowth	no significant variation	Perturbated ages, incorporation of Pb from the doped solution	yes
Mnz2	roundish grain shape after experiment	-	U, Pb depletion rejuvenation of ages which increases with temperature	n.a.
	grain growth, roundish subhedral grains	-		n.a.
		-		n.a.

Table 2-2 (2/2)

3. DATATIONS DE MONAZITES DE VEINES ALPINES

Interpretation of Th-Pb and U-Pb in-situ ages of hydrothermal monazite: Evidence from a large-scale regional study in clefts from the western Alps

(Article nécessitant des révisions pour sa publication définitive à Mineralogy and Petrology)

A. Grand'Homme[1], E. Janots[1], V. Bosse[2], A.M. Seydoux-Guillaume[3], R. De Ascenção Guedes

[1]ISTerre, Univ. Grenoble Alpes, BP 53, 38041 Grenoble, France (alexis.grandhomme@ujf-grenoble.fr)
[2]LMV, Clermont Université, Université Blaise Pascal, BP 10448, 63000 Clermont-Ferrand, France
[3]GET, UMR 5563 CNRS-UPS-IRD, Toulouse, France

Keywords Monazite; Alps; Hydrothermal activity; U-Th-Pb dating; Xenotime; LA-ICPMS; Tectonic exhumation

Note: Supplementary material 3-1 and 3-2 correspond to Annexes 3-1 and 3-2 and Fig.X or Table X to Fig. 3-X or Table 3-X

Abstract

Alpine clefts correspond to orogenic mineralizations that formed during deformation under retrograde metamorphic conditions (T < 450°C). In these veins, large monazite (and xenotime) crystals up to few millimeters long can precipitate from hydrothermal fluids. The monazite crystals in clefts are commonly zoned in composition and age, indicating successive growth episodes. In one single crystal, in-situ dating through different compositional domains then offers a unique possibility to investigate not only the timing but also the duration and episodicity of monazite growth under hydrothermal conditions.

In this study, eleven open hydrothermal veins (clefts) have been investigated in the western Alps (external and internal massifs) through in-situ LA-ICPMS dating on monazite and xenotime crystals. Cleft monazite gives well-resolved Th-Pb ages (typically with 0.1-0.3 Ma resolution) indicative of growth episodes with a duration shorter than the analytical resolution. Most generally, dating in distinct compositional domains gives overlapping ages, but some crystals have registered distinct crystallization episodes that can be separated by up to 2 Ma. In three grains (RDN sample), ages vary progressively from core (10.3 Ma) to rim (8.1 Ma) suggesting continuous growth. However, the microstructure of this grain is indicative of a replacement by coupled dissolution-precipitation processes that may have disturbed the U-Th-Pb systematics. Comparison of U-Pb and Th-Pb dating indicates that the U-Pb systematics can be successfully used for monazite with low Th/U ratio (typically <30). In one cleft, with coexisting monazite and xenotime, xenotime was dated using the monazite analytical protocol. Hydrothermal xenotime has remarkably high Th/U ratios and U-Pb dating shows evidence of ^{206}Pb excess. In comparison, Th-Pb dating gives reliable ages (between 33.6 ± 2.1 and 36.2 ± 1.5 Ma) that are close but higher than the monazite date obtained in the same cleft (32.3 ± 0.3 Ma).

The Th-Pb dataset obtained here confirms brief episodic monazite crystallization that is likely attributed to periods of higher tectonic activity. Correlation with other

geochronological data suggests that this crystallization occurred shortly after the late ductile deformation stages, in a host-rock that had already cooled down to a temperature close to the zircon fission track. In the Belledonne massif, the new monazite ages confirm two periods of hydrothermal activity in the vertical veins at around 13-11 Ma and 8-6 Ma, respectively. Remarkably, these ages are equivalent to those previously published for the Aar massif. Only one vertical cleft monazite was investigated in the Mont-Blanc massif but it gives an age similar to that of the early population of the Belledonne massif (11.1 ± 0.2 Ma). Monazite dating therefore indicates similar late-stage tectonic activity from the Belledonne to the Aar massifs, probably due to dextral movements along major strike slip faults. On the other hand, monazite dating in the Argentera (20.6 ± 0.3 Ma) confirms the regional diachronism observed from South to the North in the External Crystalline Massifs (ECM) along the western Alps. The Th-Pb dating in two clefts are the first to date the hydrothermal activity in the Internal Domains in the western Alps. As expected from other thermochronometers, hydrothermal activity in the Internal Alpine domains (Briançonnais) is older than in the ECM. In the Briançonnais zone, monazite with an age of 32.3 ± 0.3 Ma coincides with the exhumation along the Penninic front. In the second cleft, monazite with an age of 23.3 ± 0.2 Ma is more complex to attribute to a specific deformation stage.

3.1. Introduction

Alpine clefts correspond to hydrothermal mineralization in an orogenic context. These veins were formed during deformation under retrograde metamorphic conditions at maximum temperature and pressure of respectively 450-500°C and 3-4 kbar (e.g. Mullis et al. 1994; Mullis 1996). Vein formation is characterized by an important structural control, with major crustal accidents allowing hydrothermal fluid circulation. Similar to gold-bearing veins studied in the Alps (Marshall et al. 1998; Pettke et al. 1999), the veins formed during late-stage orogenic activity, simultaneously with a change to large-scale strike-slip faulting and rapid exhumation (Goldfarb et al. 2001), in metamorphic units.

However, the age and duration of hydrothermal mineralization in these veins are necessary to define the link between deformation, exhumation and fluid circulation. In these centimeter to meter-sized veins, hydrothermal fluids react with the host-rock, leading to mass transfer and subsequent precipitation of hydrothermal minerals, including monazite (LREE, Th, U)PO_4, on the hanging walls. Relatively ubiquitous in metamorphic veins and mesozonal ore deposits, monazite is successfully used to determine the timing of mineralization (e.g. Rasmussen et al. 2007; Kempe et al. 2008). Due to negligible diffusion of radiogenic Pb in monazites under cleft formation conditions (Cherniak et al. 2004; Gardés et al. 2006a; 2007), U-Pb and Th-Pb isotopic systems are very useful for dating mineral growth and distinguishing between possible successive crystallization episodes. Experimental (Teufel and Heinrich 1997; Seydoux-Guillaume et al. 2002a; Harlov and Hetherington 2010; Hetherington et al. 2010; Harlov et al. 2011; Williams et al. 2011; Budzyn et al. 2011) and petrological (Poitrasson et al. 1996; Poitrasson et al. 2000; Mathieu et al. 2001; Bosse et al. 2009; Poujol et al. 2010; Tartese et al. 2012; Seydoux-Guillaume et al. 2012; Didier et al. 2013) studies have shown that, in the presence of fluid, monazite can recrystallize by a dissolution-precipitation process with element fractionation. In a hydrothermal environment, monazite can re-precipitate with a distinct Th/U ratio (Seydoux-Guillaume et al. 2012), incorporating various amounts of initial or radiogenic Pb (e.g. Krenn et al. 2011; Didier et al. 2013), which can significantly affect chemical/isotopic ages. The understanding of U-Pb and Th-Pb chronometer behavior is then crucial for interpreting hydrothermal crystal ages.

A first attempt at in-situ Th-Pb dating on cleft monazites was successfully performed by Gasquet et al. (2010) to propose a late Miocene tectonic scenario in the External Crystalline Massifs (ECM) for the 15-5 Ma period. Based on this study, Janots et al. (2012) showed that U-Pb and Th-Pb dating of cleft monazites in the central Alps (Aar and Gotthard massifs) can provide new constraints on the hydrothermal fluid evolution together with crystallization ages. Berger et al. (2013) suggested a link between cleft monazite crystallization ages and brittle deformation in the central Alps (Aar massif) and indicated that these ages may be similar to zircon fission track (ZFT) ages. In the Tauern

Window (central Alps), Gnos et al. (2015) determinated U-Pb and Th-Pb cleft monazite ages, linking monazite composition to host-rock reduction/oxidation conditions. In hydrothermal veins, monazite dating of grain compositional domains suggests a short-lived (<0.1 Ma) episodic growth rather than long-lived crystallization (>1 Ma) due to progressive cooling of the cleft fluid (Janots et al. 2012). These studies demonstrate that cleft monazite is a powerful aid for dating late-stage orogenic hydrothermal activity associated with brittle deformation during the Alpine belt exhumation.

This study presents an extended Th-Pb and U-Pb isotopic dataset of cleft monazite and xenotime ([Y, HREE, U, Th]PO_4) in both the External Crystalline Massifs (south Mont Blanc, Belledonne and Argentera) and the Internal Domains (Briançonnais Zone) of the western Alps (Fig.1). Monazite ages are discussed and compared to zircon fission track dating (closure temperature below 280° C, e.g. Yamada et al. 1995; Bernet 2009) or $^{40}Ar/^{39}Ar$ deformation/cooling ages on mica to correlate the timing of monazite growth with late-stage deformation events and cooling during the exhumation of the western Alps. This large dataset provides new insights for interpreting hydrothermal monazite ages and their implications for the timing of hydrothermal activity at the western Alps scale.

3.2. Geological settings of the western Alps

The Alps result from the closure of the Ligurian part of the Tethys Ocean and the collision between Eurasian and African plates. From west to east, the main units of the western Alps (Fig. 1) are: the External (Dauphiné or Helvetic) Domains, and the Internal Domains composed of the lower Penninic units (Valais and Briançonnais Zone) and the upper Penninic units (Piedmont Internal Crystalline massif, Liguria-Piedmont “Schistes Lustrés” and Austro-Alpine units). Internal units correspond to a collisional prism, ormed during subduction-collision of the Tethyan Ocean and parts of the European continental margin. In

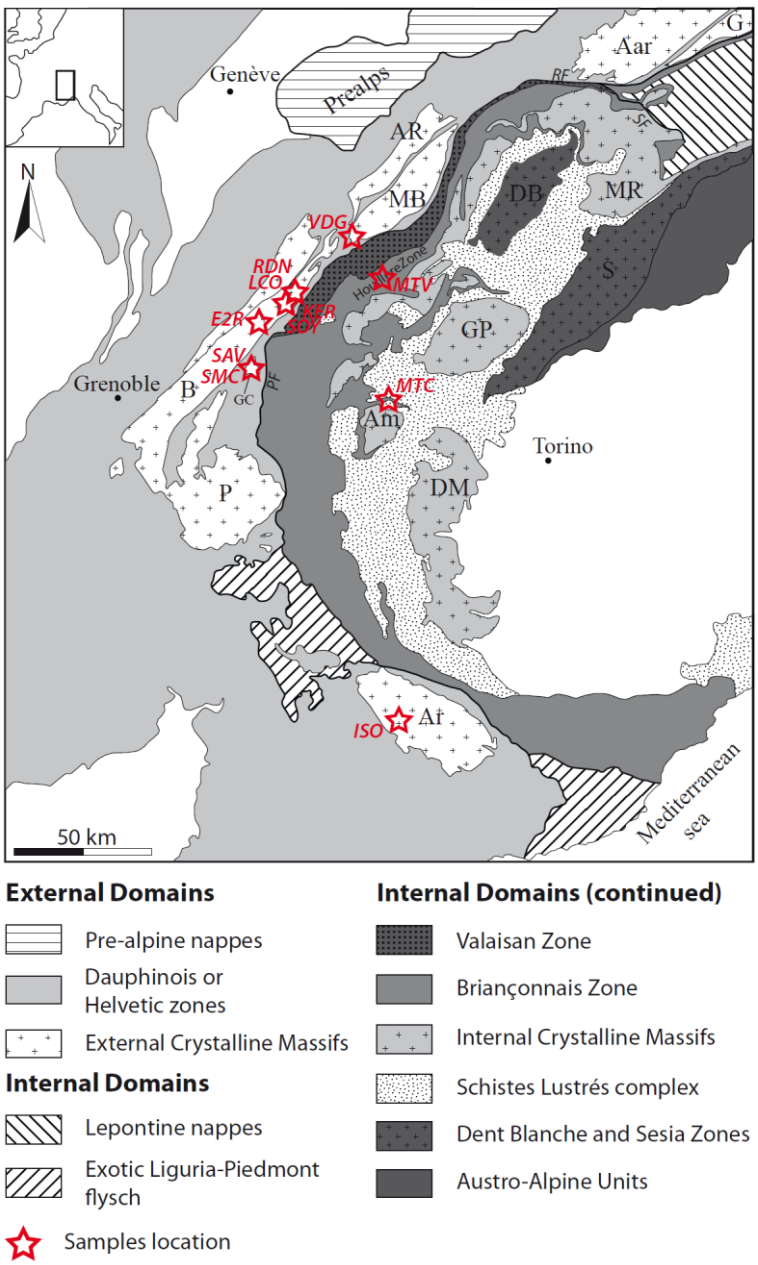

Figure 3-1 Geological settings of the western Alps. External Domains: Aar; G: Gotthard; AR: Aiguilles Rouges; MB: Mont Blanc; B: Belledonne; GC : Grand Châtelard ; P: Pelvoux; Ar: Argentera. Internal Domains: MR: Monte Rosa; DB: Dent Blanche; S: Sesia; GP: Gran Paradiso; Am: Ambin; DM: Dora Maira. RF: Rhone Fault; SF: Simplon Fault; PF: Penninic Front. The stars show the location of studied samples

the western Alps, subduction of the Tethys Ocean started during the Cretaceous and lasted until the Eocene (Rubatto et al. 1999). The first high pressure/low temperature(HP/LT) event is recorded in these oceanic units simultaneously (Agard et al. 2002). The European continental margin subduction occurred during the upper to middle Eocene (Duchene et al. 1997) together with HP to ultra-high pressure (UHP) metamorphism of the Internal Crystalline Massifs (ICM), and HP metamorphism of the Briançonnais domain. Exhumation of these internal units was mainly initiated during collision, during the Upper Eocene to Oligocene (Simon-Labric et al. 2009). The External Domains, separated from the Internal Domains by the Penninic Front, are composed of the pre-Alpine basement, corresponding to the ECM (Aar-Gothard, Mont Blanc, Aiguilles Rouges, Belledonne, Pelvoux, Argentera), and its Mesozoic to Cenozoic sedimentary cover. The ECM were underthrusted below the internal units, following the activation of the Penninic Front. Shortening of the external Alps was initiated during the Upper Eocene to Lower Oligocene, when the main orogenic collision phase took place (Ceriani et al. 2001). Mineral assemblages and fluid inclusion studies indicate that the ECM reached maximum metamorphic conditions of 450°C, 6 kbar in the Aar (Challandes et al. 2008) and 400°C, 3 to 5 kbar in the Mont Blanc massif (Rolland et al. 2003; Rossi et al. 2005). The sedimentary cover, detached from the crystalline basement, was folded and transported to form the Dauphinois or Helvetic nappes. Exhumation of the ECM took place during a Miocene shortening phase (Corsini et al. 2004), while the deformation front migrated westwards of the Alpine arc (Schmid and Kissling 2000).

In the External Domains of the western Alps, structures are attributed to either Alpine or inherited Variscan deformations. After the Oligocene, three main late Alpine phases can be identified (D4 event, Dumont et al. 2008):

- A first shortening event characterized by a horizontal extension dated at 22.2 ± 0.3 Ma from phengites in a shear zone in the Argentera massif (Corsini et al. 2004) and at 22.4 ± 0.1 to 22.8 ± 0.6 Ma from biotite in shear zones in the Mont Blanc massif (Leloup et al. 2005).

- A second shortening phase, also related to shear zone formation (Rossi and Rolland 2014) is probably responsible for the formation of horizontal quartz veins around 16 Ma in the Mont Blanc massif.
- A third phase, related to the youngest stage of deformation, is attributed to a polyphased transpressive regime (around ca. 11-10 Ma and 7-5 Ma in the Belledonne massif) responsible for the "en echelon" arrangement of the vertical veins (Gasquet et al. 2010).

3.3. Analytical methods

U-Th-Pb geochronology of monazite and xenotime and trace element analyses of monazite were performed by laser ablation inductively coupled plasma spectrometry (LA-ICPMS) at the Laboratoire Magmas et Volcans (LMV), Clermont-Ferrand (France). Analytical procedures for monazite dating are reported in detail in Didier et al. (2013) and Didier et al. (2014). Ages are given at the 2σ level and the spot size is 9, 11, 20 and 25 µm depending on the samples (Supplementary material 3-2). Data disturbed by inclusions, fractures or age mixing (between different areas of a single grain) were not taken into account in the calculations. The occurrence of initial Pb in the sample can be monitored by the change in the ^{204}(Pb+Hg) signal intensity, but no Pb correction was applied. Monazite and xenotime data are corrected for U–Pb and Th–Pb fractionation occurring during laser sampling and for instrumental mass discrimination (mass bias) by standard bracketing with repeated measurements of the Moacyr monazite standard (Cruz et al. 1996; Seydoux-Guillaume et al. 2002a; Gasquet et al. 2010; Fletcher et al. 2010) or C83-32 monazite (Corfu 1988; Didier 2013). At the beginning and end of every run, repeated analyses of the Manangoutry monazite (Paquette and Tiepolo 2007) standard, treated as unknown, independently controlled the reproducibility and accuracy of the corrections. Data reduction was carried out using the GLITTER® software package (van Achterbergh et al. 2001; Jackson et al. 2004). Calculated ratios were exported and age diagrams were generated using the Isoplot software package by Ludwig (2001). The

concentrations of U-Th-Pb were calibrated with respect to the certified contents of the Moacyr monazite (Seydoux-Guillaume et al. 2004).

Only $^{208}Pb/^{232}Th$ ages are discussed in the case of young hydrothermal monazite dating because: 1. the commonly high Th/U ratio of hydrothermal monazite (Poitrasson et al. 2000; Pyle 2006; Janots et al. 2012; Seydoux-Guillaume et al. 2012); 2. U decay series could be in disequilibrium in young monazites (Scharer 1984), resulting in overestimated $^{206}Pb/^{238}U$ ages. Secular equilibrium among the intermediate decay products of Th occurs after about 30 years, so it seems reasonable to assume that the initial ^{208}Pb is absent; 3. ^{232}Th is so abundant that ^{208}Pb originating from initial Pb is generally negligible compared to radiogenic ^{208}Pb (Bosse et al. 2009; Janots et al. 2012).

Trace element (Sr, Eu, HREE+Y, Supplementary material 3-1) analyses were also carried out with LA-ICPMS in each grain domain (BSE) using Moacyr monazite as external standard and La for monazite and Y for xenotime as internal standards. During the monazite and xenotime analytical session, the synthetic glass NIST610 and the Manangoutry Monazite (Paquette and Tiepolo 2007) were used as secondary standards. The spot size was 15 µm. Data reduction was carried out using the GLITTER® software package from Macquarie Research Ltd (van Achterbergh et al. 2001).

Hydrothermal crystals were extracted from the cleft, mounted in epoxy and polished. They were then systematically characterized by backscattered electron imaging (BSE) on a HITACHI S-2500 scanning electron microscope at the ISTerre laboratory (Grenoble).

3.4. Cleft Monazite

3.4.1. Cleft locations

The investigated samples (Fig. 1, Table 1) were taken from clefts located in the ECM (Mont Blanc, Belledonne, Argentera) and the Briançonnais units (Late-Carboniferous to Permo-Triassic metasediments). Most samples were obtained from mineral collectors.

However, except for the Mont Blanc and Argentera samples, clefts were reinvestigated for this study through fieldwork aimed at characterizing the host-rock, cleft orientations and, when possible, collecting new mineral (monazite).

Regarding the ECM, along the Mont Blanc and Belledonne massifs, the monazite-bearing clefts studied were located on the eastern side of the massifs, close to major tectonic contacts (Penninic Front and Ornon-Roselend fault). The Mont Blanc massif is composed of granite intruding paragneisses, orthogneisses and migmatites (e.g. Bonin et al. 1993; Bussy and von Raumer 1994). The massif is crosscut by sub-vertical shear zones associated with sub-horizontal quartz veins (Rossi et al. 2005; Rossi and Rolland 2014), and linked to a dextral transpressional system (Rolland et al. 2008). The investigated sample (VDG) was taken from the "vallée des glaciers" moraine, in the SW extremity of the massif, in a group of bedded Variscan micaschists and gneiss imprinted with Alpine metamorphism.

In the Belledonne massif, investigated clefts are located in the Lauzière (RDN, LCO, KER, SOY, E2R samples) and Grand Châtelard massifs (SAV, SMC samples). The Lauzière massif is composed of Variscan metamorphic rocks and granites bordered to the west and east by Mesozoic formations. A detailed description of the several lithological units can be found in Gasquet et al. (2010). Monazite-bearing clefts are found in the NE part of the massif, between the Lauzière granite in the west and the Bonneval formation in the east, in units parallel to the NE-SW extent of Belledonne (Fig. 2). South of the Lauzière massif, the Grand Châtelard massif is a second exposure of the Variscan basement associated with its detached sedimentary cover. It is mainly composed of a large gneissic series intruded by leucogranite (Gasquet 1979). The Alpine clefts studied are located on the western side of the massif, in Variscan gneisses/micaschists, close to the contact with Triassic and Liassic cover.

Table 3-1 Locations of the analyzed cleft monazites and xenotimes

Locality	Sample	nb. of grains	Alpine Unit	Coordinates			Host-rock
				Lat. (°)	Long. (°)	Alt. (m)	
Vallée des glaciers, Bourg-Saint-Maurice, Savoie	*VDG*	1	Mont Blanc, ECM	*45°45'30"*	*06°45'59"*	*~ 2500*	micaschists
Naves road, La Léchère, Savoie	*RDN*	4	Belledonne, ECM	*45°31'39"*	*06°29'23"*	*630*	mylonitic gneisses and micaschists
Les Combes, La Léchère, Savoie	*LCO*	4	Belledonne, ECM	*45°31'43"*	*06°29'02"*	*610*	mylonitic gneisses and micaschists
Bois Kersy, Bonneval, Savoie	*KER*	3	Belledonne, ECM	*45°31'42"*	*06°27'45"*	*830*	mylonitic gneisses and micaschists
Le Cretet, Saint-Oyen, Savoie	*SOY*	2	Belledonne, ECM	*45°30'48"*	*06°28'12"*	*1050*	mylonitic gneisses and micaschists
Entre Deux Roches, La Léchère, Savoie	*E2R*	4	Belledonne, ECM	*45°27'21"*	*06°22'41"*	*2350*	gneisses and granite
Ancienne carrière, Saint-Avre, Savoie	*SAV*	4	Belledonne, ECM	*45°20'49"*	*06°19'02"*	*590*	mylonitic gneisses
Le Sarroux, Sainte-Marie-de-Cuines, Savoie	*SMC*	1	Belledonne, ECM	*45°19'15"*	*06°18'24"*	*760*	mylonitic micaschists
La Sauchéra, Isola, Alpes-Maritimes	*ISO*	1	Argentera, ECM	*44°12'34"*	*07°06'02"*	*~ 1630*	migmatitic gneisses
Le Châtelard, Montvalezan, Savoie	*MTV*	2	Briançonnais zone, ID	*45°36'52"*	*06°51'48"*	*1460*	micaschists
Mont-Cenis lake, Lanslebourg, Savoie	*MTC*	3	Briançonnais zone, ID	*45°14'57"*	*06°54'58"*	*1980*	metapelite (dolomitic matrice) in gypsum and cargneule
Mont-Cenis lake, Lanslebourg, Savoie	*XMTC*	5	Briançonnais zone, ID	*45°14'57"*	*06°54'58"*	*1980*	

ECM: External Crystalline Massifs; *ID:* Internal Domains

In the Argentera, a single crystal was investigated, in the SW part of the massif (ISO sample). The Argentera massif is composed of two major metamorphic units (Faure-Muret, 1955) on both sides of a NW-SE mylonitic zone. The Valetta Shear Zone (VSZ) separates the occidental Tinée complex from the oriental Malinvern complex to the east. The SW Tinée complex is characterized by micaschists, migmatites and gneisses, the NE Malinvern complex by migmatites and gneisses intruded by late-Variscan Argentera granites. Both complexes were subjected to eclogitic to granulitic metamorphism during the Variscan deformation. The Alpine structures in the Argentera massif correspond to the development of a ductile shear zone similar to the other ECM (e.g. Mont Blanc) dated as Early Miocene (Corsini et al. 2004). The sample investigated comes from a gneiss

scree block in the Tinée complex, west of the Valetta shear zone, and at the same latitude as Isola.

In the Internal Domains, two clefts were investigated in the Briançonnais Zone: a first in the Houillère Zone (MTV sample) and a second at the contact with the Piedmont zone (MTC sample).

The Briançonnais Zone Houillière (ZH) represents the most external part of the Briançonnais paleogeographic domain, separated from the Valaisan oceanic units by the Houillier Front (Bertrand et al. 1996; Fügenschuh et al. 1999). This unit is characterized by a Carbono-Permian sequence of continental deposits (Fabre 1961) and a Mesozoic cover intruded by volcanic sills and dykes (Debelmas et al. 1991). The ZH was subjected to low-grade alpine metamorphism (350-400°C and 4-5 kbar, Bucher et al. 2003). The ZH is subdivided into the upper and lower Houiller units (Lanari et al. 2012), both constituted by black schists with anthracite levels, arkoses and conglomerates and these units are separated by the Drayère shear zone. The cleft system investigated in the ZH is located in the northern part of the lower Houiller unit. The other sample from the Internal Domains comes from the Mont-Cenis area. Here, small monazite-bearing veins were found in Triassic metapelites with a dolomitic matrix (sedimentary Briançonnais formation) located in gypsum and cargneule (decollement level), and interpreted as tectonic breccia (Fudral et al. 1994). This corresponds to the most internal Briançonnais zone separating the Briançonnais units from the Piedmont-Liguria units ("Schistes lustrés"). In these veins, xenotime (XMTC sample) was also dated in-situ using the monazite standard and its age was compared with that of monazite. In the subsequent text, three capital characters (e.g. RDN or E2R) refer to samples localization and italics three capital characters plus numbers refers to one single grain (e.g. *RDN02* or *E2R01*).

3.4.2. Cleft mineralogy and geometry

In the ECM, two major populations of cleft are distinguished, sub-horizontal and vertical. Horizontal veins or "fours alpins" (as named in the Mont Blanc massif) were formed

before the vertical veins and are mainly filled with quartz, chlorite, epidote, albite and calcite (Gasquet et al. 2010; Rossi and Rolland 2014). Vertical veins display the same mineral assemblages but sometimes contain numerous species of rare minerals such as anatase, rutile, ilmenite, hematite, apatite, monazite or xenotime. Monazite is often associated with anatase in vertical clefts, and is the major REE mineral. In the Belledonne massif, the numerous clefts investigated are systematically vertical and oriented close to N110° (Fig. 2), perpendicular to the main schistosity of the host-rock (N020 to N040°E trending, subvertical). Argentera and Mont Blanc samples have been collected in scree. The geometry of these clefts is therefore unknown. In the Internal Domains, a first cleft system was investigated in the Briançonnais unit. This corresponds to centimetric vertical veins oriented N120° associated with larger N160° vertical quartz veins. Here, the host-rock foliation is oriented NNE-SSW and dips 60° westwards. The other monazite samples of the Internal Domains were found in small non-oriented metamorphic veins located in Triassic metapelites tectonically carried in gypsum, which represents the contact between the Briançonnais Zone and the "Schistes Lustrés" unit. These veins also contain hematite, xenotime and rare Th-U-REE+Y minerals such as thorite, dessauite-(Y), hingganite-(Y).

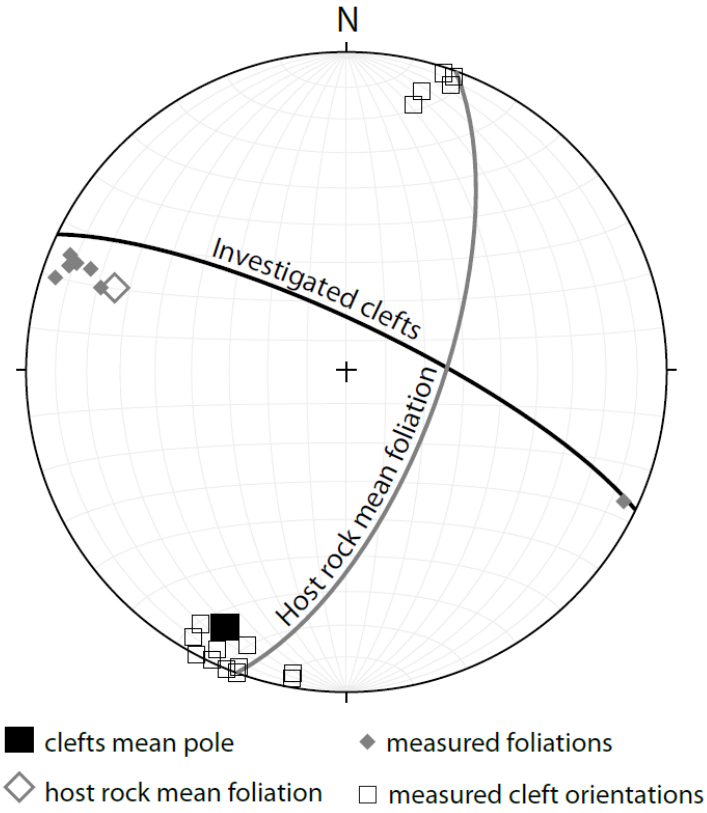

Figure 3-2 Orientation data of clefts in the Belledonne massif in stereographic projection (Schmidt net, lower hemisphere)

3.4.3. Monazite texture and composition

Hydrothermal monazite can be found either as yellowish, orange or pinkish grains 0.2 to 9 mm diameter. KER monazite samples correspond to a cluster of micrometric (typically tens of microns) pinkish grains. Monazite compositions show no significant variations in REE+Y contents (Supplementary material 3-1) between the different samples. Europium anomalies may be less noticeable in two samples (E2R and RDN). Only the Sr, Th and U contents vary significantly within different grains or compositional domains of one grain and are generally homogeneous within one compositional domain. The different samples present a large range of Th and U contents (Fig. 3), even within the same sample (e.g.

E2R sample). Generally, the monazites have low Th and U contents in comparison to monazite found in magmatic and high-grade metamorphic rocks (Janots et al. 2012). Th content varies between 6 and 55900 ppm and U between 13 and 2100 ppm. Hydrothermal monazite Th/U ratios (from 1 to 523) range from low-grade metamorphic monazite (lower ratios) to hydrothermal monazite (higher ratios), based on the study by Janots et al. (2012).

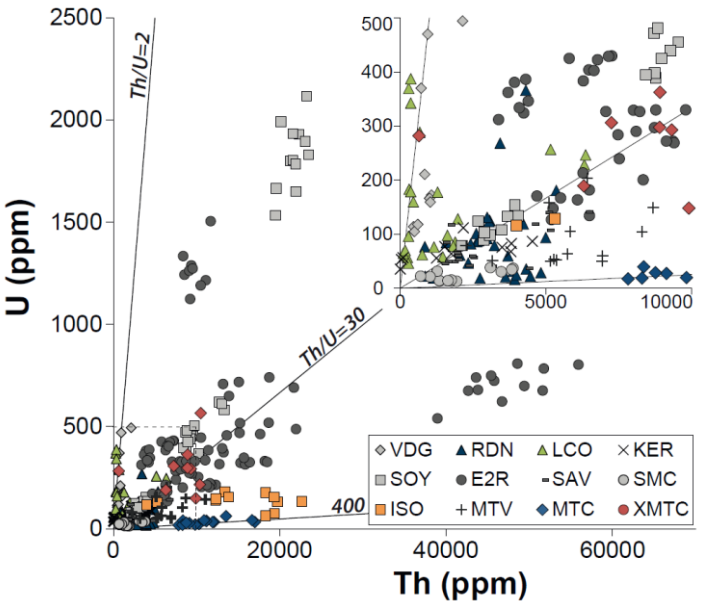

Figure 3-3 U and Th concentrations data of studied monazites and xenotimes deduced from LA-ICPMS measurements. Dashed lines represent the zoomed area

In the *VDG01* monazite (Fig. 4a), no core/rim zoning was observed. It has a low Th/U ratio (between 2 and 6), with Th and U contents respectively from 463 to 2144 ppm and 105 to 494 ppm. *RDN01, RDN02* and *RDN04* monazites (Fig. 4b, c, d) show a complex zoning with a highly porous and compositionally heterogeneous core (patchy zone) surrounded by a more homogeneous rim.

Figure 3-4

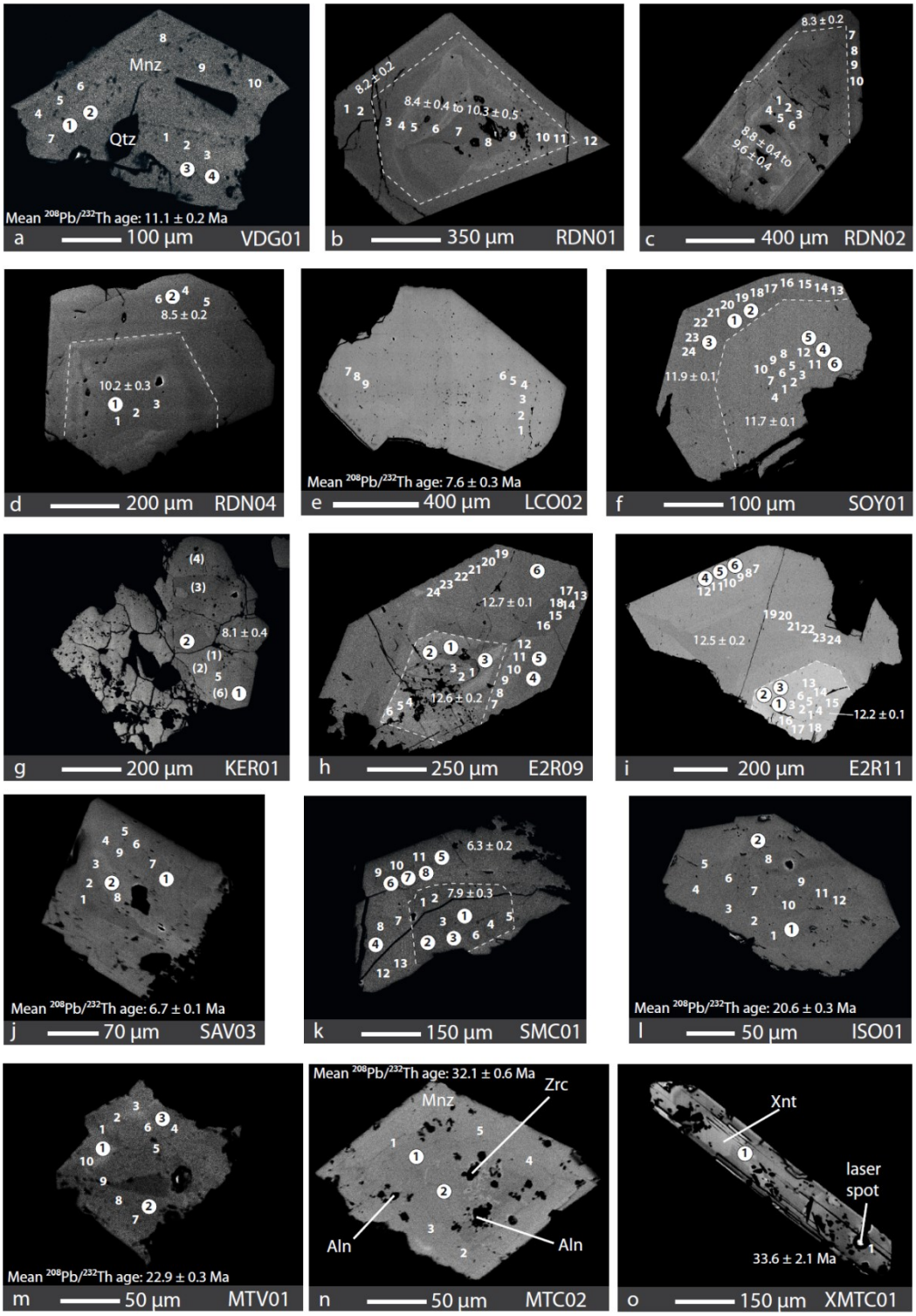
Mnz
Qtz
Mean 208Pb/232Th age: 11.1 ± 0.2 Ma
a 100 µm VDG01
8.2 ± 0.2
8.4 ± 0.4 to 10.3 ± 0.5
b 350 µm RDN01
8.3 ± 0.2
8.8 ± 0.4 to 9.6 ± 0.4
c 400 µm RDN02
8.5 ± 0.2
10.2 ± 0.3
d 200 µm RDN04
Mean 208Pb/232Th age: 7.6 ± 0.3 Ma
e 400 µm LCO02
11.9 ± 0.1
11.7 ± 0.1
f 100 µm SOY01
8.1 ± 0.4
g 200 µm KER01
12.7 ± 0.1
12.6 ± 0.2
h 250 µm E2R09
12.5 ± 0.2
12.2 ± 0.1
i 200 µm E2R11
Mean 208Pb/232Th age: 6.7 ± 0.1 Ma
j 70 µm SAV03
6.3 ± 0.2
7.9 ± 0.3
k 150 µm SMC01
Mean 208Pb/232Th age: 20.6 ± 0.3 Ma
l 50 µm ISO01
Mean 208Pb/232Th age: 22.9 ± 0.3 Ma
m 50 µm MTV01
Mean 208Pb/232Th age: 32.1 ± 0.6 Ma
Mnz
Zrc
Aln
Aln
n 50 µm MTC02
Xnt
laser spot
33.6 ± 2.1 Ma
o 150 µm XMTC01

Previous page : **Figure 3-4** Backscattered electron selected images of cleft monazites and xenotimes. External Crystalline Massifs: a: Mont Blanc; b, c, d, e, f, g ,h, i, j, k: Belledonne-Grand Châtelard; l: Argentera. Briançonnais Zone: m: Houillère Zone; n, o: Briançonnais Mesozoic cover. Zoning are mostly due to variations in U and Th contents; white numbers refers to LA-ICPMS dating spots (Supplementary material 3-2), circled black numbers refers to LA-ICPMS trace element spots (Supplementary material 3-1), $^{208}Pb/^{232}Th$ ages (2σ level) refer to corresponding grains or compositional domains

The *RDN04* grain core is more preserved (less patchy) than the other grain core. Th/U ratios are higher in the patchy zones, ranging from 12 to 236 (Th content from 857 to 5361 ppm, U content from 17 to 366 ppm), than in rims with ratios from 11 to 41 (Th content from 847 to 3431, U content from 61 to 268 ppm). *LCO1* to *LCO04* monazites (four grains, Fig. 4e) present no clear compositional zoning. Th content ranges from 113 to 6368 ppm and U content from 47 to 387 ppm. Th/U ratios are between 1 and 28. The KER sample (three monazite crystals *KER01* to *KER03*, Fig. 4g) present a patchy zoning associated with porosity. The *KER01* monazite has areas with almost no Th and U, which could not be used to determine ages (Supplemental material 3-2). Th and U contents are between 6 and 4540 ppm and 36 and 112 ppm respectively. Th/U ratios range from 0.2 to 56. *SOY01* monazite (Fig. 4f) presents clear core and rim texture. Th content is between 8439 and 23486 ppm and U content between 389 and 2117 ppm. Th/U ratios are between 10 and 13 for the core, 18 and 23 for the rim. In the same cleft, the *SOY02* monazite presents no significant compositional zoning. Th content ranges from 2122 to 10257 ppm, U content from 79 to 368 ppm. Th/U ratios are between 22 and 32. The E2R monazites (four grains *E2R01*, *E2R08*, *E2R09* and *E2R11*, Fig. 4h, i) present compositional zoning with different compositions in U and Th but no systematic Th/U correlation (between 6 and 76). In this sample, each grain has a distinct Th/U signature (Fig. 7b) except *E2R11* monazite rim which has the same Th/U as *E2R09* monazite. Th content ranges from 3379 to 55906 ppm, U content from 127 to 1504 ppm. In *E2R08*, *E2R09* and *E2R11* monazites, Sr content decreases from core to rim ranging from 712 to 3146 ppm. The SAV sample (four grains, *SAV01* to *SAV04*, Fig. 4j) presents no significant compositional zoning and Th/U ratios are between 14 and 116. Th content ranges from 1080 to 6383 ppm and U

content from 32 to 141. The *SMC01* monazite (Fig. 4k) presents a core/rim zoning with Th and U content differences slightly pronounced but clear Sr (and minor HREE+Y) signature within domains (around 1500 ppm in grain core and 700 ppm in grain rim, Supplementary material 3-1). Th/U ratios are between 31 and 147, with Th content ranging from 701 to 3877 ppm and U content from 13 to 39 ppm. The *ISO01* monazite (Fig. 4l) shows a light patchy compositional zoning. The Th/U ratios are between 34 and 289. Th content ranges from 3992 to 22646 ppm, U content from63 to 179 ppm. The MTV sample (two monazites, *MTV01* and *MTV02*, (Fig. 4m) presents no visible compositional zoning. Th/U ratios are between 29 and 137, Th content between 2258 and 11059 ppm and U content between 50 and 204 ppm. The MTC sample (Fig.4 n, o) corresponds to both monazite and xenotime grains (three monazites *MTC01* to *MTC03* and five xenotime grains *XMTC01* to *XMTC05*). They both contain porosity and chlorite, albite or apatite inclusions. Monazite also contains inclusions of allanite-(Ce) and zircon. BSE images of monazite grains show patchy light zoning attributed mainly to Th and U variations. Th/U ratios are the highest of all analyzed samples ranging from 210 to 523, with Th content from 7827 to 17012 ppm and U content from 18 to 61 ppm. Xenotime crystals have remarkably high Th/U ratios of 2 to 67 (Fig. 3). Th content ranges from 646 to 10506 ppm and U content from 148 to 565 ppm.

3.4.4. $^{208}Pb/^{232}Th$ and $^{206}Pb/^{238}U$ monazite ages

Twenty-nine cleft monazites from eleven locations were investigated for U-Th-Pb analyses in the western Alpine arc (Tab. 1). When intragrain compositional variations (e.g. Th/U variations) were observed, in situ LA-ICPMS analyses were performed in the different mineral domains. Distinct ages are presented for the compositional domains identified when they were significantly different.

Figure 3-5

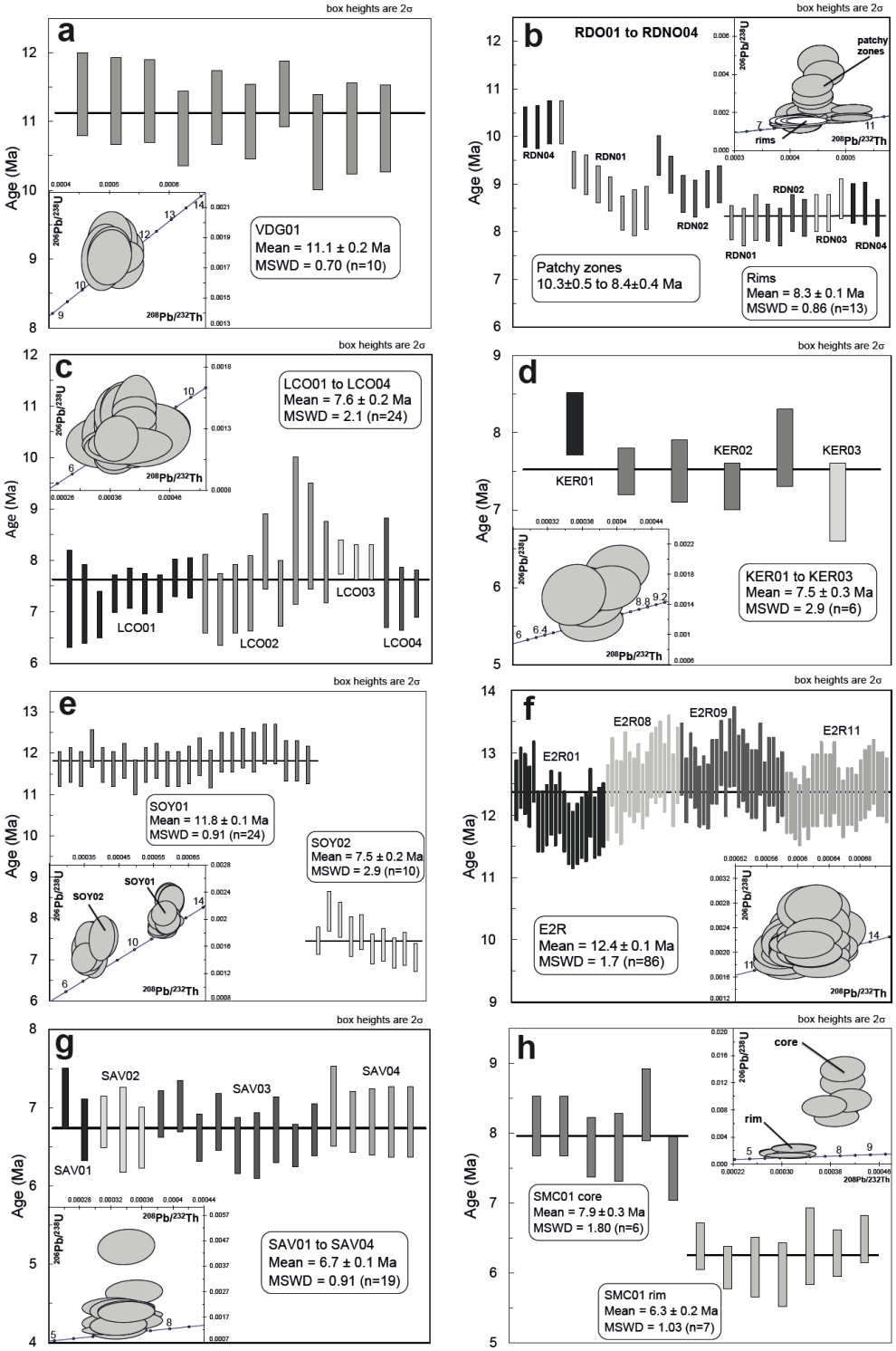
box heights are 2σ
a
VDG01
Mean = 11.1 ± 0.2 Ma
MSWD = 0.70 (n=10)
b
RDO01 to RDNO04
patchy zones
rims
RDN04
RDN01
RDN02
RDN03
Patchy zones
10.3±0.5 to 8.4±0.4 Ma
Rims
Mean = 8.3 ± 0.1 Ma
MSWD = 0.86 (n=13)
c
LCO01 to LCO04
Mean = 7.6 ± 0.2 Ma
MSWD = 2.1 (n=24)
LCO01
LCO02
LCO03
LCO04
d
KER01
KER02
KER03
KER01 to KER03
Mean = 7.5 ± 0.3 Ma
MSWD = 2.9 (n=6)
e
SOY01
Mean = 11.8 ± 0.1 Ma
MSWD = 0.91 (n=24)
SOY02
Mean = 7.5 ± 0.2 Ma
MSWD = 2.9 (n=10)
f
E2R01
E2R08
E2R09
E2R11
E2R
Mean = 12.4 ± 0.1 Ma
MSWD = 1.7 (n=86)
g
SAV01
SAV02
SAV03
SAV04
SAV01 to SAV04
Mean = 6.7 ± 0.1 Ma
MSWD = 0.91 (n=19)
h
core
rim
SMC01 core
Mean = 7.9 ± 0.3 Ma
MSWD = 1.80 (n=6)
SMC01 rim
Mean = 6.3 ± 0.2 Ma
MSWD = 1.03 (n=7)
Age (Ma)
206Pb/238U
208Pb/232Th

Previous page : **Figure 3-5** ^{232}Th-^{208}Pb weighted mean ages and ^{238}U/^{206}Pb vs ^{232}Th-^{208}Pb diagrams of samples of the Mont Blanc (a) and the Belledonne massifs (b, c, d, e, f, g, h)

In the Mont Blanc massif, a single homogeneous monazite grain (*VDG01*) yields a ^{208}Pb/^{232}Th weighted mean age of 11.1 ± 0.2 Ma (MSWD = 0.7, n=10) (Fig. 5a). In the Belledonne massif, twenty-one monazite grains were dated from seven different clefts (Fig. 5b to 5h) located in the Lauzière and Grand Châtelard massifs and La Léchère area, north of Belledonne. In the RDN sample (four monazite grains, *RDN01* to *RDN04*, Fig. 5b), ^{208}Pb/^{232}Th ages range from 10.3 ± 0.5 to 8.1 ± 0.4 Ma. Eighteen analyzes conducted in the patchy zone (Fig. 4b) give ^{208}Pb/^{232}Th ages between 10.3 ± 0.5 and 8.4 ± 0.4 Ma. The *RDN04* grain core and a single analysis in the core of *RDN01* indicate older ^{208}Pb/^{232}Th ages at 10.3 ± 0.2 Ma (MSWD=0.07, n=4). ^{208}Pb/^{232}Th ages in the rims are younger at 8.3 ± 0.1 Ma (MSWD=0.9, n=13). Located in the same geological unit, four monazite grains *LCO01* to *LCO04* (Fig. 5c) give a ^{208}Pb/^{232}Th age of 7.6 ± 0.2 Ma (MSWD=2.1, n=24). On the other side of the Isère valley, the KER sample (three grains, *KER01* to *KER03*, Fig. 5d) gives a ^{208}Pb/^{232}Th age of 7.5 ± 0.3 Ma (MSWD= 2.9, n=6). In the SOY sample (Fig. 5e), the *SOY01* monazite grain gives a ^{208}Pb/^{232}Th age of 11.8 ± 0.1 Ma (MSWD=0.9, n=24) whereas the *SOY02* monazite gives a younger and slightly scattered ^{208}Pb/^{232}Th age of 7.5 ± 0.2 Ma (MSWD= 2.9, n=10). Four monazite grains from the E2R sample give a ^{208}Pb/^{232}Th age of 12.4 ± 0.1 Ma (MSWD = 1.7, n=86). In the Grand Châtelard massif, two clefts were investigated. The SAV sample (*SAV01* to *SAV04* monazites, Fig. 5g) gives a ^{208}Pb/^{232}Th age of 6.7 ± 0.1 Ma (MSWD=0.9, n=19). The *SMC01* monazite (Fig. 5h) shows two distinct age groups at 7.9 ± 0.3 Ma (MSWD=1.8, n=6) in the core and 6.3 ± 0.2 Ma (MSWD=1.0, n=7) in the rim. Further South, in the Argentera massif, the *ISO01* monazite (Fig. 6a) gives a ^{208}Pb/^{232}Th age of 20.6 ± 0.3 Ma (MSWD=1.8, n=12). In the Internal Domains (the Houillère zone), the MTV sample (*MTV01* and *MTV02* monazites, Fig. 6b) taken from a vertical cleft, gives a ^{208}Pb/^{232}Th age of 23.0 ± 0.3 Ma (MSWD=1.4, n=14). The MTC sample (three monazites, *MTC01* to *MTC03*, Fig. 6c) shows a ^{208}Pb/^{232}Th age of 32.3 ± 0.3 Ma (MSWD=0.7, n=15). In parallel, U-Th-Pb analyses were performed on 5 xenotime grains

(*XMTC01* to *XMTC05*, Fig. 6d) taken from the same cleft. They give a $^{208}Pb/^{232}Th$ age of 34.9 ± 0.5 Ma (MSWD=1.1, n=9), slightly older than the monazite ages.

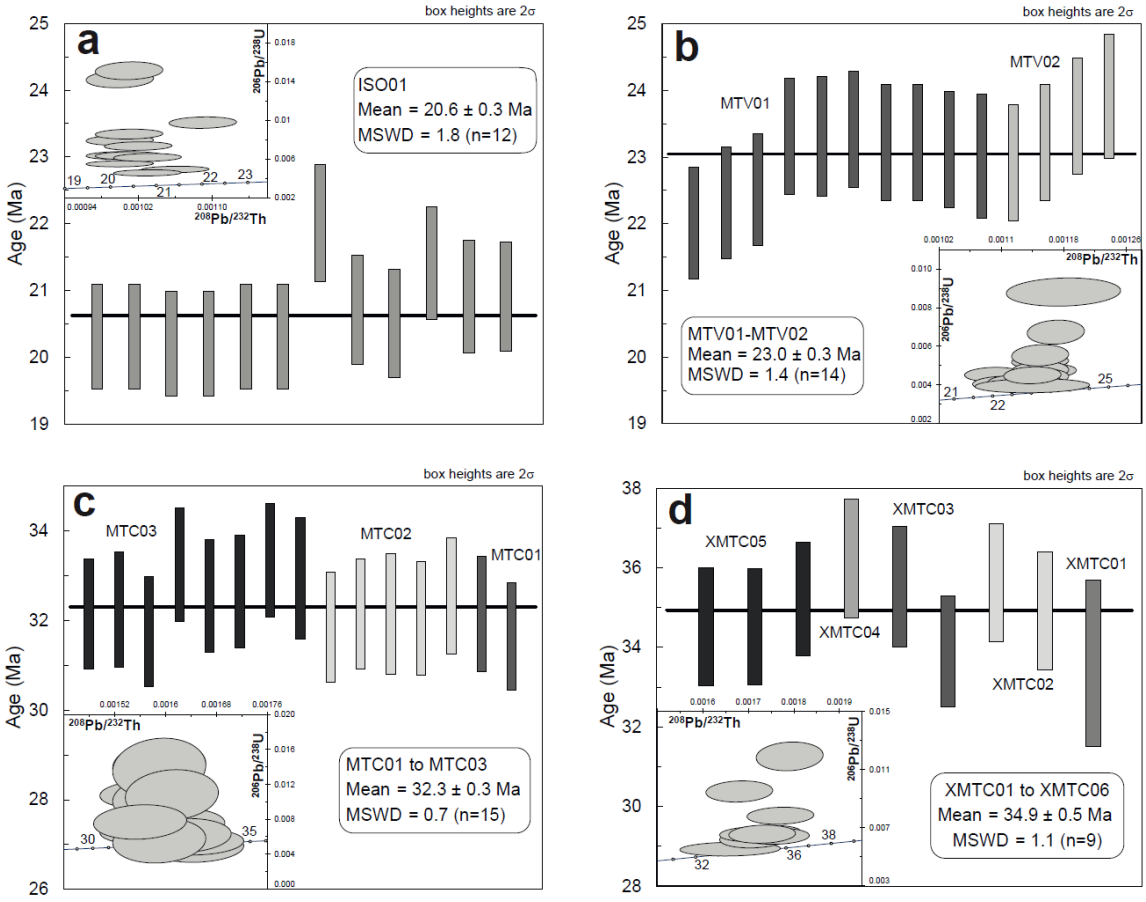

Figure 3-6 ^{232}Th-^{208}Pb weighted mean ages and $^{238}U/^{206}Pb$ vs ^{232}Th-^{208}Pb diagrams of the sample of the Argentera (a) and the samples of the Briançonnais Zone (b, c, d)

Concerning the U-Pb analyses, most of the samples provide discordant $^{206}Pb/^{238}U$ vs $^{207}Pb/^{235}U$ ages because of: 1. U decay series disequilibrium commonly observed in young monazite and resulting in ^{206}Pb excess, 2. incorporation of varying amounts of initial Pb and 3. significant uncertainty in the $^{207}Pb/^{235}U$ ages due to low U contents (and thus very low ^{207}Pb) in young monazites. Regarding the $^{206}Pb/^{238}U$ ages in the light of the $^{208}Pb/^{232}Th$ ages ($^{208}Pb/^{232}Th$ vs $^{206}Pb/^{238}U$ diagrams, Fig. 5, 6), most of the monazite analyses (55%, Supplementary material 3-2) give similar ages for both systems in the investigated monazites (except for the ISO sample). In all the samples, apparent older

$^{206}Pb/^{238}U$ ages are also measured due to ^{206}Pb excess and/or common Pb incorporation. The effect of these processes is not readily distinguishable due to the low U content of the monazite, except for some samples such as the ISO sample (fig. 7a). Some of these disturbed $^{206}Pb/^{238}U$ ages are obtained in heterogeneous patchy domains (RDN sample) or in the relictual core of the monazite grain (SMC sample). $^{206}Pb/^{238}U$ ages are also older in the xenotime compared to the $^{208}Pb/^{232}Th$ ages for the same reasons.

3.5. U-Th-Pb dating of Alpine cleft monazite and xenotime

3.5.1. Th-Pb versus U-Pb dating of young hydrothermal monazite

With the development of in-situ U-Th-Pb dating techniques (e.g. Paquette and Tiepolo 2007), the application of monazite as a geochronometer has continued to increase. However, analytical protocols vary depending on the dating techniques and, as a result, the presentation of Th-Pb versus U-Pb ages is sometimes controversial. In young monazite, the Th-Pb systems are preferred to the U-Pb systems (e.g. Janots et al. 2012) due to the preferential incorporation of Th versus U in monazite (VanEmden et al. 1997). The preferential Th/U fractionation between monazite and its environment ($f_{Th/U}$ in equilibrium with rock, melt, fluid) has two main implications on U-Th-Pb ages. First, the contribution of initial Pb (incorporated during monazite growth) to the total Pb measured will be lower for the $^{232}Th/^{208}Pb$ system that has higher isotopic radiogenic concentration than the other two isotopic systems ($^{235}U/^{207}Pb$ and $^{238}U/^{206}Pb$). Second, the preferential incorporation of ^{230}Th, an intermediate product of the ^{238}U decay series, leads to ^{206}Pb excess (Schärer, 1984). The contribution of ^{206}Pb excess decreases with time, but also strongly depends on $f_{Th/U}$. In Alpine hydrothermal monazite, it has been shown (Janots et al. 2012) that the ^{206}Pb excess can reach up to 69 % of the total ^{206}Pb (common, radiogenic and excess) due to the unfavorable combination of young Miocene ages with extreme $f_{Th/U}$ values between monazite and hydrothermal fluid. On the other hand, (Kempe et al. 2008) have shown that U-Pb dating of hydrothermal Th-poor monazite can

be successful in defining the timing of ore mineralization (23 Ma, Llallagua tin-porphyry deposit, Bolivia). In this special case, the low Th/U ratio of monazite reflects a lower Th/U ratio in the fluid and/or a lower $f_{Th/U}$ value between monazite and fluid that could account for the restricted ^{206}Pb excess in the Th-poor hydrothermal monazite of the Llallagua tin-porphyry deposit. Similarly, in the Alpine clefts of the Tauern (Gnos et al. 2015), the U-Pb age of 17 Ma obtained in Th-poor monazite is coherent with the Th-Pb dating of Th-rich monazite dated in adjacent veins (between 19 and 15 Ma). In this study, the use of the Th-Pb systematics was preferred in order to determine the crystallization age of monazite and for further age interpretations (see 3. Analytical Methods). Furthermore, the comparison of $^{206}Pb/^{238}U$ age and $^{208}Pb/^{232}Th$ age of numerous hydrothermal monazite specimens (29 crystals; Table 1) with various Th/U ratios (from 1 to 523) highlights new limitations regarding the applicability of U-Pb dating to young hydrothermal monazite. Some of the cleft monazites present various contributions of initial Pb and/or ^{206}Pb excess as shown in the Tera-Wasserburg diagrams of ISO and E2R samples (Fig. 7c, 7d). In these Tera-Wasserburg diagrams, the Pb composition results from the contribution of radiogenic Pb, initial Pb (close to common Pb composition) and ^{206}Pb excess produced by ^{230}Th (shift toward the origin; Janots et al. 2012).

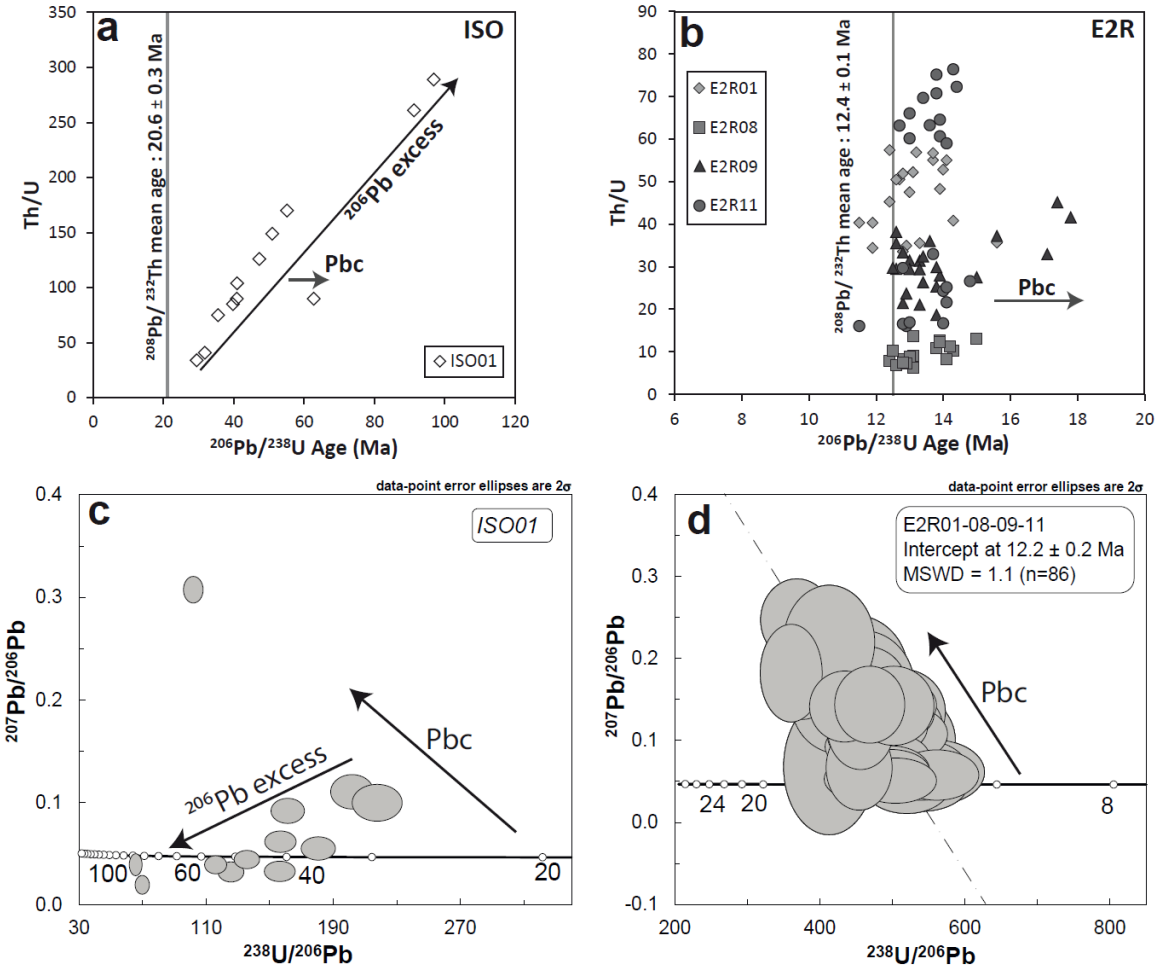

Figure 3-7 Th/U versus $^{206}Pb/^{238}U$ age diagrams of *ISO01* and *E2R01*, *E2R08*, *E2R09* and *E2R11* samples (a, b) showing the relation between Th/U ratios and the U-Pb age overestimation (due to ^{206}Pb excess or common Pb), and associated Tera-Wasserburg ($^{207}Pb/^{206}Pb$ vs $^{238}U/^{206}Pb$) diagrams (c, d)

Most of the samples (VDG, LCO, KER, SOY, E2R, SAV, SMC) give U-Pb ages that are similar or only slightly older than $^{208}Pb/^{232}Th$ ages (maximum 2 Ma difference). Remarkably, all the monazite grains with relatively low Th/U ratios (<30) have U-Pb ages that coincide, within the measurement error range, with the $^{208}Pb/^{232}Th$ age. For these monazites, Th content is generally low (<10,000 ppm, except *SOY01* and *E2R* samples) in comparison to the Th concentration measured in monazite with higher Th/U ratio investigated in our study or previously published (between 15,000 to 60,000 ppm in

Janots et al. 2012 and 5000 to 50,000 ppm in Berger et al. 2013). The U content of low Th/U ratio monazite ranges from 10 to 500 ppm (as in Janots et al. 2012 and Berger et al. 2013). Low Th/U ratios are attributed to low Th content. In these clefts, monazite is the only Th-bearing mineral identified and the low Th content is difficult to explain by a preferential Th fractionation (including ^{230}Th) between the fluid and another mineral phase, at least in the cleft. Fluids from which low-Th monazite has crystallized may simply have low Th contents, due to lower Th concentrations of the host-rock or a restricted mass transfer from host-rock to cleft. In comparison to high Th/U ratio monazite crystals found in clefts hosted by gneiss and granite (this study; Janots et al. 2012; Berger et al. 2013) the low-Th monazite bearing clefts of this study are mostly located in micaschists. Remarkably, whole-rock compositions in the ECM (Thiébaud et al. 2010, Belledonne massif) have shown that micaschists (Feissons micaschites, e.g. LCO, RDN samples) often have a lower Th content of 12 ppm (for 3 ppm of U) than the rocks of the crystalline basement (Lauzière granite or ortho-gneiss, close to E2R sample), with a Th content that can reach 46 ppm (for 8 ppm of U). These observations may indicate host-rock control on hydrothermal monazite composition. However, the low Th/U ratios in monazite grains taken from a cleft in Lauziere granite (*E2R08* monazite) indicate that host-rock composition is not the only factor that controls the Th/U ratio of hydrothermal monazite.

On the other hand, samples with a wide range of high Th/U ratios, give older U-Pb dates compared to Th-Pb ages (RDN, ISO, MTV and MTC). In high Th/U ratio monazite, there is a systematic correlation between the age overestimation (due to ^{206}Pb excess) and the Th/U ratio measured in monazite (ISO sample; Fig. 7a). Monazites with lower Th/U ratios are less affected by this aging effect (E2R sample; Fig. 7b). Assuming equilibrium within the ^{238}U decay series, the proportion of ^{206}Pb excess can be directly correlated to the $f_{\mathrm{Th/U}}$ fractionation between fluid and solid, according to the following expression:

$$^{206}\mathrm{Pb\ excess\ (in\ \%)} = 100\left[\frac{\lambda_{238}}{\lambda_{230}}(f-1) * \frac{1}{e^{\lambda_{238}T}-1}\right] \text{ where } f = \left[\frac{(\mathrm{Th/U})_{\mathrm{mineral}}}{(\mathrm{Th/U})_{\mathrm{liquid}}}\right] \quad (1)$$

Therefore, the linear correlation between Th/U ratio in monazite and the age overestimation indicates that a high Th/U ratio in monazite clearly reflects high Th/U fractionation between monazite and its environment. The causes of this extreme fractionation are unclear (fluid or solid paragenesis at equilibrium), but are often encountered in an Alpine hydrothermal environment (Janots et al. 2012; Berger et al. 2013; Gnos et al. 2015). In our study, monazites with a high Th/U ratio have the lowest U contents (<100 ppm, SMC and MTC samples). Furthermore, they are systematically associated with hematite in the clefts, indicating oxidizing conditions where hexavalent U(VI), which cannot be incorporated by monazite, may have dominated over tetravalent U(IV) (e.g. Cuney and Mathieu 2000). Therefore, our results confirm that an extremely high Th/U in monazite is probably controlled by the redox conditions under which hydrothermal monazite crystallized (Janots et al. 2012; Gnos et al. 2015). But the presence of hematite may not be a sufficient indicator for possible U-Pb disturbance induced by high Th/U fractionation, since some hydrothermal monazites of Bonanza-style mineralization of palladiferous gold in specular hematite-rich lodes show low Th/U ratios and give reliable U-Pb ages (Cabral et al. 2014).

3.5.2. U-Pb and Th-Pb dating of hydrothermal xenotime crystals

Numerous studies have shown that U-Pb dating of xenotime is a useful tool for investigating the diagenesis of siliciclastic rocks (e.g. Rasmussen 2005) and hydrothermal mineralization or metamorphic events (e.g. Kositcin et al. 2003; Vallini et al. 2006; Rasmussen et al. 2007; Tartèse et al. 2015). Xenotime has low initial Pb content, and is extremely resistant to Pb loss by volume diffusion at cleft forming conditions (< 600°C, Cherniak 2006). While xenotime is known to preferentially incorporate U over Th (low $f_{Th/U}$, VanEmden et al. 1997), hydrothermal xenotime grains can have high Th/U ratios (>1, Kositcin et al. 2003; Lan et al. 2013). In this study, the Th/U ratios of investigated hydrothermal xenotimes (XMTC sample) were found to be between 2 and 67. By comparison, monazites (MTC sample) from the same veins have a Th/U ratio between

210 and 523. Owing to the typically low $f_{Th/U}$ in xenotime, the high Th/U ratio measured (together with Th and U contents) in the investigated samples is consistent with a hydrothermal environment (Kositcin et al. 2003), and is indicative of a very low U(IV) content in fluid, and oxidizing conditions (see 5.1.). The Th content (up to 1 wt %, Fig. 3) reflects the high-Th concentration in the hydrothermal fluid (also attested by the presence of thorite) and it is thus possible to investigate the reliability of both U-Pb and Th-Pb systematics in xenotime. Xenotime crystals are usually dated using the U-Pb systematics (Rasmussen 2005). However, Th-Pb dating gives more homogeneous and reliable results here than U-Pb dating in the Alpine cleft xenotime. In the XMTC sample, 9 analyses on 5 xenotime grains (*XMTC01* to *XMTC05*) give a well-defined mean $^{208}Pb/^{232}Th$ age of 34.9 ± 0.5 (MSWD = 1.1), which is close to but slightly older than the Th-Pb monazite age (32.3 ± 0.3 Ma). Like the cleft monazite (e.g. Fig. 7c), xenotime U-Pb dates suffer from various contributions of common Pb and ^{206}Pb excess ($^{238}U/^{206}Pb$ vs ^{232}Th-^{208}Pb diagram, Fig. 6d). As a result, the $^{206}Pb/^{238}U$ ages are heterogeneous and older in comparison to the $^{208}Pb/^{232}Th$ age (34.9 ± 0.5 Ma). In the MTC and XMTC samples, the difference between monazite and xenotime ages may have several causes, e.g.: matrix effect on the calibration of Th-Pb and U-Pb isotope ratios (xenotime standardized on monazite), initial/common Pb contribution, or may simply result from the earlier crystallization of xenotime compared to monazite. Roger et al. (2015) have shown that xenotimes dated by LA-ICPMS and standardized on monazite give U-Pb ages that are consistent with monazite ages. However, in this study, xenotime Th-Pb ages were found to be slightly older than monazite Th-Pb ages (around 4%) and it was proposed that the difference between the two ages is a matrix effect. Th-Pb dating of xenotime (standardized on monazite) is not a trivial matter and the matrix effect on Th-Pb dating remains to be addressed in order to understand whether the age difference has a meaning. A combination of Th-Pb dating of hydrothermal xenotime and monazite would be then attractive to determine the chronology and duration of mineral precipitation in hydrothermal veins.

Assuming the xenotime Th-Pb age to be reliable would imply that xenotime grew earlier than monazite. In the cleft investigated, the crystallization sequence is unclear but one early growth is consistent with the study of Gnos et al. (2015) suggesting that hydrothermal cleft xenotime crystallization is not in equilibrium with monazite with respect to the monazite-xenotime thermometer from Heinrich et al. (1997). However, monazite-xenotime thermometers (Gratz and Heinrich 1997; Heinrich et al. 1997; Andrehs and Heinrich 1998; Seydoux-Guillaume et al. 2002b) have not been calibrated in hydrothermal conditions (i.e. below 400°C). Successive monazite and xenotime precipitation (separated by a few Ma) indicates that the fluid reached xenotime oversaturation earlier than monazite. The difference in oversaturation between monazite and xenotime depends on their respective solubility (xenotime is less soluble than monazite in these conditions) or different REE concentrations in the fluid (higher HREE concentrations compared to LREE). The HREE/LREE difference in the fluid may be due to preferential alteration of HREE>LREE minerals or by incongruent dissolution (replacement reactions) with preferential HREE mobility, that is unclear without any host-rock characterization.

3.5.3. Consequences of hydrothermal monazite replacement on Th-Pb ages

The hydrothermal monazite crystals investigated show different textures that can be linked to crystallization processes (BSE images; Fig. 4). While few monazite crystals are chemically and isotopically homogeneous, indicative of a single growth episode (Fig. 4e), most specimens show concentric zoning with sharp and straight interfaces between the compositional domains suggesting successive growth episodes (e.g. Fig. 4f, i). Within a single crystal, $^{208}Pb/^{232}Th$ dating in the successive rims gives ages that can overlap (e.g. *E2R11* monazite, Fig. 5f) or be separated by several Ma (Fig. 5h). Within one compositional domain, the age reproducibility reflects negligible isotopic disturbance in the Th-Pb systematics during hydrothermal growth. This is independently confirmed by the good agreement of U-Pb and $^{208}Pb/^{232}Th$ dates in low Th/U monazite domains. In the

RDN sample, the three monazites *RDN01*, *RDN02* and, to a lesser extent *RDN04*, show a more complex texture with a patchy core and homogeneous rim (Fig. 4b, c). In the patchy domain, $^{208}Pb/^{232}Th$ dating gives intermediate ages between 10.3 ± 0.5 Ma and 8.4 ± 0.4 Ma (rim age, Fig. 5b) that may correspond to continuous crystallization or mixing between the rim and relic core domains. In comparison to the rest of the grains, the patchy domains have a high Th/U ratio (up to 236) and U-Pb ages are significantly disturbed by ^{206}Pb excess (Table 1). Texturally (Fig. 4b, c), these patchy zones are characterized by abundant porosity, suggesting replacement processes. During mineralization in the cleft system, primary monazite may be in disequilibrium with the hydrothermal fluid due to new equilibrium conditions (change in temperature or mineral paragenesis in a closed system) or new fluid infiltration (open system). Experimental studies (Teufel and Heinrich 1997; Seydoux-Guillaume et al. 2002a; Harlov and Hetherington 2010; Hetherington et al. 2010; Harlov et al. 2011; Williams et al. 2011; Budzyn et al. 2011), demonstrated that monazite can react by dissolution and precipitation processes, leading to partial or total replacement of primary monazite by a secondary monazite with a different composition (at equilibrium with the experimental fluid). Replacement domains are typically marked by patchy zoning textures (Ayers et al. 1999; Townsend et al. 2001) and the presence of abundant porosity (Putnis 2002; Putnis and Putnis 2007; Putnis and Austrheim 2010), as observed in the *RDN01*, *RDN02* and *RDN04* monazites. In monazites where such replacement processes were observed, age interpretation is often affected by U-Th-Pb disturbance, especially when there is no relation between age and geometry of the growth zones (Gnos et al. 2015). Contrary to Janots et al. (2012) and Didier et al. (2013), these replacement zones do not indicate an older age than that of monazite core or pristine monazite, indicating no (or limited) radiogenic/common Pb inheritance at the reaction interface. Intermediate $^{208}Pb/^{232}Th$ ages in patchy zones are then interpreted as age mixing between core and rim domains due to incomplete replacement. The replacement will be triggered here by a new fluid pulse linked to a deformation or tectonic event, or simply by new equilibrium conditions (discussed in section 6.1.).

3.6. Monazite crystallization and age interpretation

3.6.1. Short crystallization episodes

The abundant hydrothermal monazite ages presented in this study give a precious insight on the duration and periodicity of monazite crystallization. The in-situ Th-Pb dating typically shows that monazite crystallizes by repetitive growth over short period(s) of time. Brief growth episodes are attested by the homogeneity of Th-Pb ages within a single compositional domain (typically around 0.1-0.2 Ma for Alpine monazite) and through distinct domains. The overlapping ages of distinct compositional domains measured in most of the investigated cleft monazite (e.g. *E2R11* Fig. 4i, 5f) indicate that monazite crystals grew over a period clearly shorter than 0.3 Ma. Dating core and rim domains gives distinct ages separated by 1-2 Ma in only two crystals (*SMC01* and *RDN04*), as in Janots et al. (2012) and Berger et al. (2013). However, this is slightly different from the cleft monazite of the Tauern (Gnos et al. 2015) that gives ages scattered over 3-4 Ma, with the interpretation that the monazite crystallized during progressive cooling between ~ 300-200°C. In a single cleft (SOY sample), two specimens gave distinct ages separated by more than 4 Ma with well-defined Th-Pb ages of 11.8 ± 0.1 Ma (MSWD=0.9) and 7.5 ± 0.2 ma (MSWD=2.9). This indicates two distinct crystallization episodes in the same cleft. The repetition of brief periods of monazite growth suggests that monazite crystallization is driven by discontinuous tectonic activity (e.g. Janots et al. 2012; Berger et al. 2013). Fracturing by tectonic activity (and/or associated subsequent hydraulic fracturing; Baietto et al. 2009) is efficient to enhance new crystallization by promoting new fluid flows in the system and/or by perpetuating alteration reactions in the fractured host-rock (Berger et al. 2013). In the ECM, stable isotopes (e.g. Rossi and Rolland 2014) or fluid inclusion studies (e.g. Mullis et al. 1994) suggest that cleft minerals mainly precipitate from an evolving fluid in a closed system. In that case, episodic growth would be triggered more by fracturing episodes (with possible associated pressure change) rather than by new fluid infiltration. The brief growth episodes (<0.2 Ma within domains) could therefore be indicative of a period of intense tectonic activity.

In comparison with Alpine cleft monazites from the Eastern Tauern Windows (Gnos et al. 2015), monazites from the investigated ECM generally show crystallization over a shorter time interval. The Eastern Alps cleft monazites commonly show complex compositional and isotopic zoning with growth episode ages ranging from 19 to 15 Ma that could suggest a longer period of continuous activity. More generally, monazite crystallization appears more temporally restricted than certain other minerals, like adularia (Rossi and Rolland 2014). Indeed, ^{40}Ar-^{39}Ar dating of adularia samples collected from a horizontal cleft in the Mont-Blanc massif indicates several crystallization episodes over a period of 4-5 Ma (between 16 and 11 Ma). However, since monazite and adularia ages were obtained in different vein populations, it is difficult to compare the ages recorded by the two chronometers.

One interesting feature emerging from this study concerns the variability of the Th/U ratio of monazite in a single cleft. The Th/U ratio signatures of cleft monazite investigated here (Fig. 3) can be typical of monazite found commonly in a metamorphic environment (low Th/U ratios) or hydrothermal environment (high Th/U ratios), indicating that the Th/U ratio in hydrothermal monazite may not always be related to geological forming conditions. Remarkably, different crystals taken from the most studied cleft (E2R sample) have distinct Th/U ratio signatures (Fig. 3, 8b) for a similar age of 12.4 ± 0.1 Ma. Each grain has a specific Th/U ratio interval (e.g. *E2R01*: 34 to 57). Only *E2R11* (Fig. 4i) has two signatures with a rim composition (Th/U ratio between 16 and 33) overlapping that of another grain (*E2R09*). The difference in Th/U ratio in the distinct grains suggests that the growth of the cleft monazite crystals was not coeval. In the E2R cleft, it is suggested that monazite grew successively from a fluid with evolving Th/U composition and/or different Th/U fractionation between fluid and monazite. This is in agreement with other observations in the investigated cleft that generally presents a rim with lower Th and U contents compared to the core. This may be due to Th (and in a lesser extend U) depletion of fluid during monazite crystallization or rapid change of mineral assemblages in equilibrium with monazite during successive short crystallization episodes (below ~ 1Ma).

3.6.2. Comparison of Th-Pb age with deformation/exhumation ages

A summary of the deformation and exhumation ages of the western Alps is proposed in Figure 8, together with the integration of cleft monazite (and xenotime) ages obtained in this study. For this summary, dating in the shear zone (Ar-Ar or K-Ar) is assumed to give the ages of the ductile regime, probably close to the metamorphic peak. Zircon and apatite fission tracks are thermochronometers that give constraints on the cooling temperatures below 280-240°C and 120-60°C, respectively (Yamada et al. 1995; Bernet 2009 and e.g. Gallagher et al. 1998). This regional comparison allows the age limits of hydrothermal activity in the tectonic history to be defined.

As already proposed by Berger et al. (2013) and Gnos et al. (2015), there is a systematic overlap between monazite and zircon fission track ages along the Alpine Arc. This indicates monazite crystallization below the ZFT annealing zone (below 280 °C, Yamada et al. 1995; Bernet 2009) or for hydrothermal activity in a cooling host-rock. Similarly, this dataset shows the close relation between monazite ages (hydrothermal activity) and late stages of development of shear zones in the Alpine Arc during ductile to brittle deformation transition. Using deformation and hydrothermal monazite ages, the timing of the late stages of deformation can be described as follows: (1) During ductile deformation, mylonitic shear zones developed to accommodate regional transpression and constituted pathways for fluid flow (e.g. Rolland et al. 2009). (2) Deformation during the ductile to brittle transition formed Alpine clefts, involving pervasive mineral reactions in the host-rocks. Meanwhile, shear zones were still active (e.g. Rossi and Rolland 2014), and clefts also accommodated the major hydrothermal fluid flow (Baietto et al. 2009). (3) Hydrothermal monazites crystallized coevally with the late stages of shear zone functioning, i.e. at the end of the ductile to brittle transition (~ 300 °C; Bergemann et al. submitted), during short hydrothermal mineralization episodes.

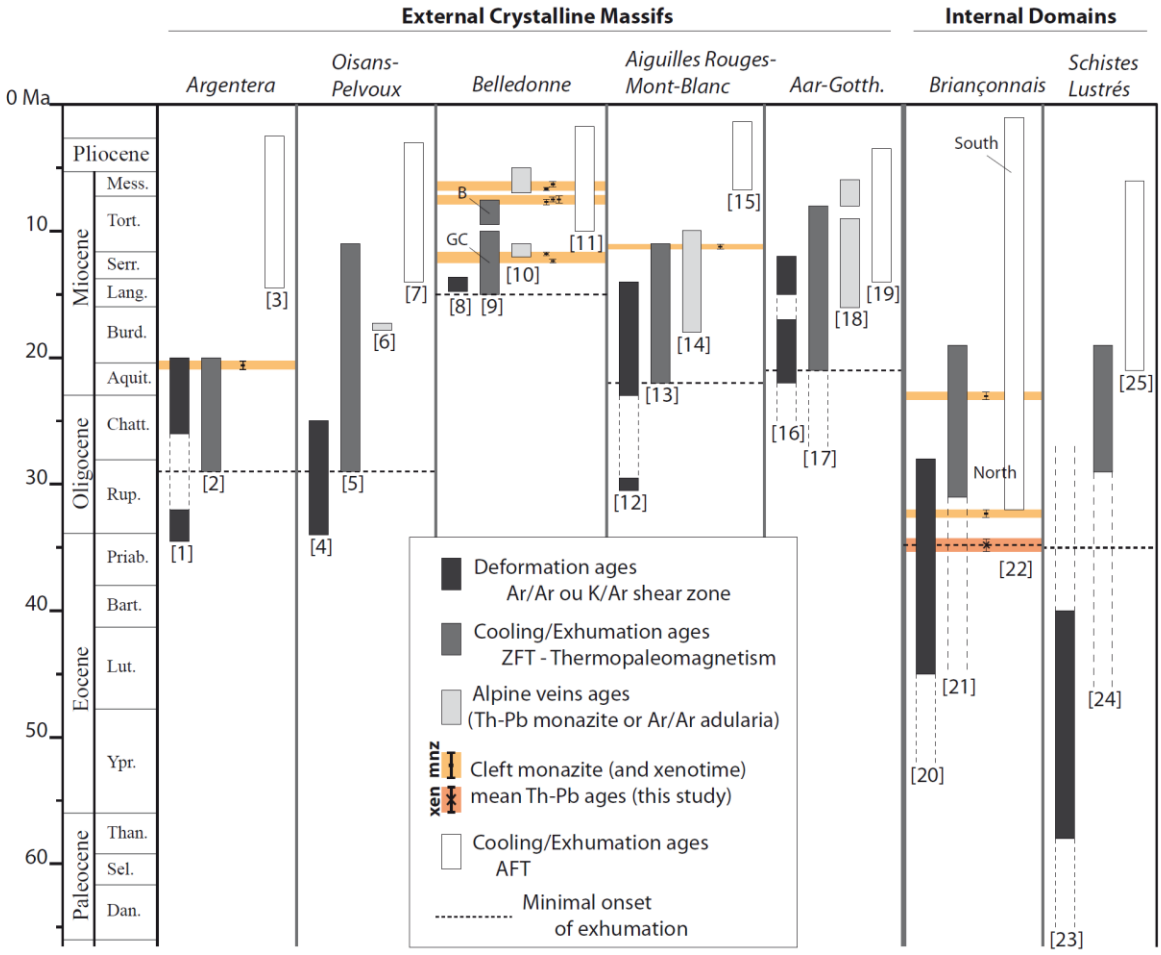

Figure 3-8 Synthesis of deformation and cooling ages of the western Alps with integration of cleft monazites ages. [1] Corsini et al. 2004; Sanchez et al. 2011 [2] Bigot-Cormier et al. 2006 [3] Bogdanoff et al. 2000; Sanchez et al. 2011a; Bigot-Cormier et al. 2006; [4] Nziengui 1993; Simon-Labric et al. 2009; Bellanger et al. 2015 [5] Crouzet et al. 2001; van der Beek et al. 2010 [6] Gasquet et al. 2010 [7] Stabil 1995; Seward et al. 1999; Van der Beek et al. 2010; Beucher et al. 2012 [8] Gasquet 1979 [9] Seward and Mancktelow 1994; Fügenschuh and Schmid 2003 [10] Gasquet et al. 2010 [11] Lelarge 1993; Seward and Mancktelow 1994; Fügenschuh et al. 1999; Fügenschuh and Schmid 2003 [12] Crespo-Blanc et al. 1995; Kirschner et al. 2003; Leloup et al. 2005; Rolland et al. 2008; Cenki-Tok et al. 2014 [13] Soom 1990; Carpena 1992; Seward and Mancktelow 1994; Glotzbach et al. 2011 [14] Leutwein et al. 1970; Marshall et al. 1998; Rossi and Rolland 2014 [15] Soom 1990; Seward and Mancktelow 1994; Leloup et al. 2005 [16] Dempster 1986; Michalski and Soom 1990; Kralik et al. 1992; Challandes et al. 2008;

Rolland et al. 2009 [17] Michalski and Soom 1990; Glotzbach et al. 2010 [18] Kralik et al. 1992; Janots et al. 2012; Berger et al. 2013; Rossi and Rolland 2014 [19] Glotzbach et al. 2010 [20] Freeman et al. 1997; Freeman et al. 1998; Lanari et al. 2012; Strzerzynski et al. 2012; Lanari et al. 2014; Villa et al. 2014 [21] Vance 1999; Schwartz 2000; Fügenschuh and Schmid 2003; Malusà and Vezzoli 2006; Beucher 2009 [22] Malusà et al. 2005; Seward and Mancktelow 1994; Fügenschuh et al. 1999; Tricart et al. 2007; Beucher 2009 [23] review in Agard et al. 2002 [24] [25] Schwartz et al. 2007

3.6.3. Timing of hydrothermal activity in the western Alps

At the western Alps scale, this large dataset of LA-ICPMS hydrothermal mineralization dating has provided important systematics.

The major events around 13 to 11 Ma and 8.5 to 6.5 Ma earlier determined by Gasquet et al. (2010) in the Belledonne massif have been here confirmed by 8 clefts dated in this study. Remarkably, these two episodes of monazite crystallization, probably reflecting periods of higher tectonic activity, are found not only in the Belledonne but also in the Mont Blanc and the Aar and Gotthard massifs of the Central Alps. In the Mont-Blanc massif, this is the first time that hydrothermal monazites have been dated but adularia Ar-Ar dating in horizontal veins gives ages ranging from 11 to 16 Ma. There have already been a few studies presenting monazite ages in the Central Alps (Janots et al. 2012; 2013; Berger et al. 2013; Bergemann et al. submitted). Horizontal cleft monazite ages from 15.5 ± 0.2 to 13.8 ± 0.2 Ma in the Aar-Gotthard massifs (Janots et al. 2012) are slightly older than those obtained in this study on sample taken from the Mont Blanc and the Belledonne massif. These results are not surprising, given that the horizontal clefts linked to exhumation (vertical movement) are prior to vertical clefts (Gasquet et al. 2010). This is independently confirmed by new monazite dating obtained in the vertical and horizontal veins of the Grimsel pass (Aar massif, Bergemann et al. submitted) that both give Th-Pb ages around 11 Ma and 7 Ma. In the Aar massif, Berger et al. (2013) determined vertical cleft monazite ages between 8.03 ± 0.22 to 6.25 ± 0.60 linked to dextral movements, comparable to the younger ages in the Belledonne massif between 8.3

± 0.2 Ma (rim of RDN sample) and 6.3 ± 0.2 Ma (rim of *SMC01*monazite). This cleft formation is attributed to dextral movements along the Ornon-Roselend fault (Gasquet et al. 2010) and the Rhone-Simplon fault (Campani et al. 2010), that initiates at 13.7-11 Ma (Rolland et al. 2009; Campani et al. 2010) and may have been active, at least episodically, until around 6 Ma. It is also coeval with movement along the Mont Blanc shear zone between ~12-6 Ma (Leloup et al. 2005).

In comparison, the timing of deformation/exhumation and hydrothermal activity in the Argentera and Pelvoux (and further north in the Tauern Window, Gnos et al. 2015) massifs appears to be dissociated from that of the Belledonne, Mont Blanc and Aar massifs. In the Argentera massif, the new monazite crystal age of 20.6 ± 0.3 Ma is only slightly younger than the 22.2 ± 0.3 Ma age (Fig. 8) determined by Ar-Ar dating on neocrystallized phengites (Corsini et al. 2004) taken from a ductile Alpine shear zone (Frema Morte) during the major shortening phase and overlapping with the end of the ZFT dataset at 20 Ma (Bigot-Cormier et al. 2006). This confirms the diachronism between the hydrothermal activity in the Belledonne and Pelvoux massifs (around 17 Ma) previously noted by Gasquet et al. (2010). The new Argentera age therefore suggests a general age rejuvenation of hydrothermal activity from South to North in the ECM of the Western Alps.

As expected from other thermochronometers, there is also a diachronism between the internal and external massifs. In the Internal Domains, which have been subjected to more intense metamorphic conditions, deformation is more pronounced and ductile deformation ages are more decoupled from exhumation ages than in the ECM (Fig. 8). The monazite ages of 23.0 ± 0.2 Ma and 32.3 ± 0.3 Ma, determined from hydrothermal cleft samples, are the first ages of late-stage hydrothermal activity in the Briançonnais Zone. The MTC monazites age of 32.3 ± 0.3 Ma coincides with the plate collision, activation of the Penninic Front and westward propagation of deformation during the upper Eocene to lower Oligocene (e.g. Simon-Labric et al. 2009). This also corresponds to the timing of late stages of ductile deformation around 32 Ma (Fügenschuh and Schmid 2003). In the MTV sample (Houillère Zone), monazite dating gave 23.0 ± 0.2 Ma age that

corresponds to the ZFT ages determined by Fügenschuh and Schmid (2003) between 23 and 19 Ma. This age cannot be related to a precise tectonic or deformation event in the Internal Domains.

3.7. Conclusions

In this study, 29 cleft monazites (~270 analyses) were successfully dated by LA-ICPMS. The comparison between U-Pb and Th-Pb dating showed that U-Pb dating of young monazite can be effective for monazite with low Th/U ratios (<30) and low Th and U contents, with limited ^{206}Pb excess. Hydrothermal Th-rich xenotimes dated by LA-ICPMS using a monazite standard gives a reliable Th-Pb age slightly older than monazite and needs further investigation in order to be fully understood. Generally, the investigated hydrothermal monazite has only minor U-Th-Pb disturbance due to monazite growth and reequilibration in open system conditions. Only in the *RDN01, RDN02* and *RDN04* grains, Th-Pb dating show possible age disturbance (Pb inheritance or age mixing) related to replacement during fluid-mineral interactions in hydrothermal environments. These replacement zones are characterized by complex compositional textures, high Th/U ratios and porosity. This dataset corroborates the fact that compositional domains of hydrothermal monazites have crystallized briefly during hydrothermal activity over a short period (< 0.5 Ma). These correlations between cleft monazite (and xenotime) ages and the existing time-constraint on the formation of the Alps show close relations between hydrothermal activity, monazite precipitation and deformation/exhumation. This suggests that hydrothermal monazite might be useful for tracing the late stages of deformation history of orogens, relevant for short, intense tectonic episodes recorded along the western Alps. Hydrothermal monazites have recorded the timing of mineralization under the ductile-brittle transition conditions, during the Oligocene to Miocene deformation phases of the Alps. Their dating can be an alternative to other thermochronometric techniques (Ar-Ar or K-Ar) on syn-kinematic white mica or clay

minerals that can be disturbed (e.g. isotopic resetting, Ar loss or ^{40}Ar excess), to date the late stages of deformation in shear zones or brittle to brittle-ductile faults.

Acknowledgments

We thank J. Valverde and F. Guichon for providing monazite crystals and their locations, V.Magnin for its help with microprobe analyses and N. Findling for his assistance with the SEM. This project is funded by the ANR-JC grant (Mona, 2012).

4. DURÉE ET TEMPÉRATURE DE CRISTALLISATION DES MONAZITES HYDROTHERMALES ALPINES

Hydrothermal circulation during late stages of exhumation constrained by fluid inclusion analyses, and zircon fission-track and monazite Th-Pb dating (Belledonne massif, Western Alps)

(Article en préparation)

A. Grand'Homme[1], E. Janots[1], D. Guillaume[2], M. Bernet[1], V. Bosse[3], A.M. Seydoux-Guillaume[2]

[1]ISTerre, Univ. Grenoble Alpes, BP 53, 38041 Grenoble, France (alexis.grandhomme@ujf-grenoble.fr)
[2]LMV, Département de Géologie, Université Jean Monnet, Saint-Étienne, 42023, Saint-Etienne, France
[3]LMV, UMR 6524, BP 10448, 63000 Clermont-Ferrand, France

Keywords Exhumation; monazite Th-Pb dating; fluid inclusions; zircon fission track analysis; Belledonne massif

Note: Supplementary material 4-1 corresponds to Annexes 4-1 and Fig.X or Table X to Fig. 4-X or Table43-X

Abstract

Alpine veins formed during brittle deformation under retrograde metamorphic conditions (T<450°C). In these veins, monazite crystals can precipitate from the hydrothermal fluids. The monazite crystals in hydrothermal veins are commonly zoned in composition and age, indicating successive growth episodes. Previous studies on hydrothermal Alpine monazites indicate short episodic growth episodes (<0.5 Ma) or conversely slow growth during cooling and exhumation (3-4 Ma), depending on the massifs. They also showed a link between monazite ages and zircon fission-track ages in the external crystalline massif (ECM). This seems to indicate monazite crystallization temperature close to the ZFT annealing zone between 300-200 °C, depending on the rate of cooling. However, despite this apparent link between zircon fission-track ages and monazite ages, the monazite crystallization temperature is still unconstrained. To understand the influence of fluid circulations on the geothermal gradient and the significance of monazite ages, we used a multidisciplinary approach, based on zircon fission-track dating, fluid inclusion analysis and Th-Pb dating of hydrothermal monazite and applied to a hydrothermal vein located in the Belledonne massif (Western Alps).

The results of this study helped to constrain thermally and chronologically the age and duration of hydrothermal circulations associated with vein opening during exhumation. The microthermometric study indicates at least two populations of fluid inclusions: one that represents most of the fluid inclusions in quartz crystals with homogenization temperature (T_h) around 200°C and the other that represents most of the inclusions in monazite crystals with T_h around 300-320°C. We showed that hydrothermal monazites crystallize early (compared to most of the quartz) in the vein (at 12.4 ± 0.1 Ma) from a "hot" fluid (400-450°C), with respect to the host rock already "cooled" around 240-280°C, 2 Ma earlier (around 15 Ma). These fluid circulations (~120 °C hotter than the host rock) were sufficient to reset the zircon fission-track ages of samples taken from the wall rocks of the hydrothermal vein. This probably implies a vertical fluid flow in an open system at the time of the vein opening. Conversely, the zircon fission-track samples,

located at 30 and 60m of the vein, were not affected (or only partially annealed). This study shows that the monazite crystallized rapidly, sporadically and shortly after the opening of the studied vein, and could therefore date the tectonic event responsible for the opening of the vein.

4.1. Introduction

The timing of the late stages of exhumation of orogenic belts during ductile-brittle transition and brittle deformation are difficult to constrain, especially in low-grade metamorphic units. In addition to structural analysis, others techniques, such as fluid inclusion analysis (e.g. Poty et al., 1974; Mullis et al., 1994) or fission-track analysis (e.g. Fügenschuh and Schmid, 2003; Seward and Mancktelow, 1994) are required to resolve the cooling history during exhumation and the link between deformation, exhumation and fluid circulation. The timing of hydrothermal activity and its influence on the geothermal settings is also crucial to reconstruct the exhumation history. Several recent studies have documented and dated the recent deformation and fluid circulations events that affected the External Alps (Fig. 1) by in-situ (U-)Th-Pb dating on hydrothermal monazite (Gasquet et al., 2010; Janots et al., 2012; Berger et al., 2013; Gnos et al., 2015; Grand'Homme et al., submitted) from Alpine veins (or cleft). Alpine veins correspond to hydrothermal crystallizations formed during brittle deformation under retrograde metamorphic conditions at temperatures and pressures below 400-450°C and 3-4 kbar respectively (Mullis et al., 1994; Mullis, 1996). These studies on Alpine monazite dating demonstrated that hydrothermal monazite is a powerful aid for dating late-stage orogenic hydrothermal activity associated with brittle deformation during exhumation of the Alpine belt. Some previous studies (Berger et al., 2013; Gnos et al., 2015) on hydrothermal monazite have highlighted a link between zircon fission-track (ZFT) ages and hydrothermal monazite ages indicating monazite crystallization temperatures close to the ZFT annealing zone between 300-200 °C, depending on the rate of cooling. This suggests monazite crystallization during cooling related to exhumation. However, this

assumption is in contradiction with short and episodic growth of monazite crystals (Janots et al., 2012) during intense tectonic events (Gasquet et al., 2010; Grand'Homme et al., submitted).

In this study, we propose a multidisciplinary approach to constrain the paleogeothermal settings associated with fluid circulation in Alpine veins responsible for hydrothermal monazite crystallization, during the late stages of exhumation. This approach is based on zircon fission-track dating, fluid inclusion analysis and Th-Pb dating of hydrothermal monazite and applied to a hydrothermal vein located in the Belledonne massif (Western Alps) to analyse fluid temperature conditions responsible for monazite crystallization in veins and its influence on the thermal gradient of the host rock.

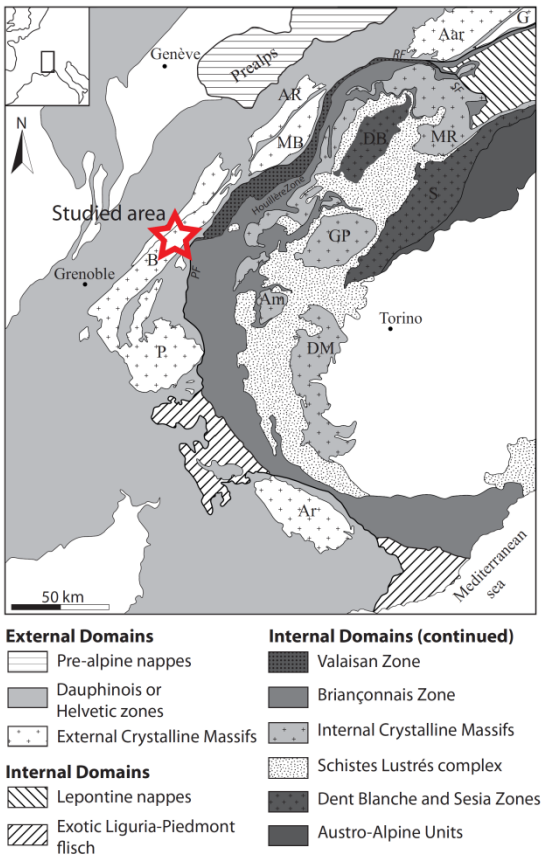

Figure 4-1 Geological settings of the western Alps. External Domains: Aar; G: Gotthard; AR: Aiguilles Rouges; MB: Mont Blanc; B: Belledonne; GC : Grand Châtelard ; P: Pelvoux; Ar: Argentera. Internal Domains: MR: Monte Rosa; DB: Dent Blanche; S: Sesia; GP: Gran Paradiso; Am: Ambin; DM: Dora Maira. RF: Rhone Fault; SF: Simplon Fault; PF: Penninic Front. The stars show the location of the studied area

4.2. Geological Settings and previously published age data

The Alps resulted from the closure of the Ligurian part of the Tethys Ocean and the collision between the Eurasian and African plates. From west to east, the western Alps are composed of two main domains: the External Domains separated from the Internal Domains by the Penninic Front (Fig. 1). The External Domains corresponds to the pre-Alpine basement (External Crystalline Massif, ECM) and its Mesozoic to Cenozoic sedimentary cover. This Domain was underthrusted under the Internal Domains, following the activation of the Penninic Front. The Internal Domains correspond to a collisional prism, formed during subduction-collision of the Tethyan Ocean and parts of the European continental margin. This study is located in the Lauzière massif, north of the Belledonne massif, in the ECM (Fig. 1). The Belledonne massif is composed of two units, an external branch to the west and an internal branch to the east, separated by a layer of Triassic and Liassic sedimentary rocks (Median Fault). The Grand Châtelard massif (Fig. 2A), associated to the Belledonne massif corresponds to a second exposure of the Variscan basement with its detached sedimentary cover. The Lauzière massif represents the northern prolongation of the internal branch of the Belledonne massif between the Arc and the Isère valleys (Fig. 2A). The main units are parallel to each other, striking in NE-SW direction. They are, from north-west to south-east: (1) the Epierre granite (dated at 335 ± 13 Ma, Debon et al. 1998), the northward prolongation of the Sept Laux granite, (2) a series of Paleozoic paragneisses and micaschists (Bordet and Bordet, 1963; Gasquet, 1979), (3) a complex of migmatized Paleozoic orthogneisses (Poncerry, 1981), (4) the Lauzière granite (dated at 341± 13 Ma, Debon et al. 1998), intruding the Paleozoic orthogneiss, (5) a formation of gneisses, amphibolites and leptynites defined as the Leptyno-amphibolitic complex, also intruded by the Lauzière granite, (6) the Villard-Benoit Formation, a series of lower Carboniferous black schists, sandstones and conglomerates (Barféty et al., 1984), (7) the mylonitic Bonneval Formation corresponding to gneisses and micaschists interspersed with layers of the Villard-Benoit Formation conglomerates. These units are parallel to each other, striking in NE-SW direction.

Figure 4-2

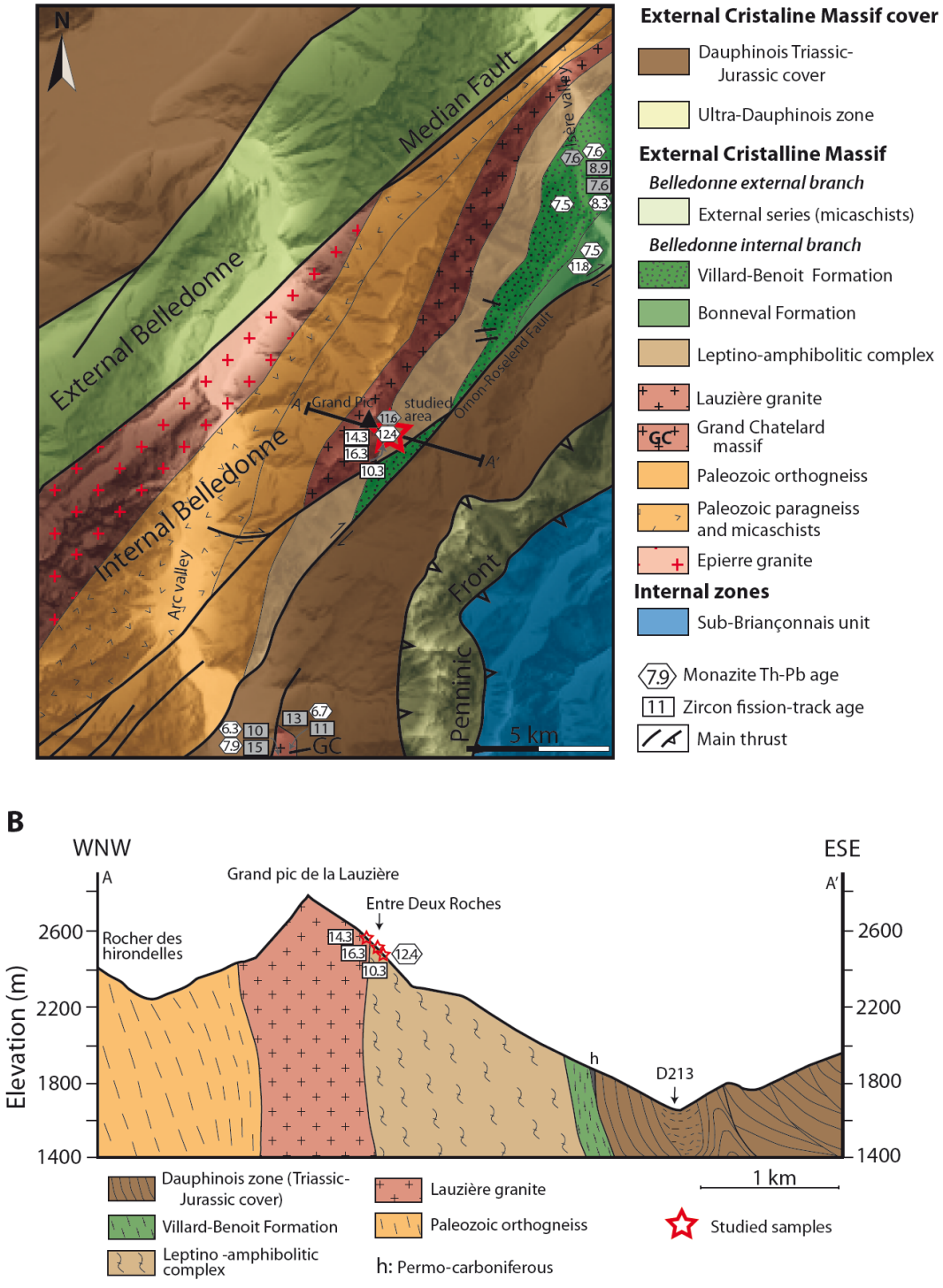
A
N
Median Fault
External Belledonne
Internal Belledonne
Arc valley
Isère valley
Ornon-Roselend Fault
Grand Pic
studied area
A
A'
11.6
14.3
12.4
16.3
10.3
7.6
8.9
7.6
7.5
8.3
7.5
11.8
Front
Penninic
5 km
6.3
10
7.9
15
13
6.7
11
GC
External Cristaline Massif cover
Dauphinois Triassic-Jurassic cover
Ultra-Dauphinois zone
External Cristalline Massif
Belledonne external branch
External series (micaschists)
Belledonne internal branch
Villard-Benoit Formation
Bonneval Formation
Leptino-amphibolitic complex
Lauzière granite
Grand Chatelard massif
Paleozoic orthogneiss
Paleozoic paragneiss and micaschists
Epierre granite
Internal zones
Sub-Briançonnais unit
7.9 Monazite Th-Pb age
11 Zircon fission-track age
Main thrust
B
WNW
ESE
A
A'
Grand pic de la Lauzière
Entre Deux Roches
Rocher des hirondelles
14.3
16.3
12.4
10.3
h
D213
Elevation (m)
2600
2200
1800
1400
1 km
Dauphinois zone (Triassic-Jurassic cover)
Villard-Benoit Formation
Leptino -amphibolitic complex
Lauzière granite
Paleozoic orthogneiss
h: Permo-carboniferous
Studied samples

Previous page: **Figure 4-2** Geological settings. Simplified geological map and representation of the main interfaces (A), from Barféty et al. (1984), Debelmas et al. (1989), Marquer et al. (2006), Gasquet et al. (2010) and representative geological cross-section of the studied area (B), from Barféty et al. (1984) and Gely (1989). Grey rectangles are zircon fission-track central ages from Fügenschuh and Schmid (2003), white rectangle are from this study, grey polygons are monazite Th-Pb ages from Gasquet et al. (2010) and white polygons are from Grand'Homme et al. (submitted)

A more detailed description of these units is given in Gasquet et al. (2010). Between the Lauzière granite and the Bonneval Formation, the Alpine imprint results in the low grade metamorphic, N010° to N030°E trending, and vertical schistosity. The eastern flank of the Lauzière massif is separated from its Triassic to Liassic cover (Dauphinois zone) by the Ornon-Roselend Fault, also marked by the presence of Lower-Carboniferous material ("houiller", Fig. 2B). This cover was overthrusted from the east by Carboniferous to Eocene rocks that form the Ultra-Dauphinois Zone (Fig. 2). The Ultra-Dauphinois Zone is itself separated from the Internal Domains (Sub-Brianconnais unit) by the Penninic Front. The study area corresponds to the contact between the Lauzière granite and the Leptino-amphibolitic complex (Fig. 2A and 2B).

In the Belledonne massif, only a few ZFT data have been published. Two ZFT ages of 8.9 ± 0.5 and 7.6 ± 0.4 Ma have been obtained in the Bonneval Formation (Fügenschuh and Schmid, 2003), just north of the studied area (Fig. 2A). In the same study, four ZFT ages of 10.3 ± 0.8, 10.6 ± 0.8, 12.7 ± 0.7 and 14.9 ± 1.2 Ma in the Grand Châtelard massif, south-east of the Lauzière massif, were presented. Further north, a single ZFT age of 10.6 ± 1.6 Ma was determined at the northern end of the external branch of the Belledonne massif (Seward and Mancktelow, 1994). In the ECM, two major populations of sub-horizontal and vertical hydrothermal veins or fissures are distinguished. The formation of horizontal quartz veins is related to horizontal shortening and shear zone formation during exhumation in the Mont Blanc massif (Poty, 1969; Rossi et al., 2005; Rossi and Rolland, 2014). The vertical veins formed later and cross-cut Alpine schistosity and horizontal quartz veins. These veins have an en-echelon habitus

and are related to a dextral transpressive tectonic regime during the late deformation stages (Gasquet et al., 2010; Berger et al., 2013). Horizontal veins or "fours alpins" (as named in the Mont Blanc massif) are mainly filled with quartz, chlorite, epidote, albite and calcite (Gasquet et al. 2010; Rossi and Rolland, 2014). Vertical veins display the same mineral assemblages but sometimes contain numerous species of rare minerals such as anatase, rutile, ilmenite, hematite, apatite, monazite or xenotime. A single phengite K-Ar age of 14.2 ± 0.6 Ma (Gasquet, 1979) has been reported for horizontal quartz vein in the Belledonne massif. In the Mont-Blanc massif adularia Ar-Ar dating gives ages ranging from 11 to 16 Ma (Rossi and Rolland, 2014). A horizontal fissure monazite Th-Pb age at 17.6 ± 0.3 Ma has also been reported in the Pelvoux massif (south Belledonne, Gasquet et al., 2010). In the Belledonne massif, the monazite Th-Pb ages indicate two periods of hydrothermal activity and monazite crystallization in the vertical veins at around 13-11 Ma and 8-6 Ma (Gasquet et al., 2010; Grand'Homme et al., submitted).

4.3. Analytical procedure

4.3.1. Zircon fission-track

Samples of ~5 kg were collected and zircons were extracted using common procedures for heavy mineral separation, including crushing, magnetic and heavy-liquid separation and hand picking. Mineral aliquots were mounted in Teflon® sheets and polished. Zircons were etched in NaOH and KOH melt at 228°C for 6 – 18 hours to expose fission-tracks, and subsequently covered with mica sheets as external detectors. All samples were irradiated with thermal neutrons ($0.5x10^{15}$ n/cm^2) at the FRMII research reactor in Garching, Germany, together with Fish Canyon Tuff age standards and IRMM541 dosimeter glasses. After irradiation the mica detectors were etched for 18 min in 48% HF at 20°C. Fission-tracks were counted dry at 1250x using an Olympus BH2 microscope and the FTStage 4.04 system. Because of the low sample quality with many zircons with

fractures and strong zoning, only 7-12 grains were analysed per sample and central ages were calculated using the RadialPlotter program of Vermeesch (2009).

4.3.2. Fluid inclusions

Fluid inclusions assemblages were identified on double-polished, ~200 to 300-µm-thick thin sections, using the criteria of Roedder (1984) and Goldstein and Reynolds (1994). Microthermometric measurements were performed with a Linkam THMS600 heating freezing stage mounted on a BX-51 Olympus microscope at the Geosciences Environnement Toulouse (GET) laboratory, following the procedures outlined by Roedder (1984) and Sheperd et al. (1985). Pure CO_2 fluid inclusions in quartz from Camperio (Poty and Stadler, 1974; Mullis et al., 1994) were used for calibration at CO_2 triple point (-56.6 °C) temperature and synthetic H_2O fluid inclusions in quartz for calibration at H_2O triple point (0°C) and critical point (374 °C) temperatures. Accuracy of the measure is estimated at ± 0.2 °C for temperature below 0°C and at ± 1°C for homogenization temperature. Low temperature, first melting (T_e) and final ice melting (T_m) measurement were performed before homogeneization temperature (T_h) measurement, following Bodnar (2003b), to reduce the risk of decrepitating the inclusions. Salinity (wt.% NaCl eq.), bulk density and dP/dT isochore slopes were calculated using the HokieFlincs-H_2O-NaCl spreadsheet of Steele-MacInnis et al. (2012).

4.3.3. LA-ICPMS dating

U-Th-Pb geochronology was performed by laser ablation inductively coupled plasma spectrometry (LA-ICPMS) at the Laboratoire Magmas et Volcans (LMV), Clermont-Ferrand (France). Analytical procedures for monazite dating are reported in detail in Didier et al. (2013) and Didier et al. (2014). Ages are given at the 2σ level and the spot size is 11µm. (Table 4). Data disturbed by inclusions, fractures or age mixing (between different areas of a single grain) were not taken into account in the calculations. The occurrence of initial Pb in the sample can be monitored by the change in the ^{204}(Pb+Hg)

signal intensity, but no Pb correction was applied. Monazite data are corrected for U–Pb and Th–Pb fractionation occurring during laser sampling and for instrumental mass discrimination (mass bias) by standard bracketing with repeated measurements of the Moacyr monazite standard (Cruz et al. 1996; Seydoux-Guillaume et al. 2002a; Gasquet et al. 2010; Fletcher et al. 2010). At the beginning and end of every run, repeated analyses of the Manangoutry monazite (Paquette and Tiepolo 2007) standard, treated as unknown, independently controlled the reproducibility and accuracy of the corrections. Data reduction was carried out using the GLITTER® software package (van Achterbergh et al. 2001; Jackson et al. 2004). Calculated ratios were exported and age diagrams were generated using the Isoplot software package by Ludwig (2001). The concentrations of U-Th-Pb were calibrated with respect to the certified contents of the Moacyr monazite (Seydoux-Guillaume et al. 2004).

Only $^{208}Pb/^{232}Th$ ages are discussed in the case of young hydrothermal monazite dating because: 1. the commonly high Th/U ratio of hydrothermal monazite (Poitrasson et al. 2000; Pyle 2006; Janots et al. 2012; Seydoux-Guillaume et al. 2012); 2. U decay series could be in disequilibrium in young monazites (Scharer 1984), resulting in overestimated $^{206}Pb/^{238}U$ ages. Secular equilibrium among the intermediate decay products of Th occurs after about 30 years, so it seems reasonable to assume that the initial ^{208}Pb is absent; 3. ^{232}Th is so abundant that ^{208}Pb originating from initial Pb is generally negligible compared to radiogenic ^{208}Pb (Bosse et al. 2009; Janots et al. 2012).

4.3.4. LA-ICP-MS fluid analysis

LA-ICP-MS analyses were carried out at the G2R laboratory (Nancy, France). The LA-ICP-MS system is composed of a 193 nm GeoLas Excimer laser (ArF, Microlas, Göttingen, Germany), with a microscope for sample observation and laser beam focus onto the sample, and an Agilent 7500c quadrupole ICP-MS, equipped with a collision-reaction cell which decreases strongly mass interferences. For each sample, rare earth elements from La to Sm, ^{7}Li, ^{24}Mg, ^{29}Si, ^{39}K, ^{43}Ca, ^{47}Ti, ^{57}Fe, ^{75}As, ^{88}Sr, ^{89}Y, ^{232}Th and

^{238}U were analysed. Data were collected with an integration time of 0.01 s per channel for Li, Si, Na, K, Ca, Mg, Fe, Ti and Sr, 0.02 s for Y, U and Th, 0.03 for La, Ce, Pr, Nd, Sm and As. Data were acquired as raw counts (cps) using the time resolved mode. For each individual analysis (external standard and sample), the background was measured for 20 s (used for data reduction) and the overall signal acquisition was recorded for 170 s. The certified glass reference materials NIST SRM 610 (Pearce et al., 1997) was used as calibrators for the LA-ICP-MS and the calculated concentrations of Na from microthermometry were used as internal standard (Table 3). Spot sizes of 44 and 60 µm were used. The data reduction (quantification and limits of detection) was carried out using in-house software based on the equations developed by Longerich et al., (1996). More details of the analytical procedure are given in Leisen et al. (2012) and Lach et al. (2013).

4.4. Results

4.4.1. Sample location

The studied area corresponds to the contact between the Lauzière granite and the Leptino-amphibolitic complex in the internal branch of the Belledonne massif (Fig. 2, 3). The investigated Alpine vein (Fig. 3B) corresponds to an open hydrothermal mineralized vein, 50 cm to 1 m wide, vertical and oriented close to N110°, perpendicular to the main schistosity of the host-rock (N020 to N040°E trending, subvertical). This vein is mainly filled by quartz, albite, adularia, anatase, rutile, chlorite and also contains numerous species of rare minerals such as ilmenite, hematite, apatite, monazite or xenotime.

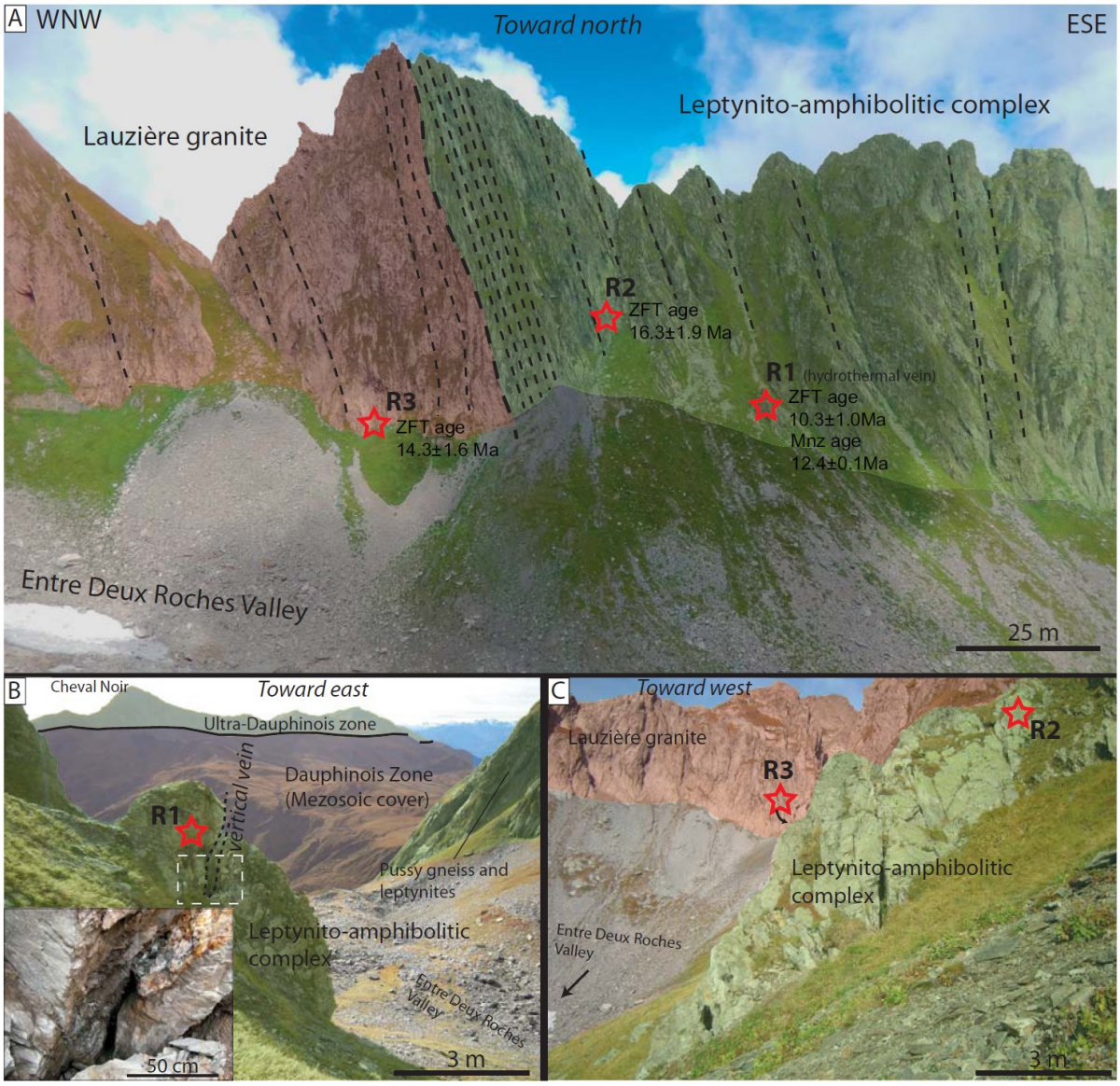

Figure 4-3 Photographs of the studied area with lithological limits, main alpine schistosity and location of ZFT samples. (A) *Entre Deux Roches* valley samples profile with ZFT central ages and monazite Th-Pb ages. (B) Alpine cleft (*R1* ZFT sample, quartz and monazite samples for microthermometric study and monazite for Th-Pb dating). (C) *R2* and*R3* ZFT samples

The three ZFT data (*R1*, *R2* and *R3*) in this study cover a ~100 m profile. The *R1* ZFT rocks sample corresponds to gneissic rocks (Leptino-amphibolitic complex) sampled the hanging walls of the Alpine vein (Fig. 3B) where monazite and quartz were extracted for Th-Pb LA-ICPMS measurements and the microthermometric study. The *R2* sample corresponds to rocks of the same unit located ~30 m in direction of the contact with the Lauzière granite (Fig. 3C). The last *R3* sample corresponds to granitic rocks of the Lauzière granite and was sampled at ~60 m from the previous sample and ~30 m from the contact between the Lauzière granite and the gneissic rocks of the Leptino-amphibolitic complex (Fig. 3A).

4.4.2. Zircon fission-track

The *R1* sample gave a ZFT central age of 10.3 ± 1 Ma (Fig. 4A), with an age range between 7.2 and 16.7 Ma. The *R2* sample gave a ZFT central age of 16.3 ± 1.9 Ma (Fig. 4B), for an age range between 10.2 and 50.4 Ma. The *R3* sample gave a ZFT central age of 14.3 ± 1.6 Ma (Fig. 4C), with individual grain ages between 5.2 and 20.1 Ma. All samples show relatively high dispersion in the grain age distributions and low $\chi 2$ values.

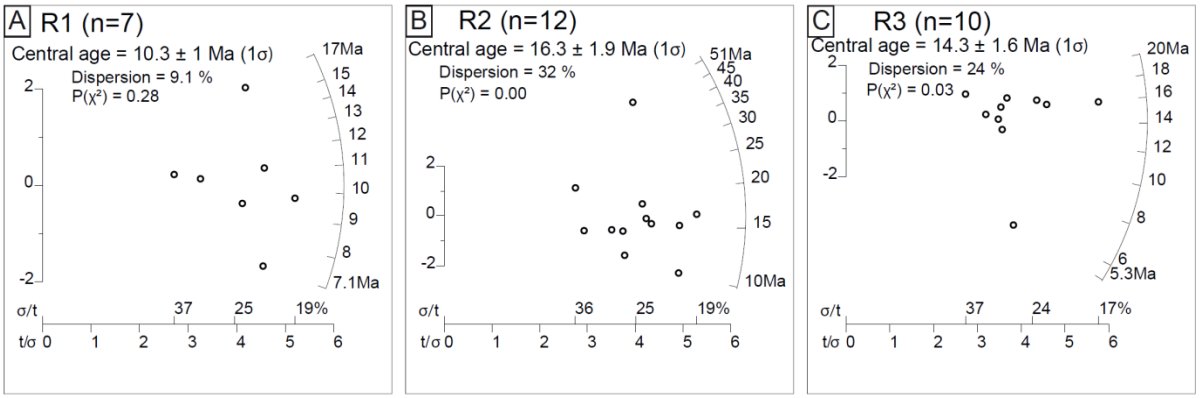

Figure 4-4 Radial plots of zircon ages. (A) *R1* sample (cleft). (B) *R2* sample (~30m from the cleft). (C) *R3* sample (~30m from the cleft)

4.4.3. Fluid inclusions

Fluid inclusions were observed in quartz and monazite samples crystallized on the hanging walls of the investigated Alpine vein (Fig. 3B). Six samples of monazite + quartz (Fig. 5A, B, C, E) or isolated quartz (Fig. 5D) have been investigated. In monazite crystals, primary inclusions are isolated (Fig. H) or along trails of 2-3 inclusions (Fig. 5F, G) and secondary inclusions are located in cicatrized fracture planes (Fig. 5F-H). The size of fluid inclusions is ~10x10 µm for primary inclusions and less than 4x4 µm for secondary inclusions. In quartz crystals, primary inclusions are also isolated (Fig. 5I, J) or along trails of 4-5 inclusions (Fig. 5K) parallels to quartz growth, and secondary inclusions are also located on planes which traverse the crystals from rim to core (Fig. 5K). The size of primary inclusions is mostly comparable to those of monazite (~10x10 µm) but could reach ~20x30 µm, and those of the secondary inclusions is smaller than 5x5 µm. All the inclusions investigated were bi-phased, liquid and vapour (L-V type), and homogenize to liquid. No solid phase (e.g. halite) was observed in the studied fluid inclusions.

Microthermometric data for the different fluid inclusions types of each sample are reported in Table 1 and are displayed graphically in Figure 6. Eutectic or initial ice melting temperature could not be determined accurately but are comprised between -21.2 and -23 °C, in good agreement with eutectic temperature for H_2O-NaCl and H_2O-NaCl-KCl systems, respectively at -21.2 and -22.9 °C (Bodnar, 2003; Hall et al., 1988). This indicates that most of the salt dissolved in inclusions is NaCl, with a variable small amount of KCl and that NaCl-equivalent salinity (Bodnar, 1993) and isochors (Bodnar & Vityk, 1994) could be calculated. For all the dataset, ice melting temperature (T_m) range from -6.0 to -9.6 °C, which corresponds to salinities ranging from 9.2 to 13.5 wt.% NaCl equivalent. The high temperature measurements provide homogenization temperature (T_h) ranging from 204 to 345°C for monazite fluid inclusions and 121 to 315 °C for quartz fluid inclusions.

Table 4-1

Microthermometric data

Sample	F.I. number	Mineral	Type	T_e (°C)	T_m (°C)	T_h (°C)	NaCl eq. (wt.%)	Density (g/cm^3)	Population
E2R1	1	quartz	Primary	-21.3	-7.8	210.4	11.5	0.94	QzP2
E2R1	2	quartz	Secondary	-21.3	-6.7	120.6	10.1	1.01	QzS
E2R1	3	quartz	Primary	-	-8.2	219.3	11.9	0.94	QzP2
E2R2	1	mnz	Primary	-	-7.5	315.5	11.1	0.81	MnzP
E2R2	2	mnz	Primary	-	-8.0	327.3	11.7	0.80	MnzP
E2R2	3	mnz	Primary	-22.9	-7.7	345.3	11.4	0.77	MnzP
E2R2	4	mnz	Primary	-23.1	-9.6	327.6	13.5	0.82	MnzP
E2R2	5	mnz	Secondary	-	-9.5	241.6	13.4	0.92	MnzS
E2R2	6	mnz	Primary	-22.8	-8.5	328.4	12.3	0.80	MnzP
E2R2	7	quartz	Primary	-22.4	-7.6	184.3	11.2	0.97	QzP2
E2R2	8	quartz	Primary	-	-7.4	314.9	11.0	0.81	QzP1
E2R2	9	quartz	Primary	-	-8.6	208.2	12.4	0.95	QzP2
E2R2	10	quartz	Primary	-23.0	-7.7	184.6	11.4	0.97	QzP2
E2R2	11	quartz	Primary	-22.7	-7.8	202.8	11.5	0.95	QzP2
E2R2	12	quartz	Primary	-	-6.1	187.7	9.3	0.95	QzP2
E2R2	13	quartz	Primary	-	-6.5	189.6	9.9	0.95	QzP2
E2R2	14	quartz	Primary	-	-6.3	190.8	9.6	0.95	QzP2
E2R2	15	quartz	Primary	-	-7.0	194.5	10.5	0.95	QzP2
E2R2	16	quartz	Primary	-	-7.4	278.3	11.0	0.86	QzP1
E2R3a	1	mnz	Secondary	-21.2	-8.4	215.7	12.2	0.94	MnzS
E2R3a	2	mnz	Secondary	-	-7.8	203.8	11.5	0.95	MnzS
E2R3a	3	quartz	Primary	-	-6.7	200.4	10.1	0.94	QzP2
E2R3a	4	quartz	Primary	-	-6.2	190.5	9.5	0.95	QzP2
E2R3a	5	quartz	Primary	-21.3	-7.8	215.8	11.5	0.94	QzP2
E2R3a	6	quartz	Primary	-	-8.1	212.9	11.8	0.94	QzP2
E2R3a	7	quartz	Secondary	-21.3	-6.5	133.5	9.9	1.00	QzS
E2R3a	8	quartz	Primary	-	-7.4	218.6	11.0	0.93	QzP2
E2R3a	9	quartz	Secondary	-	-6.6	140.4	10.0	1.00	QzS
E2R3a	10	quartz	Primary	-	-6.8	201.4	10.2	0.94	QzP2
E2R3b	1	quartz	Primary	-21.3	-6.7	200.2	10.1	0.94	QzP2
E2R3b	2	quartz	Primary	-21.3	-6.9	197.5	10.4	0.95	QzP2
E2R3b	3	quartz	Primary	-	-7.3	207.9	10.9	0.94	QzP2
E2R3b	4	quartz	Primary	-21.3	-6.6	178.3	10.0	0.96	QzP2
E2R3b	5	quartz	Primary	-22.8	-7.7	214.7	11.4	0.94	QzP2
E2R3b	6	quartz	Primary	-	-6.7	210.3	10.1	0.93	QzP2
E2R3b	7	quartz	Primary	-	-6.7	191.9	10.1	0.95	QzP2
E2R3c	1	quartz	Primary	-21.2	-6.8	201.6	10.2	0.94	QzP2
E2R3c	2	quartz	Primary	-	-6.8	201.0	10.2	0.94	QzP2
E2R3c	3	quartz	Secondary	-21.2	-7.0	138.9	10.5	1.00	QzS
E2R3c	4	quartz	Primary	-21.0	-6.5	194.5	9.9	0.95	QzP2
E2R3c	5	quartz	Primary	-	-8.5	223.3	12.3	0.94	QzP2
E2R3c	6	quartz	Primary	-	-6.0	201.4	9.2	0.93	QzP2
E2R4	1	mnz	Primary	-	-7.8	306.6	11.5	0.83	MnzP
E2R4	2	mnz	Primary	-	-8.2	313.5	11.9	0.82	MnzP
E2R4	3	mnz	Primary	-	-8.1	305.3	11.8	0.83	MnzP
E2R4	4	mnz	Primary	-	-8.1	290.5	11.8	0.85	MnzP
E2R4	5	mnz	Primary	-	-8.2	283.2	11.9	0.86	MnzP
E2R4	6	quartz	Primary	-	-8.8	299.6	12.6	0.85	QzP1
E2R4	7	quartz	Primary	-22.8	-9.0	210.7	12.9	0.95	QzP2
E2R4	8	quartz	Primary	-	-9.2	211.0	13.1	0.95	QzP2
E2R4	9	quartz	Primary	-22.9	-7.5	210.0	11.1	0.94	QzP2
E2R4	10	quartz	Primary	-	-7.7	210.3	11.4	0.94	QzP2
E2R4	11	quartz	Secondary	-	-7.9	131.6	11.6	1.02	QzS
E2R4	12	quartz	Secondary	-	-8.0	131.6	11.7	1.02	QzS
E2R4	13	quartz	Secondary	-	-7.9	133.5	11.6	1.02	QzS
E2R4	14	quartz	Secondary	-	-7.9	147.7	11.6	1.00	QzS
E2R4	15	quartz	Primary	-23.0	-8.7	300.4	12.5	0.84	QzP1

T_e: eutectic temperature; T_m: ice melting temperature; T_h: L-V to L homogenization temperature

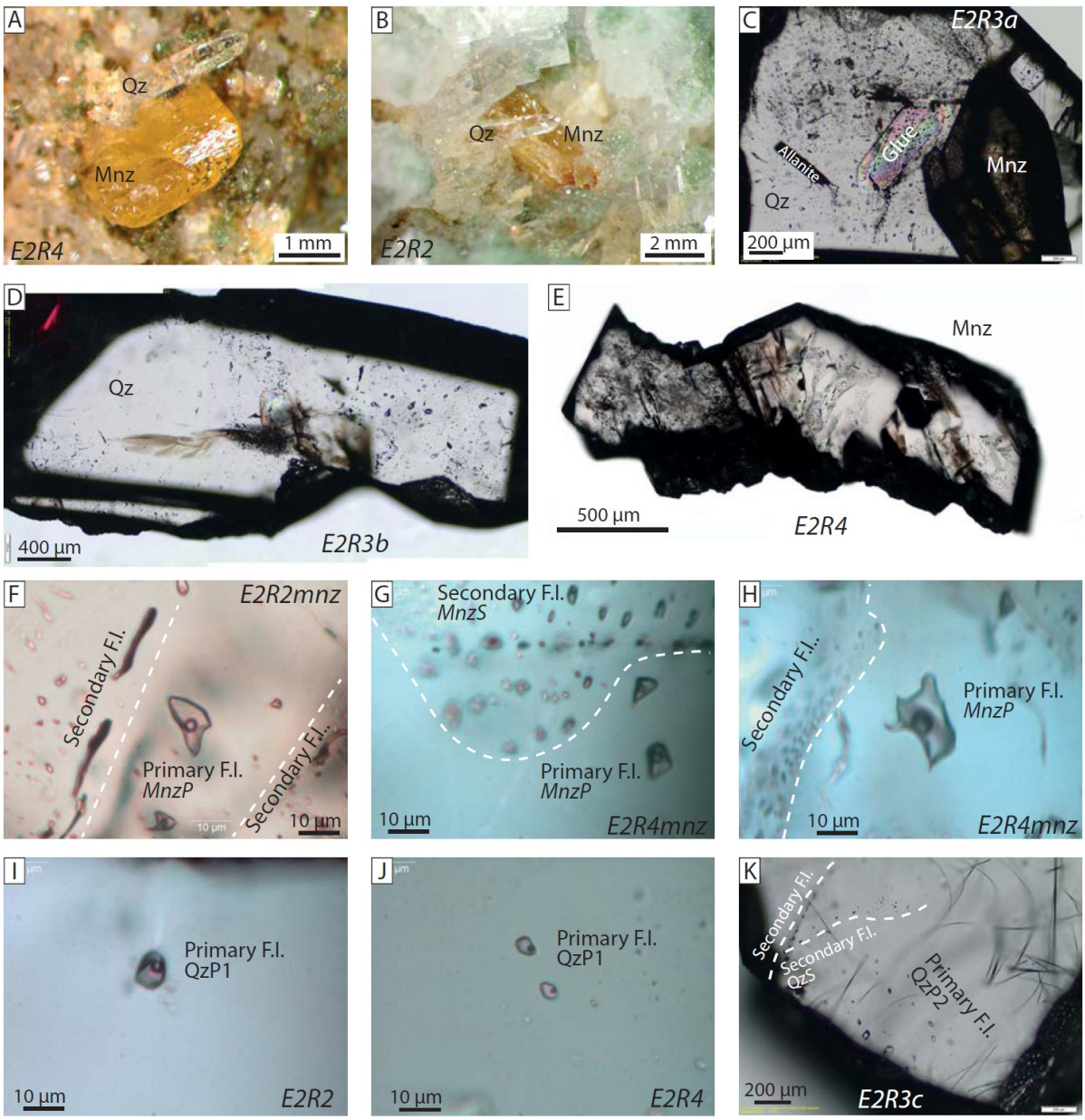

Figure 4-5 Microphotographs of monazite and quartz samples and representative fluid inclusions analyzed by microthermometry. (A, B) Coexisting monazite and quartz crystals before preparation for microthermometric measurements. (C, D, E) Polished separated quartz and monazite crystals. Note the presence of allanite (C). (F, G, H) Primary and secondary fluid inclusions in monazite crystals. (I, J, K) Primary and secondary fluid inclusions in quartz crystals.

Based on the petrologic (Fig. 5) and microthermometric studies (Table 1), we can distinguish five fluid inclusions populations (Fig. 6, Table 2). The *MnzP* population corresponds to primary fluid inclusions in monazite and is equivalent to the *QzP1* population that corresponds to primary inclusions in quartz samples coexisting with monazite, regarding T_m and T_h values. *MnzP* and *QzP1* populations are characterized by the highest mean T_h values of 314 and 298 °C, respectively. The *QzP2* population also corresponds to primary inclusions in quartz and is represented in all the quartz samples (Table 1). *QzP2* population presents the widest range of T_m values between -9.2 and -6.0 °C and a mean T_h value of 202 °C. Three secondary inclusions in monazite crystals (*MnzS*) were big enough to perform microthermometric measurements. The T_m and T_h values of these inclusions range in the *QzP2* population field (Fig. 6). Secondary inclusions located in quartz samples (*QzS* population) were also investigated. They show T_m values between -8.0 and -6.5 °C and a mean Th value of 135 °C.

Table 4-2 Mean physical properties of the fluid inclusions populations

F.I. Population	n	mean T_m (°C)	mean T_h (°C)	NaCl eq. (wt.%)	Density (g/cm^3)	dP/dT (bar/°C)
MnzP	10	-8.2	314.3	11.9	0.82	11.04
MnzS	3	-8.6	220.4	12.3	0.94	16.26
QzP1	4	-8.1	298.3	11.8	0.84	11.80
QzP2	32	-7.3	202.4	10.8	0.95	16.99
QzS	8	-7.3	134.7	10.9	1.01	21.44

MnzP: monazite primary F.I.; MnzS: monazite secondary F.I.; QzP1: quartz primary F.I. population 1; QzP2: quartz primary F.I. population 2; QzS: quartz secondary F.I.

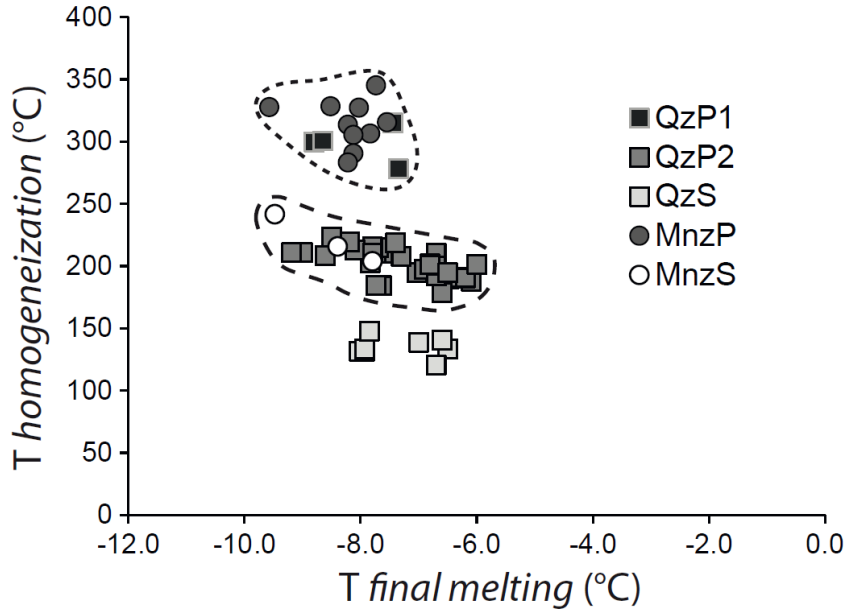

Figure 4-6 T_h vs. T_m diagram of the fluid inclusions data. *QZP1*: population 1 of primary F.I. in quartz; *QZP2*: population 1 of primary F.I. in quartz; *QzS*: secondary F.I. in quartz; MnzP: primary F.I. in monazite; MnzS: secondary F.I. in monazite

Mean T_m, T_h, salinity and bulk density was calculated for each population (Table 2) to trace the corresponding isochors (Fig. 7). *MnzP* and *QzP1* fluid inclusions populations give P-T relationships at 11-11.8 bar/°C, *MnzS* and *QzP2* population give 16.3-17 bar/°C and *QzS* give 21.4 bar/°C.

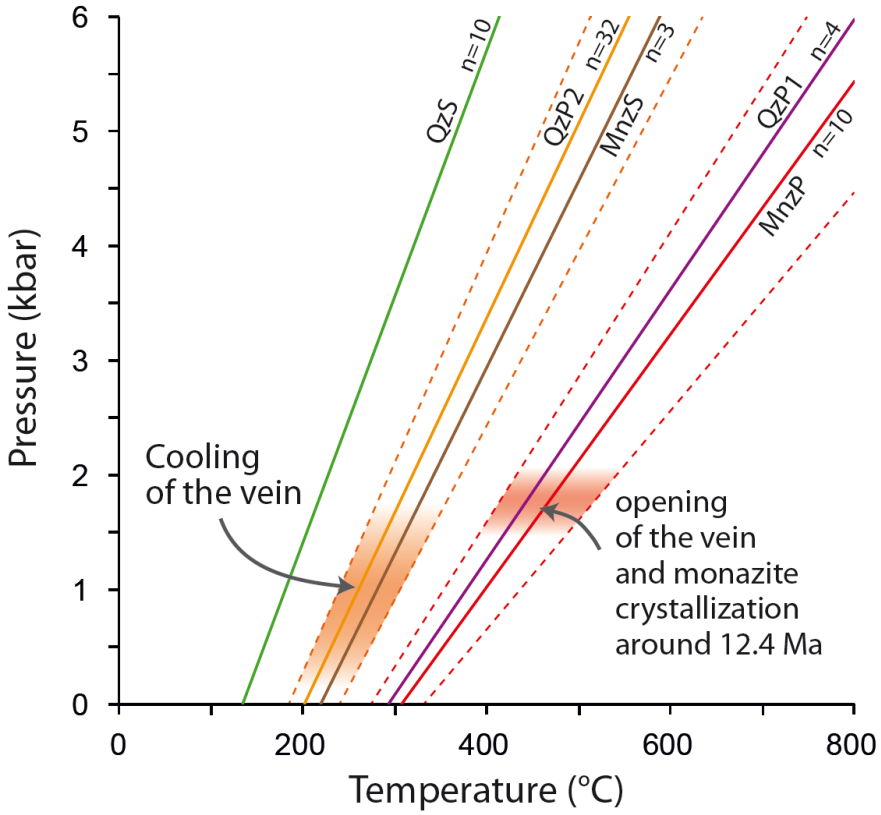

Figure 4-7 Mean isochoric P-T relationships calculated from microthermometric measurements on monazite and quartz crystals. F.I. population and number of analyses are indicated. Filled areas corresponds to the range of each population

Unfortunately, LA-ICP-MS measurement of fluid inclusions have not allowed to provide information on REE, U and Th concentrations in hydrothermal fluids, as they were invariably below the detection limits (Table 3).

Table 4-3 LA-ICP-MS fluid inclusion element concentration data

Analysis	Sample	wt.%	Element concentrations (ppm)																
		NaCl	Li (7)	Na (23)	Mg (24)	K (39)	Ca (43)	Ti (47)	Fe (57)	As (75)	Sr (88)	Y (89)	La (139)	Ce (140)	Pr (141)	Nd (146)	Sm (147)	Th (232)	U (238)
DL			*26*	*1836*	*32*	*180*		*37*	*383*	*12*	*1*	*1*	*0*	*0*	*0*	*2*	*2*	*1*	*1*
3A-09	E2R3A	9.15	176	35994	bdl	9826	bdl	bdl	bdl	19	360	bdl	bdl	bdl	bdl	bdl	bdl	bdl	bdl
3A-12	E2R3A	9.15	283	35994	bdl	9513	bdl	bdl	bdl	31	442	bdl	bdl	bdl	bdl	bdl	bdl	bdl	bdl
3B-07	E2R3B	9.15	210	35994	bdl	9411	bdl	bdl	bdl	45	387	bdl	bdl	bdl	bdl	bdl	bdl	bdl	bdl
31A-03	ER31A	13.4	352	52830	bdl	14639	bdl	bdl	bdl	90	422	bdl	bdl	bdl	bdl	bdl	bdl	bdl	bdl
31A-05	ER31A	13.4	351	52830	13	15506	bdl	bdl	bdl	55	842	bdl	bdl	bdl	bdl	bdl	bdl	bdl	bdl
31A-06	ER31A	13.4	283	52830	bdl	13647	bdl	161	bdl	30	455	bdl	bdl	bdl	bdl	bdl	bdl	bdl	bdl
31A-07	ER31A	13.4	389	52830	bdl	14674	bdl	71	528	14	1752	bdl	bdl	bdl	bdl	bdl	bdl	bdl	bdl
31A-08	ER31A	13.4	501	52830	34	13304	bdl	176	1193	62	1278	bdl	bdl	bdl	bdl	bdl	bdl	bdl	bdl
31A-10	ER31A	13.4	368	52830	bdl	15268	bdl	58	bdl	63	1329	bdl	bdl	bdl	bdl	bdl	bdl	bdl	bdl
31B-04	E2R31B	13.5	358	53263	bdl	13792	bdl	bdl	bdl	33	906	bdl	bdl	bdl	bdl	bdl	bdl	bdl	bdl
31B-08	E2R31B	13.5	297	53263	bdl	14132	bdl	bdl	bdl	32	949	bdl	bdl	bdl	bdl	bdl	bdl	bdl	bdl
31B-10	E2R31B	13.5	336	53263	bdl	15290	bdl	bdl	bdl	45	1049	bdl	bdl	bdl	bdl	bdl	bdl	bdl	bdl
31B-11	E2R31B	13.5	421	53263	36	15780	bdl	bdl	bdl	58	1326	bdl	bdl	bdl	bdl	bdl	bdl	bdl	bdl
31B-13	E2R31B	13.5	317	53263	38	11290	bdl	80	bdl	25	852	bdl	bdl	bdl	bdl	bdl	bdl	bdl	bdl

DL: detection limits

4.4.4. ^{232}Th-^{208}Pb dating

For all grains, in situ LA-ICP-MS analysis was performed at multiple locations in the different compositional domains (Fig. 8).

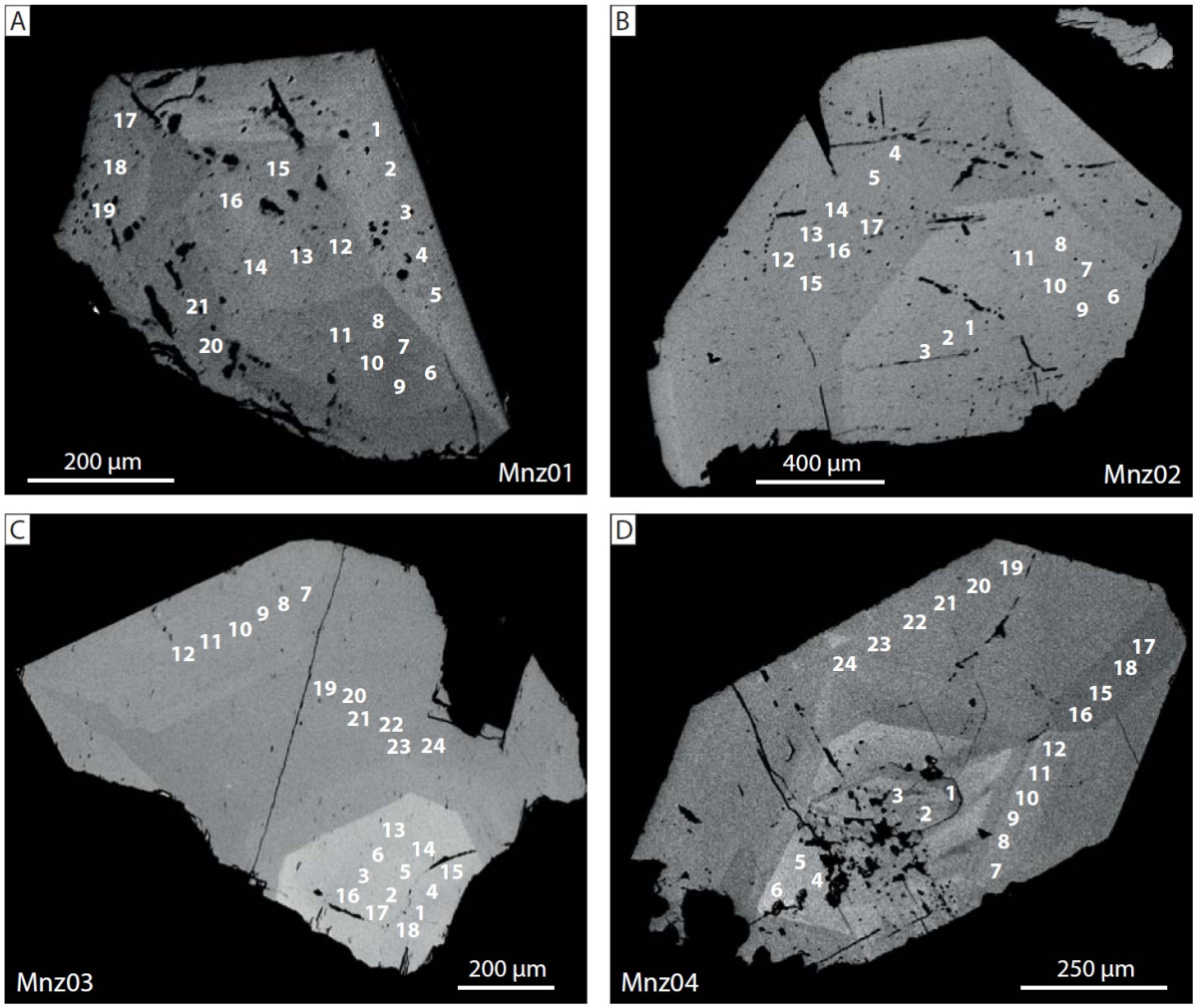

Figure 4-8 Backscattered electron images of cleft monazites dated. White numbers correspond to the location of the laser spot and refer to Supplementary material 4-1

Four monazite grains have been analysed from the cleft and give a $^{208}Pb/^{232}Th$ age of 12.4 ± 0.1 Ma (MSWD = 1.7, n=86; Fig. 9). The U-Pb systematics give a similar age of 12.2 ± 0.2 Ma (MSWD = 1.1). Detailed results are given in Supplementary material 4-1.

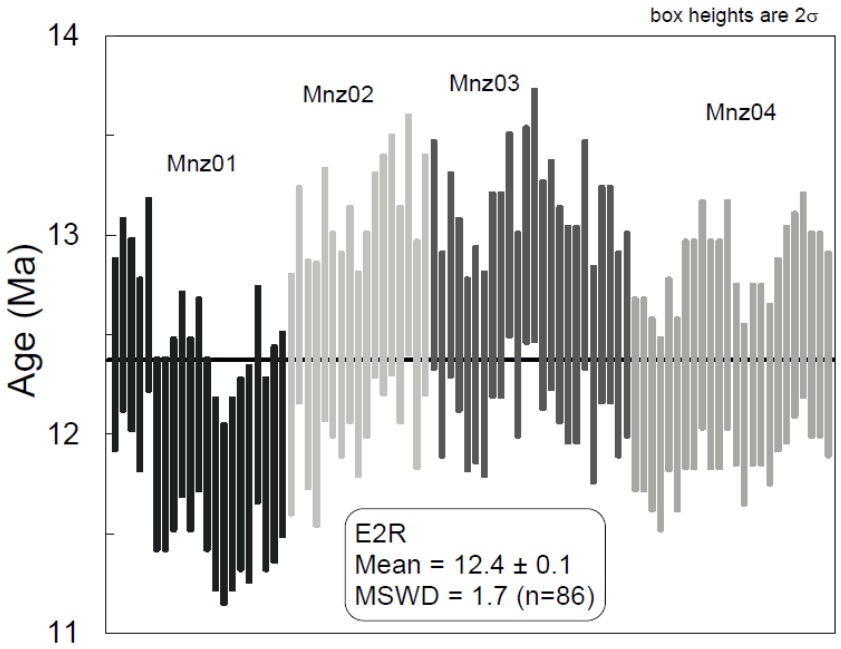

Figure 4-9 ^{232}Th-^{208}Pb weighted mean ages of monazite samples analysed by LA-ICPMS

4.5. Discussion

4.5.1. Influence of fluid circulations on the paleogeothermal gradient

Combination of zircon fission-track dating, fluid inclusion analysis and hydrothermal monazite dating provide valuable information on the timing of fluid circulation during the exhumation of the Belledonne massif and on the influence of hydrothermal circulation on the paleogeothermal gradient. Structural geology data indicate the opening direction of the vertical veins perpendicularly to the main Alpine schistosity in a dextral transpressive

regime (Gasquet et al., 2010; Berger et al., 2013). The microthermometric study of monazite and quartz crystals in a vertical vein brings new constraints on temperatures of hydrothermal fluid circulation. Our microthermometric data indicate at least two main crystallization episodes: first only represented by monazite and quartz crystals, corresponding to the highest T_h of 315-300 °C (Fig. 6) and second corresponding to most of the quartz inclusions with T_h of 220-200 °C. Fluid inclusion studies in Alpine (horizontal) veins in the Mont Blanc massif indicate temperatures of 300-400 °C and pressures of 1.5-4 kbar (Poty et al., 1974; Fabre et al., 2002), similar to those estimated for vein chlorites by Rossi et al. (2005). Although there is only a few studies in vertical Alpine veins in the ECM, temperature and pressure conditions have been determined in the range of 265-285 °C and 0.7-1.4 kbar in a vertical gold-bearing vein of the Mont Blanc massif dated at 9.9 ± 1 Ma by Ar-Ar analysis on hydrothermal adularia (Marshall et al., 1998). Further north, in the Aar massif, isochors from fluid inclusions in quartz of vertical veins indicates quartz crystallization at 220-280 °C and ~0.8 kbar (Soom, 1986). Taking into account the previously published microthermometric data on Alpine veins and the fact that vertical veins are posterior to horizontal veins, the studied vertical vein may have formed at pressures around 1.5-2 kbar. Based on this pressure, isochors will indicate a monazite (and coeval quartz) crystallization temperature of ~400-450 °C (Fig. 7) at 12 Ma (Fig. 9). The main quartz crystallization episodes then range between 200-300 °C, probably with decreasing pressure during the exhumation. The ZFT ages determined in this study of 16.3 ± 1.9, 14.3 ± 1.6 and 10.3 ± 1.0 Ma are consistent with the previous published data in the Grand Châtelard massif between ~15-10 Ma (Fügenschuh and Schmid, 2003; Seward and Mancktelow, 1994). The ZFT ages of 9-7.5 Ma (Fügenschuh and Schmid, 2003), north of the study area, are consistent with previously determined monazite Th-Pb ages around 8 Ma (Gasquet et al., 2010; Grand'Homme et al., submitted). The ZFT ages of ~15 Ma in the host rocks are older than the ZFT 10.3 ± 1.0 Ma age of the hanging walls of the vertical quartz vein. It shows that the sampled units where already cooled below temperature of ZFT annealing at ~240-280 °C (e.g. Yamada et al., 1995; Bernet, 2009) at the time of vertical vein opening and

monazite crystallization. The well-resolved Th-Pb age on four monazite crystals (12.4 ± 0.1 Ma, MSWD = 1.7) indicate growth episodes with a duration shorter than the analytical resolution (typically 0.5-0.6 Ma for one single analysis) and an overall monazite crystallization time <1 Myr. The temperature of monazite crystallization (~400-450°C) during the early fluid circulation in the vein was sufficient to anneal ZFT in the sample from the hanging wall at short distance from the vein but not the entire area as the other ZFT samples are not affected or only partially annealed, given the relatively short time of heating (< 1 Ma), the distance to the vein (30 and 90 m) and the ambient temperature of the host rock at the time (below 280 °C). This corresponds to a ~120 °C overheating in the Alpine vein and implies a functioning of the vein as an open system at the beginning of its formation. The vertical nature of these veins could enable and/or facilitate the upward fluid flow percolation of deeper and hotter crustal fluids. However, despite the temperature, the early fluids do not differ from the fluid from which most of the quartz of the vein has crystallized (e.g. salinity, inclusion nature with two phases). A stable isotope ($\delta^{18}O$ or $\delta^{13}C$) study of fluid inclusions of the two populations identified would be interesting to trace the fluid source and better constrain the scale of fluid flow as this has already been done for horizontal veins in the Mont-Blanc massif (Rossi and Rolland, 2014).

4.5.2. Cleft monazite ages interpretation

These results have crucial implications on the interpretation of hydrothermal monazite and ZFT ages related to Alpine veins. There is still no consensus on the interpretation of hydrothermal monazite ages, whether monazite records episodic fluid circulations (e.g. Janots et al., 2012; Grand'Homme et al., submitted) or slow cooling of the host rock and vein (e.g. Gnos et al., 2015). The results of this study support the hypothesis that hydrothermal monazite crystallize from episodic hot fluid circulation in the earlier stages of its functioning, shortly after the vein opening. This is important because if hydrothermal monazite records the age of the vein opening, it also records the timing of

the tectonic event responsible for the vein formation. It has been shown that hydrothermal monazite ages determined in the western Alps are mainly similar to those of major tectonic events (Grand'Homme et al., submitted), as for example the functioning of major shear zones or thrusting along the Penninic Front. The fluid flow associated to these tectonic events is facilitated by the opening of the veins, and allowed the crystallization of hydrothermal monazite crystals. This differs from the study of Gnos et al. (2015) in the Tauern window were monazite crystallized late in the vein at estimated temperatures of ~300-200 °C and recorded the timing of ~4 Myr of exhumation and cooling. However, in that study of Gnos et al. (2015), the temperature determined for monazite crystallization is constrained by low-temperature thermochronology (ZFT and [U-Th]/He) and discussed at a regional scale, in contrary to our study at the vein scale. Fluid circulation may have affected and possibly (partially) reset the thermochronological data, as in our study. Moreover, the metamorphic conditions reached in the Tauern window have been higher than in the ECM, and a different significance of the monazite crystallisation age at lower temperatures in a different geological context could not be excluded.

Although quartz crystallizes over a wide range of temperatures, monazite microthermometric results indicate the highest temperature of crystallization recorded in the hydrothermal vein. It is unclear why hydrothermal monazite in the studied Alpine vein record episodic events rather than continuous fluid circulation throughout the functioning of the vein and two hypotheses are proposed. (1) Authigenic monazite formation has been reported in diagenetic environments (Evan and Zalaziewicz, 1996) and alteration of monazite by dissolution-precipitation at low temperatures (200-300°C) has also been reported in natural samples (Poitrasson et al., 1996, 2000; Seydoux-Guilllaume et al., 2012). However most of the studies on metamorphic or hydrothermal monazites indicate first appearance in the lower greenschist facies (review in Spear and Pyle, 2002) although authigenic monazites have already been reported (e.g. Evans and Zalasiewicz, 1996). Monazite could not be stable during retrograde metamorphism (T< 300°C) in favour of allanite (Janots et al., 2007; Spear, 2010), which is also reported in the studied Alpine vein (Fig. 5C). The opening and the first stages of fluid circulation in

the Alpine vein would therefore coincide with the monazite crystallization domain. (2) Another explanation is that monazite may not crystallize as large (millimetric) crystals at low temperature (< 300 °C) but rather as cluster of micrometric grains. The size of hydrothermal monazite increases with metamorphic conditions (Schandl and Gordon, 2004) and only large monazite crystals (>500 μm), easily identifiable and usable for microthermometric study, have been investigated in this study. It is possible that smaller (and maybe younger) monazite grains can be found in the vein with further petrologic studies.

4.6. Conclusion

The multidisciplinary approach presented in this work, based on zircon fission-track dating, fluid inclusion analysis and Th-Pb dating of hydrothermal monazite is able to constrain chronologically and thermally the fluid flow associated to Alpine vein opening in the ECM during the late stages of exhumation. It shows that hydrothermal monazites crystallize early in veins from fluids hotter (400-450°C) than the host-rock, which had already cooled below the ZFT annealing zone (240-280°C), at least 2 Ma earlier. These fluid circulations were able to basically fully anneal the ZFT of the rocks of the hanging wall of the vein, but the heating may have only a partial annealing effect, of at all, on the more. This study also demonstrates that monazites have grown episodically at the timing of the vein opening and therefore could date the tectonic event responsible for the vein formation.

Acknowledgments

We thank M.C. Boiron for helping with fluid inclusions LA-ICP-MS measurements. This project is funded by the ANR-JC grant (Mona, 2012).

5. EXPÉRIENCES D'ALTÉRATION HYDROTHERMMALE

Experimental study of monazite-fluid interaction and importance of nano-pores and nano-fractures for propagation of the dissolution-precipitation process

(Article en préparation)

A. Grand'Homme[1], E. Janots[1], A.M. Seydoux-Guillaume[2], D. Guillaume[2], V. Magnin[1], J. Hövelmann[3], C. Höschen[4], M.C. Boiron[5]

[1]ISTerre, Univ. Grenoble Alpes, Grenoble, France (alexis.grandhomme@ujf-grenoble.fr)
[2]LMV, Département de Géologie, Université Jean Monnet, Saint-Étienne, 42023, Saint-Etienne, France
[3]GEO, Univ. Bremen, Germany
[4]Chair of Soil Science, Univ. München, Germany
[5]GeoRessources, Boulevard des Aiguillettes B.P. 239 F-54506, Vandoeuvre les Nancy, France

Keywords Monazite, Dissolution-precipitation, Experimental petrology, Synthetic fluid inclusions, REE mobility

Note: Supplementary material 5-X corresponds to Annexe 5-X and Fig.X or Table X to Fig. 5-X or Table 5-X

Abstract

Monazite, the light rare earth elements (LREE) phosphate is the main source of thorium and a major source of rare earth elements (REE) in the crust. Numerous experimental and petrological studies have shown that during hydrothermal alteration, monazite can be replaced by a dissolution-precipitation process with element fractionation. The partitioning of REE and actinides (U, Th) between pristine and altered monazite and fluid-monazite has been investigated through hydrothermal alteration experiments at 200 MPa in cold-seal autoclaves in terms of various parameters including fluid composition (H_2O, NaCl 10 wt.% and NaOH 1 or 2M), temperature between 300 and 600°C, fluid-monazite ratio and oxygen fugacity. Pre-fractured quartz crystals were added in the experiments to trap the hydrothermal fluids during alteration reactions. We also doped the reactive fluids with ^{18}O to trace the eventual recrystallization and to study the oxygen partitioning between monazite and quartz. Experiments have been performed with the Manangotry monazite standard, chemically homogeneous and Th-rich (13 wt.% ThO_2). The solid products were characterized by SEM imaging, EPMA analysis, Raman analyses, Nano-SIMS mapping and TEM imaging. Entrapped experimental fluid inclusions in quartz were analysed by LA-ICP-MS. Experimental fluids are characterized by lower Th/U and LREE/HREE ratios than the starting monazite, indicating for a higher mobility of U and HREE in our conditions. Only the experiments with alkali fluids (NaOH 1 or 2M) show evidence of alteration by a dissolution-precipitation mechanism. Here, we showed that the reaction kinetics is hard to resolve, the monazite products involving replaced domains, overgrowths or neo-formed crystals with distinct chemical compositions. The nano-scale TEM images of altered monazite domains indicate a key role of pores and cracks in the progression of the replacement reaction through a non-linear reaction front. This mechanism leads to an intimate nano-scale mixing of secondary and pristine monazite in the altered domains. This mixture has important implications for dating of altered monazite domains. The presence of fractures, which may be attributed to radiation damages, also have crucial implications for nuclear waste storage and actinides mobility.

5.1. Introduction

In the continental crust, the rare earth elements (REE; considered as lanthanide + Y), Th and U are mainly hosted by accessory minerals and more particularly by monazite (Bea et al., 1996). Indeed, monazite is relatively ubiquitous in sediments of detrital origin, magmatic or metamorphic rocks as well as in hydrothermal ore deposits. Monazite is a rare earth phosphate that preferentially incorporates the light rare earth elements (LREE; here La to Gd), compared to heavy rare earth elements and Y (HREE+Y) of which concentrations increase with temperature (Gratz and Heinrich, 1997, 1998; Heinrich et al., 1997; Pyle et al., 2001; Seydoux-Guillaume et al., 2002b). The actinides Th and U are incorporated into monazite structure through two coupled substitution (Van Emden et al., 1997): (1) $Si^{4+} + Th^{4+}(U^{4+}) = REE^{3+} + P^{5+}$ (huttonite) and (2) $Ca^{2+} + Th^{4+}(U^{4+}) = 2REE^{3+}$ (cheralite). Owing to its complex solid solution, monazite frequently presents compositional (REE, Th, U, Si and Ca) and isotopic (Pb, O) zoning. As solid state diffusion is very slow in monazite (Cherniak et al. 2004; Gardés et al. 2006; 2007), the compositional domains correspond to successive growth and/or replacement induced by dissolution-precipitation process during hydrothermal alteration or metamorphic reactions that release fluid (aqueous or melt).

With high Th (and U) content, low content of initial Pb (Parrish, 1990; Montel et al., 1996) and negligible diffusion of radiogenic Pb below 800°C (Cherniak et al. 2004; Gardés et al. 2006a; 2007), monazite is widely used in U-Th-Pb geochronology. However, in nature, monazite recrystallized by replacement can incorporate or preserve significant amounts of Pb (radiogenic and/or non-radiogenic), with possible disturbance of U-Pb and Th-Pb isotopic systems (Bosse et al., 2009; Seydoux-Guillaume et al., 2012; Didier et al., 2013; Wawrzenitz et al., 2012). Due to its high durability and resistance to chemical alteration during geological processes, monazite is also considered as a potential matrix of radionuclides, in the field of long-term radioactive waste storage (e.g. Weber et al., 1998). The behaviour of Th, U and Pb during recrystallization episodes is

controversial, having crucial implications on the monazite U-Th-Pb chronometer, and actinides and Pb mobility.

Numerous experimental (Teufel and Heinrich, 1997; Seydoux-Guillaume et al., 2002a; Harlov and Hetherington, 2010; Hetherington et al., 2010; Harlov et al., 2011; Williams et al., 2011; Budzyń et al., 2011; Budzyń et al., 2015; Shazia et al., 2015) and petrological (Poitrasson et al. 1996; Poitrasson et al. 2000; Mathieu et al. 2001; Bosse et al. 2009; Poujol et al. 2010; Tartèse et al. 2012; Seydoux-Guillaume et al. 2012; Didier et al. 2013) studies have shown that, in the presence of fluid, monazite can be replaced by a dissolution-precipitation process with element fractionation. The determining of Th/U or LREE/HREE fractioning during monazite dissolution-precipitation is crucial to trace the fluid conditions (temperature, composition, oxygen fugacity, etc.) responsible for monazite alteration. Other experimental studies (Ayers and Watson, 1991; Liu and Byrne, 1997; Oelkers and Poitrasson, 2002; Poitrasson et al., 2004; Cetiner et al., 2005; Schmidt et al., 2007; Pourtier et al., 2010; Tropper et al., 2011, 2013) have investigated the solubility of monazite with various temperature, pressure and fluid compositions. However, partitioning of REE+Y, Th and U between fluid/ monazite or pristine monazite (Mnz1) / secondary monazite (Mnz2) remains unknown depending on hydrothermal/metamorphic conditions and is crucial to reconstruct the precipitation environment of ore deposit or metamorphic rocks. In addition to elementary composition, the oxygen isotopic composition of monazite and coexisting quartz could be analysed to obtain precipitation temperature (Breecker and Sharp, 2007). However, this thermometer is mostly calibrated above 600 °C and not below 400 °C. The understanding of the monazite-quartz thermometry in hydrothermal conditions is crucial for comparison with thermochronological studies, as well as reconstruction of ore deposit environments. A synthesis of previous studies of monazite experimental dissolution-precipitation and solubility determination is presented in section 5-2.

Here, we present an experimental study of monazite alteration and solubility at temperature between 300 and 600°C and at 200 MPa to investigate the REE+Y, Th, U, Pb, and O isotopic partitioning between fluid/monazite and Mnz1/Mnz2 depending on the

alteration conditions (fluid composition, fluid/rock ratio, oxygen fugacity, temperature). Using pre-fractured quartz crystal to trap the fluid during alteration reactions, both monazite and fluid products have been analysed after experiments. Starting fluid compositions includes pure H_2O, NaOH (1 and 2M) and NaCl (10 wt.%). Experimental products have been characterized by Electron Probe Micro-Analyser (EPMA) and Secondary Ion Mass Spectrometry (Nano-SIMS) with high resolution. In parallel, experimental fluid inclusions trapped during the experiments have been investigated by Laser Ablation Inductively Coupled Plasma Spectrometry (LA-ICP-MS). ^{18}O has been used as a secondary minerals tracer in experiments analysed by both Raman spectroscopy and Nano-SIMS technics. Its utilisation also allowed to investigate the O isotopes partitioning between monazite and quartz between 300 and 600°C, in hydrothermal conditions. Nano-scale investigation of experimental products by Transmission Electron Microscopy (TEM) reveals a new pores and fracture-aided alteration mechanism that has severe implications for the trace elements and isotopic partitioning.

5.2. Previous experimental studies

Numerous experiments were conducted to study the solubility and the dissolution kinetics (Table 1) of natural monazite (Oelkers and Poitrasson, 2002; Schmidt et al., 2007; Tropper et al., 2011) or synthetic pure end-members (Liu and Byrne, 1997; Poitrasson et al., 2004; Cetiner et al., 2005; Schmidt et al., 2007; Pourtier et al., 2010; Tropper et al., 2011, 2013). These studies showed that monazite was very slightly soluble in pure water and its solubility increased with increasing or decreasing pH and was depend of the nature of the ligands in solutions (e.g. F^-, OH^-, Cl^-, CO_2^-, SO_4^{2-}).

Table 5-1 Experimental background on monazite solubility experiments

Reference	T (°C)	P (MPa)	Duration (hours)	Fluid composition	pH	Starting Mnz	Selected results	Methods
Tropper et al., 2013	800	1000	12	H_2O-NaF	near neutral	pure $CePO_4$	monazite solubility greater in NaF than in NaCl	weight-loss
Tropper et al., 2011	800	1000	90	H_2O	near neutral	pure $CePO_4$	low solubility in pure H_2O	weight-loss
			12-90	H_2O-NaCl		pure $CePO_4$	solubility increase with NaCl concentration	
			12	H_2O-NaCl		[1]North Carolina		
*Pourtier et al., 2010	350-800	200	72-360	H_2O	1-8	pure $NdPO_4$	$Nd(OH)3^0$ main species at 650 °C and 2000 bars (pH from 4 to 6)	weight-loss and ID-TIMS
							$Nd(OH)^{2+}$ in acidic conditions, $Nd(OH)_2^+$ in neutral conditions and	
	300-800			H_2O-NaCl		pure $NdPO_4$	$Nd(OH)_3^0$ in alkaline solution at 300 °C and 2000 bars.	
Schmidt et al., 2007	25-800	0.1-2000	0.8-11	H_2O+HCl±NaCl	-0.5-1	pure $LaPO_4$	lower mobility of Y, Gd, and Th compared to that of the LREE	in situ SR-XRF
				H_2O+HCl		[2]Kakola monazite	strong enrichment of Th relative to the LREE and Pb in monazite	
Cetiner et al., 2005	23 and 50	-	20 (days)	H_2O+HCl±NaCl	1-1.2	pure $LaPO_4$	retrograde monazite solubility from 23 to 150 °C	ICP-AES ICP-MS (solution)
						pure $SmPO_4$	low solubility up to 300°C, even at low pH and high chloride concnentrations	
	23, 50 and 150	1-1.4				pure $NdPO_4$		
Poitrasson et al., 2004	21, 70, 200, 300	-	0-296 (days)	H_2O+HCl	2	pure $NdPO_4$	retrograde solubility under acidic conditions from 70 to 300 °C	ICP-MS (solution)
	21					pure $GdPO_4$		
Oelkers and Poitrasson, 2002	50-230	-	0-14 (days)	H_2O±HCl±NaOH ±(NH_4OH+NH_4Cl)	1.5-10	[3]Manangotry	low solubilty at 70°C, near neutral pH	ICP-MS (solution)
							solubility increase with pH increase (10) or decrease (2)	
Liu and Byrne, 1997	25	-	2days-5months	$HClO_4$ (0.1m)	1	Pure $REEPO_4$	HREE+Y solubility higher than LREE solubility	spectrophotometry (P)
Ayers and Watson, 1991	800-1100	1000-2800	24	H_2O, HCl (1M), NaCl(1M)	neutral to acidic	-	same solubility with NaCl and H_2O	weight-loss
							decrease the pH increase solubility	

[1]Heavy mineral sand deposit located in Cleveland County, North Carolina (UCLA, Department of Geology mineral collection catalog number MS-1762); see Williams et al., 2011

[2]natural monazite from Kakola, Turku, Finland (Suominen, 1991)

[3]Manangotry monazite from Anosyan granite, Madagascar; see e.g. Montel et al., 1996, Seydoux-Guillaumet et al., 2004

*Extend of previous data obtained by Gibert and Montel, 1996 and Devidal et al., 1998

However, among the few of them that have investigated natural monazite solubility, none investigated the monazite solubility with NaCl brines, representative of hydrothermal environments as Alpine veins for example (e.g. Mullis et al., 1994), below 800°C. Furthermore, fluid entrapping in quartz recrystallized during monazite alteration experiments was never attempted. It would permit to analyze the fluid composition during the experiment, avoiding the problem of secondary minerals precipitation from the fluid during quenching.

Among the dissolution-precipitation experimental studies, some have investigated the monazite chronometer resetting (Teufel and Heinrich, 1997; Seydoux-Guillaume et al., 2002; Williams et al., 2011; Budzyń et al., 2015) and others the monazite stability in presence of hydrothermal fluids (Seydoux-Guillaume et al., 2002a; Harlov et al., 2007; Hetherington et al., 2010 Harlov et al., 2010; Williams et al., 2011; Harlov et al., 2011; Budzyń et al., 2011, 2015; Richard et al., 2015; Shazia et al., 2015). Their experimental conditions and the main results are summarized in the Table 2. These studies have shown that the fluid composition played a major role in the control of monazite stability, alkali fluids (NaOH, KOH ou $Na_2Si_2O_5$) being more efficient to reproduce experimentally the dissolution-precipitation textures as observed in nature, compared to brines (NaCl, KCl) with which only dissolution pores are observed (Hetherington et al., 2010; Richard et al., 2015). However, the fluids have never been analyzed in these experiments and the partitioning between monazite and fluid depending on hydrothermal conditions is still unconstrained. Furthermore, many studies have investigated the elementary partitioning in monazite during dissolution-precipitation using the same natural starting monazite (Hetherington et al., 2010; Harlov and Hetherington, 2010; Williams et al., 2011; Harlov et al., 2011; Budzyń et al., 2011) which seems not to be really homogeneous (Williams et al., 2011; see also Table 2), such as monazite used by Budzyń et al. (2015). It is difficult in these conditions to discuss small compositional variations between pristine and secondary monazite.

Table 5-2 Experimental background on monazite by monazite replacement (by dissolution-precipitation) - To clarify, only the successful experiments have been reported

Reference	T (°C)	P (MPa)	Duration (days)	Fluid composition	Starting solid assemblage	Starting Mnz	F/M ratio	Mnz size (µm)	Mnz1 compo. (wt.%)		
									ThO_2	UO_2	PbO
Budzyń et al., 2015	250	200	40	$Na_2Si_2O_5+H_20$	Mnz+Ab+Kfs+Bt+Ms+SiO_2	[1]Burnet	1.9	50-250 crushed grains	9.4-17	0.3-0.4	0.51-0.68
	350	200	40				1.9				
	350	400	20				2				
Shazia et al., 2015	800	200	19	H_20	Mnz+Kfs+SiO_2	[3]North Carolina	2	50-200 crushed grains	7.3-8.2	0.4-0.6	0.13-0.14
Budzyń et al., 2011	450	450	16	$Na_2Si_2O_5+H_20$	Mnz+Ab+Ms+SiO_2+CaF_2	North Carolina	2	50-100 crushed grains	7.3-8.4	0.3-0.7	0.09-0.14
	500	450	16		Mnz+Ab+Kfs+Ms+Bt+SiO_2+CaF_2		2				
Harlov et al., 2011	900	1000	25	NaOH 2N	Mnz+SiO_2+Al_2O_3	[4]Brazil heavy sand deposit	3	5-200 crushed grains	6.3-8.1	0.2-0.5	0.11-0.17
	900	1000	8	$Na_2Si_2O_5+H_20$	Mnz		2				
	900	1000	2	$Na_2Si_2O_5+H_20$	Mnz		2.1				
	900	1000	8	$Na_2Si_2O_5+H_20$	Mnz+Al_2O_3		2.1				
	900	1000	7	KOH 2N	Mnz+SiO_2		1.3				
	900	1000	8	KOH 2N	Mnz+SiO_2+Al_2O_3		2.3				
	600	1000	49	KOH 2N	Mnz+SiO_2+Al_2O_3		1.7				
	600	1000	23	NaOH 2N	Mnz+SiO_2+Al_2O_3+$ThSiO_4$		1.3				
	600	1000	23	$Na_2Si_2O_5+H_20$	Mnz+SiO_2+Al_2O_3+$ThSiO_4$		2.1				
	900	1000	25	KOH 2N	Mnz+SiO_2+Al_2O_3		3.3				
	900	1000	2	$Na_2Si_2O_5+H_20$	Mnz+Al_2O_3		2				
Williams et al., 2011	450	450	16	$Na_2Si_2O_5+H_20$	Mnz+Ab+Ms+CaF_2	North Carolina	2	50-300 crushed grains	7.1-8.8	0.4-0.6	0.14-0.16
Harlov and Hetherington, 2010	900	1000	8	$Na_2Si_2O_5+H_20$	Mnz	Brazil heavy sand deposit	2	50-200 crushed grains	7-8	0.4-0.5	0.12-0.13
Hetherington et al., 2010	900	1000	8	NaOH 2N	Mnz	Brazil heavy sand deposit	0.2	100-500 crushed grains	7.8±0.2	0.6±0.1	n.a.
	900	1000	8	$Na_2Si_2O_5+H_20$	Mnz		0.1				
Seydoux-Guillaume et al., 2002	1000	1000	21	$CaCl_2$ 10 wt.% + SiO_2	Mnz	Brazil Itambe pegmatite (Moacyr)	5.2	200-400 rounded grains	6.92	0.13	0.16
	1000	1000	14	HNO_3+Pb(std)+SiO_2	Mnz		11.2				
Teufel and Heinrich, 1997	400	300	28	H_2O	Mnz	[6]Metapelite, Bavaria	2	<1-15 sharp edges	-	0.09	0.09
	650	300	28								
	750	300	28								

Secondary minerals	Observations			Pb in Mnz2
	Textures	Mnz2 compositions /Mnz1	Mnz2 Th-U-Pb compositions	
Stc+Mnz2 REE-Ap+Stc+Amph+Mnz2 REE-Ap+Stc+Amph+Mnz2	strong dissolution with porosity, internal zoning (patchy	LREE enrichment HREE+Y depletion increase of LREE/HREE+Y	ThO_2 (4-5 wt. %), UO_2 (0.5-0.1 wt.%) and PbO (0.06 to 0.14 wt. %) depletion	yes
Mnz2	internal sector zoning, no porosity	no REE significant variation slight Si increase and Ca decrease with Th increase	Th enrichment or constant; Pb concentration increases with Th or constant between Mnz1 and Mnz2	no
Mnz2+F-Ap+Brit+Trk	strong dissolution with porosity, internal zoning (patchy)	LREE enrichment HREE+Y, Ca depletion increase of LREE/HREE+Y	strong Th and U depletion, Pb below detection limit	no
Mnz2 (± britholite nano-inclusions)	Extensive ThSiO4-enriched textures on monazite rim	LREE, Si enrichment HREE+Y, Ca depletion increase of LREE/HREE+Y	Systematic Th enrichment, no significant U variations, Significant Pb depletion in only one experiment	yes yes yes n.a.
	ThSiO4-enriched texture along the rim of some Mnz grain	no significant variation		yes yes
	ThSiO4-enriched texture along the rim of one Mnz grain	LREE, Si enrich.; HREE, Ca depl.		yes yes
	Faint reaction rim	no significant variation		n.a. yes n.a.
Mnz2 + inclusions (?)	Lobate reaction front at the edges of the original grain or arround inclusions and fractures	LREE, Si enrichment HREE+Y, Ca depletion increase of LREE/HREE	ThO_2 depletion (1-2 wt.%), UO_2 almost absent (0-0.2 wt.%), PbO almost absent (between 0-40 ppm)	no
Mnz2	Extensive ThSiO4-enriched textures on monazite rim, no porosity	No significant variation	ThO_2 enrich. (11-16 wt.%), UO_2 slight depletion (0.2 wt.%), No PbO in Mnz2	no
Mnz2	prononced porosity and dissolution channels with Mnz2 domains around	No significant variation of REE	No significant variation of Th, U	n.a.
	limited pore development, unclear internal zoning or sharp Mnz2 domain along Mnz1 rim	heterogeneous variation of REE	ThO_2 slight enrich. (9 wt.%), UO_2 slight depletion (0.2 wt.%)	n.a.
Mnz2	significant overgrowth	(HREE+Y) depletion	Th enrichment at the interface and in Mnz2 U depletion, no Pb in Mnz2	no
	significant overgrowth	no significant variation	Perturbated ages, incorporation of Pb from the doped solution	yes
Mnz2	roundish grain shape after experiment	-	U, Pb depletion rejuvenation of ages which increases with temperature	n.a.
	grain growth, roundish subhedral grains	-		n.a.
		-		n.a.

Legend on the next page

Legend of Table 5-2 (previous page):

[1]Pegmatite in Burnet County, Texas, USA (see Budzyń et al., 2015)

[2]Ruschel et al., 2012

[3]Heavy mineral sand deposit located in Cleveland County, North Carolina (UCLA, Department of Geology mineral collection catalog number MS-1762); see Williams et al., 2011

[4]Heavy mineral sands deposit at Cumuruxatiba, Bahia State, Brazil.; highly suspected to be the same monazite than 3

[5]Moacyr standar monazite from Itambe pegmatite district (Brazil, Cruz et al., 1998)

[6]Monazite from a lower amphibolite-facies metapelite from NE, Bavaria, Germany; also described in Heinrich et al., 1996

F/M ratio: Fluid/Monazite (mg); Mnz: monazite; Mnz2: secondary monazite; n.a.: not analizyed; Ab: albite; Kfs: K feldspar; Bt: biotite; Ms:muscovite; Stc: Steacyite; Ap: Apatite; Amph: amphibole; Brit: britholite; Trk: turkestanite

The only low temperature experiments (below 400°C) are those performed by Budzyń et al. (2011, 2015) and they investigated the monazite stability with respect to other REE or Th-rich minerals from a complex starting material assemblage (Table 2) from which REE and Th were preferentially redistributed in newly formed silicates. Thus, no experimental studies have investigated the REE+Y, Th, U, Pb, and O partitioning in monazite in terms of temperature below 600°C.

5.3. Experimental Procedure and Analytical methods

5.3.1. Hydrothermal experiments

In total, 18 hydrothermal experiments of monazite alteration were conducted in this study (Table 3). The monazite used in experiments is the natural Manangotry monazite standard (555 ± 2 Ma, ID-TIMS; Paquette and Tiepolo, 2007). It is chemically homogeneous (Oelkers and Poitrasson, 2002; Montel et al., 1996; Seydoux-Guillaume et al., 2004) with high Th content (~13 wt% ThO_2). Experimentally, ~30 mg of 50 to 100-µm-sized crushed grains of monazite were introduced with a pre-fractured quartz crystal (~2 mm wide and 8 mm long) and fluid (around 150 ml) in a 3 mm-wide and 25 mm-long Au capsule. Two additional experiments were performed using 1mm-sized cubes, and higher fluid/rock ratio (*AG13-07* and *AG13-08*). Most experimental fluids (H_2O, 10 wt.% NaCl, 1-2 M

NaOH) were prepared using $H_2{}^{18}O$ (97 atom %, Sigma-Aldrich). Pre-fractured quartz lamellas from inclusions-free natural crystals sampled at Kerguelen Island were used to trap fluid at the P-T conditions of the experiments. The synthesis of these fluid inclusions was conducted following a procedure inspired from Sterner and Bodnar (1984) and widely adopted in more recent studies (e.g. Gibert et al., 1998; Jacquemet et al., 2014). Quartz lamellas (~8 x 2 x 2 mm size) were heated at 700°C for 15-2 min, quenched in pure water to produced micro-fractures and dried at ~100°C to evaporate capillarity water. All fluids were doped with ~200 ppm Rb and Cs, prepared from aqueous chloride solution of 10000 ppm Rb-Cs ($RbCl_2$+$CsCl_2$+H_2O), for use as internal standard for LA-ICP-MS data reduction. In two experiments (*AG13-01* and *AG13-02*; Table 3), redox conditions were buffered using pure hematite (and magnetite) powder located in a clamped extremity of the Au capsule. Hematite-magnetite (He-Ma) composition was quantified, by Rietveld refinement of XRD analyses, at 95%He-5%Ma before experiments and 86%He-14%Ma, 16%He-84%Ma for *AG13-01* and *AG13-02* respectively, after experiments. The Au capsules were then arc-welded shut and left during one night at 110°C to check for leakage. Capsules were then placed in cold-seal pressure vessels at 300, 400, 500 and 600°C, and 200 MPa for duration from 14 days and up to 114 days. Experiments were performed in both ISTerre (Grenoble) and G.E.T. laboratories (Toulouse), France. Temperature was controlled using a thermocouple placed in the autoclave at the capsule level. After experimental run, autoclaves were quenched using compressed air for a few minutes. The Au capsules were weighted again to check for possible leakage during hydrothermal experiment and carefully opened. Experimental solid products (monazite and quartz) were washed in pure-water and dried. Monazites were mounted in epoxy and then polished using diamond powder solutions. Quartz lamellas were double-polished for microscopy and LA-ICP-MS analyses.

Table 5-3 Experimental conditions

Run	T (°C)	P (MPa)	Duration (days)	Monazite	Quartz	Fluid	^{18}O doped	Fluid composition	Fluid/Mnz ratio	Monazite replacement
AG12-02	600	200	40	31.0	52.1	149.1		H_2O	5	
AG14-03	300	200	101	29.2	67.4	141.5	x	NaCl 10 wt%	5	
AG14-04	400	200	101	29.9	78.2	138.2	x	NaCl 10 wt%	5	
AG14-01	500	200	68	30.8	61.2	138.8	x	NaCl 10 wt%	5	
AG14-02	600	200	68	30.1	61.3	141.6	x	NaCl 10 wt%	5	
AG13-06	300	200	114	29.9	112.1	142.4	x	NaOH (1M)	5	
AG13-05	400	200	114	30.6	65.5	125.4	x	NaOH (1M)	4	x
AG13-07*	500	200	22	6.2	-	103.6		NaOH (1M)	17	x
AG13-09*	500	200	22	9.4	88	103.9		NaOH (1M)	11	x
AG12-07	500	200	29	28.4	60.7	179.4	x	NaOH (1M)	6	x
AG13-03	500	200	114	30.78	63.17	142.71	x	NaOH (1M)	5	x
AG12-08	600	200	21	30.1	58.3	166.9	x	NaOH (1M)	6	x
AG13-08*	600	200	22	7.4	-	93.5		NaOH (1M)	13	x
AG13-10*	600	200	22	8.5	70	108.3		NaOH (1M)	13	x
AG12-04	600	200	40	21.1	60.1	103.1		NaOH (1M)	5	x
AG13-04	600	200	114	29.6	79.8	141.7	x	NaOH (1M)	5	x
AG13-01**	500	200	21	30.66	77	163.56	x	NaOH (2M)	5	x
AG13-02**	600	200	14	28.7	106.9	175.9	x	NaOH (2M)	6	x

** cube experiments*
*** HeMa buffered experiments*
Monazite, quartz and fluid quantites are given in mg.

5.3.2. EPMA

All electron probe micro-analyzer (EPMA) analyses were undertaken at ISTerre laboratory (Grenoble, France) on a Jeol JXA-8230, following the slightly modified protocol of Scherrer et al. (2000) in Janots et al. (2008). First, high contrast backscattered electron of grain (mounted in epoxy) cross section were realized to identify recrystallized areas with a distinct chemical composition (Mnz2) from pristine monazite (Mnz1). Quantitative analyses (Table 4, 5) were carried using a beam diameter of 1µm, an accelerating voltage of 25 kV and a beam current of 50 nA. using following X-ray lines: Si*Kα,* U*Mβ*, ThM*α*, CaKα, P*Kα*, Y*Lα*, Dy*Lβ,* Gd*Lβ*, Sm*Lβ,* Pr*Lβ,* Nd*Lα*, Ce*Lα*, La*Lα,* Pb*Mβ*. Natural minerals and synthetic glasses standards, including Smithsonian REE phosphates, were used for calibration. We used counting times between 20 and 40 s for

standards and between 30 and 200 s for experimental samples, depending on element concentrations in monazite. A calibrated overlap correction of 0.0064 was applied for peak interference of ThMγ on Umβ. Elemental mapping (Supplementary material 5-3 to 5-6) was carried out using an accelerating voltage of 15 kV, beam current of 250 nA, a pixel size of 0.5 μm and a dwell time of 500 ms per pixel. Vertical scales are X-ray counts.

5.3.3. Raman

Raman analyses of a partly replaced monazite grain were conducted using a Horiba XploRA dispersive Raman spectrometer. The 632 nm line of a He-Ne laser was used as excitation source. The scattered light was collected in a 180° backscattering geometry and analysed with a charge-coupled device (CCD) detector after being dispersed by a grating of 1800 grooves/mm and passed through a 50 μm entrance slit. A linescan across the replacement interface was performed using a step size of 1 μm. Spectra at each point along the line were obtained using a confocal hole of 500 μm, a 100x objective and an acquisition time of 5 sec. Each spectrum was taken 50 times and integrated to improve the signal-to-noise ratio. Corrections for system drift were done using the 520.7 nm Raman band of a silicon standard.

Similarly to the ^{18}O isotope incorporation in apatite (Kasioptas et al., 2011; Jonas et al., 2014), using Raman technic, the heavier oxygen isotope incorporation in monazite leads to a frequency shift of the vibration bands that involve the motion of oxygen. This incorporation in monazite structure leads to the generation of four new Raman bands in the Raman spectrum of monazite, in addition to the ν_1 ($P^{16}O_4$) observed at 971 cm^{-1} (Fig. 6A). These new bands are attributed to the oxygen-related isotopologues of the PO_4 group, i.e., to $P^{16}O_{4-i}{}^{18}O_i$ ($1 \leq i \leq 4$; Kasipotas et al., 2011).

5.3.4. Nano-SIMS

Elemental maps were produced with the Cameca NanoSIMS 50L at the Lehrstuhl für Bodenkunde, Technische Universität Munchen (TUM), Freising, Germany. Analyses were performed on monazite samples mounted in epoxy, polished and coated by C. Measurements of ^{89}Y, ^{140}Ce, ^{208}Pb, ^{16}O and ^{18}O were performed using the Cs primary ion beam, focused to obtain a lateral resolution of about 150 nm. Measurements of ^{232}Th and ^{238}U were performed using the O primary ion beam. Instead of ^{18}O intensity maps, $^{18}O/^{16}O$ intensity map were preferred due to charging effect in both ^{18}O and ^{16}O maps that can be diminished by dividing them.

5.3.5. TEM

The TEM foils were prepared with the HELIOS 600i FIB Dual Beam instrument at LAAS-CNRS RENATECH network. The foils were analyzed by TEM using a JEOL 2100F Transmission Electron Microscope operated at 200 KeV, equipped with EDS, STEM and a high-angle annular dark field (HAADF) detector and also with a JEOL cold FEG ARM200F operated at 200 KeV, equipped with a CS corrector, EDS, STEM HAADF detector and a GIF QUANTUM; both TEM are located in the UMS3623 Raimond Castaing in Toulouse (France).

5.3.6. LA-ICP-MS

LA-ICP-MS analyses were carried out at the G2R laboratory (Nancy, France). The LA-ICP-MS system is composed of a 193 nm GeoLas Excimer laser (ArF, Microlas, Göttingen, Germany), with a microscope for sample observation and laser beam focus onto the sample, and an Agilent 7500c quadrupole ICP-MS, equipped with a collision-reaction cell which decreases strongly mass interferences. For each experiment, fourteen rare earth elements, ^{23}Na, ^{29}Si, ^{85}Rb, ^{89}Y, ^{133}Cs, ^{232}Th and ^{238}U were analysed. Data were collected with an integration time of 0.01 s per channel for Si, Na, Rb, Cs, La, Ce, Pr, Nd,

Sm, Eu, Th and 0.02 s for Y, Gd, Tb, Dy, Ho, Er, Tm, Yb, Lu and U. Data were acquired as raw counts (cps) using the time resolved mode. For each individual analysis (external standard and sample), the background was measured for 20 s (used for data reduction) and the overall signal acquisition was recorded for 170 s. The certified glass reference materials NIST SRM 610 (Pearce et al., 1997) was used as calibrators for the LA-ICP-MS. Spot sizes of 24, 32, 44 and 60 µm were used. The data reduction (quantification and limits of detection) was carried out using in-house software based on the equations developed by Longerich et al., (1996). More details of the analytical procedure are given in Leisen et al. (2012) and Lach et al. (2013).

5.4. Results

5.4.1. Textural characterization of the solid products

Experimental conditions and results of all hydrothermal experiments are summarized in Table 3.

In experiments with H_2O or NaCl (10 wt. %) fluids, secondary monazite precipitation was not observe, either new minerals precipitation.

In the experiment with NaOH fluid at 300°C (*AG13-06*), there is no evidence of secondary monazite precipitation (Fig. 1A; Table 3). However, monazite dissolution is attested by dissolution features on monazite grain surface and precipitation of secondary apatite and REE-Th-rich minerals (Fig. 2A) that are identified as britholite (Table 5). At 400, 500 and 600 °C, monazite products are associated with REE-Th-rich minerals precipitation identified as steacyite-group minerals and britholite (Fig. 2, Table 5).

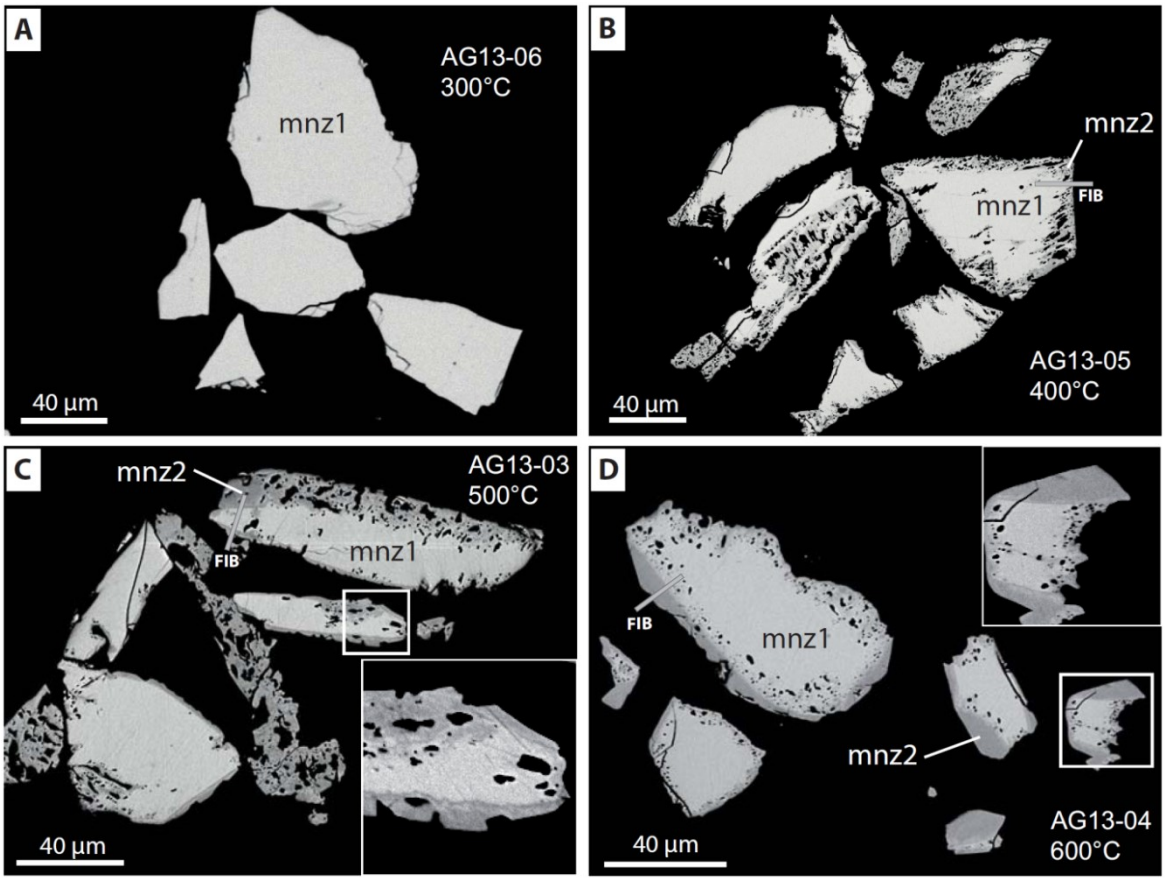

Figure 5-1 Backscattered electron image (SEM) of reacted monazite grain at 300(A)-400(B)-500(C)-600°C(D), 200 MPa in a NaOH(1M) solution for 114 days. White squares correspond to zoomed areas with possible overgrowth. Darker areas correspond to secondary monazite. mnz1: pristine monazite; mnz2: secondary monazite

Monazite hydrothermal alteration features are characterized by the presence of monazite with a distinct chemical composition (Mnz2) mostly along rim and within the pristine monazite domain (Mnz1), and the development of porosity. The interface between Mnz1 and Mnz2 domains is usually irregular in shape showing breakthrough of Mnz2 domains toward Mnz1 domains, decreasingly from 400°C to 600°C. Generally, the extent of porosity decreases with increasing temperature together with an increase of replaced Mnz2 volume.

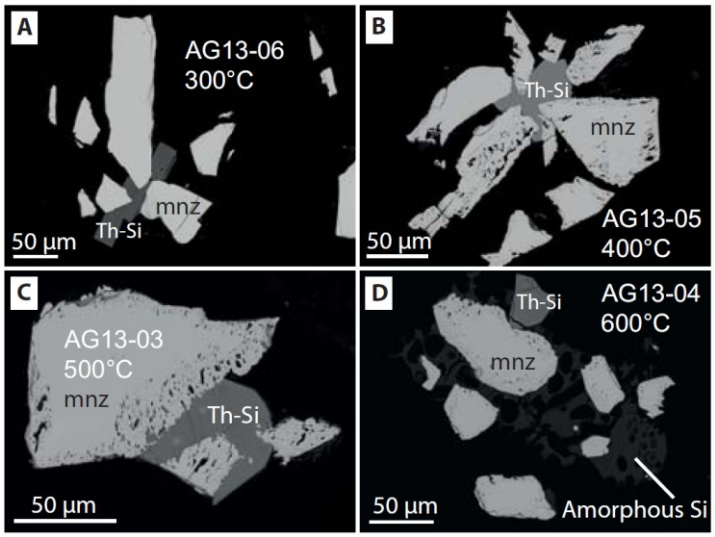

Figure 5-2 Backscattered electron image (SEM) of reacted monazite grain and Th-silicate formed at 300(A)-400(B)-500(C)-600°C(D)), 200 MPa in a NaOH(1M) solution for 114 days. mnz: monazite, Th-Si: Th silicate

Pores are elongated and show preferential orientation in monazite grains at 400°C (Fig. 1B), but are more irregular at 500°C (1C) and rounded at 600°C (Fig. 1D). They are located in both Mnz1 and Mnz2 domains at 400 and 500°C and mostly in Mnz1 domain at 600°C. The extent of Mnz2 domain depends strongly on temperature and experiment duration. For a same fluid/monazite (F/M) ratio, higher temperature and duration lead to a higher volume of Mnz2 domain. In experiments with NaOH at 500 and 600°C, the presence of an amorphous Si-rich deposit is observed after quenching (Fig. 2D, 3A-B) on monazite surface. At the highest experimental temperature (600°C), this secondary products is more abundant with large and rounded pores (Fig. 2D). The presence of well-shaped faces of secondary Mnz2, particularly in experiments at 600°C (Fig. 2D) may attest for monazite overgrowth and is discussed further in discussion. In the experiments without SiO_2 (*AG13-07* and *AG13-08*), monazite was strongly altered (and fractured) at 600°C and in a lesser extent at 500°C (Fig. 3C, D). The secondary minerals have been identified as rhabdophane-group mineral and probably thorianite (Table 5).

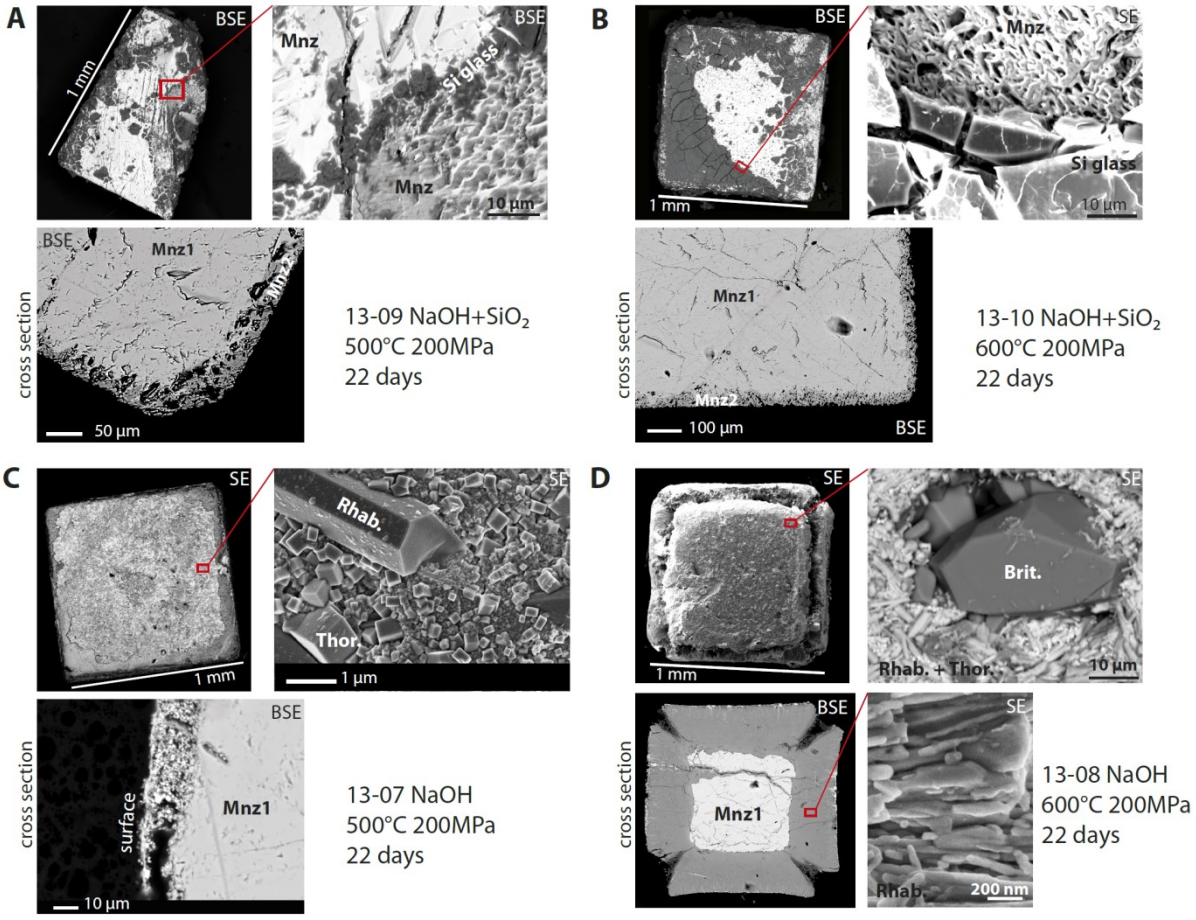

Figure 5-3 SEM images of monazite cube (surface and cross-section) experiments with NaOH (1M) + SiO_2 (solid) at 500°C (A), 600°C (B), 200 MPa for 22 days and with NaOH (1M), 200 MPa for 22 days but without SiO_2 at 500°C (C) and 600°C (D). Mnz1: pristine monazite; Mnz2: secondary monazite; Rhab: rhabdophane; thor: thorianite; brit: britholite. Note the higher degree of replacement in experiments without SiO2.

5.4.2. Chemical characterization of the reaction products

Element chemistry of Mnz2 domains from NaOH experiments was studied using both EPMA measurement and Nano-SIMS mapping. Mean element concentrations and representative analyses of Mnz1 and Mnz2 domains depending on the temperature are presented in Table 4 and element concentrations of secondary minerals different from monazite are given in Table 5.

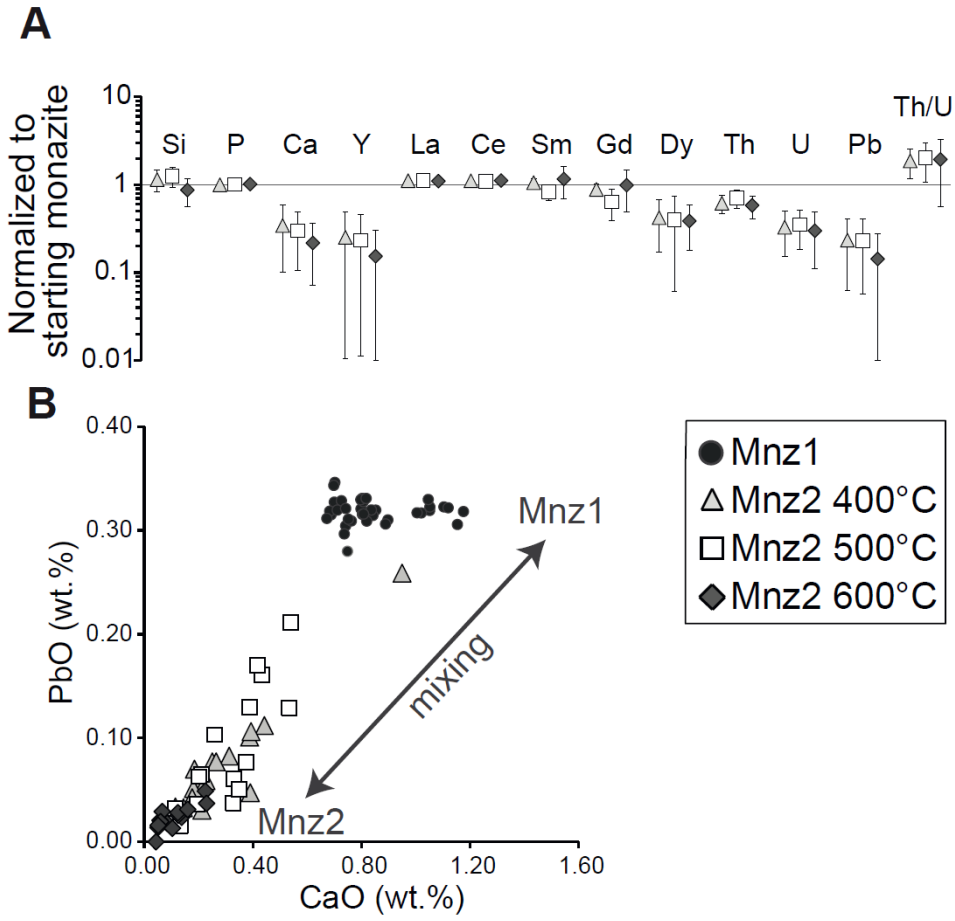

Figure 5-4 Electron Probe Micro-Analyser (EPMA) results of: A: Secondary monazite for the overall dataset of experiments at 400, 500 and 600°C. The mean values (Mnz2) for each temperature are normalized to the mean of unaltered monazite composition (Mnz1) and are plotted with their associated standard deviations. B: Pbo vs Cao (wt.%) as marker of mixing between pristine monazite (Mnz1) and secondary (Mnz2) domains.

Table 5-4 EPMA major element data for replaced monazites

Exp. conditions	Mineral	Sample	Element concentration (wt.%)														
			SiO_2	P_2O_5	CaO	Y_2O_3	La_2O_3	Ce_2O_3	Pr_2O_3	Nd_2O_3	Sm_2O_3	Gd_2O_3	Dy_2O_3	PbO	ThO_2	UO_2	Total
	Mnz1	mean (n=37)	2.35	27.07	0.85	0.16	14.08	28.77	2.86	9.89	0.95	0.39	0.07	0.32	12.83	0.16	100.74
		SD	0.24	0.53	0.15	0.03	0.33	0.34	0.04	0.16	0.07	0.04	0.02	0.01	0.49	0.02	0.63
400°C (NaOH)	Mnz2	mean (n=17)	2.70	27.06	0.29	0.04	15.65	31.84	3.16	10.91	1.00	0.35	0.03	0.07	7.88	0.05	101.05
		SD	0.70	0.66	0.20	0.04	0.40	0.84	0.08	0.40	0.07	0.04	0.02	0.05	1.78	0.03	0.96
		AG13-05	*2.11*	*27.45*	*0.39*	*0.05*	*15.61*	*31.56*	*3.11*	*10.47*	*0.96*	*0.34*	*0.04*	*0.10*	*8.13*	*0.05*	*100.38*
		AG13-05	*2.46*	*26.90*	*0.12*	*0.06*	*15.62*	*31.99*	*3.18*	*11.19*	*1.10*	*0.40*	*0.03*	*0.03*	*7.06*	*0.03*	*100.22*
500°C (NaOH)	Mnz2	mean (n=21)	2.93	27.22	0.25	0.04	15.79	31.54	3.06	10.23	0.78	0.25	0.03	0.07	9.09	0.06	101.34
		SD	0.67	1.03	0.16	0.03	0.76	1.48	0.14	0.50	0.15	0.09	0.02	0.06	2.17	0.03	1.12
		AG12-07	*3.00*	*29.94*	*0.13*	*0.01*	*15.68*	*31.56*	*3.08*	*10.46*	*0.82*	*0.20*	*0.05*	*0.07*	*7.24*	*0.04*	*102.28*
		AG13-03	*2.72*	*27.62*	*0.35*	*0.09*	*15.13*	*29.93*	*2.82*	*9.58*	*0.79*	*0.30*	*0.03*	*0.05*	*9.79*	*0.08*	*99.34*
		AG13-03	*2.43*	*26.22*	*0.26*	*0.07*	*16.08*	*31.33*	*3.00*	*9.92*	*0.80*	*0.29*	*0.06*	*0.10*	*9.22*	*0.04*	*99.82*
		AG13-09	*3.19*	*27.90*	*0.04*	*0.00*	*15.78*	*33.14*	*3.34*	*11.18*	*0.59*	*0.06*	*0.01*	*0.03*	*6.31*	*0.03*	*101.60*
600°C (NaOH)	Mnz2	mean (n=23)	2.05	27.48	0.18	0.02	15.48	32.12	3.12	11.12	1.10	0.39	0.03	0.05	7.46	0.05	100.65
		SD	0.69	1.39	0.12	0.03	1.31	1.35	0.31	1.23	0.43	0.19	0.01	0.04	2.15	0.03	1.45
		AG12-04	*2.36*	*26.80*	*0.21*	*0.00*	*14.94*	*30.98*	*3.04*	*10.97*	*1.18*	*0.43*	*0.04*	*0.01*	*8.83*	*0.08*	*99.88*
		AG12-08	*2.81*	*27.92*	*0.29*	*0.02*	*15.29*	*30.60*	*2.97*	*10.10*	*0.76*	*0.23*	*0.04*	*0.07*	*9.62*	*0.08*	*100.80*
		AG13-02	*1.97*	*25.94*	*0.28*	*0.00*	*16.56*	*32.48*	*3.04*	*10.05*	*0.64*	*0.18*	*0.02*	*0.06*	*7.33*	*0.03*	*98.58*
		AG13-04	*0.98*	*28.10*	*0.04*	*0.01*	*18.19*	*34.78*	*2.32*	*10.19*	*0.53*	*0.12*	*0.01*	*bdl*	*3.55*	*0.01*	*98.84*
		AG13-04	*2.12*	*26.44*	*0.10*	*0.01*	*14.53*	*31.40*	*3.25*	*11.71*	*1.42*	*0.58*	*0.03*	*0.01*	*8.70*	*0.03*	*100.34*
		AG13-10	*2.68*	*28.38*	*0.20*	*0.03*	*17.42*	*32.53*	*2.98*	*9.30*	*0.53*	*0.16*	*0.00*	*0.07*	*8.04*	*0.05*	*102.38*

Mnz1: pristine monazite; Mnz2: reprecipitated monazite

Table 5-5 EPMA major element data for replaced monazites

Exp. Conditions	Starting material	Presumed Mineral	Sample	Element concentration (wt.%)															
				Na_2O	SiO_2	P_2O_5	CaO	Y_2O_3	La_2O_3	Ce_2O_3	Pr_2O_3	Nd_2O_3	Sm_2O_3	Gd_2O_3	Dy_2O_3	PbO	ThO_2	UO_2	Total
[1]NaOH 400 - 600°C	Mnz+Qz	Steacyte-group minerals	mean (n=9)	6.32	56.47	0.15	4.92	0.03	0.16	0.48	0.08	0.42	0.12	0.15	0.03	bdl	29.56	0.59	99.47
			SD	*1.55*	*1.17*	*0.27*	*0.78*	*0.04*	*0.25*	*0.57*	*0.07*	*0.35*	*0.12*	*0.06*	*0.02*	*bdl*	*1.32*	*0.13*	*1.05*
[2]NaOH 300 - 600°C	Mnz+Qz	britholite	mean (n=5)	2.15	27.20	12.11	2.31	0.06	10.28	21.21	2.14	7.20	0.62	0.27	0.03	0.03	15.56	0.29	100.2
				2.24	*11.54*	*6.5*	*1.22*	*0.07*	*4.67*	*9.18*	*1.08*	*3.46*	*0.34*	*0.13*	*0.04*	*0.03*	*5.48*	*0.20*	*1.43*
NaOH 300°C	Mnz+Qz	Apatite	*AG13-06*	0.155	0.07	39.14	42.78	0.05	0.09	0.39	0.05	0.29	0.00	0.19	bdl	0.01	bdl	bdl	83.20
			AG13-06	0.162	0.10	40.55	46.45	0.05	0.09	0.39	0.04	0.25	0.07	0.13	bdl	0.02	bdl	bdl	88.29
NaOH 600°C *AG13-08*	Mnz	Rhabdophane-group	mean (n=4)	n.a.	2.85	24.90	0.81	0.10	12.19	25.29	2.47	8.33	0.75	0.31	0.04	0.01	13.23	0.15	91.42
			SD	-	*0.63*	*1.05*	*0.07*	*0.06*	*0.16*	*0.27*	*0.07*	*0.25*	*0.05*	*0.03*	*0.01*	*0.01*	*0.66*	*0.01*	*0.94*

bdl: below detection limit

[1]experiments *AG13-03, AG13-04, AG13-05*

[2]experiments *AG13-03, AG13-04, AG13-05, 13-06*

Mnz2 domains show enrichment in LREE, Si and depletion in HREE+Y, Ca, Th, U and Pb compared to Mnz1 (Fig. 4A). Th/U ratio of Mnz2 domains (~ 150) is higher than Mnz1 domain (79±11), with no significant variation depending on temperature. The PbO vs CaO (wt.%) diagram (Fig. 4B) indicates a continuous evolution between a pristine Mnz1 composition and a secondary Mnz2 with almost no Pb and Ca. It would be also the case for U and Y which are also slightly reincorporated in Mnz2 (Table 4). Element intensity maps (uncorrected from background noise) have been performed by EPMA and are given in Supplementary material 5-1 to 5-4. They show the presence of Si-rich inclusions in Mnz1 and Mnz2 domains, associated with porosity (e.g. Supplementary material 5-2), and confirms the compositional variations between Mnz1 and Mnz2.

Isotopic intensity maps of ^{140}Ce, ^{89}Y, ^{232}Th, ^{238}U and ^{208}Pb have been performed for NaOH experiments at 400, 500 and 600°C (respectively sample *AG13-05*, *AG13-03* and *AG13-04*, Fig. 5). Nano-SIMS images show variation in Ce, Y, Th, U and Pb between Mnz1 and Mnz2 domains. At 400°C (Fig. 5A), monazite shows enrichment in Ce along rim and correlated depletion in Y, U, Pb and minor Th. Mnz2 domain is highly depleted in Y, U and Pb. The progress of recrystallization appears oriented toward the monazite core. At 500°C (Fig. 5B), the BSE image and the map show a secondary mineral (Th-silicate, probably steacyite group mineral) crystallized during the experiment, associated with monazite, also containing in Y and U. In this grain, Mnz2 domain is enriched in Ce and depleted in Y, Th, U and Pb. This depletion appears heterogeneous as patches in the highly porous zone (mostly on the left side of the map). At 600°C (Fig. 5C), the BSE image and the map show a Th-silicate crystal crystallized on the monazite crystal. The reacted monazite show a large replacement domain homogeneously enriched in Ce and depleted in Th and highly depleted in Y, U and Pb. A second replacement domain, highly porous, is present as a thin band penetrating the Mnz1 and heterogeneously depleted in Y, Th, U and Pb. In the 400 to 600°C experiments, LREE-silicates (probably britholite) have also been identified.

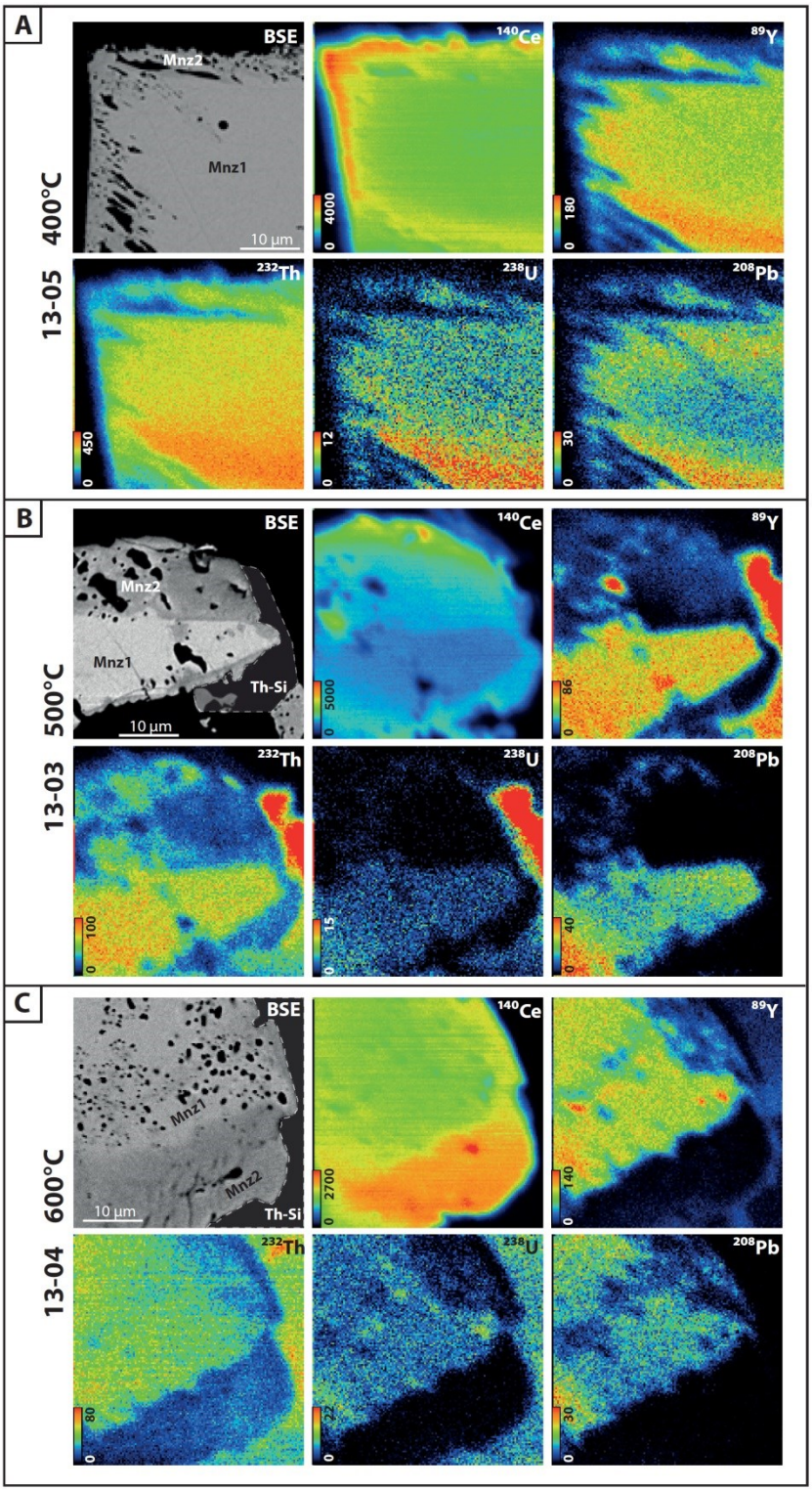

Figure 5-5 Nano-SIMS intensity maps (^{140}Ce, ^{89}Y, ^{232}Th, ^{238}U, ^{208}Pb) and associated BSE images for reacted monazite samples at 400°C (A), 500°C (B) and 600°C (C) and 200MPa with NaOH (1M) solution for 114 days. Mnz1: pristine monazite; Mnz2: secondary monazite; Th-Si: Th silicate.

5.4.3. ^{18}O incorporation in the replacement domains

In this study, we used both mass spectrometric techniques (Nano-SIMS) and Raman spectroscopy to characterize ^{18}O incorporation in the framework structure of secondary monazite. Using the Raman technic, the fraction of ^{18}O in the PO_4 group of monazite domains (Mnz1 and Mnz2) was calculated using the equation:

$$f^{18}O(\%) = \left(\sum_{i=1}^{4}\left[\frac{5-i}{4}\cdot a_i\right] / \sum_{i=1}^{5} a_i\right)\cdot 100 \quad (1)$$

where a_i ($1 \leq i \leq 5$) represents the integral intensities of the Raman bands at 919, 928, 939, 949 and 971 cm^{-1}, respectively (Kasioptas et al., 2011). The positions of these new bands observed (νobs) and theoretical (νcalc) are given in Table 6.

Table 5-6 Observed (νobs) and theoretical (νcalc) frequencies of the different oxygen-related isotopic species of PO4 in monazite.

Isotopic species	$\nu(PO_4)_{obs}$ (cm^{-1})	$\nu(PO_4)_{calc}$ (cm^{-1})
$P^{16}O_4$	971	-
$P^{16}O_3{}^{18}O$	949	957.4
$P^{16}O_2{}^{18}O_2$	939	943.6
$P^{16}O^{18}O_3$	928	929.7
$P^{18}O_4$	919	915.5

The high porosity of altered monazite grain is problematic to make precise Raman maps of these relative intensities. Nevertheless, the ^{18}O incorporation is fairly well resolved (Supplementary material 5-5, 5-6). A 20 µm profile along Mnz1 and Mnz2 domains has been performed with a point of analysis each micrometer (Fig. 6) on a monazite grain that reacted with the 1M NaOH solution (enriched with ~97 at.% $H_2{}^{18}O$) at 600°C, 200MPa for 114 days (*AG13-04*). The waterfall plot of the Raman spectra of the profile (Fig. 6A) shows the shifting and splitting of Raman bands due to the incorporation of ^{18}O in the PO_4 tetrahedron of monazite. The calculated amounts of ^{18}O

incorporated along the profile (Fig. 6B) reveal no ^{18}O in Mnz1 domain, constant amounts in Mnz2 domain and only a slightly variation close to the interface. From rim to core, the ^{18}O content in Mnz2 domain is ~50 %, with a single point up to 56% reaching interface and two point at 11 and 4 % just before Mnz1 domain with no ^{18}O.

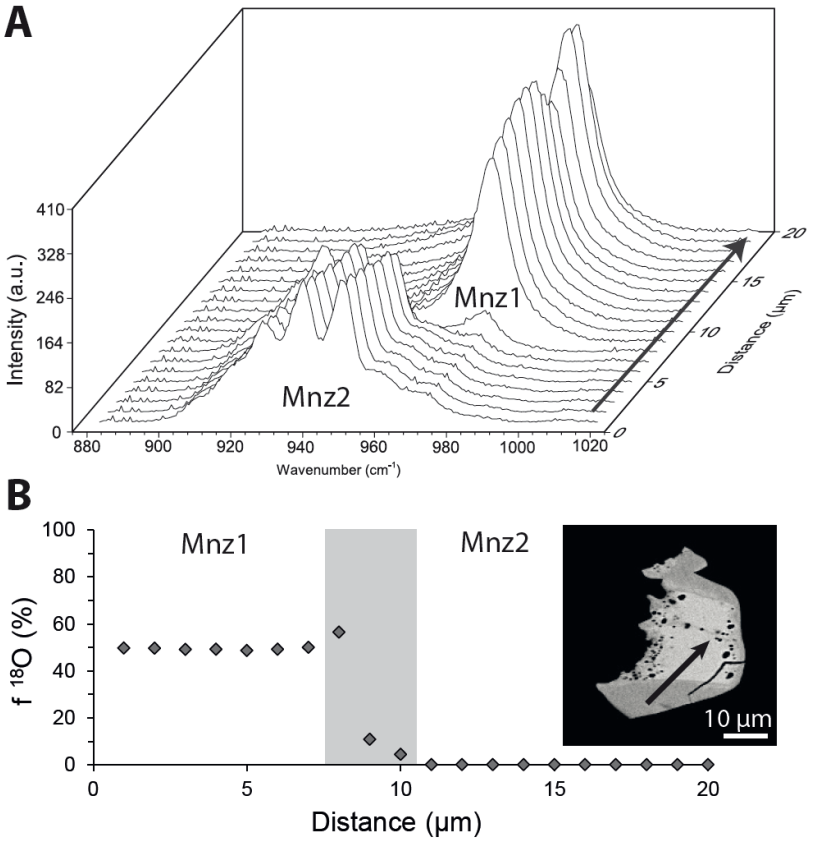

Figure 5-6 A: Waterfall plot of Raman spectra of a 20 µm profile along secondary monazite (Mnz2) and pristine monazite (Mnz2) showing the incorporation of ^{18}O in into the PO_4 tetrahedron of monazite (see Kasioptas et al., 2011 for further information) that reacted with the 1M NaOH solution (enriched with ~97 at.% $H_2{}^{18}O$) at 600°C, 200MPa for 114 days. B: Calculated values of ^{18}O content (%) in the PO_4 tetrahedron of monazite along the profile from rim (Mnz2) to core (Mnz1) determined from Raman line profile (A), and location of the profile on BSE image.

Two Nano-SIMS ^{18}O maps are shown in Figure 7, corresponding to monazite grain that reacted with the 1M NaOH solution (enriched with ~97 at.% $H_2{}^{18}O$) at 400 and 600°C, 200MPa for 114 days (*AG13-05*, *AG13-04*). Each map is associated with its corresponding BSE image and a drawn pattern (Fig. 7A-B). In the Nano-SIMS maps, all the blue domains correspond to Mnz2 domains, except for the right part of the 600°C map (Fig. 7B) that is an amorphous Si deposit. The dark domains correspond to Mnz1 domains, porosity or epoxy at the grain boundary. These different domains are schematized on the drawn patterns below Nano-SIMS maps. The $^{18}O/^{16}O$ intensity map from the monazite reacted at 400°C (Fig.7A) show an intimate mixture of Mnz1 and Mnz2 domains and suggests orientated recrystallization of Mnz2 domains (between the upper left corner and the bottom right corner). The $^{18}O/^{16}O$ intensity map from the monazite reacted at 600°C (Fig.7B) show a large Mnz2 domain on the lower part of the grain and a breakthrough of recrystallization on the upper part associated with extended porosity. The map show also some patches of Mnz2 domains (with ^{18}O) within Mnz1 domains, often located on the edge of pores.

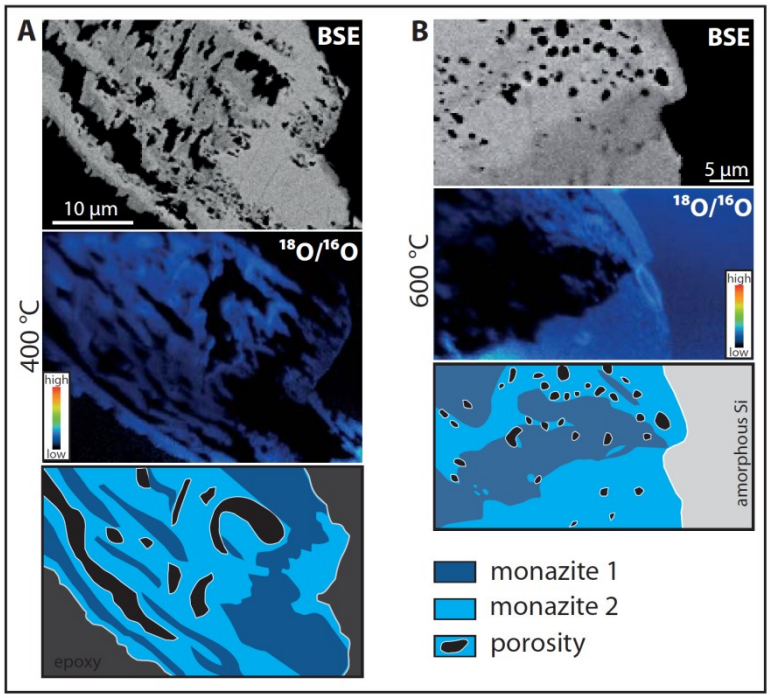

Figure 5-7 BSE image, Nano-SIMS intensity map ($^{18}O/^{16}O$) and drawn pattern of reacted monazite with 1M NaOH solution (enriched with ~97 at.% $H_2{}^{18}O$) at 400°C (A) and 600°C (B), 200MPa for 114 days, showing the ^{18}O incorporation in secondary monazite and the patchy texture resulting of the mixing between pristine monazite (Mnz1) and secondary monazite (Mnz2)

5.4.4. Nanostructures in the altered monazite

In the TEM images (Fig. 8, 9 and 10), the unaltered monazite (Mnz1) can be easily identify due to the presence of typical mottled diffraction contrasts due to a distorted lattice resulting from radiation damage (Seydoux-Guillaume et al., 2002b and 2004), in contrast to the newly formed monazite (Mnz2), whose lattice is free of such damage. TEM investigation (FIB cut foil location on Fig. 1) into reacted monazite grains at 400°C (*AG13-05*), 500°C (*AG13-03*) and 600°C (*AG13-04*) shows several characteristics: large epitaxial recrystallization domain (Fig. 8), nano-pores and inclusions (Fig. 9) and nano-cracks at an interface between Mnz1 and Mnz2 domains (Fig. 10).

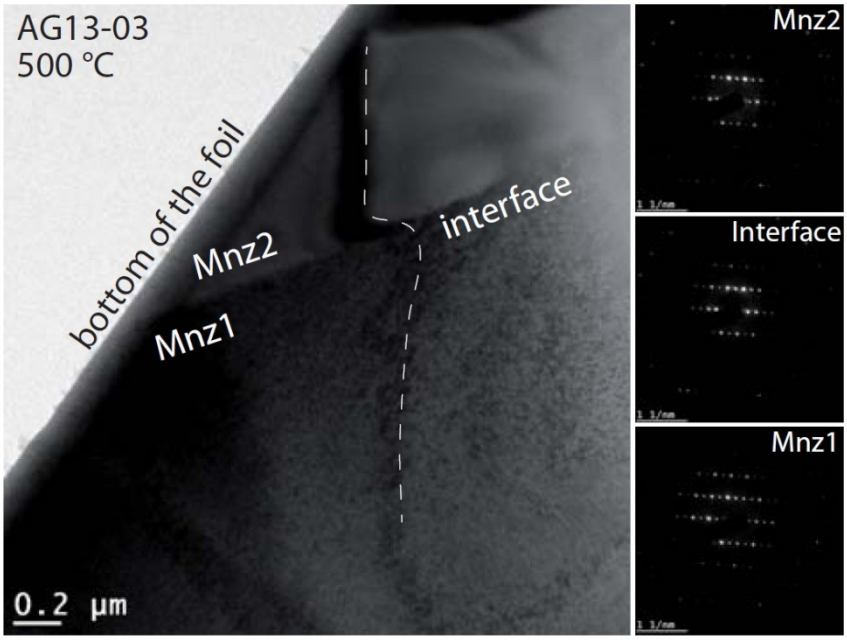

Figure 5-8 TEM images in Bright Field mode (BF-TEM) from FIB foil prepared in monazite grain from experiment AG13-03 (500°C, 200MPa, 1 M NaOH solution for 114 days), showing an epitaxial growth of secondary monazite (Mnz2). The electron diffraction patterns in the right are taken in Mnz1 (pristine monazite), across the interface and in Mnz2, and show the consistency of Mnz1 and Mnz2 lattices, also confirmed by the Bragg lines continuity (dashed line)

The TEM image in Bright Field mode (BF-TEM) in a grain from experiment at 500°C, 200MPa, 1 M NaOH solution for 114 days (*AG13-03*, Fig. 8) show a recrystallization of Mnz2 with a sharp interface with Mnz1. The electron diffraction patterns taken from Mnz1, interface and Mnz2 indicate an epitaxial growth of Mnz2 with consistency of Mnz1 and Mnz2 lattices. In this area, no pores were observed in either Mnz1 or Mnz2 domains.

The TEM investigation (BF-TEM) of nano-porosity and inclusions (Fig. 9) in monazite experiments at 400°C (Fig. 9A), 500°C (Fig. 9B) and 600°C (Fig. 9C) revealed that Mnz2 is intimately connected to nanopores (Fig. 9A, B, C), and that nano-domains of Mnz2 are located around pores and inclusions. In the three images, pores are partially filled by inclusions of amorphous Si. In the grain from experiments at 500°C (Fig. 9B) and 600°C (Fig. 9C) pores also contains neo-formed nano-sized monazite inclusions indicating crystallization from the fluid phase. The bright part of the image without defects (Fig. 9C) corresponds to amorphized area during sample preparation (FIB).

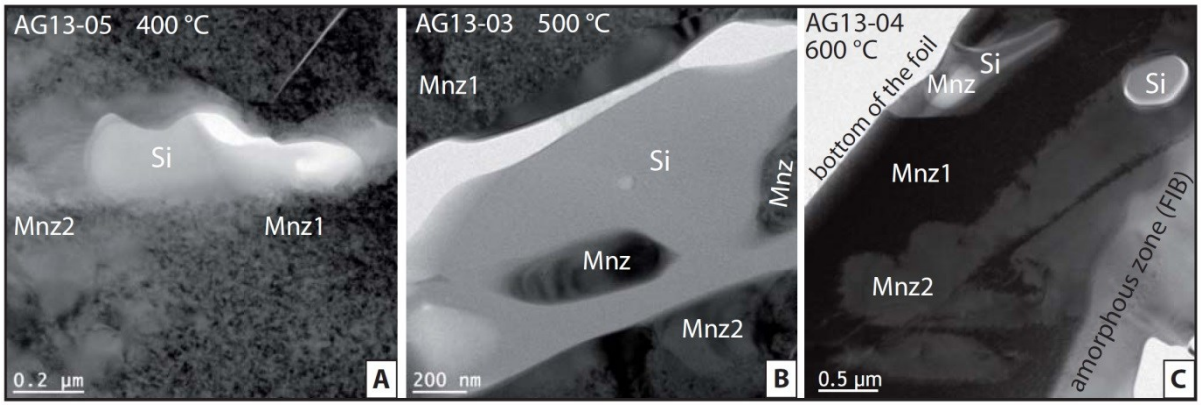

Figure 5-9 TEM images in Bright Field mode (BF-TEM) from FIB foils prepared in experimental grains (A-400°C, B-500°C, C-600°C) showing the nano-porosity partially filled by amorphous Si (A-B-C) and neoformed monazite (B). Note the nano-domains of secondary monazite (Mnz2) in pristine monazite (Mnz1) around pores (A-B) and the mixing between Mnz1 and Mnz2 domains (C); see Table 3 for experimental conditions and Figure 1 for the location of the FIB cut foil

The STEM images in Dark Field mode (ADF-TEM) and the TEM images in Bright Field mode (BF-TEM) from experiment at 500°C (*AG13-03*, Fig. 10A-C) and 400°C (*AG13-05*, Fig. 10D, E) respectively, focuses on the non-linear interface between Mnz1 and

Mnz2 domains (Fig. 10A, B, D). In both samples, Mnz2 domains appear penetrating Mnz1 domain. In the 500°C experiment, the tip of the recrystallization is extended by a µm-long fracture penetrating Mnz1 domain (Fig. 10A). Different fracture parallels to the former are visible in Mnz1 domains. In the enlarged images (Fig. 10B-C), we also distinguished a second population of curved nano-cracks (darker areas) located at the interface between Mnz1 and Mnz2 domains. The size of this interface is about 100 nm. Fractures at the interface are more visible when the image is defocused (Fig. 10C) compared to the focused image (Fig. 10B). The 400°C experiment shows a breakthrough of recrystallization of Mnz2 domains toward Mnz1 domains (Fig. 10D). Here, a crack has also been observed initiating in a pore, at the reaction front (Fig. 10E).

Next page: **Figure 5-10 S**TEM images in Dark Field mode (ADF-TEM) from FIB foil prepared in monazite grain from experiment AG13-03 (500°C, 200MPa, 1 M NaOH solution for 114 days) showing (A) a secondary monazite domain (Mnz2) on pristine monazite (Mnz1) and (B-C) images of the interface. Note the progress of recrystallization along cracks (A) and the curved nano-cracks at the interface (B-C). TEM images in Bright Field mode (BF-TEM) from FIB foil prepared in monazite grain from experiment AG13-05 (400°C, 200MPa, 1 M NaOH solution for 114 days) showing the breakthrough of Mnz2 toward Mnz1 domain (D) and cracks initiating in a pore located at the interface between Mnz1 and Mnz2 domains (E).

Figure 5-10

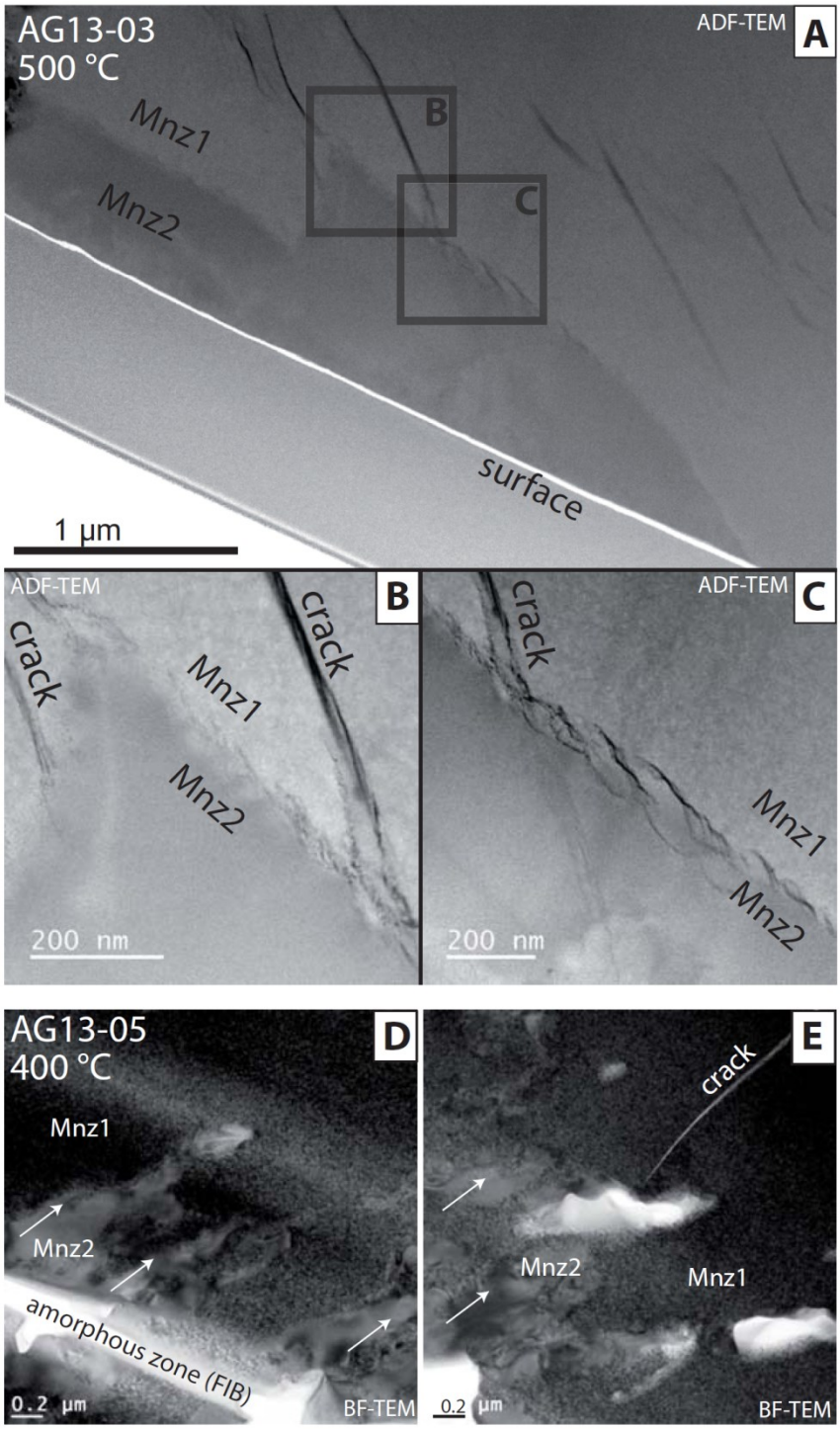
AG13-03
500 °C
ADF-TEM
A
Mnz1
Mnz2
B
C
surface
1 µm
ADF-TEM
B
crack
crack
Mnz1
Mnz2
200 nm
ADF-TEM
C
crack
Mnz1
Mnz2
200 nm
AG13-05
400 °C
D
Mnz1
Mnz2
amorphous zone (FIB)
0.2 µm
BF-TEM
E
crack
Mnz2
Mnz1
0.2 µm
BF-TEM

5.4.5. Fluid inclusions characterization

Together with monazite grains, a pre-fractured quartz crystal (~2 mm wide and 8 mm long) was introduced in the gold capsule of most of the experiments (Table 3). During experiments, quartz recrystallizes trapping the fluid as fluid inclusions. Unfortunately, quartz recrystallization strongly depends on fluid nature, temperature and duration of hydrothermal experiments. Another problem emerged in this study is neo-formed monazite grain or secondary minerals that can crystalize on the quartz surface or deep in cracks before quartz recrystallization and then pollute the entire quartz crystal which does not allow the analysis of fluid inclusions. Thus, only four experiments gave significant results (Table 7) on solid and fluid inclusions and corresponding to experiments with NaOH solution at 500 and 600°C, with oxygen buffer or not. Quartz used in H_2O, H_2O+NaCl and NaOH (300°C) experiments were not properly recrystallized (Supplementary material 5-7) and therefore could not be analysed. Quartz used in long duration experiments with NaOH at 500 and 600°C (*AG13-03* and *AG13-04*) were entirely dissolved and inclusions were analysed in neo-formed quartz crystals (Supplementary material 5-7). The petrological study of inclusions indicates is the presence of both Si melt phase (resulting on amorphous Si glass after quenching) and fluid phase during experiment giving fluid or glass inclusions (Supplementary material 5-8). In the 1M NaOH solution, 400°C, 200MPA for 114 days experiment (*AG13-05*) experiments, quartz is well recrystallized but REE-rich crystals have crystallized on its surface during its growth (Supplementary material 5-8) resulting in pollution of the sample.

Table 5-7 LA-ICP-MS trace element data for experimental fluid and solid inclusions

Sample	Analysis	Incl. Type	Element concentrations (ppm)																				
			Na (23)	Rb (85)	Y (89)	Cs (133)	La (139)	Ce (140)	Pr (141)	Nd (146)	Sm (147)	Eu (153)	Gd (157)	Tb (159)	Dy (163)	Ho (165)	Er (166)	Tm (169)	Yb (172)	Lu (175)	Th (232)	U (238)	Th/U
AG1301-	01	Si	59686	195	72	154	350	1847	287	1373	288	1	141	10	30	3	4	bdl	bdl	bdl	4612	45	**103**
	02	Fluid	60294	195	5	184	32	75	8	45	13	1	6	bdl	bdl	bdl	bdl	bdl	bdl	bdl	54	5	**11**
	03	Si	64476	195	132	142	555	2445	368	1797	440	2	238	18	54	5	8	1	bdl	bdl	5556	90	**62**
	04-1	Si	62740	195	150	134	577	2627	420	2026	525	bdl	291	21	68	5	12	1	3	bdl	4875	112	**43**
	04-2	Si	71329	195	276	139	948	4298	668	3323	884	3	494	37	112	11	16	1	4	bdl	8764	167	**53**
	05-1	Si	61332	195	84	145	429	1898	281	1322	307	1	155	12	34	4	4	bdl	bdl	bdl	3729	70	**53**
	05-2	Si	68948	195	108	141	573	2700	379	1815	420	2	205	15	45	4	6	bdl	bdl	bdl	5876	79	**75**
	06	Si	74972	195	na	136	663	3082	471	2363	655	3	360	28	85	8	13	bdl	3	bdl	6168	112	**55**
	07-1	Si	72224	195	na	139	504	2291	358	1712	388	1	191	14	41	4	5	bdl	bdl	bdl	5525	69	**80**
	07-2	Si	69480	195	na	148	611	2207	322	1502	341	1	161	11	35	4	5	bdl	bdl	bdl	4917	58	**85**
	08	Si	70740	195	na	142	544	2503	359	1680	394	2	202	15	41	4	6	bdl	bdl	bdl	5625	76	**74**
AG1302-	02	Si	40909	211	54	181	327	1416	205	966	200	1	106	8	24	2	4	bdl	bdl	bdl	4840	39	**124**
	03-1	Si	40429	211	58	181	293	1318	207	998	214	1	116	9	28	3	4	bdl	bdl	bdl	4908	42	**116**
	03-2	Si	40733	211	54	186	319	1383	217	985	197	1	104	8	24	2	3	bdl	bdl	bdl	4804	39	**124**
	04-1	Si	18144	211	64	219	278	1358	216	990	232	1	125	10	30	3	4	bdl	bdl	bdl	5374	52	**104**
	04-2	Si	39688	211	59	182	343	1435	223	957	205	1	109	8	26	3	4	bdl	bdl	bdl	5056	39	**129**
	05-1	Si	41736	211	na	175	311	1392	196	918	216	1	117	9	28	3	4	bdl	bdl	bdl	4647	32	**144**
	05-2	Si	42024	211	na	173	292	1279	186	883	213	1	117	9	27	3	4	bdl	bdl	bdl	4479	34	**133**
	06	Si	40142	211	na	174	167	947	153	805	250	1	159	13	43	4	6	bdl	bdl	bdl	5619	39	**145**
	07	Si	41616	211	na	164	251	1203	184	963	234	1	127	9	30	3	4	bdl	bdl	bdl	4747	31	**153**
AG1303-	02-1	Fluid	20775	260	34	211	46	145	20	81	25	bdl	18	2	12	1	2	bdl	bdl	bdl	206	28	**7**
	02-2	Fluid	20430	260	26	209	49	140	19	80	23	1	16	2	9	1	2	bdl	bdl	bdl	171	21	**8**
	03	Fluid	20513	260	9	211	35	101	13	54	11	bdl	10	1	4	bdl	bdl	bdl	bdl	bdl	55	5	**11**
	05	Fluid	24844	260	bdl	219	bdl	bdl	bdl	bdl	bdl	bdl	bdl	bdl	bdl	bdl	bdl	bdl	bdl	bdl	bdl	bdl	**-**
	06	Fluid	19262	260	4	206	19	62	8	32	6	bdl	3	bdl	bdl	bdl	bdl	bdl	bdl	bdl	13	1	**13**
	07	Fluid	20390	260	8	204	37	112	16	62	14	bdl	10	1	4	1	bdl	bdl	bdl	bdl	45	6	**8**
	08	Fluid	20708	260	3	215	19	61	8	31	7	bdl	6	bdl	bdl	bdl	bdl	bdl	bdl	bdl	15	2	**9**
AG1304-	01	Fluid	15636	257	bdl	271	bdl	bdl	bdl	bdl	bdl	bdl	bdl	bdl	bdl	bdl	bdl	bdl	bdl	bdl	bdl	bdl	**-**
	03	Fluid	14252	260	bdl	243	3	13	1	9	bdl	bdl	bdl	bdl	bdl	bdl	bdl	bdl	bdl	bdl	5	bdl	**-**
	05	Fluid	9781	257	1	271	2	bdl	bdl	bdl	bdl	bdl	bdl	bdl	bdl	bdl	bdl	bdl	bdl	bdl	6	bdl	**-**
	10-1	Fluid	18450	257	32	201	62	226	33	144	48	bdl	38	4	14	1	2	bdl	bdl	bdl	186	8	**23**
	10-2	Fluid	19026	257	19	227	41	141	21	100	40	bdl	23	4	10	1	bdl	bdl	bdl	bdl	134	10	**14**
AG1305-	02	Fluid	15961	241	bdl	224	bdl	bdl	bdl	bdl	bdl	bdl	bdl	bdl	bdl	bdl	bdl	bdl	bdl	bdl	bdl	bdl	**-**
	10	Fluid	15820	241	bdl	226	bdl	5	bdl	bdl	bdl	bdl	bdl	bdl	bdl	bdl	bdl	bdl	bdl	bdl	4	bdl	**-**
	13	Fluid	17813	241	bdl	228	bdl	bdl	bdl	bdl	bdl	bdl	bdl	bdl	bdl	bdl	bdl	bdl	bdl	bdl	bdl	bdl	**-**

bdl: below detection limit; na: non analized

Trace element concentrations have been determined by laser ablation inductively coupled plasma mass spectrometry (LA-ICP-MS) using Rb-Cs tracer in the experimental solution (~ 200-250 ppm) as internal standard. Results of quantifications of trace elements in the fluid (Table 7) are also given in Figure 11 as trace element spectra normalized to chondrite (McDonough and Sun, 1995), together with mean concentrations in Mnz1 and Mnz2 determined by EPMA (Table 4).

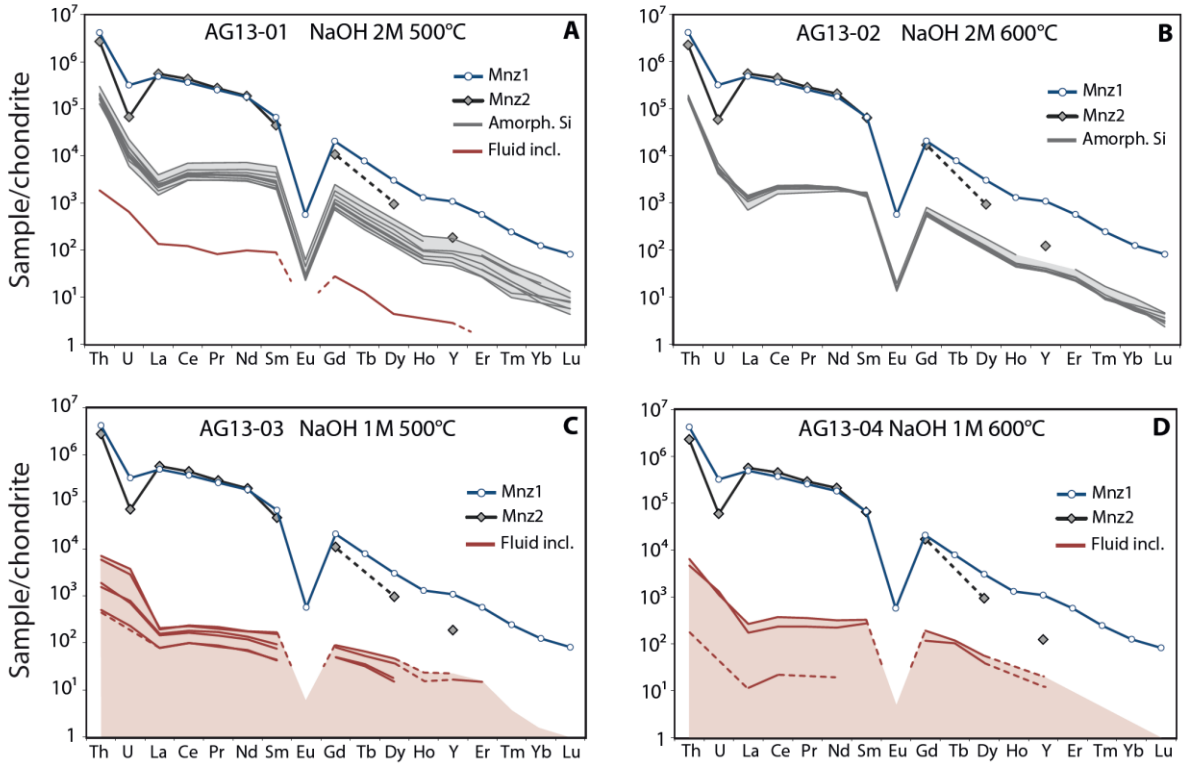

Figure 5-11 Trace element (REE+Y, Th and U) contents normalized to chrondite (McDonough and Sun, 1995) of fluid and solid (amorphous Si) inclusions in secondary quartz during experiments (A: AG13-01, B: AG13-02, C: AG13-03, D: AG1304), determined by LA-ICP-MS. Mnz1 (pristine monazite) and Mnz2 (secondary monazite) trace element spectrum corresponds to means of EPMA measurements (Table 4). Patterns (C-D) show the variability of trace element contents between the minimum and maximum values (Table 7). Dotted lines were used when a point was missing (below detection limit) between two successive points. See Table 3 for experimental conditions.

These two types of inclusions (solid and fluid) could be analysed in a single sample *AG13-01* (Fig. 11A) corresponding to 2M NaOH solution, 500°C, 200MPa for 21 days experiment (with redox buffered). Here, Si glass contains hundreds to thousands ppm of LREE+Th and few ppm of HREE+Y+U. Th/U ratios (Table 7) are comparable to those of pristine Mnz1 (78) between 50 and 100. A flattening of the spectra is observed for the LREE. The fluid inclusion analysed in the same sample contains tens of ppm of LREE+Th, few ppm of MREE+Y+U and HREE are below detection limits. The Th/U ratio is equal to 11 and the spectrum is also flattened for LREE. In the 2M NaOH solution, 600°C, 200MPA, redox buffered, for 14 days experiment (*AG13-02*, Fig. 11B), the amorphous Si glass gave comparable but slightly lower concentrations and spectra with the same shape. Th/U ratios are higher between 104 and 153. In the 1M NaOH solution, 500°C, 200MPA for 114 days experiment (*AG13-03*), only fluid inclusions could be analysed in neo-formed quartz grains although amorphous Si glass was also present in these experiments (Fig. 2,7,9). Here, trace elements contents ranges from concentrations below detection limit (Table 7) to tens to hundreds of ppm of LREE+Th and few ppm of HREE+Y+U. LREE spectra are also flattened compared to Mnz1 and Th/U ratios range from 7 to 13. In the 1M NaOH solution, 600°C, 200MPA for 114 days experiment, only three inclusions gave significant results, others were below detection limits. Only one glass inclusion has been observed, but it could not be analysed because of its depth (Supplementary material 5-8). Trace elements contents, as well as spectra shape, are comparable with those of the *AG13-03* experiments but slightly higher. Th/U ratios range from 14 to 23. In the 1M NaOH solution, 400°C, 200MPA for 114 days experiment (*AG13-05*) experiments, only fluid inclusions located in the quartz core (prematurely recrystallized) could be analysed and gave concentrations below the detection limits (Table 7). The late inclusions located in the overgrowth were unfortunately polluted by secondary precipitates.

5.5. Discussion

5.5.1. Fluid-monazite interaction process

It is now well-established that monazite has very low diffusion rates below high grade metamorphic conditions (Cherniak et al., 2004; Gardès et al., 2006; Cherniak and Pyle, 2008). By contrast, many experimental studies have addressed the stability of monazite in presence of fluids (Teufel and Heinrich, 1997; Seydoux-Guillaume et al., 2002; Harlov and Hetherington, 2010; Hetherington et al., 2010; Harlov et al., 2011; Williams et al., 2011; Budzyń et al., 2011; Budzyń et al., 2015; Shazia et al., 2015) and shown that monazite can be altered by a coupled dissolution-precipitation mechanism with element fractionation, even in low-grade metamorphic conditions. During coupled dissolution-precipitation mechanism, the presence of a supersaturated interfacial fluid will allow for the pseudomorphic replacement of a mineral phase by a same mineral with a different composition or by another mineral phase (Putnis, 2002; Putnis et al., 2009; Putnis and Austhreim, 2010). In the case of monazite, this reaction results to precipitation of a new monazite with a different composition (e.g. Poitrasson et al., 1996, 2000; Harlov et al., 2011; Seydoux-Guillaume et al., 2002, 2012) or a secondary mineral enriched in monazite elements (e.g. Poitrasson et al., 2000; Harlov et al., 2007; Berger et al., 2008; Hetherington and Harlov, 2008; Seydoux-Guillaume et al., 2012). The dissolution-precipitation continues as long as the supersaturated interface is connected to fluid via porosity. In the case of our replacement experiments, the experimental monazite products show a zoning with pristine (Mnz1) surrounded by a secondary monazite (Mnz2; Fig. 1B,C,D, 3 and 5) with a different composition (Table 4), associated with the development of porosity within both Mnz1 and Mnz2 domains (Fig. 1B, C,D, 3 and 9). Additionally, the investigation of ^{18}O incorporation (Fig. 6, 7) undoubtedly show that secondary monazite have crystallized from the doped fluid by a dissolution-precipitation process. In the ^{18}O Raman profile (Fig. 6) and Nano-Sims maps (Fig. 7), the chemical interface between Mnz1 and Mnz2 domains corresponds to interface between monazite containing ^{18}O and monazite containing only ^{16}O. A solid-state diffusion process is unlikely to

explain oxygen isotope exchange due the low diffusion rate determined by Cherniak et al. (2004) at our experimental conditions (below 600°C). Mechanisms responsible of monazite replacement in our experiments are schematized in the Figure 12 and correspond to NaOH experiments for 400 to 600°C (Table 3). The starting material (Fig. 12A) corresponds to monazite+quartz in NaOH solution. Then, the dissolution of monazite leads to the formation of a supersaturated interface (Fig. 12B). Finally, the final state (Fig. 12C) presents a monazite grain with replaced domains and apparent overgrowth domains discussed further. Arrows represent the direction of replacement and numbers (8 to 10) the schematic location of TEM images corresponding to Figure 8, 9 and 10.

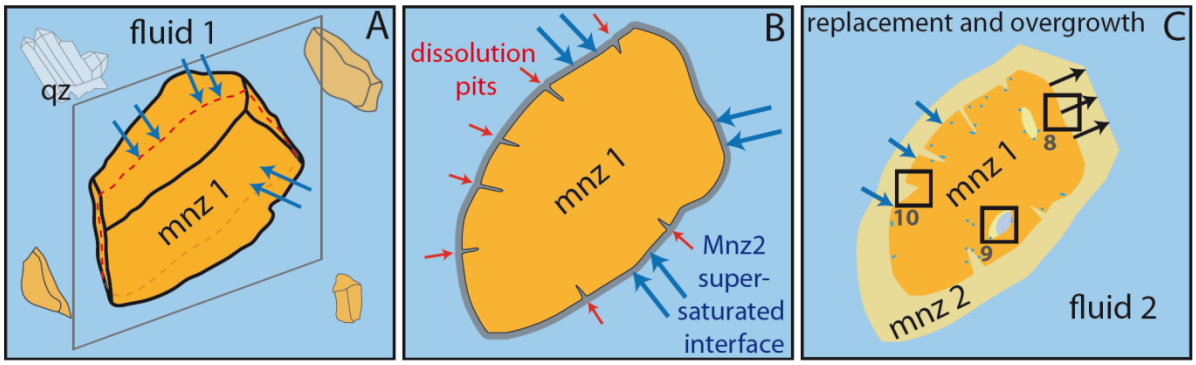

Figure 5-12 Schematic reaction of dissolution-precipitation during monazite-fluid hydrothermal experiments (inspired from Putnis and Austhreim, 2010) with 1M NaOH, between 400°C and 600°C, 200MPa. A: experiment start (whole grain); B: initiation of dissolution-precipitation process; C: final states (B-C: cross cut section of a monazite grain). The dark squares (C) and associated number corresponds to the schematic location of TEM images (Figure 8-9-10). mnz1: pristine monazite; mnz2: secondary monazite.

5.5.2. Decoupling of the dissolution-precipitation process

Our experimental results also show that dissolution-precipitation mechanism may be even more complex than the theoretical process described above. The experimental products indicate that the dissolution-precipitation process could be uncoupled in our experiments, particularly at highest experimental temperature (500 and 600°C). This decoupling results in the formation of neo-formed nano-sized monazite grains identified by TEM (Fig. 9B) located in amorphous Si-rich inclusions in porosity, and in overgrowth identifiable by SEM (enlargement Fig. 1C, D and Fig. 12) and investigate by TEM (Fig. 8) and Raman spectroscopy (Fig. 6). In the latter case, the well-shaped faces observed (enlargement Fig. 1, C) do not coincide with the crushed shape of pristine monazite (Fig. 1A). In these overgrowth zones, porosity is not observed. The TEM investigation does not show either nano-porosity (Fig. 8) and indicates an epitaxial crystallization on monazite supported by the electron diffraction patterns showing the consistency of Mnz1 and Mnz2 domains separated by a linear sharp interface. The Raman ^{18}O investigation brings new results that allow deciphering between overgrowth or replaced domains. In the investigated monazite grains (enlargement Fig. 1D), the calculated amounts of ^{18}O is zero within Mnz1 domain, increase at interface reaching 56% and is constant within Mnz2 domains at ~50%. The three points at the interface may represent mixing due to the spatial resolution of 1-1.5 µm (Hovelmann et al., 2010; Perdikouri et al., 2011), and the point at 56% is considered similar to those at ~50% within the error (±3.5%; Jonas et al., 2014), although ^{18}O content increase at the interface have already been reported (Hovelmann et al., 2010). Previous studies of ^{18}O tracer experiments reported ^{18}O content increase from rim to core of replaced mineral (Kasioptas et al., 2011; Jonas et al., 2014, respectively calcium carbonate to apatite and marble to calcium phosphate at 200°C). However, in these studies mineral replacement occurred in a non-equilibrated solution, i.e. with $[HPO_4^{2-}]aq$ that equilibrate with $[H_2{}^{18}O]$ during experiment with comparable rate of oxygen exchange and mineral replacement (Kasioptas et al., 2011).

In our experimental set-up, the ^{18}O content of the starting fluid will progressively decrease due to the releasing of ^{16}O related to Mnz1 and quartz dissolution (and reprecipitation). Similar decrease has been reported in the case of replacement of aragonite by calcite in ^{18}O doped fluid (Perdikouri et al., 2011) at 200°C due to limited isotope equilibration between the overall fluid, and interfacial fluid. Remarkably, the ^{18}O content is constant along Mnz2 domains from the interface with Mnz1 to the outermost rim (latest overgrowth). The Mnz2 domain could have crystallized from a fluid reservoir equilibrated with the overall experiment regarding oxygen isotope, rejecting the process of coupled dissolution-precipitation. This domain is interpreted as overgrowth as reported for rhombohedral-shaped calcite overgrowths in Perdikouri et al. (2011). The overgrowth formation seems to be more developed in our experimental products than in previous studies (Harlov et al., 2011) where authors estimated the coupled dissolution-precipitation process to be responsible of more than 95% of the total amounts of secondary monazite although their experimental products look similar to ours without porosity. However, epitaxial overgrowth and neoformed euhedral crystal formation has been reported in apatite replacement experiments (Kusebauch et al., 2015). In our experiments the amount and size such overgrowth domains increase with increasing temperature from 400 to 600°C and are observed together with porous replaced domains by coupled dissolution-precipitation on a same monazite grain (Fig. 1D and 12). Overgrowth domains were not identified in the cube monazite experiment (Fig. 3). The highest fluid-monazite ratio probably not allowed the supersaturation of the fluid necessary to precipitate monazite directly from the fluid, as the lower specific surface. The presence of overgrowth domains by uncoupled dissolution process in monazite has been reported in the natural example of deformation by dissolution precipitation creep and reprecipitation of synmetamorphic monazite (Wawrzneitz et al., 2012) or experimentally during monazite replacement at 1000°C in presence of $CaCl_2$ (Seydoux-Guillaume et al., 2002). In both case, the U-Th-Pb systematics was resetted during recrystallization of secondary domains contrary to domains reprecipitated by coupled dissolution-precipitation process of which ages can be perturbed (Wawrzneitz et al., 2010). In our experiments, the largest domains poor in

porosity are also more chemically and isotopically homogeneous, and the poorest in Pb (Fig. 5C, 6, 7B, Supplementary material 5-3, 5-5). It is crucial to be able to distinguish the overgrowth and the replaced domains in altered monazite to interpret the experimental results during dissolution-precipitation since these domains may present distinct chemical and isotopic compositions.

5.5.3. Key role of pores and nano-cracks in the progression of replacement

The textural investigation, including Nano-Sims maps (Fig. 5, 7) and TEM images (Fig. 9, 10) show a complex zoning pattern. These patchy zoning are reminiscent of those observed in both natural (e.g. Rasmussen and Muhling, 2007; Bosse et al., 2009; Janots et al., 2014) and experimental samples (Harlov and Hetherington, 2010; Hetherington et al., 2010; Williams et al., 2011; Budzyń et al., 2015), and attributed to fluid-induced low temperature alteration. At the lower experimental temperature (400°C), altered monazite show a strong mixing of compositional domains (Fig. 5A, 7A). The orientation of the elongate pores and Mnz2 domains suggest a preferential orientation of the dissolution-precipitation process as reported by Budzyń et al. (2015) during 250-350°C experimental monazite alteration. This mixture between domains decreases from 400°C to 600°C, with the diminution of porosity and the increase of Mnz2 domains. The mixture between Mnz1 and Mnz2 domains can be identified even at the nano-scale (Fig. 9) through the TEM investigation as breakthrough of recrystallization of Mnz2 domains toward Mnz1 domains. Such mixing textures imply an anisotropic or partial replacement of monazite characterized by a heterogeneous migration of the reaction front toward Mnz1 domains.

A major condition for coupled dissolution-precipitation process is the access of the reaction fluid to the mineral interface by porosity, fractures or grain boundaries (Ruiz-Agudo et al., 2014). Observations of porosity generation during replacement have been reported in many experimental and natural samples (e.g. Harlov et al., 2005; Putnis, 2009; Raufaste et al., 2011, Seydoux-Guillaume et al., 2012). The formation of porosity could

be attributed to molar volume and relative solubility differences of the reactive and the product mineral (Putnis, 2002; Pollock et al., 2011; Raufaste et al., 2011). In the case of significant molar volumes changes, the generated stresses induce fracturing in parent and/or product phase as reported during replacement of e.g. leucite by analcime (Putnis et al., 2007; Jamtveit et al., 2009), ilmenite by rutile (Janssen et al., 2010), aragonite by calcite (Perdikouri et al., 2011), scolecite by tobermorite (Dunkel and Putnis, 2014). Another example of fracturing occurs during the serpentinization processes (Plümper et al., 2012) and is attributed to stress generated from the growth and transformation of a metastable amorphous proto-serpentine phase in dissolution etch pits.

In our experiments, we reported for the first time a propagation of the reaction front (i.e. interface between Mnz1 and Mnz2 domains; Fig. 10A) by nano-fracturing (Fig. 10B, C) and pores propagation. The TEM images (Fig. 10) from FIB foils prepared at the non-linear interface between Mnz1 and Mnz2 domains from experiments at 500°C (*AG13-03*; Table 3) indicates a progress of recrystallization driven by fractures formation. The first group of curved nano-cracks (Fig. 10B, C) initiates at the interface spreads toward the Mnz1 domain and resorbs in recrystallized Mnz2 domains. This mechanism occurs over a horizontal distance of 100 nm which does not allow its detection by SEM. The longer fractures indicates the same process, but this time over a horizontal distance of 1 μm, leading to formation of preferential paths of dissolution-precipitation. Such nano-cracks located at the reaction interface have never been reported and hypothesis on their formation belong highly speculative and needs further investigation. During monazite-monazite replacement, or more generally during the replacement of a mineral by the same mineral, the molar volume is not sufficiently significant to induce fracturing of parent and/or product mineral. STEM and TEM images (Fig. 10) show that nano-cracks are filled only by hydrothermal fluid during experiments. No amorphous Si-rich phase have been identified in fractures and the mechanism of fracture propagating by growth and transformation of an amorphous phase observed and modelled by Plumper et al. (2012) could also be excluded. However, the fracture propagation in replaced monazite needs stress to initiate and develop toward parent monazite. The fracturing takes place in an

environment without external forces and the stresses driving them can only come from monazite itself. The newly formed Mnz2 crystallizes without internal strain and could not explain the fracturing. However, the former Mnz1 has internal stresses due to defects of lattice disorientation (Seydoux-Guillaume et al., 2002b; Seydoux-Guillaume et al., 2004). These defects are caused by radiation damage during radioactive decay, and are all the more important that the content of actinides is high and the age old. The radiation damages result in changes of monazite properties, as hardness diminution, amorphisation or swelling (e.g. Picot et al., 2008; Deschanels et al., 2014). The monazite used in our experiments contains ~13 wt.% ThO_2, are aged of 555 ± 2 Ma and thus have suffered radiation damage (Madagascar monazite in Seydoux-Guillaume et al., 2004) that can be seen in TEM images (Fig. 8, 9 and 10). The formation of the secondary monazite, in a sufficient volume, acts as a shell on the former monazite which would release its internal stresses by fracturing as we can see at 500°C. With the progress of the reaction front toward Mnz1, the localization of defects may initiate the generation of the longest fractures driving the reaction front. At the lower temperature (400°C), the limited volume of replaced Mnz2 may not be sufficient to coerce Mnz1 and allow stresses dissipation by fracturing. However, the analytical conditions (BF-TEM, Fig. 10D, E) were different to those with observed fracturing at 500°C (ADF-TEM, Fig. 10A-C) and the presence of nano-cracks at the interface between Mnz1 and Mnz2 domains could not be excluded for this sample, as well as for the 600°C experiment.

In the experiments at 400°C, 500°C and 600°C, the porosity is always related to Mnz2 domain precipitation (Fig. 9) and thus plays an important role for the dissolution-precipitation propagation. Pores are more elongated at 400°C (Fig. 1B) allowing the replacement process progression along a non-linear interface (Fig. 10 D, E). At 500°C, the mechanism is similar around pores (Fig. 9B) and nano-cracks appear when the interface between Mnz1 and Mnz2 is more linear or when the Mnz2 volume is sufficient to coerce Mnz1 domain and induce fracturing. The link between the porosity formation and the fractures propagation is not clearly constrained but the presence of cracks initiating in a small elongated pore at 400°C (Fig. 10E), and following the direction of

replacement could indicate a coupling between these two mechanism during the process of dissolution-precipitation. These preliminary results are promising and a new experimental approach coupled with TEM analyses is needed to develop an understanding of this mechanism of propagation of the reaction front with coupled nano-pores and cracks. Numerical modelling of stresses linked to radiation damages and/or experimental replacement of annealed and old natural monazite, are also likely to be most applicable for this purpose.

5.5.4. Experimental parameters control on monazite replacement

The influence of experimental hydrothermal conditions on monazite replacement has been investigated through different parameters in this study: fluid composition, temperature, duration, and grain shape (Table 3). In experiments with H_2O or NaCl (10 wt. %), no monazite replacement was observed from 300 to 600°C as reported in previous studies (Seydoux-Guillaume et al., 2002; Richard et al., 2015). The only textural changes in these experiments revealed by optical microscopy is the increasing discoloration of grains with increasing temperature from yellowish orange to whitish grey between 300 and 600°C, as reported by previous studies (Teufel and Heinrich, 1997; Seydoux-Guillaume et al., 2002). Here, only the experiments with NaOH fluid leaded to monazite replacement (Fig. 1B,C,D and 3) similarly to previous studies that observed experimental monazite replacement in alkali conditions (Hetherington et al., 2010; Harlov et al., 2010, 2011; Williams et al., 2011; Budzyń et al., 2011, 2015). Contrary to others experiments in alkali conditions at low temperature (Budzyń et al., 2015), no monazite replacement was observed at 300°C. However, the precipitation of Th-silicates (Fig. 2A) indicates dissolution of the primary monazite, although this was not identifiable in cross-section (Fig. 1A). This is certainly due to the fact that smaller grains or edges of the larger reacted first. Furthermore, Budzyń et al. (2015) experimental parameters are different using $Na_2Si_2O_5$+H_2O fluid certainly more reactive for monazite (e.g. Hetherington et al., 2010), and an assemblages of monazite + K-feldspar ± albite ± labradorite + muscovite +

biotite + SiO2 + CaF2 as starting solids. The absence of monazite replacement at 300°C with NaOH fluid could be attributed to the reaction kinetics too slow in our conditions, apparently limited by the very slow growth rate of monazite at low P-T conditions (Ayers al., 1999). In experiments performed with monazite cubes 1 mm-sized (Fig. 3), monazite replacement was similar to 50-100 µm-sized grains (Fig. 3A, B). The thickness of the reaction zone is slightly greater in the case of cubes compared to grains for the same temperature, even for a shorter duration. This could be explained by the higher fluid/solid ratio, respectively 11 and 13 at 500 and 600°C and ~5 with grain experiments. Although the temperature changes (between 400 and 600°C) have a limited effect on the Mnz2 composition variations, they affect the texture of altered monazites. With decreasing temperature, the Mnz2 domains are smaller and orientated within Mnz1 domain leading to a more intimate mixing indistinguishable at the micro-scale (SEM, EPMA) and potentially affecting any analytical technics at this scale.

5.5.5. Fluid-monazite elemental partitioning during hydrothermal alteration

Due to the complexity of the experimental system, the duration of the experiments and the kinetics unconstrained (timing of monazite overgrowth and LREE/Th-silicates precipitation), the results of fluid inclusions LA-ICP-MS measurements do not represents solubility measurement. The fluid composition could not remain constant if the fluid is not equilibrated with monazite and secondary minerals precipitating during experiments but elements partitioning between monazite and fluid can be analysed to investigate trace element fractioning. Moreover, we showed that the pre-fractured quartz recrystallization is highly dependent of fluid composition and temperature. Quartz recrystallization is much more effective in high temperature (500-600°C) and alkali conditions than at low temperature (300-400°C) or in NaCl brine solution. Another problem reported from our experiments is that secondary minerals as LREE or Th-silicates could precipitate in cracks or surface of the quartz crystals polluting and making the sample unusable for LA-

ICP-MS measurements. Then, the presence of an amorphous Si-rich phase identified in the monazite surface (Fig. 2D and 3A, B), in the porosity (Fig. 9) and as amorphous Si inclusions (Supplementary material 5-8) together with the fluid (mostly $NaOH+H_2O$) indicates the presence of two different liquid phases during experiment. At the beginning of the experiments, the fracture healing results in fluid inclusions entrapment in the quartz core. Then, the fluid enriches in Si and become saturated in Si until demixing and coexistence of two fluids equilibrated (liquid + melt). In our high alkaline conditions, the supersaturation of SiO_2 of the primary fluid may lead to formation of a Si melt immiscible with the aqueous fluid although it never been reported in other monazite experiments (Hetherington et al., 2010; Harlov et al., 2011). However, our experimental conditions are characterized by higher amounts of SiO_2, highly soluble in high pH conditions (Crerar and Anderson, 1971). These two coexisting phase are reported in nature and corresponds to the occurrence of immiscible silicate melts and fluid at the magmatic-hydrothermal transition conditions (Kamenetsky and Kamenetsky, 2010).

Despite difficulties encountered to obtain fluid inclusions results, this study brings new constraints on partitioning between fluid and monazite during replacement reaction in alkali conditions at 500 and 600°C. The increase of LREE/HREE+Y ratio of low-temperature metamorphic monazite is reported in several studies of natural samples (e.g. Janots et al., 2008; Hetherington and Harlov, 2008; Rasmussen and Muhling, 2009; Seydoux-Guillaume et al., 2012; Allaz et al., 2013) and also observed in our dataset (Fig. 4A). The increase of Th/U ratios during monazite replacement has been reported in natural samples (e.g. Poitrasson et al., 2000; Hetherington and Harlov, 2008; Janots et al., 2012). It is also observed in our experimental samples with Th/U ratios at ~150-200 in replaced Mnz2 higher than the ratio of the pristine Mnz1 at ~80. The increase of LREE/HREE+Y and Th/U ratios in replaced Mnz2 results in lower LREE/HREE+Y and Th/U in the fluid. This indicates a higher mobility of HREE+Y and U than LREE+Th during monazite alteration and replacement. In parallel, the element concentrations of the amorphous Si-rich inclusions are more suggestive for a stoichiometric dissolution of the monazite despite a depletion of LREE. The presence of Mnz2 domains or LREE-rich

secondary minerals could explain the depletion of LREE of this phase. This crystallization of LREE-silicates (britholite), as already been reported during monazite replacement experiments (Harlov et al., 2011). Due to the limited number of analyses, we cannot really observe predominant role of the temperature or oxidizing conditions (experiments *AG13-01* and *AG13-02*) on the REE, Th and U composition in the reactive fluid.

5.5.6. Implications

5.5.6.1. Monazite thermometry

Within errors, the temperature does not seem to control significantly the Mnz2 composition determined by EPMA (Fig. 4, Table 4). It is just notable that only the 600°C Mnz2 show analyses without almost no Pb, U, and HREE+Y. Taking into account the textural results indicating nano-mixing of Mnz1 and Mnz2 domains during replacement, it is clearly evident that most of analyses could represent mixing analyses between two poles (Mnz1 and Mnz2). This is especially true when the volume of reprecipitated Mnz2 is small at lower temperature (400 and 500°C). In these conditions, the Y+HREE thermometry (Gratz and Heinrich, 1997, 1998; Heinrich et al., 1997; Pyle et al., 2001; Seydoux-Guillaume et al., 2002b) could not be used as the spatial resolution of EPMA does not resolve properly the distinct domains.

Regarding the ^{18}O monazite-quartz thermometry (Breecker and Sharp, 2007), the same problem arises due to the limited equilibrated volume of Mnz2. Moreover, it is possible that there is a decoupling between monazite and quartz recrystallization kinetics. This decoupling is underlined by the presence of inclusions free of monazite-elements in already recrystallized quartz (Table 7) and the presence of REE-rich solids precipitated during quartz growth (Supplementary material 5-8). Therefore, it would have been useless to try to interpret oxygen partitioning between monazite and quartz in this apparently complex system.

5.5.6.2. Monazite dating

The Mnz2 is assuming not incorporate Pb (Williams et al., 2011) and no Pb-rich nano-domains (Seydoux-Guillaume et al., 2003) have been observed during the TEM study (Fig.8, 9 and 10). Moreover, previous studies (Hetherington et al., 2010; Harlov et al., 2010, 2011; Williams et al., 2011) have shown that during replacement using alkali-bearing fluids, Th is preferentially reincorporated by the huttonite substitution (Van Emden et al., 1997): $Si^{4+} + Th^{4+}(U^{4+}) = REE^{3+} + P^{5+}$ than the brabantite substitution: $Ca^{2+} + Th^{4+}(U^{4+}) = 2REE^{3+}$. Thus, the Mnz2 pole should contain really low amounts of both Pb and Ca. This assumption is supported by the low Pb and Ca contents measured in the largest homogeneous Mnz2 recrystallized at 600°C (Fig. 1D, Table 4). Considering PbO vs Cao (wt.%) contents (Fig. 4B) it is clear that there is much more chance to analyze mixing domains with decreasing temperature. The mixing of Mnz1 and Mnz2 domains during replacement identified in the study has very huge implications for geochronology as Pb could be measured in apparent Mnz2 domains, actually an intimate mixing of Mnz1 and Mnz2 domains. Without isotopical (e.g. LA-ICP-MS) or nano-textural (TEM) control, the chemical U-Th-Pb age could be meaningless due to the scale difference between micro-analyses and nano-domains.

5.5.6.3. Matrix for nuclear waste

The effect of radiation damages accumulation and their effects on monazite properties is a key parameter to assess the durability of monazite that could be used to storage for nuclear waste (e.g. Weber et al., 1998). The presence of actinides results in the formation of defects which may cause (or contribute) nano-cracks during dissolution-precipitation processes associated to porosity formation. The reprecipitation during fluid-monazite interaction also leads to the actinides mobility, highly problematic in the case of nuclear waste storage. This fracturing mechanism, observed in our experimental products,

favoring actinides mobility obviously need further investigation, but could have crucial implications if confirmed, as it occurs at a relative low temperature.

5.6. Summary/Conclusions

Interaction of monazite and fluid via dissolution precipitation process in high-alkali conditions may be associated with uncoupled dissolution-precipitation and it is important to consider this mechanism for the interpretation of the experimental results. Indeed, the mechanism (overgrowth vs replacement) impact the chemical or isotopic composition of the secondary monazite domain involved.

A new mechanism of propagation of the reaction front aided by porosity development and nano-fracturing during monazite replacement has been identified. The formation of cracks would be aided by the distortion of monazite lattice due to radioactive decay. The concentration and propagation of these fractures leads to anisotropic replacement of the primary monazite and mixing with replaced domains. Further investigations are needed but it provides some interesting directions for the understanding of radioactive mineral replacement that have crucial implications for nuclear waste storage.

The mechanism of monazite replacement is highly dependent of temperature and fluid composition. However, experimental conditions between 300 and 600°C do not seem to play a prominent role on replaced monazite composition, mostly influenced by the parent monazite composition.

Fluid composition during experiments is highly buffered by monazite or secondary mineral reprecipitation composition. However, the higher mobility of HREE+Y, U compared to LREE, Th during hydrothermal/metamorphic alteration has been confirmed here. Monazites replaced by a dissolution-precipitation process and depleted in these elements, are a good tracer of fluid chemistry evolution in hydrothermal or metamorphic context.

The studied hydrothermal alteration and induced mixing mechanism of unreacted and replace monazite may explain the formation of skeletal or patchy textures of natural low-temperature altered samples. Its role could be important in monazite geochronology pitfalls that occurred in naturally fluid-mediated altered monazite studies.

Acknowledgments

We thank M.C. Boiron for fluid inclusions analysis, F. Brunet for its help with the experiments, M. Lanson for its help in the chemistry laboratory and N. Findling for his assistance with the SEM. This project is funded by the ANR-JC grant (Mona, 2012).

6. INFLUENCE DE LA DISSOLUTION PRÉCIPITATION SUR LE CHRONOMÈTRE U-Th-Pb DE LA MONAZITE

Nano-scale evidence of partial replacement in altered monazite caused U-Th-Pb age disturbance

(Article en voie de soumission à Geology)

A. GRAND'HOMME[1], E. JANOTS[1], A.M. SEYDOUX-GUILLAUME[2], D. GUILLAUME[2], V. BOSSE[3]

[1]ISTerre, Univ. Grenoble Alpes, Grenoble, France (alexis.grandhomme@ujf-grenoble.fr)
[2]LMV, Département de Géologie, Université Jean Monnet, Saint-Étienne, 42023, Saint-Etienne, France
[3]LMV, Clermont Université, Université Blaise Pascal, BP 10448, 63000 Clermont-Ferrand, France

Keywords Monazite, Dissolution-precipitation, Experimental petrology, Geochronology

Note: To facilitate reading, analytical conditions have been added to the text (italics), together with Table DR1 and DR2
Figure X corresponds to Figure 6-X and Table or Figure DRX corresponds to Annexe 6-X

Abstract

Hydrothermal alteration experiments of natural monazite crystals (Manangotry) under alkali conditions at 400, 500 and 600°C, 200MPa, were conducted to clarify the Pb uptake mechanism in replaced monazite. Experimental products show typical replacement texture: a pristine monazite (Mnz1) is surrounded by a monazite with a different composition. In the altered domains, in-situ isotopic and chemical U-Th-Pb dating yields intermediate ages between pristine monazite (555 Ma) and complete experimental resetting (0 Ma). Incomplete resetting is due to to the systematic presence of Pb, whose concentration decreases from 400°C to 600°C. Transmission electron microscope images revealed for an incomplete Mnz1 replacement by a secondary monazite (Mnz2) within the altered domain. At 400 °C, the Mnz2 component (i.e. the ratio of Mnz2 compared to Mnz1) within the altered domain is minor and restricted to a channelized network. With increasing temperature, the Mnz2 component becomes more important. From this partial replacement results the "partial resetting" of U-Th-Pb systems due to the unavoidable mixture of different proportion of Mnz1 and Mnz2 within the altered domains analyzed isotopically or chemically. It may be therefore challenging and risky to date replaced domains, even more when age datasets are determined with no reliable micro- and nano-structural documentations or in the case of potential multistage fluid circulations or thermal events. The highest Pb concentrations (due to higher Mnz1 component) measured in experimental products altered at 400°C suggest that a partial replacement mechanism may be especially active for low geological temperature conditions (diagenetic, hydrothermal and low-grade metamorphism).

6.1. Introduction

Age interpretation is challenging in geological environments that are inherently reactive due to changing equilibrium conditions. Under evolving conditions (temperature, pressure, fluid, stress), the isotopic clock of any geochronometer can be disturbed by initial inheritance and/or disequilibrium within the decay series (e.g. Corfu, 2013), as well as by post-crystallization modifications by volume diffusion, replacement or deformation. With three decay series, in-situ U-Th-Pb dating is one of the most powerful technic to determine reliable crystallization age and evaluate for possible age disturbance that may have affected a chronometer. Amongst the U-Th-Pb chronometers, monazite is an ubiquitous accessory mineral that is the main host of rare earth element (REE), Th and U in the continental crust (Bea, 1996). In most rocks, monazite grains are zoned and the different compositional domains attest of successive crystallization episodes under distinct equilibration conditions (growth and/or replacement). In monazite, isotopic/elementary resetting by diffusion is negligible up to high-grade metamorphism (Cherniak et al., 2004; Gardés et al., 2006) and in-situ U-Th-Pb monazite dating is successfully used to date multistage crystallizations. In comparison to other U-Th-Pb chronometers (e.g. zircon, Hietpas et al., 2010), monazite is reactive in presence of fluid at low temperature and is certainly one of the rare successful tool to date fluid-assisted crystallization in diagenetic (e.g. Evan and Zalaziewicz, 1996), hydrothermal (e.g. Janots et al., 2012), and low-grade metamorphic conditions (e.g. Rasmussen et al., 2001; Bosse et al., 2009). Monazite compositional domains rarely exceed 10's μm in length, and dating of the micrometric domains requires sometimes a spatial resolution that is only reached by chemical dating with electron microprobe (Montel et al., 1996). This method consists in determining one age from the chemical U, Th and Pb concentrations in monazite, assuming that Pb is purely radiogenic (no initial Pb incorporated) and the system remained close after crystallization (e.g. Montel et al. 1996). While this is commonly the case, this assumption has been recently weaken by natural evidences of incorporation or preservation of significant amounts of Pb in secondary monazite

domains, leading to geologically meaningless isotopic and chemical U-Th-Pb ages (e.g. Seydoux-Guillaume et al., 2012; Didier et al., 2013). In these studies, secondary monazite growth is attributed to late-stage hydrothermal alteration under geologically low temperature (typically below 400°C). Experimentally, it is well known that monazite zoning can be reproduced by dissolution-precipitation processes (e.g. Seydoux-Guillaume et al., 2002a; Harlov et al., 2011). However, while Pb was repeatedly measured in some experimentally reacted domains (e.g. Budzyń et al., 2015), it is controversial whether Pb sequestration has a great impact for reliable dating of replaced rim (Williams et al., 2011; Shazia et al., 2015).

To understand Pb behavior during monazite-fluid interactions and the role of temperature, we conducted hydrothermal experiments of monazite at 400, 500 and 600°C, under alkali conditions favoring replacement by interfacially coupled dissolution-crystallization (e.g. Hetherington et al., 2010; Harlov et al., 2011). Based on a comprehensive approach using micro- to nanoscale structural characterization associated with isotopic and chemical U-Th-Pb dating of experimental products, Pb uptake during monazite replacement and its implication on age interpretations are discussed.

6.2. Experimental and analyical procedures

Lead behavior has been investigated during mineral replacement of natural Manangotry monazite standard (555 ± 2 Ma, ID-TIMS, U-Pb, upper intercept; Paquette and Tiepolo, 2007), from the Anosyan granite-charnockite in the Androyan Complex of Southern Madagascar (Paquette et al., 1994). This pore and inclusion-free monazite is chemically homogeneous (Montel et al., 1996; Didier et al., 2013) with high Th content (~12 wt% ThO_2). Experimentally, 50 to 100 µm-sized grains of monazite are introduced with quartz stick (~2 mm wide and 8 mm long, prepared from inclusion-free pure natural crystals sampled at Kerguelen Island) and alkali fluid (NaOH 1M or 2M) in a 3 mm-wide and 25 mm-long Au capsule. The Au capsules were sealed using an electric arc under argon flow then placed in cold-seal pressure vessel at 400, 500 and 600°C, 200 MPa for duration up

to 114 days (see Table DR1 in the Data Repository for details of experimental conditions). After experimental runs, autoclaves were quenched using compressed air for a few minutes. Experimental solid products were washed in pure-water, dried, mounted in epoxy and then polished. The detailed analytical procedures are given in details in the Data Repository.

Table DR1 Experimental conditions

Run	T (°C)	P (Mpa)	Duration (days)	Mnz	SiO_2	H_2O	NaOH 1M	NaOH 2M
12-02	600	200	40	31.0	52.1	149.1		
13-06	300	200	114	29.9	112.1		142.4	
13-05	400	200	114	30.6	65.5		125.4	
12-07	500	200	29	28.4	60.7		179.4	
13-03	500	200	114	30.8	63.2		142.7	
12-08	600	200	21	30.1	58.3		166.9	
12-04	600	200	40	21.1	60.1		103.1	
13-04	600	200	114	29.6	79.8		141.7	
13-01	500	200	21	30.7	77.0			163.6
13-02	600	200	14	28.7	106.9			175.9

Solids and fluids in mg

Details for EPMA analyzes

All electron probe micro-analyzer (EPMA) analyses were undertaken at ISTerre laboratory (Grenoble, France) on a Jeol JXA-8230. First, high contrast backscattered electron of grain (mounted in epoxy) cross section were realized to identify recrystallized areas with a distinct chemical composition (Mnz2) from pristine monazite (Mnz1). Quantitative analyses (Table DR2) were carried using an accelerating voltage of 25 kV and a beam current of 50 nA. using following X-ray lines: SiKα, UMβ, ThMα, CaKα, PKα, YLα, DyLβ, GdLβ, SmLβ, PrLβ, NdLα, CeLα, LaLα, PbMβ. Natural minerals and synthetic glasses standards, including Smithsonian REE phosphates, were used for calibration. A calibrated overlap correction of 0.0064 was applied for peak interference of ThMγ on Umβ. U, Th and Pb contents were measured with counting times (peak plus background) of 400 s. For each analysis, a chemical ages (Table DR4) was calculated (Montel et al., 1996) from quantitative analyses, propagating errors through the age equation to obtain ages at 2σ level. Average ages and diagram (Fig. 3B) were obtained using weighted regression procedure using Isoplot 4.15 (Ludwig, 2001).

Details for LA-ICPMS analyzes

U-Th-Pb geochronology of monazite was performed also by laser ablation inductively coupled plasma spectrometry (LA-ICPMS) at the Laboratoire Magmas et Volcans (LMV), Clermont-Ferrand (France). Analytical procedures for monazite dating are reported in detail in Didier et al. (2013) and Didier et al. (2014). Errors are given at the 2σ level and the spot size is 7 µm (Table DR3). Monazite data are corrected for U–Pb and Th–Pb fractionation occurring during laser sampling and for instrumental mass discrimination (mass bias) by standard bracketing with repeated measurements of the C83-32 monazite (Corfu, 1988; Didier, 2013). Data reduction was carried out using the GLITTER® software package (van Achterbergh et al. 2001; Jackson et al. 2004). Calculated ratios were exported and age diagrams were generated using the Isoplot software package by Ludwig (2001). The concentrations of U-Th-Pb were calibrated with respect to the contents of the C83-32 monazite (Corfu, 1988; Didier et al., 2013).

Details for TEM

The TEM foils were prepared with the HELIOS 600i FIB Dual Beam instrument at LAAS-CNRS RENATECH network. TEM studies were carried out with the JEOL 2100F TEM at the Raimond Castaing center (Toulouse, France), operating at 200 KeV, equipped with an Energy Dispersive Spectrometer (EDS), and a High-Angle Annular Dark Field (HAADF) detector used in the Scanning Transmission Electron Microscopy (STEM) mode.

6.3. Results

6.3.1. Compositions and textures

In backscattered electron (BSE) images, cross-sections through experimental products reveal that pristine monazite is efficiently altered in all experiments from 400 to 600°C under alkali conditions (Fig. 1A-C). Experimental products show a replacement texture with pristine monazite (Mnz1) surrounded by a rim of secondary monazite with a different composition (EPM analyses reported in Table DR2 in the Data Repository). Secondary monazite is significantly depleted in U, Th and Pb (and Ca, Y and HREE) but enriched in LREE and Si compared with Mnz1 (Table DR2 in the Data Repository). Secondary domains appear not only in the rim but also in Mnz1 intra-grain domains, commonly in association with porosity (Fig. 1A-B). Experimental products show extensive development of micrometric pores and inclusions in both primary and secondary domains. From 400 to 600°C, porosity development decreases together with the increase of replacement volume. At 400°C and 500°C, micrometric pores (and inclusions) occur within both in pristine and secondary domains and can yield a skeletal aspect to the experimental product (Fig. 1A-B). At 600 °C, pores are preferentially located at the reaction front and within Mnz1 (Fig. 1C).

Table DR2 Mean monazite compositions (wt.%)

Run	Comment	n	T (°C)	P (MPa)	duration (days)	SiO_2	P_2O_5	CaO	Y_2O_3	La_2O_3	Ce_2O_3	Pr_2O_3	Nd_2O_3	Sm_2O_3	Gd_2O_3	Dy_2O_3	PbO	ThO_2	UO_2	Total
Mnz1	*Starting material mnz1	51	-	-	-	2.36	27.12	0.85	0.16	14.14	28.84	2.87	9.88	0.94	0.39	0.07	0.32	12.92	0.16	101.02
	SD					*0.22*	*0.51*	*0.15*	*0.03*	*0.34*	*0.36*	*0.04*	*0.15*	*0.07*	*0.04*	*0.01*	*0.01*	*0.51*	*0.02*	
13-05	secondary mnz2	17	400	200	114	2.70	27.06	0.29	0.04	15.65	31.84	3.16	10.91	1.00	0.35	0.03	0.07	7.88	0.05	101.05
	SD					*0.70*	*0.66*	*0.20*	*0.04*	*0.40*	*0.84*	*0.08*	*0.40*	*0.07*	*0.04*	*0.02*	*0.05*	*1.78*	*0.03*	
12-07	secondary mnz2	2	500	200	29	3.40	29.56	0.15	0.03	15.57	31.17	2.98	10.16	0.79	0.22	0.03	0.05	8.10	0.06	102.28
	SD					*0.57*	*0.54*	*0.02*	*0.02*	*0.15*	*0.55*	*0.14*	*0.42*	*0.05*	*0.03*	*0.02*	*0.02*	*1.22*	*0.03*	
13-03	secondary mnz2	16	500	200	114	2.97	26.79	0.31	0.04	15.65	31.12	3.03	10.13	0.83	0.29	0.03	0.09	9.72	0.06	101.06
	SD					*0.67*	*0.61*	*0.14*	*0.04*	*0.62*	*1.14*	*0.11*	*0.42*	*0.10*	*0.06*	*0.02*	*0.06*	*2.01*	*0.03*	
12-08	secondary mnz2	1	600	200	21	2.81	27.92	0.29	0.02	15.29	30.60	2.97	10.10	0.76	0.23	0.04	0.07	9.62	0.08	100.80
12-04	secondary mnz2	2	600	200	40	2.43	26.58	0.22	0.02	14.85	30.89	3.06	10.89	1.14	0.41	0.04	0.02	9.12	0.10	99.76
	SD					*0.11*	*0.32*	*0.01*	*0.02*	*0.14*	*0.12*	*0.03*	*0.11*	*0.06*	*0.02*	*0.01*	*0.01*	*0.41*	*0.02*	
13-04	secondary mnz2	14	600	200	114	1.76	27.32	0.11	0.02	15.29	32.62	3.20	11.83	1.32	0.48	0.02	0.02	6.49	0.03	100.51
	SD					*0.71*	*1.30*	*0.06*	*0.03*	*1.52*	*1.42*	*0.37*	*0.98*	*0.39*	*0.19*	*0.01*	*0.01*	*2.06*	*0.01*	

*Mean of 51 analyzes in unaltered zones of all experiments listed in Table1.
SD: standard deviation

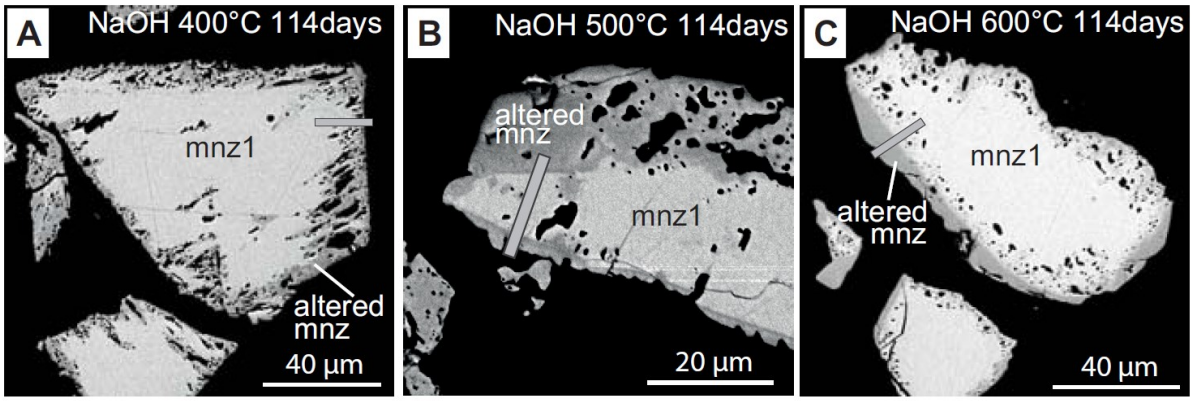

Figure 6-1 A: Backscattered electron image of reacted monazite grain at 400°C (A), 500°C (B) and 600°C(C), 2kbar, 114 days with NaOH (1M) mounted in epoxy and location of the FIB cut foil (grey rectangle). Mnz1—unreacted monazite; Mnz2—reprecipitated monazite

6.3.2. Geochronology

In situ U-Pb and Th-Pb isotopic dating were carried out by Laser ablation-inductively coupled plasma mass spectrometer (LA-ICP-MS), using monazite protocol reported in Didier et al. (2013). LA-ICPMS measurements have been performed within experimental products altered at 400, 500 and 600°C (Fig. 2 and Table DR3 in the Data Repository). Two analyses in the pristine monazite domain gave $^{208}Pb/^{232}Th$ ages of 538±17 Ma and 532±17 Ma. $^{208}Pb/^{232}Th$ ages in altered domains scatter from 548 ± 17 Ma to 52 ± 2 Ma, whereas $^{206}Pb/^{238}U$ ages are between 606 ±21 to 312 ± 13Ma. In the Tera Wasserburg diagram, concordant and discordant analyses define a trend parallel to the $^{238}U/^{206}Pb$ axis with a nearly constant $^{207}Pb/^{206}Pb$ ratio, excluding a common Pb incorporation in the altered domains (Fig. 2A). The $^{206}Pb/^{238}U$ vs $^{208}Pb/^{232}Th$ diagram (Fig. 2B) shows that both $^{238}U/^{206}Pb$ and $^{208}Pb/^{232}Th$ isotopic systems were partially reset although rejuvenation is lower for the $^{206}Pb/^{238}U$ ages than for the $^{208}Pb/^{232}Th$ ages. In the overall dataset, only one analysis yields one $^{206}Pb/^{238}U$ age at 605 ± 21 Ma older than the primary age (Fig. 2) and a $^{208}Pb/^{232}Th$ age at 548 ± 17 Ma. There is no apparent relation between temperature of experiments and isotopic ages obtained using both U-Pb and Th-Pb systems.

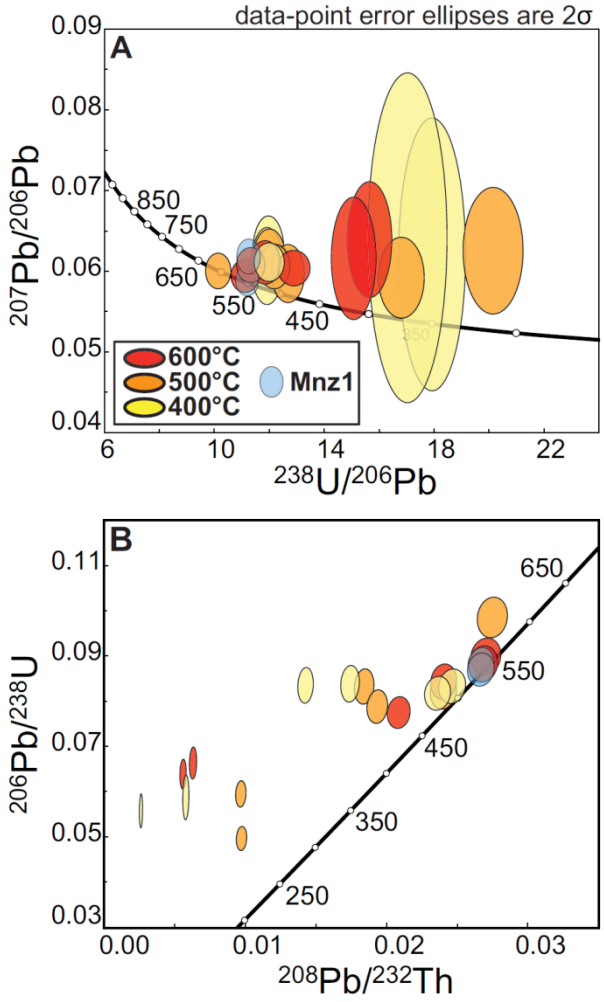

Figure 6-2 Terra-Wasserburg (A) and $^{206}Pb/^{238}U$ vs $^{208}Pb/^{232}Th$ (B) diagrams of U-Th-Pb laser ablation inductively coupled plasma spectrometry (LA-ICPMS) geochronology results from experiments at 400, 500 and 600°C. Analyses correspond to mixing domains between unreacted (Mnz1) and reprecipitated monazite (Mnz2)

Chemical U-Th-Pb ages in pristine and altered domains have been calculated from quantitative electron probe microanalyses (EPMA) based on slightly modified protocol of Scherrer et al. (2000). Unaltered Mnz1 domains yielded age of 554 ± 11 Ma (MSWD=2.0, n=51) equivalent to that determined by ID-TIMS (555±2 Ma). Lead concentrations in altered domains are systematically above detection limit (around 55 ppm) except for one analysis from a 600°C experiment (Table DR4 in the Data Repository). In the altered domains, calculated ages from runs at 400, 500 and 600°C spread in the range of 77-487, 40-440 and 0-164 Ma respectively (Fig. 3A). Weighted average ages (Fig. 3B) decrease with increasing temperature from 198 ± 61 (400°C), 163 ± 54 (500°C) and 71 ± 27 Ma (600°C).

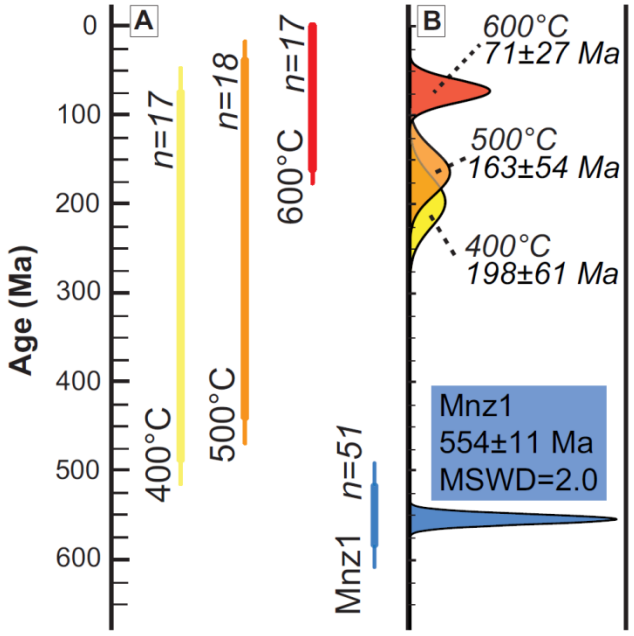

Figure 6-3 Results of U-Th-Pb electron probe micro-analyzer (EPMA) geochronology. A: domains of heterogeneous overlapping ages of unaltered (Mnz1) and reprecipitated monazite (Mnz2) between 300 and 600°C. B: Weighted average age and associated errors of corresponding samples (A)

6.3.3. TEM study

TEM observations have been done on FIB cut foils made at the interface between the pristine and altered monazite domains. In the TEM images (Fig. 4), Mnz1 is characterized by the presence of typical mottled diffraction contrasts due to a distorted lattice resulting from radiation damage (Seydoux-Guillaume et al., 2002b; 2004), in contrast to the newly formed monazite (Mnz2), whose lattice is free of such damage. At 400°C, TEM images remarkably reveal that the altered domain is mainly composed of Mnz1. Indeed, Mnz2 only occurs as nano-domains along channels (Fig. 4A) or close to porosity (Fig. 4B). With increasing temperatures, the size and volume of Mnz2 in the altered domains increase up to reach few microns at 600 °C (Fig. 4C-D),. While the altered domain is composed of patches of Mnz2 within Mnz1 at 400°C (Fig. 4A-B), it conversely corresponds to nano-sized Mnz1 relics in Mnz2 at 600°C (Fig. 4D). Reaction front, i.e. interface between Mnz1 and Mnz2 domains, is not linear but rather interpenetrative at all temperatures.

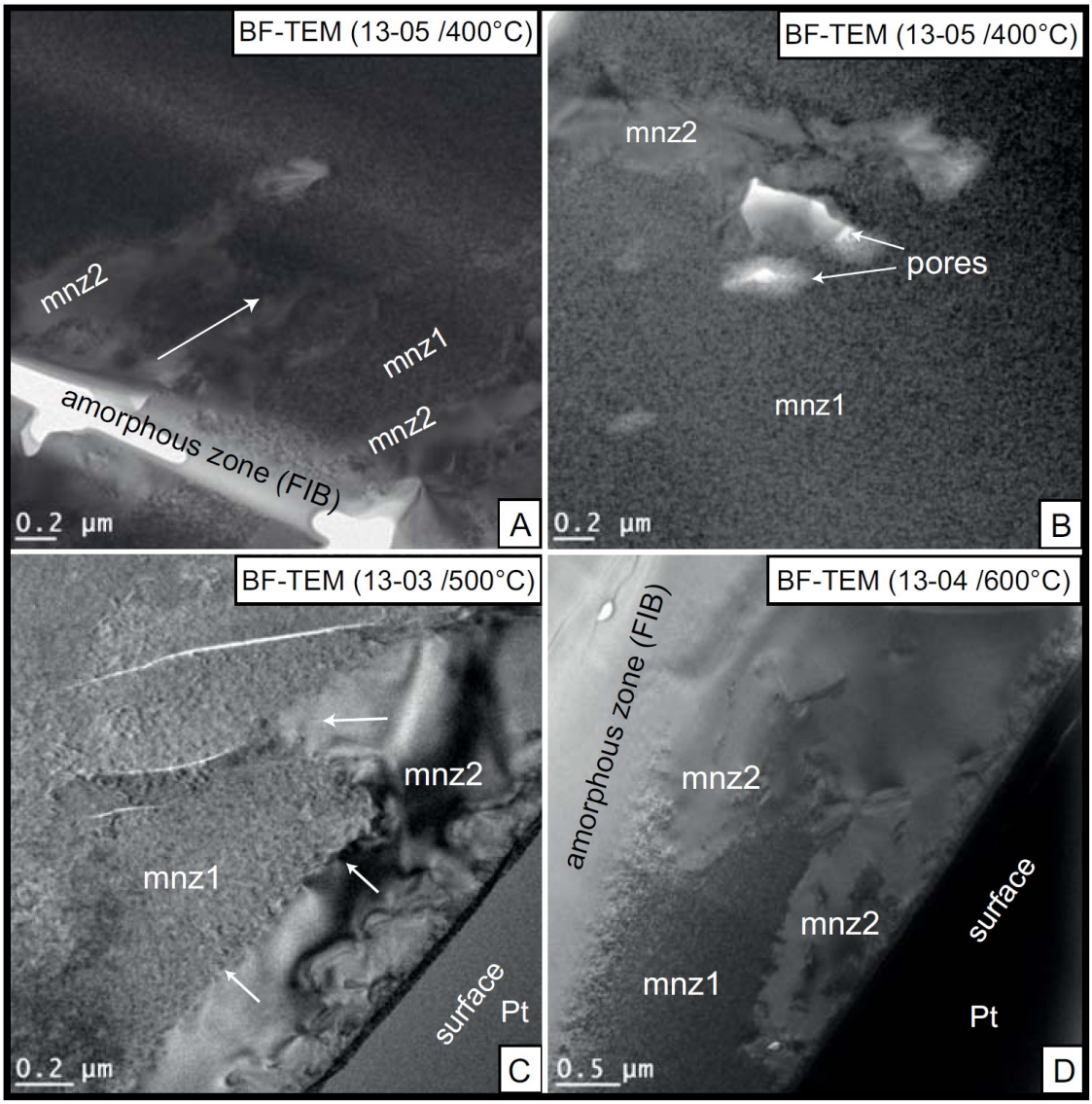

Figure 6-4 Transmission Electron Microscope images in Bright Field mode (BF-TEM) from FIB foils prepared in experimental grains (A-400°C, B-500°C and C-600°C). The unaltered monazite (Mnz1) can be easily identify due to the presence of typical mottled diffraction contrasts due to a distorted lattice resulting from radiation damage (Seydoux-Guillaume et al., 2002b and 2004), in contrast to the newly formed monazite (Mnz2), whose lattice is free of such damage. Note increasing size of the newly formed monazite domains (Mnz2) with enhanced temperature. The bright parts of the image without defects (Fig. 4A, 4D) correspond to amorphized area during FIB preparation.

No Pb-rich nano-domains, as in Seydoux-Guillaume et al. (2003), have been identified in either Mnz1 or Mnz2 and qualitative analysis by using TEM/EDS confirm the absence of Pb (and Ca) in Mnz2 (Fig. 5). In contrast to Mnz1, no Pb was measured in Mnz2 (Fig. 5)

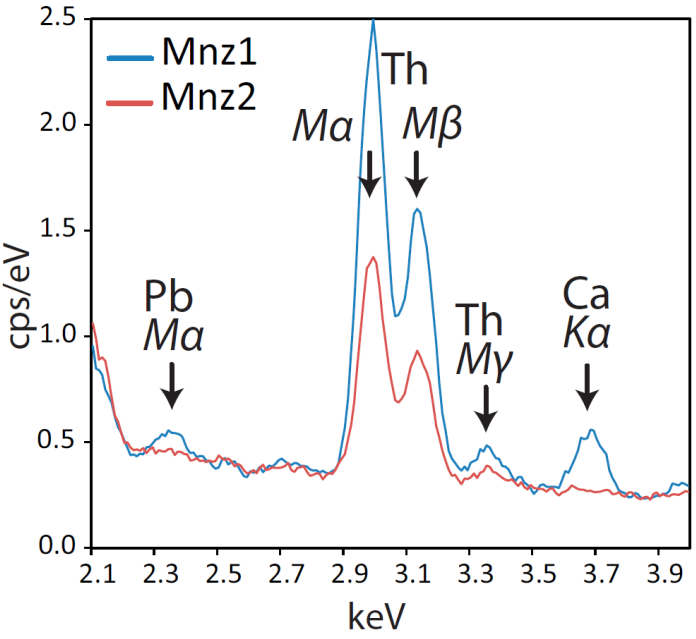

Figure 6-5 Details of the EDS spectrum obtained on Mnz1 and Mnz2 domains in a grain from the 13-03 experiments (500°C). Note the apparent absence of Pb and Ca in Mnz2 domain.

6.4. Discussion and Conclusions

6.4.1. Lead uptake mechanism in altered monazite

Similarly to previous hydrothermal experiments (Teufel and Heinrich, 1997; Seydoux-Guillaume et al., 2002a; Hetherington et al., 2010; Harlov et al., 2011; Williams et al., 2011; Budzyń et al., 2015), experimental monazite products show a zoning with initial monazite grains (Mnz1) surrounded by a secondary monazite with a different composition. The alteration reaction appears pseudomorphic with porosity development, typical for replacement by interfacially coupled dissolution-precipitation (Putnis, 2002; Harlov et al., 2011). Isotopic and chemical dating attests of the presence of Pb in the altered domain. Such systematic presence of Pb inside secondary monazite agreed with previous studies from hydrothermal experiments under alkali conditions at low temperature (250 and 350 °C, Buzdyn et al., 2015), but also above 600 °C (Harlov et al., 2011; Shazia et al., 2015), indicating that U-Th-Pb system is only partially reset in experimentally replaced domains.

In this study, TEM images reveal for a mechanism of nanosized “partial replacement” in altered domain to account for Pb uptake in secondary monazite crystallized by coupled dissolution-precipitation. Assuming negligible diffusion (Cherniak et al., 2004; Gardés et al., 2006), presence of non-radiogenic Pb in secondary monazite is commonly attributed to structural incorporation (Montel et al., 2002) or Pb-rich nano-inclusions precipitation (Seydoux-Guillaume et al., 2003). Although the possible presence of Pb-bearing (nano-) inclusions is not completely ruled out, none was observed by using TEM images. Similarly, the low Pb content measured in altered domains by TEM (Fig. 4) and locally in EPMA (analysis 1304-63; Table DR4 in the Data Repository) suggest negligible structural Pb incorporation in Mnz2. In contrast, nanoscale observations using TEM highlight that incomplete replacement of Mnz1 can account for the Pb measured within the altered domains (Fig 4). At low temperature, pristine monazite replacement is restricted to channels progressing anisotropically (400°C; Fig. 4A). With increasing temperature, Mnz2 volume within the altered domain becomes larger and replacement

reaction propagates more isotropically (Fig. 4C), as classically observed at higher temperature (Harlov et al., 2011). Such nanoscale "partial replacement" is responsible for an unavoidable mixture of Mnz1 and Mnz2 components in the volume of isotopic and chemical dating analyses (~50 μm^3 and 5 μm^3 for LA-ICP-MS and EPMA, respectively). Here, the "partial resetting" of ages or apparent "Pb loss" observed in the Tera-Wasserburg (i.e. displacement toward the right of the diagram; Fig. 2A) can be both explained by a nanosized partial replacement mechanism. With no evidence of Pb in the Mnz2 (Fig. 5), the Pb measured in the altered domain is attributed to the Mnz1 component. Isotopically, $^{206}Pb/^{238}U$ ages appear older than the $^{208}Pb/^{232}Th$ ages (Fig. 2B), certainly due to preferential U mobility in the alteration fluid compared to Th. In the investigated set-up with no Pb in the starting solution, the only possible source of Pb is provided by the alteration of the Mnz1. Indeed, Tera-Wasserburg diagram confirms that the $^{206}Pb/^{207}Pb$ ratio in the altered domain is similar to that of Mnz1, with no isotopic fractionation during alteration (Fig. 2A).

Amongst the investigated experimental conditions, temperature appears to play one crucial role on the size and structural properties (porosity) of the altered domain (Fig. 1, 4). From 400 to 600°C, the general increase of the Mnz2 volume (and concomitant decrease of the Mnz1 nano-relics) explains for the lower Pb concentration measured in the experimental product run at 600°C. This thermal control on the replacement efficiency is coherent with the observation that Pb uptake is generally reported in monazite replaced by late-stage alteration (Seydoux-Guillaume et al., 2012; Didier et al., 2013). Therefore, "partial resetting", due to mixture of nano-domains of monazite of different ages, is expected to be more significant for low-temperature replacement.

6.4.2. Implications for the meaning of monazite U-Th-Pb ages

In this study, monazite replacement experiments enable to raise conclusions on a novel reaction mechanism to explain the presence of initial Pb uptake in secondary monazite. In the experimental products investigated using TEM, the absence of radiation damage in experimentally grown Mnz2 enables to rapidly and clearly localize and identify both monazite domains. While not addressed yet in natural samples, it seems unclear whether primary nano-relics can be readily detected by TEM in naturally replaced domains, especially for low compositional differences between the primary and secondary monazite. However, we believe that the Pb uptake mechanism identified here applies to natural samples, based on the micro-structural similarities between experimental and natural monazite replacement. At low-temperature, hydrothermal or fluid-assisted monazite crystallization commonly shows complex micro-structures, including skeletal structure, with micro-porosity and/or inclusions typically localized within both primary and secondary monazite (e.g. Janots et al., 2011; Kelly et al., 2012; Seydoux-Guillaume et al., 2012). The abundance and textural position of the inclusions are compatible with an anisotropic replacement, as proposed in this study. On the other hand, the Pb sequestration mechanism proposed here is excluded for new monazite (over)growth involving spatially decoupled dissolution and precipitation (e.g. pressure-solution processes in deformed rock; Wawrzenitz et al., 2012) and experimentally reproduced in Seydoux-Guillaume et al. (2002a).

Partial monazite replacement has severe implications for its use as U-Th-Pb geochronometer. Because of the very small size of the nano-domains of monazite replaced compared to the area addressed by punctual microanalyses (Fig. 2 and 3), age mixture between Mnz1 and Mnz2 are systematically measured in apparently homogeneous Mnz2 (BSE, Fig. 1). With no control on the age concordance, interpretations of chemical U-Th-Pb ages, assuming no initial Pb, must therefore be considered with cautious when replacement rims are dated (e.g. Kelly et al., 2012; Seydoux-Guillaume et al., 2012).

As conclusions, this experimental study coupled with nanoscale observation brings insights on a novel hypothesis to account for in-situ dating pitfalls, which may in fact apply to other geochronometers partially replaced by interfacially coupled dissolution-precipitation. Furthermore, results indicate that porosity and/or inclusions presence, age scattering associated with discordance between the different isotopic systems are certainly significant markers to suspect a nanosized partial replacement (e.g. Bosse et al., 2009; Kelly et al., 2012; Seydoux-Guillaume et al., 2012). It may be challenging to recognize possible disturbance linked with mixing of nano-domains, when large age datasets are determined with no reliable micro-textural documentations, as for example in origin provenance studies.

Acknowledgments

We thank V. Magnin for its help with microprobe analyses and N. Findling for his assistance with the SEM. This work was partly supported by the French RENATECH network and the the ANR-JC grant (Mona, 2012).

7. CONCLUSIONS – PERSPECTIVES

Cette thèse s'inscrit dans la continuité des études sur les interactions entre la monazite et les fluides hydrothermaux à travers l'analyse d'échantillons naturels et une approche expérimentale. Le but de cette thèse était de mieux caractériser les compositions chimiques et isotopiques de la monazite hydrothermale en fonction des conditions physico-chimiques du fluide responsable de sa cristallisation, ainsi que les mécanismes d'altération lors des interactions fluide-monazite. Ce dernier chapitre vise à discuter les résultats et à amener des pistes de réflexions sur les problèmes soulevés par ce travail.

L'étude des monazites hydrothermales naturelles s'est construite autour d'un grand nombre de données géochronologiques et géochimiques obtenues à partir d'échantillons collectés le long de l'arc alpin occidental. Ce travail n'aurait été possible sans la participation de nombreux minéralogistes amateurs ayant acceptés de « sacrifier » leur échantillons ou de révéler les gisements qu'ils avaient découvert et souligne l'importance de ces collaborations.

Pour la première fois, les cristaux de monazites hydrothermales ont pu fournir des données géochronologiques à l'échelle des Alpes occidentales. Les chronomètres U-Pb et Th-Pb de la monazite (et du xénotime) ont pu ainsi être comparés et montrent que la datation U-Pb peut être efficace pour des cristaux présentant un faible rapport Th/U (<30), de faibles concentrations en U et Th et avec un excès de ^{206}Pb limité. Malgré sa croissance dans un système ouvert (circulations de fluides), les monazites hydrothermales analysées ne souffrent que de perturbations mineures de leurs systèmes isotopiques U-Pb et Th-Pb, liés à des épisodes de croissance et de rééquilibration. Ces perturbations se traduisent par des mélanges d'âges ou d'héritage de Pb, potentiellement dues à du remplacement par dissolution-précipitation. Ces zones de remplacement sont caractérisées par des zonations compositionnelles (textures) complexes, des rapports Th/U élevés et de la porosité. La datation in-situ haute résolution a permis de confirmer que la monazite cristallisait lors d'épisodes hydrothermaux sur une courte période (<0.5 Ma). Les âges obtenus dans les veines alpines étudiées ont pu être corrélés avec les âges disponibles sur la formation des Alpes, et révèlent des relations très étroites entre

l'activité hydrothermale, la précipitation de monazite et la déformation /exhumation. Cela suggère que la monazite hydrothermale peut être utile pour retracer les épisodes tardifs de l'histoire de la déformation pendant les orogènes, généralement mal contraints, et correspondant à des épisodes tectoniques courts et intenses pendant le Miocène dans les Alpes.

L'étude pluridisciplinaire localisée sur une veine hydrothermale, basée sur des analyses traces de fissions sur zircon, des analyses d'inclusions fluides et des datations Th-Pb sur monazite a permis de contraindre chronologiquement et thermiquement l'âge et la durée des circulations hydrothermales associées à l'ouverture des veines pendant l'exhumation. Cette étude montre que les monazites hydrothermales cristallisent précocement dans la veine à partir d'un fluide « chaud » (400-450°C) par rapport à la roche encaissante déjà « refroidie » autour de 240-280°C, deux millions d'années plus tôt. Ces circulations de fluides ont été suffisantes pour remettre à zéro les âges traces de fission sur zircon des échantillons prélevés sur les épontes de la veine hydrothermale. Cette étude montre également que la monazite a cristallisé rapidement, épisodiquement et peu de temps après l'ouverture de la veine, et donc pouvait dater l'évènement tectonique responsable de l'ouverture de la veine.

La datation de monazite hydrothermale apparait donc comme une alternative ou un accessoire complémentaire aux techniques thermochronologiques (Ar-Ar ou K-Ar) sur micas blancs ou minéraux argileux syn-cinématiques pour dater les épisodes de déformation tardifs dans les zones de cisaillements ou la déformation cassante associée aux circulations hydrothermales. Cette étude met également en évidence la nécessité d'avoir des standards fiables pour l'analyse géochronologique par LA-ICP-MS des minéraux accessoires comme le xénotime (ou le rutile), également présent dans ces veines, pour l'interprétation de leurs âges.

Dans les milieux naturels, les fluides responsables de l'altération de monazite incluent des acides (par exemple, HCl, H_2SO_4) et des saumures ou bases riches en éléments alcalins, potentiellement formés lors d'interactions entre des fluides et des

roches riches en feldspaths (Na-Ca-K) dans la croûte. Les expériences d'altération hydrothermales de monazites ont confirmé que les textures d'altérations, correspondant à du remplacement par dissolution-précipitation, ne pouvaient être reproduites qu'en présence d'un fluide alcalins, pour des températures inférieures à 600°C. Bien que les fluides employés dans les expériences réalisées au cours de cette thèse aient peu de chance de se trouver dans les milieux naturels, les textures reproduites correspondent à celles que l'on retrouve couramment dans les monazites naturelles. Les modifications compositionnelles et isotopiques ainsi que les perturbations des systèmes chronométriques des échantillons expérimentaux corroborent également le fait que des interactions avec des fluides peuvent être responsable de l'altération de ce minéral se traduisant par la mobilité de certains éléments (HREE+Y, U, Th, Pb) et de la remise à zéro potentielle de ses chronomètres.

Malgré la difficulté à interpréter les compositions chimiques et isotopiques des monazites secondaires formées durant ces expériences au regard de la température, l'analyse des fluides et des domaines secondaires de la monazite a permis de montrer que leurs compositions étaient majoritairement contrôlées par les phases secondaires précipitant lors de l'expérience, et par la composition de la monazite primaire. La plus grande mobilité des HREE+Y, U comparée aux LREE, Th a pu également être confirmée et leur appauvrissement dans les monazites naturelles ayant réagi par dissolution-précipitation pourrait être utilisé comme traceur des conditions de fluides dans les environnements métamorphiques ou hydrothermaux. Ces résultats apportent également de nouvelles données pour comprendre la mobilité de ces éléments dans la croûte, importants pour comprendre la formation des gisements de lanthanides ou actinides. L'étude systématique des produits expérimentaux à l'aide de nombreuses techniques analytiques, à différentes échelles, a également permis de mettre en évidence un nouveau mécanisme de propagation du front de réaction lors de la dissolution-précipitation. La formation et la concentration de fractures et de pores au niveau de ce front de réaction semble jouer un prépondérant pour la propagation du remplacement et conduit à un remplacement anisotrope caractérisé par le mélange de domaine remplacé et primaire à

l'échelle nanométrique. Une piste envisagée pour expliquer la formation de ces fractures dans un milieu sans contrainte externe concerne l'accumulation de défauts qui résulte en une distorsion du réseau de la monazite dus à la désintégration radioactive du Th et de l'U. D'autres investigations sont nécessaires, incluant la modélisation des contraintes responsables de ces fractures, mais ce travail fournit quelques indications intéressantes pour la compréhension des mécanismes de remplacement des minéraux radioactifs qui ont des implications cruciales pour le stockage des déchets radioactifs. Le mélange de domaines à l'échelle nanométrique lors des épisodes d'altération à basse température mis en évidence par ces travaux expérimentaux est cohérent avec les observations sur des échantillons naturelles qui montrent l'incorporation de Pb lors des épisodes d'altération. Le mécanisme de « remise à zéro partielle » du chronomètre de la monazite pourrait être expliqué par ce mécanisme de remplacement partiel, d'autant plus important à basse température. Dans le cas de minéraux présentant des textures complexes et caractéristiques d'altération hydrothermale, les résultats montrent que les datations isotopiques in-situ semblent plus adaptées que les datations chimiques et qu'une étude micro-texturale peut être nécessaire pour interpréter les âges obtenus.

Les travaux à venir concernant le domaine expérimental représentent la poursuite d'une approche expérimentale consistant à reproduire les textures naturelles en essayant de se rapprocher au mieux des conditions pouvant exister dans les environnements hydrothermaux ou métamorphiques. Ces travaux sont nécessaires, non seulement sur la monazite, mais sur tous les minéraux accessoires potentiellement porteurs de lanthanides ou d'actinides comme l'apatite, le zircon, le xénotime ou l'allanite par exemple. Ces observations naturelles et expérimentales nécessitent également une approche thermodynamique afin de vérifier les hypothèses formulées sur la base de ces observations, peu de données existants à ce jour.

8. ANNEXES

LISTE DES ANNEXES

Annexe 3-1 Résultats des analyses d'éléments en traces par LA-ICP-MS (1/2)

Electronic Supplementary Material S1 : LA-ICPMS Trace element concentrations

Standard: monazite Moacyr (Seydoux-Guillaume et al. 2002; Gasquet et al. 2010; Fletcher et al. 2010)
Internal standard La: EPMA analyzes or 15 wt.% (KER and ISO samples), Y for xenotime
Spot size: 15 µm
c: core; r: rim; pz: patchy zone; np: unspecifiated; z1, z2: different domains on grain; loc: spot position on grain; bdl: below detection limit

				Element concentration (ppm)																	
Sample	Grain	loc.	BSE ID	Sr88	Y89	La139	Ce140	Pr141	Nd146	Sm147	Eu153	Gd157	Tb159	Dy163	Ho165	Er166	Tm169	Yb172	Lu175	Pb208	Th232	U238
VDG- 01	np		1	195	6324	133765	267034	29787	109109	15826	2711	10600	940	3169	321	381	21	57	4	0.8	1236	574
VDG- 01	np		2	142	5745	133765	264776	28998	107564	15329	2633	10597	937	2950	294	341	19	49	3	0.5	1233	518
VDG- 01	np		3	255	5153	140902	267786	28011	101017	13491	2406	8886	816	2722	267	313	18	47	3	0.3	541	194
VDG- 01	np		4	293	4061	140902	269286	28910	104174	14629	2406	9453	803	2430	221	241	12	29	2	0.7	1069	452
RDN- 03	np			290	3198	135242	222192	21660	74019	10867	3010	6806	582	1706	148	168	10	33	2	0.8	1556	98
RDN- 04	pz		1	473	4650	136426	241806	26076	101392	21564	5020	14758	1138	2855	226	226	12	35	2	1.6	2924	246
RDN- 04	r		2	209	2846	134547	228471	22788	81921	13745	3246	8687	689	1797	138	145	8	24	1	1.1	1995	72
RDN- 05	np			979	6647	145325	268156	30638	128266	32451	7209	24448	1763	4271	315	305	16	46	3	3.0	6586	237
RDN- 05	np			823	6182	132592	240899	27193	111343	27122	6684	20995	1575	3945	299	297	16	46	2	1.8	4401	222
RDN- 05	np			686	7097	138732	257737	29169	117015	27541	7904	21494	1733	4535	352	340	19	51	3	1.8	4107	260
RDN- 05	np			332	2939	139652	224193	22433	80164	13294	3285	8354	644	1683	134	141	9	28	2	0.6	1466	42
RDN- 05	np			263	4838	135624	237914	25323	94706	17574	4655	12077	999	2697	222	234	14	41	2	1.3	2893	96
LCO- 03	np			155	4000	127903	237461	26154	101664	17181	3519	11121	887	2432	206	212	10	25	1	0.4	750	74
LCO- 03	np			375	7032	128201	259194	32921	144419	33829	7283	24276	1768	4571	368	358	16	38	2	1.6	4018	318
LCO- 04	np			54	4889	126851	247442	28529	112056	17378	3528	11214	906	2662	242	247	12	28	2	bdl	691	272
LCO- 04	np			262	3579	135603	257752	28438	108430	16252	3354	10167	791	2203	182	176	7	17	1	bdl	520	85
SOY- 01	r		1	1000	5086	140689	259098	28592	107265	18655	2760	8723	781	2441	237	307	23	80	5	6.0	9877	384
SOY- 01	r		2	1024	4665	140689	253814	27748	103908	17640	2552	8195	728	2259	214	283	21	74	4	6.0	9878	367
SOY- 01	r		3	503	6853	126850	254798	29685	118586	23038	3554	11794	1070	3343	322	422	30	102	6	5.6	9511	485
SOY- 01	c		4	1036	6314	113574	232575	28949	117237	24090	3556	12013	1071	3354	302	364	23	70	4	12.9	22348	1513
SOY- 01	c		5	1081	6512	113574	233483	28773	117523	23897	3605	12361	1105	3439	313	379	24	73	4	13.2	22876	1537
SOY- 01	c		6	1083	6654	131548	268272	33010	134337	27582	4084	13794	1223	3732	327	389	25	74	4	13.9	23504	1487
SOY- 02	z1			879	7002	126850	253604	28912	113399	18411	3677	12318	1076	3547	341	375	21	53	3	0.6	1212	89
SOY- 02	z2			260	4144	120848	221738	24634	96515	15399	3111	9293	782	2344	209	226	12	32	2	0.5	1352	71
SOY- 02	z2			276	4369	131548	241923	26788	103711	16411	3288	9980	821	2512	224	240	13	35	2	0.6	1497	80
KER- 01	np		1	182	4000	127903	239689	26807	106421	19307	1948	11323	882	2445	204	217	13	40	3	0.4	1197	38
KER- 01	np		2	139	3954	127903	239886	27123	108826	20487	2011	11696	903	2496	201	212	12	37	2	bdl	162	48
KER- 02	np			120	3362	127903	251700	28830	116819	20815	2066	12000	888	2289	179	176	9	28	2	0.6	2060	58
KER- 02	np			149	2990	127903	238879	27192	109001	19328	1913	10793	807	2060	160	157	8	25	2	0.7	474	58
KER- 03	np			220	3369	127903	248747	28491	117186	21013	2042	11672	863	2258	179	182	10	32	2	0.5	484	35
KER- 03	np			193	3140	127903	243162	27744	111604	19699	1901	10766	796	2044	164	167	9	29	2	0.3	684	52
E2R- 09	c		1	2678	7586	127387	240707	26126	102350	17462	3979	11414	1068	3572	343	391	22	48	2	13.7	21577	856
E2R- 09	c		2	2753	7879	127387	240097	26531	105972	18405	4206	12019	1134	3810	366	405	22	48	2	13.7	22170	1079
E2R- 09	c		3	2676	7458	129749	241087	26190	102256	17552	3967	11400	1056	3532	336	389	22	48	2	13.1	21658	1003
E2R- 09	r		4	1426	6744	136468	250963	26722	101938	16908	3710	10562	977	3168	305	375	23	56	3	8.2	12740	370
E2R- 09	r		5	1463	6977	136468	255413	27309	103832	17021	3737	10589	982	3257	315	386	24	58	3	7.7	12535	375
E2R- 09	r		6	1003	6299	140689	249436	25947	97731	15876	3416	9756	912	2999	289	347	21	52	2	5.9	9840	335
E2R- 08	c			1576	7542	130124	251724	28338	111571	19626	4681	12481	1138	3610	349	389	20	46	2	5.1	8274	1168
E2R- 08	c			1584	7434	130124	251134	28158	110939	19412	4636	12409	1132	3612	342	388	20	45	2	5.4	8505	1184

Annexe 3-1 Résultats des analyses d'éléments en traces par LA-ICP-MS (2/2)

Sample	Grain	loc.	BSE ID	Element concentration (ppm)																				
				Sr88	Y89	La139	Ce140	Pr141	Nd146	Sm147	Eu153	Gd157	Tb159	Dy163	Ho165	Er166	Tm169	Yb172	Lu175	Pb208	Th232	U238
E2R- 08	c			1600	7498	130124	255807	28702	113030	19673	4748	12729	1152	3651	347	396	21	46	2	5.3	8532	1215
E2R- 08	r			850	7279	140919	261975	28101	105134	16805	4050	10260	940	3170	324	432	28	72	4	1.7	2800	288
E2R- 08	r			756	6311	140919	260337	27597	105508	16818	4024	9870	883	2826	282	369	23	60	3	1.6	3058	251
E2R- 08	r			814	7204	140919	263863	27980	105205	16867	4107	10324	956	3168	320	422	27	71	4	1.2	2618	295
E2R- 11	c	1		3746	5094	136485	266396	29704	117266	19797	3535	11414	957	2868	245	256	13	28	1	35.3	63367	848
E2R- 11	c	2		3515	5173	136485	263744	28892	114410	19743	3454	11552	982	3000	257	261	14	29	1	34.3	59335	831
E2R- 11	c	3		3648	5460	136485	262655	29594	114454	19974	3504	11819	1004	3065	258	274	13	31	1	33.6	56821	819
E2R- 11	r	4		721	5731	135496	253886	28322	112726	19670	3669	11681	996	3071	271	309	17	40	2	5.1	8182	393
E2R- 11	r	5		712	5416	135496	255451	27903	109925	18862	3592	11354	982	2964	264	294	16	37	2	5.1	8321	399
E2R- 11	r	6		727	5715	135496	261069	28864	113780	19936	3736	11737	1024	3144	274	308	17	39	2	5.3	8567	399
SAV- 01	np			1390	9159	128158	264682	32200	130977	26217	3575	17364	1373	3964	359	392	20	48	2	1.4	3262	95
SAV- 02	np			1242	8338	136088	291942	34209	139712	25616	3407	16302	1252	3544	329	357	18	48	3	1.4	3802	111
SAV- 02	np			868	5535	138476	277283	31169	120394	19670	2465	10949	818	2293	210	239	13	35	2	0.7	2376	41
SAV- 03	np	1		821	5003	135577	265360	29651	113439	18295	2275	10137	752	2149	195	222	12	32	2	0.9	2717	42
SAV- 03	np	2		978	8606	128158	279633	33253	137747	26011	3461	16836	1283	3697	340	368	19	48	3	1.8	5444	127
SAV- 04	np			304	4177	130466	254801	28214	110402	18679	2241	9908	731	2077	191	208	11	25	1	bdl	871	37
SAV- 04	np			288	4101	130466	253005	28172	108188	18169	2229	9843	729	2061	186	208	11	26	2	bdl	846	36
SAV- 04	np			229	4795	130466	256468	28912	113709	19295	2441	10921	823	2393	219	243	12	28	2	bdl	817	42
SAV- 04	np			283	5245	130466	262338	30061	119007	20669	2610	11881	907	2628	242	268	13	31	2	0.3	1209	57
SMC- 01	c	1		1375	3471	129949	251020	27651	102510	15094	1676	7844	515	1329	118	145	9	29	2	0.5	959	9
SMC- 01	c	2		1750	4084	132401	258844	28327	108369	16601	1888	8919	601	1598	146	178	11	34	2	0.4	1249	11
SMC- 01	c	3		1723	4058	135189	266570	29549	111248	17007	1942	9347	612	1600	145	174	11	33	2	0.4	1352	11
SMC- 01	r	4		767	5382	133957	267822	29782	115019	18433	2188	9890	712	2005	197	257	17	54	4	0.4	1629	32
SMC- 01	r	5		648	5236	139840	272506	30082	113272	17827	2054	9305	675	1896	186	241	15	49	3	0.3	877	16
SMC- 01	r	6		678	4816	133322	260238	29045	110509	17179	2005	9537	679	1870	179	223	14	42	3	1.0	2509	18
SMC- 01	r	7		666	4982	133322	256295	28395	106567	16624	1961	9266	669	1852	181	231	15	44	3	0.3	1422	14
SMC- 01	r	8		596	4721	133322	256635	28056	106426	16586	1922	9062	662	1810	169	216	13	41	3	0.5	1436	14
ISO- 01	np	1		164	3535	127903	250445	28060	103775	18567	1880	9171	704	1849	154	182	12	40	3	7.2	7013	152
ISO- 01	np	2		291	2828	127903	255903	28431	105306	18406	1870	9082	667	1660	127	137	8	23	2	13.5	12955	247
MTV- 01	np	1		124	4665	127711	262435	31725	133711	28377	3688	19759	1546	3669	273	268	14	40	2	10.2	9109	145
MTV- 01	np	2		402	2878	136281	263220	29438	114352	19052	2281	11201	856	2132	162	167	9	29	2	4.9	4020	60
MTV- 01	np	3		400	8783	131079	266376	31380	131476	28315	3700	20304	1838	5303	463	554	35	121	8	10.5	9201	206
MTV- 02	np			130	1920	139103	262674	29527	115691	20576	2106	12009	759	1640	109	103	5	14	1	6.7	5897	30
MTC- 01	np			2119	3793	140693	250383	27825	102214	15435	2571	9152	733	2108	182	202	13	53	7	31.3	18892	63
MTC- 01	np			1720	4562	140693	244682	27282	105017	17391	2874	10959	890	2515	210	216	11	30	2	22.1	13176	20
MTC- 01	np			1803	4484	140693	241178	26844	101382	15503	2566	9674	755	2117	176	188	10	29	2	23.7	13611	23
MTC- 03	np			1972	4473	144956	253475	28613	107974	16795	2812	10195	822	2352	205	231	14	46	4	29.8	17790	64
MTC- 03	np			1960	4868	164227	287591	32297	119578	18892	3117	11225	919	2662	225	238	13	38	2	36.1	20996	49
MTC- 02	np	1		1820	4796	142398	247426	27636	106332	17186	2872	10877	880	2492	216	237	14	56	7	20.9	12586	65
MTC- 02	np	2		1754	4428	147088	261409	29131	109009	17394	2906	10212	833	2381	201	224	13	47	5	25.0	13797	90
Xenotime																								
XMTC- 02	np			35	354032	3	49	39	902	2967	1614	22852	6371	55224	12077	29806	3693	18369	1620	11.6	6409	211
XMTC- 04	np			19	359544	2	39	28	610	2185	1123	19516	6045	54157	12573	30840	3768	18510	1572	6.9	3967	188
XMTC- 04	np			19	359544	2	28	23	569	2229	1245	19664	5898	53345	12018	30260	3729	18003	1512	1.7	769	54
XMTC- 04	np			19	354347	5	71	44	865	2634	1167	21281	6284	54661	12097	30136	3760	19270	1685	22.3	12501	503
XMTC- 02	np			19	354032	1	26	22	538	2089	1199	19139	5716	50747	11799	29369	3584	17037	1518	1.0	666	51
XMTC- 01	np	1		18	362537	3	50	39	851	2729	1447	21601	5972	52305	11694	29231	3607	17255	1496	12.1	6055	158

Annexe 3-2 Résultats des datations U-Th-Pb par LA-ICP-MS (1/8)

Electronic Supplementary Material S2: $^{207}Pb/^{235}U$ - $^{206}Pb/^{238}U$ - $^{208}Pb/^{232}Th$ isotopic ratios, - U-Th contents calculated with LA-ICP-MS data and $^{208}Pb/^{232}Th$ and $^{206}Pb/^{238}U$ ages

Standard: monazite Moacyr (Gasquet et al. 2010) and (*)Corfu (Corfu 1988)
BSE ID refers to spot locations on Fig. 4
loc: spot position on grain;c: core; r: rim; pz: patchy zone; np: unspecifiated; z1, z2: differentdomains on grain; (-) uncalculated ages

Sample	Grain	loc.	spot (µm)	BSE ID	[Th] ppm	[U] ppm	Th/U	Isotopic ratios						Apparent age (Ma)		Age (Ma)	
								$^{207}Pb/^{235}U$	± 2σ	$^{206}Pb/^{238}U$	± 2σ	$^{208}Pb/^{232}Th$	± 2σ	$^{206}Pb/^{238}U$	± 2σ	$^{208}Pb/^{232}Th$	± 2σ
VDG-	01	np	20	1	947	470	2	0.011	0.003	0.0018	0.0001	0.00056	0.00003	11.4	0.7	11.4	0.6
VDG-	01	np	20	2	722	370	2	0.010	0.004	0.0017	0.0001	0.00056	0.00003	11.0	0.7	11.3	0.6
VDG-	01	np	20	3	843	211	4	0.014	0.006	0.0018	0.0001	0.00056	0.00003	11.7	0.8	11.3	0.6
VDG-	01	np	20	4	1076	173	6	0.012	0.006	0.0018	0.0002	0.00054	0.00003	11.8	0.9	10.9	0.5
VDG-	01	np	20	5	1009	167	6	0.014	0.005	0.0019	0.0002	0.00055	0.00003	12.0	0.9	11.2	0.5
VDG-	01	np	20	6	1036	160	6	0.015	0.006	0.0019	0.0002	0.00054	0.00003	12.2	0.9	11.0	0.5
VDG-	01	np	20	7	2144	494	4	0.014	0.003	0.0018	0.0001	0.00056	0.00003	11.4	0.6	11.4	0.5
VDG-	01	np	20	8	463	114	4	0.009	0.007	0.0018	0.0002	0.00053	0.00003	11.4	1.1	10.7	0.7
VDG-	01	np	20	9	488	105	5	0.014	0.008	0.0018	0.0002	0.00054	0.00003	11.5	1.0	10.9	0.7
VDG-	01	np	20	10	605	118	5	0.007	0.006	0.0018	0.0002	0.00054	0.00003	11.4	1.0	10.9	0.6
RDN-	01	pz	20	7	1970	79	25	0.071	0.015	0.0022	0.0002	0.00051	0.00003	13.9	1.4	10.3	0.5
RDN-	01	pz	20	11	4315	366	12	0.010	0.003	0.0016	0.0001	0.00048	0.00003	9.0	0.7	9.7	0.4
RDN-	01	pz	20	9	3936	17	236	0.044	0.031	0.0047	0.0007	0.00045	0.00003	10.1	0.6	9.0	0.4
RDN-	01	pz	20	8	2338	47	50	0.062	0.026	0.0022	0.0003	0.00045	0.00003	12.4	3.0	9.2	0.4
RDN-	01	pz	20	6	3619	21	172	0.032	0.039	0.0028	0.0005	0.00044	0.00003	30.3	4.3	8.8	0.4
RDN-	01	pz	20	10	2743	19	145	0.042	0.042	0.0019	0.0005	0.00041	0.00003	14.4	1.8	8.4	0.4
RDN-	01	pz	20	5	857	23	38	0.028	0.033	0.0014	0.0004	0.00042	0.00003	17.7	3.1	8.4	0.5
RDN-	01	pz	20	4	1143	19	60	0.034	0.044	0.0014	0.0004	0.00042	0.00003	8.8	2.3	8.5	0.5
RDN-	01	pz	20	3	3701	60	62	0.025	0.019	0.0018	0.0002	0.00046	0.00003	9.3	2.7	9.3	0.4
RDN-	01	r	20	2	2053	61	34	0.036	0.015	0.0014	0.0002	0.00040	0.00003	11.8	1.5	8.1	0.4
RDN-	01	r	20	1	847	77	11	0.013	0.014	0.0016	0.0002	0.00041	0.00003	9.1	1.4	8.3	0.5
RDN-	01	r	20	12	3431	268	13	0.008	0.004	0.0014	0.0001	0.00040	0.00003	10.4	1.3	8.2	0.4
RDN-	02	pz	20	1	4326	36	121	0.017	0.021	0.0017	0.0003	0.00043	0.00003	11.0	2.0	8.8	0.4
RDN-	02	pz	20	2	3881	32	123	-0.002	0.027	0.0021	0.0003	0.00043	0.00003	13.3	2.2	8.7	0.4
RDN-	02	pz	20	3	4834	29	167	-0.003	0.021	0.0029	0.0004	0.00044	0.00003	18.6	2.8	8.9	0.4
RDN-	02	pz	20	4	4999	94	53	0.008	0.010	0.0021	0.0002	0.00048	0.00003	13.7	1.4	9.6	0.4
RDN-	02	pz	20	5	4472	22	200	-0.007	0.028	0.0040	0.0006	0.00046	0.00003	26.0	3.6	9.2	0.4
RDN-	02	pz	20	6	3985	25	160	0.001	0.032	0.0034	0.0005	0.00044	0.00003	22.0	3.2	9.0	0.4
RDN-	02	r	20	7	2632	86	30	0.010	0.009	0.0016	0.0002	0.00040	0.00003	10.1	1.2	8.2	0.4
RDN-	02	r	20	8	2689	88	31	0.008	0.008	0.0016	0.0002	0.00040	0.00003	10.2	1.3	8.1	0.4

Annexe 3-2 Résultats des datations U-Th-Pb par LA-ICP-MS (2/8)

Sample	Grain loc.	spot (µm)	BSE ID	[Th] ppm	[U] ppm	Th/U	Isotopic ratios								Apparent age (Ma)			Age (Ma)	
							$^{207}Pb/^{235}U$	± 2σ	$^{206}Pb/^{238}U$	± 2σ	$^{208}Pb/^{232}Th$	± 2σ	$^{206}Pb/^{238}U$	± 2σ		$^{208}Pb/^{232}Th$	± 2σ
RDN- 02	r	20	9	2803	104	27	0.018	0.007	0.0015	0.0002	0.00041	0.00003	9.6	1.2		8.4	0.4
RDN- 02	r	20	10	2986	92	32	0.006	0.010	0.0016	0.0002	0.00041	0.00003	10.2	1.3		8.3	0.4
*RDN- 03	r	25		3079	126	25	0.014	0.009	0.0014	0.0001	0.00042	0.00003	8.8	0.8		8.4	0.4
*RDN- 03	r	25		3053	123	25	0.011	0.009	0.0015	0.0001	0.00042	0.00003	9.6	0.8		8.4	0.4
*RDN- 03	r	25		2612	101	26	0.019	0.011	0.0015	0.0002	0.00043	0.00003	9.6	0.9		8.7	0.4
*RDN- 04	r	25	1	2422	82	29	0.019	0.012	0.0016	0.0002	0.00042	0.00003	11.7	0.8		8.6	0.4
*RDN- 04	r	25	2	1586	85	19	0.015	0.014	0.0016	0.0002	0.00043	0.00003	10.9	0.8		8.6	0.5
*RDN- 04	r	25	3	3239	79	41	0.024	0.012	0.0017	0.0002	0.00041	0.00003	11.0	0.9		8.3	0.4
*RDN- 04	pz	25	4	5361	181	30	0.015	0.007	0.0018	0.0001	0.00051	0.00003	10.2	1.0		10.2	0.4
*RDN- 04	pz	25	5	2988	131	23	0.026	0.008	0.0017	0.0001	0.00050	0.00003	10.1	1.0		10.2	0.5
*RDN- 04	pz	25	6	4227	119	35	0.015	0.009	0.0017	0.0002	0.00051	0.00003	10.7	1.1		10.3	0.5
LCO- 01	np	20		152	61	2	0.017	0.013	0.0012	0.0002	0.00036	0.00006	7.7	1.2		7.3	0.9
LCO- 01	np	20		247	57	4	0.021	0.015	0.0013	0.0002	0.00036	0.00003	8.2	1.2		7.2	0.8
LCO- 01	np	20		760	62	12	0.014	0.014	0.0013	0.0002	0.00035	0.00003	8.2	1.3		7.0	0.5
LCO- 01	np	20		1465	58	25	0.022	0.015	0.0014	0.0002	0.00037	0.00003	8.8	1.3		7.4	0.4
LCO- 01	np	20		1622	98	17	0.030	0.011	0.0014	0.0002	0.00037	0.00003	9.2	1.1		7.5	0.4
LCO- 01	np	20		1286	178	7	0.011	0.005	0.0011	0.0001	0.00037	0.00003	6.9	0.7		7.4	0.4
LCO- 01	np	20		1982	128	15	0.013	0.007	0.0012	0.0001	0.00037	0.00003	8.0	0.8		7.4	0.4
LCO- 01	np	20		1890	86	22	0.022	0.011	0.0015	0.0002	0.00038	0.00003	9.4	1.1		7.7	0.4
LCO- 01	np	20		1821	78	23	0.008	0.015	0.0014	0.0002	0.00038	0.00003	9.3	1.2		7.7	0.4
LCO- 02	np	20	1	296	370	1	0.008	0.003	0.0012	0.0001	0.00037	0.00003	7.4	0.6		7.4	0.8
LCO- 02	np	20	2	365	387	1	0.005	0.002	0.0012	0.0001	0.00035	0.00003	7.6	0.6		7.1	0.7
LCO- 02	np	20	3	365	343	1	0.006	0.003	0.0011	0.0001	0.00036	0.00003	7.3	0.6		7.3	0.7
LCO- 02	np	20	4	309	183	2	0.010	0.003	0.0012	0.0001	0.00037	0.00003	7.6	0.7		7.4	0.7
LCO- 02	np	20	5	363	179	2	0.009	0.005	0.0011	0.0001	0.00040	0.00003	7.3	0.8		8.2	0.7
LCO- 02	np	20	6	453	160	3	0.010	0.005	0.0011	0.0001	0.00037	0.00003	7.2	0.8		7.4	0.6
LCO- 02	np	20	8	113	65	2	0.003	0.011	0.0013	0.0002	0.00042	0.00006	8.3	1.2		8.6	1.4
LCO- 02	np	20	9	173	70	2	0.009	0.011	0.0013	0.0002	0.00042	0.00006	8.1	1.3		8.5	1.0
LCO- 02	np	20	10	286	47	6	0.016	0.014	0.0014	0.0002	0.00040	0.00003	9.3	1.6		8.0	0.8
LCO- 03	np	25		6323	228	28	0.013	0.005	0.0015	0.0001	0.00040	0.00003	9.3	0.6		8.1	0.3
LCO- 03	np	25		6368	247	26	0.015	0.004	0.0013	0.0001	0.00040	0.00003	8.4	0.6		8	0.3
LCO- 03	np	25		5166	257	20	0.008	0.004	0.0014	0.0001	0.00040	0.00003	8.8	0.6		8	0.3
LCO- 04	np	25		287	96	3	0.026	0.010	0.0012	0.0001	0.00039	0.00006	7.5	0.8		7.8	1.1
LCO- 04	np	25		674	289	2	0.008	0.004	0.0012	0.0001	0.00036	0.00003	7.6	0.5		7.3	0.6
LCO- 04	np	25		1161	76	15	0.000	0.015	0.0012	0.0002	0.00037	0.00003	7.9	1.0		7.4	0.5
***KER-** 01	np	20	1	99	57	2	-	-	-	-	-	-	-	-		-	-
*KER- 01	np	20	2	41	54	1	-	-	-	-	-	-	-	-		-	-

Annexe 3-2 Résultats des datations U-Th-Pb par LA-ICP-MS (3/8)

Sample	Grain loc.	spot (µm)	BSE ID	[Th] ppm	[U] ppm	Th/U	Isotopic ratios						Apparent age (Ma)		Age (Ma)	
							$^{207}Pb/^{235}U$	± 2σ	$^{206}Pb/^{238}U$	± 2σ	$^{208}Pb/^{232}Th$	± 2σ	$^{206}Pb/^{238}U$	± 2σ	$^{208}Pb/^{232}Th$	± 2σ
*KER- 01	np	20	3	6	36	0	-	-	-	-	-	-	-	-	-	-
*KER- 01	np	20	4	1532	77	20	-	-	-	-	-	-	-	-	-	-
*KER- 01	np	20	5	1756	64	27	-	-	-	-	-	-	-	-	-	-
*KER- 01	np	20	6	3497	76	46	0.089	0.029	0.0019	0.0003	0.0004	0.00003	12.0	1.7	8.1	0.4
*KER- 02	np	20		4540	87	52	0.014	0.023	0.0012	0.0002	0.00037	0.00003	7.5	1.4	7.5	0.3
*KER- 02	np	20		3818	83	46	0.023	0.023	0.0014	0.0002	0.00037	0.00003	9.0	1.5	7.5	0.4
*KER- 02	np	20		3800	68	56	0.006	0.028	0.0016	0.0003	0.00036	0.00003	10.1	1.7	7.3	0.3
*KER- 02	np	20		2167	112	19	0.051	0.021	0.0016	0.0002	0.00039	0.00003	10.4	1.5	7.8	0.5
*KER- 03	np	20		1245	56	22	0.057	0.037	0.0015	0.0003	0.00035	0.00003	9.9	2.0	7.1	0.5
SOY- 01	c	11	1	22330	1930	12	0.021	0.003	0.0019	0.0001	0.00058	0.00003	12.2	0.6	11.6	0.4
SOY- 01	c	11	2	21305	1799	12	0.021	0.003	0.0019	0.0001	0.00058	0.00003	11.9	0.6	11.7	0.4
SOY- 01	c	11	3	21613	1804	12	0.021	0.003	0.0019	0.0001	0.00057	0.00003	12.4	0.6	11.6	0.4
SOY- 01	c	11	4	20137	1990	10	0.022	0.003	0.0020	0.0001	0.00060	0.00003	12.7	0.6	12.1	0.5
SOY- 01	c	11	5	21940	1784	12	0.021	0.003	0.0019	0.0001	0.00058	0.00003	12.1	0.6	11.7	0.4
SOY- 01	c	11	6	19585	1665	12	0.021	0.003	0.0019	0.0001	0.00058	0.00003	12.2	0.6	11.6	0.4
SOY- 01	c	11	7	21605	1933	11	0.020	0.003	0.0018	0.0001	0.00058	0.00003	11.8	0.6	11.8	0.4
SOY- 01	c	11	8	23486	1829	13	0.021	0.003	0.0018	0.0001	0.00057	0.00003	11.9	0.6	11.4	0.4
SOY- 01	c	11	9	23080	1895	12	0.020	0.003	0.0019	0.0001	0.00058	0.00003	12.1	0.6	11.7	0.4
SOY- 01	c	11	10	23213	2117	11	0.021	0.003	0.0019	0.0001	0.00058	0.00003	12.2	0.6	11.8	0.4
SOY- 01	c	11	11	19485	1534	13	0.024	0.004	0.0019	0.0001	0.00058	0.00003	12.2	0.7	11.6	0.4
SOY- 01	c	11	12	21970	1650	13	0.020	0.003	0.0019	0.0001	0.00057	0.00003	12.0	0.6	11.6	0.4
SOY- 01	r	11	13	13320	581	23	0.023	0.007	0.0020	0.0002	0.00058	0.00003	13.0	1.0	11.7	0.5
SOY- 01	r	11	14	12748	619	21	0.028	0.006	0.0020	0.0002	0.00059	0.00003	12.6	0.9	11.9	0.5
SOY- 01	r	11	15	13035	610	21	0.028	0.007	0.0020	0.0002	0.00057	0.00003	13.1	1.0	11.6	0.5
SOY- 01	r	11	16	8771	389	23	0.045	0.013	0.0023	0.0002	0.00059	0.00003	15.0	1.2	12.0	0.5
SOY- 01	r	11	17	8745	398	22	0.045	0.013	0.0023	0.0002	0.00060	0.00003	14.5	1.2	12.0	0.5
SOY- 01	r	11	18	8439	395	21	0.055	0.011	0.0023	0.0002	0.00060	0.00003	14.5	1.1	12.1	0.5
SOY- 01	r	11	19	9550	455	21	0.052	0.010	0.0023	0.0002	0.00059	0.00003	14.8	1.1	12.0	0.5
SOY- 01	r	11	20	9278	440	21	0.055	0.011	0.0023	0.0002	0.00060	0.00003	14.7	1.2	12.2	0.5
SOY- 01	r	11	21	8970	425	21	0.046	0.011	0.0023	0.0002	0.00060	0.00003	14.7	1.1	12.2	0.5
SOY- 01	r	11	22	8717	472	18	0.028	0.009	0.0020	0.0002	0.00059	0.00003	13.0	1.0	11.8	0.5
SOY- 01	r	11	23	8840	481	18	0.016	0.008	0.0020	0.0002	0.00059	0.00003	12.7	1.0	11.8	0.5
SOY- 01	r	11	24	9738	504	19	0.019	0.008	0.0021	0.0002	0.00058	0.00003	13.4	1.0	11.7	0.5
*SOY- 02	z1	20		10257	368	28	0.021	0.007	0.0014	0.0001	0.00037	0.00003	9.0	0.7	7.5	0.3
*SOY- 02	z1	20		2674	124	22	0.052	0.023	0.0017	0.0002	0.00041	0.00003	11.1	1.6	8.2	0.5
*SOY- 02	z1	20		2863	89	32	0.028	0.029	0.0017	0.0003	0.00040	0.00003	11.1	1.7	8.0	0.4
*SOY- 02	z1	20		2122	79	27	0.051	0.029	0.0016	0.0003	0.00037	0.00003	10.5	1.8	7.6	0.5
*SOY- 02	z1	20		3084	99	31	0.039	0.026	0.0014	0.0002	0.00038	0.00003	9.2	1.6	7.7	0.4

Annexe 3-2 Résultats des datations U-Th-Pb par LA-ICP-MS (4/8)

Sample	Grain loc.	spot (µm)	BSE ID	[Th] ppm	[U] ppm	Th/U	Isotopic ratios						Apparent age (Ma)		Age (Ma)	
							$^{207}Pb/^{235}U$	± 2σ	$^{206}Pb/^{238}U$	± 2σ	$^{208}Pb/^{232}Th$	± 2σ	$^{206}Pb/^{238}U$	± 2σ	$^{208}Pb/^{232}Th$	± 2σ
*SOY- 02	z2	20		3939	154	26	0.015	0.017	0.0014	0.0002	0.00036	0.00003	8.7	1.1	7.3	0.4
*SOY- 02	z2	20		3692	133	28	0.013	0.019	0.0015	0.0002	0.00037	0.00003	9.4	1.2	7.4	0.4
*SOY- 02	z2	20		3481	108	32	0.004	0.023	0.0016	0.0002	0.00035	0.00003	10.1	1.4	7.2	0.4
*SOY- 02	z2	20		2893	103	28	0.025	0.021	0.0017	0.0002	0.00036	0.00003	11.0	1.4	7.3	0.4
*SOY- 02	z2	20		4054	134	30	0.011	0.016	0.0014	0.0002	0.00035	0.00003	9.2	1.2	7.1	0.3
E2R- 01	np	11		15287	322	47	0.019	0.007	0.0020	0.0002	0.00061	0.00003	13.0	1.1	12.4	0.5
E2R- 01	np	11		15853	314	51	0.019	0.006	0.0020	0.0002	0.00062	0.00003	12.7	1.1	12.6	0.5
E2R- 01	np	11		16404	325	50	0.016	0.008	0.0020	0.0002	0.00062	0.00003	12.6	1.1	12.5	0.5
E2R- 01	np	11		18204	331	55	0.018	0.008	0.0021	0.0002	0.00061	0.00003	13.7	1.2	12.3	0.5
E2R- 01	np	11		18489	326	57	0.024	0.008	0.0021	0.0002	0.00063	0.00003	13.7	1.2	12.7	0.5
E2R- 01	np	11		12309	214	57	0.027	0.013	0.0019	0.0002	0.00059	0.00003	12.4	1.3	11.9	0.5
E2R- 01	np	11		11772	214	55	0.031	0.012	0.0022	0.0002	0.00059	0.00003	14.1	1.4	11.9	0.5
E2R- 01	np	11		11598	222	52	0.026	0.012	0.0020	0.0002	0.00060	0.00003	13.1	1.4	12.0	0.5
E2R- 01	np	11		10577	204	52	0.026	0.011	0.0020	0.0002	0.00060	0.00003	12.8	1.5	12.2	0.5
E2R- 01	np	11		11517	202	57	0.029	0.011	0.0021	0.0002	0.00059	0.00003	13.2	1.4	12.0	0.5
E2R- 01	np	11		11248	213	53	0.029	0.013	0.0022	0.0002	0.00060	0.00003	14.0	1.4	12.2	0.5
E2R- 01	np	11		10204	253	40	0.015	0.008	0.0018	0.0002	0.00059	0.00003	11.5	1.2	11.9	0.5
E2R- 01	np	11		12748	316	40	0.012	0.007	0.0019	0.0002	0.00058	0.00003	11.9	1.1	11.7	0.5
E2R- 01	np	11		15703	347	45	0.012	0.007	0.0019	0.0002	0.00058	0.00003	12.4	1.1	11.6	0.5
E2R- 01	np	11		9367	272	34	0.016	0.008	0.0019	0.0002	0.00058	0.00003	11.9	1.2	11.7	0.5
E2R- 01	np	11		9402	269	35	0.024	0.007	0.0020	0.0002	0.00058	0.00003	12.9	1.2	11.8	0.5
E2R- 01	np	11		5247	148	36	0.028	0.012	0.0021	0.0003	0.00058	0.00003	13.3	1.7	11.8	0.5
E2R- 01	np	11		6492	182	36	0.023	0.023	0.0024	0.0003	0.00060	0.00003	15.6	2.0	12.2	0.5
E2R- 01	np	11		9138	272	34	0.020	0.009	0.0020	0.0002	0.00059	0.00003	12.8	1.2	11.8	0.5
E2R- 01	np	11		5194	127	41	0.056	0.019	0.0022	0.0003	0.00059	0.00003	14.3	2.0	11.9	0.5
E2R- 01	np	11		6497	135	48	0.049	0.018	0.0022	0.0003	0.00059	0.00003	13.9	1.8	12.0	0.5
E2R- 08	c	11		9380	1288	7	0.020	0.005	0.0020	0.0002	0.00060	0.00003	13.1	1.0	12.2	0.6
E2R- 08	c	11		9238	1124	8	0.027	0.004	0.0020	0.0001	0.00063	0.00003	12.8	0.8	12.7	0.5
E2R- 08	c	11		11701	1504	8	0.022	0.005	0.0019	0.0002	0.00061	0.00003	12.4	0.9	12.3	0.6
E2R- 08	r	11		3379	312	11	0.031	0.009	0.0021	0.0002	0.00060	0.00003	13.8	1.5	12.2	0.7
E2R- 08	r	11		3924	381	10	0.038	0.009	0.0022	0.0002	0.00063	0.00003	14.3	1.3	12.7	0.6
E2R- 08	c	11		11112	1216	9	0.022	0.004	0.0020	0.0001	0.00062	0.00003	13.1	0.8	12.5	0.5
E2R- 08	c	11		10504	1190	9	0.026	0.004	0.0020	0.0001	0.00061	0.00003	13.0	0.8	12.4	0.5
E2R- 08	c	11		8390	1334	6	0.019	0.004	0.0020	0.0001	0.00062	0.00003	13.1	0.8	12.6	0.5
E2R- 08	c	11		8557	1243	7	0.023	0.004	0.0020	0.0001	0.00061	0.00003	12.6	0.7	12.3	0.5
E2R- 08	c	11		9127	1262	7	0.024	0.004	0.0020	0.0001	0.00062	0.00003	12.9	0.7	12.5	0.5
E2R- 08	c	11		9533	1273	7	0.024	0.004	0.0020	0.0001	0.00063	0.00003	12.8	0.7	12.8	0.5
E2R- 08	r	11		3703	362	10	0.036	0.012	0.0019	0.0002	0.00063	0.00003	12.5	1.1	12.8	0.6

Annexe 3-2 Résultats des datations U-Th-Pb par LA-ICP-MS (5/8)

Sample	Grain loc.	spot (µm)	BSE ID	[Th] ppm	[U] ppm	Th/U	Isotopic ratios						Apparent age (Ma)		Age (Ma)	
							$^{207}Pb/^{235}U$	± 2σ	$^{206}Pb/^{238}U$	± 2σ	$^{208}Pb/^{232}Th$	± 2σ	$^{206}Pb/^{238}U$	± 2σ	$^{208}Pb/^{232}Th$	± 2σ
E2R- 08	r	11		4309	387	11	0.043	0.011	0.0022	0.0002	0.00064	0.00003	14.2	1.2	12.9	0.6
E2R- 08	r	11		5804	425	14	0.032	0.010	0.0020	0.0002	0.00062	0.00003	13.1	1.1	12.6	0.5
E2R- 08	r	11		4396	346	13	0.037	0.012	0.0022	0.0002	0.00064	0.00003	13.9	1.2	13	0.6
E2R- 08	r	11		4242	324	13	0.041	0.013	0.0023	0.0002	0.00061	0.00003	15.0	1.2	12.4	0.6
E2R- 08	r	11		4088	334	12	0.049	0.013	0.0022	0.0002	0.00063	0.00003	13.9	1.3	12.8	0.6
E2R- 09	c	11	1	13192	708	19	0.041	0.009	0.0021	0.0002	0.00064	0.00003	13.8	1.3	12.9	0.6
E2R- 09	c	11	2	13911	649	21	0.031	0.007	0.0020	0.0002	0.00061	0.00003	12.8	1.0	12.4	0.5
E2R- 09	c	11	3	15095	718	21	0.035	0.006	0.0021	0.0002	0.00063	0.00003	13.3	0.9	12.8	0.5
E2R- 09	c	11	4	18745	741	25	0.033	0.006	0.0021	0.0002	0.00062	0.00003	13.8	0.9	12.6	0.5
E2R- 09	c	11	5	21708	690	31	0.034	0.006	0.0020	0.0002	0.00061	0.00003	13.0	0.9	12.3	0.5
E2R- 09	c	11	6	21968	487	45	0.092	0.018	0.0027	0.0003	0.00061	0.00003	17.4	1.9	12.4	0.5
E2R- 09	c	11	7	13252	374	35	0.020	0.008	0.0020	0.0002	0.00061	0.00003	12.6	1.2	12.3	0.5
E2R- 09	c	11	8	13086	393	33	0.017	0.006	0.0020	0.0002	0.00063	0.00003	12.8	1.1	12.7	0.5
E2R- 09	c	11	9	17657	463	38	0.022	0.006	0.0020	0.0002	0.00063	0.00003	12.6	1.0	12.7	0.5
E2R- 09	c	11	10	18673	518	36	0.023	0.006	0.0021	0.0002	0.00064	0.00003	13.6	1.1	13.0	0.5
E2R- 09	c	11	11	15229	517	29	0.030	0.008	0.0020	0.0002	0.00062	0.00003	12.6	1.1	12.5	0.5
E2R- 09	c	11	12	10533	445	24	0.029	0.007	0.0020	0.0002	0.00064	0.00003	12.9	1.1	13.0	0.5
E2R- 09	r	11	13	4695	171	27	0.046	0.017	0.0023	0.0003	0.00065	0.00003	15.0	1.9	13.1	0.6
E2R- 09	r	11	14	5507	167	33	0.067	0.019	0.0027	0.0003	0.00063	0.00003	17.1	1.9	12.7	0.6
E2R- 09	r	11	15	6087	164	37	0.073	0.021	0.0024	0.0003	0.00063	0.00003	15.6	1.9	12.8	0.6
E2R- 09	r	11	16	8343	201	42	0.069	0.020	0.0028	0.0003	0.00062	0.00003	17.8	1.8	12.6	0.5
E2R- 09	r	11	17	6278	214	29	0.032	0.012	0.0020	0.0002	0.00062	0.00003	13.0	1.5	12.5	0.5
E2R- 09	r	11	18	7522	240	31	0.028	0.011	0.0021	0.0002	0.00062	0.00003	13.3	1.4	12.5	0.5
E2R- 09	r	11	19	7477	284	26	0.018	0.008	0.0021	0.0002	0.00064	0.00003	13.4	1.4	12.9	0.6
E2R- 09	r	11	20	8102	290	28	0.027	0.008	0.0022	0.0002	0.00061	0.00003	13.9	1.4	12.3	0.5
E2R- 09	r	11	21	8731	297	29	0.023	0.008	0.0021	0.0002	0.00063	0.00003	13.3	1.3	12.7	0.5
E2R- 09	c	11	22	11415	384	30	0.029	0.008	0.0019	0.0002	0.00063	0.00003	12.5	1.2	12.7	0.5
E2R- 09	c	11	23	13635	456	30	0.032	0.008	0.0021	0.0002	0.00061	0.00003	13.8	1.1	12.4	0.5
E2R- 09	c	11	24	15169	468	32	0.031	0.006	0.0021	0.0002	0.00062	0.00003	13.4	1.1	12.5	0.5
E2R- 11	c	11	1	51748	784	66	0.036	0.009	0.0020	0.0002	0.00060	0.00003	13.0	1.3	12.2	0.5
E2R- 11	c	11	2	55906	802	70	0.033	0.007	0.0021	0.0002	0.00060	0.00003	13.4	1.1	12.2	0.5
E2R- 11	c	11	3	49406	698	71	0.037	0.008	0.0021	0.0002	0.00060	0.00003	13.8	1.1	12.1	0.5
E2R- 11	c	11	4	48583	808	60	0.032	0.008	0.0020	0.0002	0.00060	0.00003	13.0	1.2	12.0	0.5
E2R- 11	c	11	5	45793	724	63	0.037	0.008	0.0021	0.0002	0.00061	0.00003	13.6	1.1	12.3	0.5
E2R- 11	c	11	6	42666	675	63	0.039	0.008	0.0020	0.0002	0.00060	0.00003	12.7	1.2	12.1	0.5
E2R- 11	r	11	7	7266	430	17	0.022	0.007	0.0020	0.0002	0.00061	0.00003	13.0	1.1	12.4	0.6
E2R- 11	r	11	8	7153	429	17	0.016	0.007	0.0022	0.0002	0.00061	0.00003	14.0	1.3	12.4	0.6
E2R- 11	r	11	9	6776	423	16	0.014	0.006	0.0018	0.0002	0.00063	0.00003	11.5	1.1	12.6	0.6
E2R- 11	r	11	10	6478	404	16	0.017	0.007	0.0020	0.0002	0.00061	0.00003	12.9	1.2	12.4	0.6

Annexe 3-2 Résultats des datations U-Th-Pb par LA-ICP-MS (6/8)

Sample	Grain loc.	spot (µm)	BSE ID	[Th] ppm	[U] ppm	Th/U	Isotopic ratios $^{207}Pb/^{235}U$	± 2σ	$^{206}Pb/^{238}U$	± 2σ	$^{208}Pb/^{232}Th$	± 2σ	Apparent age (Ma) $^{206}Pb/^{238}U$	± 2σ	Age (Ma) $^{208}Pb/^{232}Th$	± 2σ
E2R- 11	r	11	11	6287	384	16	0.017	0.006	0.0020	0.0002	0.00061	0.00003	12.9	1.2	12.4	0.6
E2R- 11	r	11	12	6653	403	17	0.014	0.006	0.0020	0.0002	0.00062	0.00003	12.8	1.1	12.6	0.6
E2R- 11	c	11	13	43833	679	65	0.035	0.007	0.0022	0.0002	0.00061	0.00003	13.9	0.9	12.3	0.5
E2R- 11	c	11	14	45416	749	61	0.035	0.007	0.0022	0.0002	0.0006	0.00003	13.9	0.9	12.1	0.5
E2R- 11	c	11	15	43603	739	59	0.043	0.007	0.0022	0.0002	0.00061	0.00003	14.1	0.9	12.3	0.5
E2R- 11	c	11	16	51614	676	76	0.032	0.008	0.0022	0.0002	0.00061	0.00003	14.3	1.0	12.3	0.5
E2R- 11	c	11	17	46727	622	75	0.041	0.008	0.0022	0.0002	0.0006	0.00003	13.8	0.9	12.2	0.5
E2R- 11	c	11	18	38965	539	72	0.045	0.009	0.0022	0.0002	0.00061	0.00003	14.4	1.0	12.4	0.5
E2R- 11	r	11	19	7062	327	22	0.020	0.013	0.0022	0.0002	0.00062	0.00003	14.1	1.3	12.5	0.5
E2R- 11	r	11	20	8011	329	24	0.039	0.011	0.0022	0.0002	0.00062	0.00003	14.0	1.2	12.6	0.5
E2R- 11	r	11	21	8226	327	25	0.034	0.013	0.0022	0.0002	0.00063	0.00003	14.1	1.2	12.7	0.5
E2R- 11	r	11	22	8776	330	27	0.045	0.012	0.0023	0.0002	0.00062	0.00003	14.8	1.3	12.5	0.5
E2R- 11	r	11	23	9803	330	30	0.039	0.011	0.0020	0.0002	0.00062	0.00003	12.8	1.2	12.5	0.5
E2R- 11	r	11	24	11039	335	33	0.042	0.012	0.0021	0.0002	0.00061	0.00003	13.7	1.2	12.4	0.5
SAV- 01	np	20		2266	42	54	0.152	0.038	0.0027	0.0004	0.00035	0.00003	17.3	2.6	7.1	0.4
SAV- 01	np	20		1644	118	14	0.042	0.011	0.0016	0.0002	0.00033	0.00003	10.2	1.2	6.7	0.4
SAV- 02	np	20		4332	37	116	0.411	0.060	0.0045	0.0006	0.00034	0.00003	28.7	3.7	6.8	0.3
SAV- 02	np	20		1753	49	36	0.032	0.038	0.0016	0.0005	0.00033	0.00003	10.5	2.9	6.7	0.5
SAV- 02	np	20		1551	50	31	0.022	0.026	0.0016	0.0003	0.00033	0.00003	10.0	1.9	6.6	0.4
SAV- 03	np	20	1	5054	107	47	0.095	0.019	0.0021	0.0002	0.00034	0.00003	13.5	1.4	6.9	0.3
SAV- 03	np	20	2	4525	118	38	0.075	0.014	0.0018	0.0002	0.00035	0.00003	11.5	1.2	7.0	0.3
SAV- 03	np	20	3	4998	140	36	0.018	0.007	0.0012	0.0002	0.00033	0.00000	7.7	1.0	6.6	0.3
SAV- 03	np	20	4	2415	57	42	0.001	0.024	0.0018	0.0003	0.00034	0.00003	11.6	2.0	6.8	0.4
SAV- 03	np	20	5	1913	53	36	0.012	0.024	0.0021	0.0003	0.00032	0.00003	13.5	2.0	6.5	0.4
SAV- 03	np	20	6	1439	46	31	0.012	0.026	0.0015	0.0003	0.00032	0.00003	9.7	2.0	6.5	0.4
SAV- 03	np	20	7	1080	32	33	0.064	0.036	0.0013	0.0003	0.00033	0.00003	8.1	2.2	6.7	0.4
SAV- 03	np	20	8	6383	141	45	0.026	0.009	0.0012	0.0002	0.00032	0.00000	7.8	0.9	6.5	0.3
SAV- 03	np	20	9	3088	41	76	0.043	0.030	0.0020	0.0004	0.00033	0.00003	12.8	2.4	6.7	0.3
*SAV- 04	np	20		1480	85	17	0.047	0.029	0.0016	0.0003	0.00035	0.00003	10.0	1.1	7.0	0.5
*SAV- 04	np	20		2383	59	40	0.019	0.039	0.0014	0.0003	0.00033	0.00003	9.0	1.5	6.8	0.4
*SAV- 04	np	20		1861	60	31	0.054	0.039	0.0014	0.0003	0.00033	0.00003	9.0	1.5	6.8	0.4
*SAV- 04	np	20		1859	65	28	0.033	0.040	0.0020	0.0003	0.00034	0.00003	12.6	1.4	6.8	0.5
*SAV- 04	np	20		1883	61	31	0.063	0.038	0.0019	0.0003	0.00034	0.00003	12.3	1.4	6.8	0.5
SMC- 01	c	20	1	1772	13	133	1.319	0.179	0.0122	0.0016	0.00040	0.00003	78.1	10.4	8.1	0.4
SMC- 01	c	20	2	1939	13	147	1.476	0.180	0.0140	0.0015	0.00040	0.00003	89.9	9.8	8.1	0.4
SMC- 01	c	20	3	1756	16	111	0.918	0.133	0.0082	0.0011	0.00039	0.00003	52.4	7.4	7.8	0.4
SMC- 01	c	20	4	1352	14	97	0.690	0.151	0.0070	0.0011	0.00039	0.00003	44.7	7.3	7.8	0.5

Annexe 3-2 Résultats des datations U-Th-Pb par LA-ICP-MS (7/8)

Sample	Grain loc.	spot (µm)	BSE ID	[Th] ppm	[U] ppm	Th/U	Isotopic ratios						Apparent age (Ma)		Age (Ma)	
							$^{207}Pb/^{235}U$	± 2σ	$^{206}Pb/^{238}U$	± 2σ	$^{208}Pb/^{232}Th$	± 2σ	$^{206}Pb/^{238}U$	± 2σ	$^{208}Pb/^{232}Th$	± 2σ
SMC- 01	c	20	5	1342	15	92	0.899	0.156	0.0094	0.0014	0.00041	0.00003	60.6	9.0	8.4	0.5
SMC- 01	c	20	6	1640	14	113	0.896	0.156	0.0086	0.0013	0.00037	0.00003	55.0	8.2	7.5	0.5
SMC- 01	r	20	7	3877	37	104	0.094	0.054	0.0025	0.0005	0.00032	0.00003	15.8	3.1	6.4	0.3
SMC- 01	r	20	8	3829	35	110	0.038	0.027	0.0019	0.0004	0.00030	0.00003	12.2	2.5	6.1	0.3
SMC- 01	r	20	9	1275	32	40	0.033	0.042	0.0019	0.0004	0.00030	0.00003	11.9	2.8	6.1	0.4
SMC- 01	r	20	10	1027	22	47	0.103	0.046	0.0017	0.0006	0.00030	0.00003	10.7	3.6	6.0	0.5
SMC- 01	r	20	11	701	23	31	0.037	0.051	0.0015	0.0005	0.00032	0.00003	9.4	3.1	6.4	0.5
SMC- 01	r	20	12	3099	39	80	0.051	0.027	0.0013	0.0003	0.00031	0.00003	8.6	1.9	6.3	0.3
SMC- 01	r	20	13	3471	31	112	0.175	0.053	0.0024	0.0005	0.00032	0.00003	15.2	3.1	6.5	0.3
***ISO-** 01	np	25	1	13394	179	75	0.042	0.007	0.0055	0.0003	0.001	0.00003	35.6	1.8	20.3	0.8
*ISO- 01	np	25	2	18303	176	104	0.029	0.007	0.0064	0.0003	0.001	0.00003	41.0	2.1	20.3	0.8
*ISO- 01	np	25	3	19735	132	149	0.035	0.009	0.0080	0.0004	0.001	0.00003	51.0	2.6	20.2	0.8
*ISO- 01	np	25	4	19388	74	261	0.038	0.015	0.0143	0.0007	0.001	0.00003	91.3	4.6	20.2	0.8
*ISO- 01	np	25	5	18284	63	289	0.081	0.019	0.0151	0.0008	0.00101	0.00003	96.9	4.9	20.3	0.8
*ISO- 01	np	25	6	22646	133	170	0.046	0.009	0.0086	0.0004	0.00101	0.00003	55.2	2.7	20.3	0.8
*ISO- 01	np	25	7	12299	137	90	0.414	0.025	0.0098	0.0005	0.00109	0.00003	62.8	3.0	22	0.9
*ISO- 01	np	25	8	19319	154	126	0.045	0.008	0.0074	0.0004	0.00102	0.00003	47.3	2.3	20.7	0.8
*ISO- 01	np	25	9	13873	154	90	0.054	0.008	0.0064	0.0003	0.00101	0.00003	40.9	2.1	20.5	0.8
*ISO- 01	np	25	10	5307	129	41	0.075	0.010	0.0050	0.0003	0.00106	0.00003	31.8	1.7	21.4	0.8
*ISO- 01	np	25	11	3992	116	34	0.063	0.010	0.0046	0.0003	0.00103	0.00003	29.5	1.7	20.9	0.8
*ISO- 01	np	25	12	12337	146	85	0.078	0.009	0.0062	0.0003	0.00103	0.00003	39.8	2.0	20.9	0.8
MTV- 01	np	20	1	5835	105	55	0.117	0.017	0.0046	0.0003	0.00109	0.00003	29.3	2.0	22.0	0.8
MTV- 01	np	20	2	8301	105	79	0.037	0.011	0.0041	0.0003	0.00110	0.00003	26.2	1.8	22.3	0.8
MTV- 01	np	20	3	11059	143	77	0.025	0.009	0.0042	0.0003	0.00112	0.00003	27.0	1.7	22.5	0.8
MTV- 01	np	20	4	8683	149	58	0.168	0.016	0.0052	0.0003	0.00115	0.00003	33.6	1.9	23.3	0.9
MTV- 01	np	20	5	5116	158	32	0.153	0.017	0.0047	0.0003	0.00116	0.00003	30.4	1.9	23.3	0.9
MTV- 01	np	20	6	6425	204	32	0.058	0.008	0.0040	0.0002	0.00116	0.00003	26.0	1.4	23.4	0.9
MTV- 01	np	20	7	5158	50	103	0.079	0.018	0.0048	0.0004	0.00115	0.00003	30.6	2.5	23.2	0.9
MTV- 01	np	20	8	5367	52	103	0.064	0.020	0.0044	0.0004	0.00115	0.00003	28.4	2.4	23.2	0.9
MTV- 01	np	20	9	5272	54	97	0.065	0.017	0.0042	0.0004	0.00114	0.00003	26.8	2.4	23.1	0.9
MTV- 01	np	20	10	2258	79	29	0.036	0.014	0.0040	0.0003	0.00114	0.00006	25.5	2.0	23.0	0.9
MTV- 02	np	20		5745	64	90	0.074	0.018	0.0045	0.0004	0.00114	0.00003	28.9	2.3	22.9	0.9
MTV- 02	np	20		6950	60	116	0.200	0.027	0.0055	0.0005	0.00115	0.00003	35.6	2.8	23.2	0.9
MTV- 02	np	20		6933	51	137	0.276	0.034	0.0067	0.0005	0.00117	0.00003	43.3	3.2	23.6	0.9
MTV- 02	np	20		3172	51	62	0.550	0.049	0.0088	0.0006	0.00118	0.00006	56.6	3.9	23.9	0.9
MTC- 01	np	9		7827	18	443	0.053	0.238	0.0056	0.0021	0.00159	0.00006	44.5	10.0	32.1	1.3

Annexe 3-2 Résultats des datations U-Th-Pb par LA-ICP-MS (8/8)

Sample	Grain loc.	spot (µm)	BSE ID	[Th] ppm	[U] ppm	Th/U	Isotopic ratios						Apparent age (Ma)		Age (Ma)	
							$^{207}Pb/^{235}U$	± 2σ	$^{206}Pb/^{238}U$	± 2σ	$^{208}Pb/^{232}Th$	± 2σ	$^{206}Pb/^{238}U$	± 2σ	$^{208}Pb/^{232}Th$	± 2σ
MTC- 01	np	9		17012	33	523	0.217	0.148	0.0077	0.0016	0.00156	0.00006	35.4	10.5	31.6	1.2
MTC- 02	np	9		13532	61	221	0.097	0.078	0.0109	0.0013	0.00157	0.00006	42.6	7.8	31.8	1.2
MTC- 02	np	9		10298	23	453	0.457	0.208	0.0103	0.0022	0.00159	0.00006	30.9	9.0	32.1	1.2
MTC- 02	np	9		8365	40	210	0.718	0.196	0.0142	0.0022	0.00159	0.00006	47.9	10.9	32.1	1.4
MTC- 02	np	9		9831	20	490	1.350	0.294	0.0139	0.0028	0.00159	0.00006	47.6	9.7	32.0	1.3
MTC- 02	np	9		8306	19	437	0.832	0.242	0.0108	0.0024	0.00161	0.00006	34.7	7.7	32.5	1.3
MTC- 03	np	9		9143	27	333	0.213	0.113	0.0069	0.0016	0.00159	0.00006	39.5	10.3	32.1	1.2
MTC- 03	np	9		8763	29	303	0.178	0.165	0.0055	0.0017	0.00160	0.00006	69.7	8.4	32.2	1.3
MTC- 03	np	9		11211	38	294	-0.043	0.106	0.0066	0.0012	0.00157	0.00006	66.2	14.2	31.7	1.2
MTC- 03	np	9		12114	33	363	0.017	0.151	0.0048	0.0014	0.00165	0.00006	90.9	14.0	33.2	1.3
MTC- 03	np	9		11931	33	364	0.222	0.150	0.0075	0.0017	0.00161	0.00006	88.8	17.9	32.5	1.3
MTC- 03	np	9		11155	38	296	-0.011	0.136	0.0074	0.0015	0.00162	0.00006	69.2	15.1	32.6	1.3
MTC- 03	np	9		16676	42	399	0.028	0.116	0.0054	0.0012	0.00165	0.00006	35.8	13.4	33.3	1.3
MTC- 03	np	9		10883	41	268	0.166	0.139	0.0062	0.0016	0.00163	0.00006	49.5	10.3	32.9	1.4
XMTC- 01	np	20	1	646	282	2	0.040	0.010	0.0055	0.0004	0.00166	0.00009	40.2	3.2	33.6	2.1
XMTC- 02	np	20		9321	293	32	0.057	0.010	0.0078	0.0005	0.00177	0.00006	42.2	2.7	35.6	1.5
XMTC- 02	np	20		6304	189	33	0.086	0.018	0.0066	0.0005	0.00173	0.00006	43.3	2.4	34.9	1.5
XMTC- 03	np	20		7252	306	24	0.051	0.011	0.0064	0.0005	0.00176	0.00006	76.5	5.1	35.5	1.5
XMTC- 03	np	20		10385	216	48	0.153	0.020	0.0095	0.0006	0.00168	0.00006	41.2	2.8	33.9	1.4
XMTC- 04	np	20		9913	148	67	0.131	0.023	0.0119	0.0008	0.00179	0.00006	61.0	3.8	36.2	1.5
XMTC- 05	np	20		8909	298	30	0.089	0.018	0.0063	0.0005	0.00171	0.00006	50.4	3.0	34.5	1.5
XMTC- 05	np	20		10506	565	19	0.057	0.010	0.0066	0.0004	0.00171	0.00006	42.2	3.3	34.5	1.4
XMTC- 05	np	20		8920	363	25	0.080	0.009	0.0067	0.0004	0.00174	0.00006	35.6	2.6	35.2	1.4

Annexe 4-1 Résultats des datations U-Th-Pb par LA-ICP-MS (1/2)

Sample	Grain	spot (µm)	BSE ID	[Th] ppm	[U] ppm	Th/U	Isotopic ratios						Age (Ma)	
							$^{207}Pb/^{235}U$	± 2σ	$^{206}Pb/^{238}U$	± 2σ	$^{208}Pb/^{232}Th$	± 2σ	$^{208}Pb/^{232}Th$	± 2σ
E2R-	Mnz01	11	1	15287	322	47	0.019	0.007	0.0020	0.0002	0.00061	0.00003	12.4	0.5
E2R-	Mnz01	11	2	15853	314	51	0.019	0.006	0.0020	0.0002	0.00062	0.00003	12.6	0.5
E2R-	Mnz01	11	3	16404	325	50	0.016	0.008	0.0020	0.0002	0.00062	0.00003	12.5	0.5
E2R-	Mnz01	11	4	18204	331	55	0.018	0.008	0.0021	0.0002	0.00061	0.00003	12.3	0.5
E2R-	Mnz01	11	5	18489	326	57	0.024	0.008	0.0021	0.0002	0.00063	0.00003	12.7	0.5
E2R-	Mnz01	11	6	12309	214	57	0.027	0.013	0.0019	0.0002	0.00059	0.00003	11.9	0.5
E2R-	Mnz01	11	7	11772	214	55	0.031	0.012	0.0022	0.0002	0.00059	0.00003	11.9	0.5
E2R-	Mnz01	11	8	11598	222	52	0.026	0.012	0.0020	0.0002	0.00060	0.00003	12.0	0.5
E2R-	Mnz01	11	9	10577	204	52	0.026	0.011	0.0020	0.0002	0.00060	0.00003	12.2	0.5
E2R-	Mnz01	11	10	11517	202	57	0.029	0.011	0.0021	0.0002	0.00059	0.00003	12.0	0.5
E2R-	Mnz01	11	11	11248	213	53	0.029	0.013	0.0022	0.0002	0.00060	0.00003	12.2	0.5
E2R-	Mnz01	11	12	10204	253	40	0.015	0.008	0.0018	0.0002	0.00059	0.00003	11.9	0.5
E2R-	Mnz01	11	13	12748	316	40	0.012	0.007	0.0019	0.0002	0.00058	0.00003	11.7	0.5
E2R-	Mnz01	11	14	15703	347	45	0.012	0.007	0.0019	0.0002	0.00058	0.00003	11.6	0.5
E2R-	Mnz01	11	15	9367	272	34	0.016	0.008	0.0019	0.0002	0.00058	0.00003	11.7	0.5
E2R-	Mnz01	11	16	9402	269	35	0.024	0.007	0.0020	0.0002	0.00058	0.00003	11.8	0.5
E2R-	Mnz01	11	17	5247	148	36	0.028	0.012	0.0021	0.0003	0.00058	0.00003	11.8	0.5
E2R-	Mnz01	11	18	6492	182	36	0.023	0.023	0.0024	0.0003	0.00060	0.00003	12.2	0.5
E2R-	Mnz01	11	19	9138	272	34	0.020	0.009	0.0020	0.0002	0.00059	0.00003	11.8	0.5
E2R-	Mnz01	11	20	5194	127	41	0.056	0.019	0.0022	0.0003	0.00059	0.00003	11.9	0.5
E2R-	Mnz01	11	21	6497	135	48	0.049	0.018	0.0022	0.0003	0.00059	0.00003	12.0	0.5
E2R-	Mnz02	11	1	9380	1288	7	0.020	0.005	0.0020	0.0002	0.00060	0.00003	12.2	0.6
E2R-	Mnz02	11	2	9238	1124	8	0.027	0.004	0.0020	0.0001	0.00063	0.00003	12.7	0.5
E2R-	Mnz02	11	3	11701	1504	8	0.022	0.005	0.0019	0.0002	0.00061	0.00003	12.3	0.6
E2R-	Mnz02	11	4	3379	312	11	0.031	0.009	0.0021	0.0002	0.00060	0.00003	12.2	0.7
E2R-	Mnz02	11	5	3924	381	10	0.038	0.009	0.0022	0.0002	0.00063	0.00003	12.7	0.6
E2R-	Mnz02	11	6	11112	1216	9	0.022	0.004	0.0020	0.0001	0.00062	0.00003	12.5	0.5
E2R-	Mnz02	11	7	10504	1190	9	0.026	0.004	0.0020	0.0001	0.00061	0.00003	12.4	0.5
E2R-	Mnz02	11	8	8390	1334	6	0.019	0.004	0.0020	0.0001	0.00062	0.00003	12.6	0.5
E2R-	Mnz02	11	9	8557	1243	7	0.023	0.004	0.0020	0.0001	0.00061	0.00003	12.3	0.5
E2R-	Mnz02	11	10	9127	1262	7	0.024	0.004	0.0020	0.0001	0.00062	0.00003	12.5	0.5
E2R-	Mnz02	11	11	9533	1273	7	0.024	0.004	0.0020	0.0001	0.00063	0.00003	12.8	0.5
E2R-	Mnz02	11	12	3703	362	10	0.036	0.012	0.0019	0.0002	0.00063	0.00003	12.8	0.6
E2R-	Mnz02	11	13	4309	387	11	0.043	0.011	0.0022	0.0002	0.00064	0.00003	12.9	0.6
E2R-	Mnz02	11	14	5804	425	14	0.032	0.010	0.0020	0.0002	0.00062	0.00003	12.6	0.5
E2R-	Mnz02	11	15	4396	346	13	0.037	0.012	0.0022	0.0002	0.00064	0.00003	13	0.6
E2R-	Mnz02	11	16	4242	324	13	0.041	0.013	0.0023	0.0002	0.00061	0.00003	12.4	0.6
E2R-	Mnz02	11	17	4088	334	12	0.049	0.013	0.0022	0.0002	0.00063	0.00003	12.8	0.6
E2R-	Mnz03	11	1	13192	708	19	0.041	0.009	0.0021	0.0002	0.00064	0.00003	12.9	0.6
E2R-	Mnz03	11	2	13911	649	21	0.031	0.007	0.0020	0.0002	0.00061	0.00003	12.4	0.5
E2R-	Mnz03	11	3	15095	718	21	0.035	0.006	0.0021	0.0002	0.00063	0.00003	12.8	0.5
E2R-	Mnz03	11	4	18745	741	25	0.033	0.006	0.0021	0.0002	0.00062	0.00003	12.6	0.5
E2R-	Mnz03	11	5	21708	690	31	0.034	0.006	0.0020	0.0002	0.00061	0.00003	12.3	0.5
E2R-	Mnz03	11	6	21968	487	45	0.092	0.018	0.0027	0.0003	0.00061	0.00003	12.4	0.5
E2R-	Mnz03	11	7	13252	374	35	0.020	0.008	0.0020	0.0002	0.00061	0.00003	12.3	0.5
E2R-	Mnz03	11	8	13086	393	33	0.017	0.006	0.0020	0.0002	0.00063	0.00003	12.7	0.5
E2R-	Mnz03	11	9	17657	463	38	0.022	0.006	0.0020	0.0002	0.00063	0.00003	12.7	0.5
E2R-	Mnz03	11	10	18673	518	36	0.023	0.006	0.0021	0.0002	0.00064	0.00003	13.0	0.5
E2R-	Mnz03	11	11	15229	517	29	0.030	0.008	0.0020	0.0002	0.00062	0.00003	12.5	0.5
E2R-	Mnz03	11	12	10533	445	24	0.029	0.007	0.0020	0.0002	0.00064	0.00003	13.0	0.5
E2R-	Mnz03	11	13	4695	171	27	0.046	0.017	0.0023	0.0003	0.00065	0.00003	13.1	0.6
E2R-	Mnz03	11	14	5507	167	33	0.067	0.019	0.0027	0.0003	0.00063	0.00003	12.7	0.6
E2R-	Mnz03	11	15	6087	164	37	0.073	0.021	0.0024	0.0003	0.00063	0.00003	12.8	0.6
E2R-	Mnz03	11	16	8343	201	42	0.069	0.020	0.0028	0.0003	0.00062	0.00003	12.6	0.5
E2R-	Mnz03	11	17	6278	214	29	0.032	0.012	0.0020	0.0002	0.00062	0.00003	12.5	0.5
E2R-	Mnz03	11	18	7522	240	31	0.028	0.011	0.0021	0.0002	0.00062	0.00003	12.5	0.5
E2R-	Mnz03	11	19	7477	284	26	0.018	0.008	0.0021	0.0002	0.00064	0.00003	12.9	0.6
E2R-	Mnz03	11	20	8102	290	28	0.027	0.008	0.0022	0.0002	0.00061	0.00003	12.3	0.5
E2R-	Mnz03	11	21	8731	297	29	0.023	0.008	0.0021	0.0002	0.00063	0.00003	12.7	0.5
E2R-	Mnz03	11	22	11415	384	30	0.029	0.008	0.0019	0.0002	0.00063	0.00003	12.7	0.5
E2R-	Mnz03	11	23	13635	456	30	0.032	0.008	0.0021	0.0002	0.00061	0.00003	12.4	0.5
E2R-	Mnz03	11	24	15169	468	32	0.031	0.006	0.0021	0.0002	0.00062	0.00003	12.5	0.5
E2R-	Mnz04	11	1	51748	784	66	0.036	0.009	0.0020	0.0002	0.00060	0.00003	12.2	0.5
E2R-	Mnz04	11	2	55906	802	70	0.033	0.007	0.0021	0.0002	0.00060	0.00003	12.2	0.5
E2R-	Mnz04	11	3	49406	698	71	0.037	0.008	0.0021	0.0002	0.00060	0.00003	12.1	0.5

Annexe 4-1 Résultats des datations U-Th-Pb par LA-ICP-MS (2/2)

Sample	Grain	spot (µm)	BSE ID	[Th] ppm	[U] ppm	Th/U	Isotopic ratios						Age (Ma)	
							$^{207}Pb/^{235}U$	± 2σ	$^{206}Pb/^{238}U$	± 2σ	$^{208}Pb/^{232}Th$	± 2σ	$^{208}Pb/^{232}Th$	± 2σ
E2R-	Mnz04	11	4	48583	808	60	0.032	0.008	0.0020	0.0002	0.00060	0.00003	12.0	0.5
E2R-	Mnz04	11	5	45793	724	63	0.037	0.008	0.0021	0.0002	0.00061	0.00003	12.3	0.5
E2R-	Mnz04	11	6	42666	675	63	0.039	0.008	0.0020	0.0002	0.00060	0.00003	12.1	0.5
E2R-	Mnz04	11	7	7266	430	17	0.022	0.007	0.0020	0.0002	0.00061	0.00003	12.4	0.6
E2R-	Mnz04	11	8	7153	429	17	0.016	0.007	0.0022	0.0002	0.00061	0.00003	12.4	0.6
E2R-	Mnz04	11	9	6776	423	16	0.014	0.006	0.0018	0.0002	0.00063	0.00003	12.6	0.6
E2R-	Mnz04	11	10	6478	404	16	0.017	0.007	0.0020	0.0002	0.00061	0.00003	12.4	0.6
E2R-	Mnz04	11	11	6287	384	16	0.017	0.006	0.0020	0.0002	0.00061	0.00003	12.4	0.6
E2R-	Mnz04	11	12	6653	403	17	0.014	0.006	0.0020	0.0002	0.00062	0.00003	12.6	0.6
E2R-	Mnz04	11	13	43833	679	65	0.035	0.007	0.0022	0.0002	0.00061	0.00003	12.3	0.5
E2R-	Mnz04	11	14	45416	749	61	0.035	0.007	0.0022	0.0002	0.0006	0.00003	12.1	0.5
E2R-	Mnz04	11	15	43603	739	59	0.043	0.007	0.0022	0.0002	0.00061	0.00003	12.3	0.5
E2R-	Mnz04	11	16	51614	676	76	0.032	0.008	0.0022	0.0002	0.00061	0.00003	12.3	0.5
E2R-	Mnz04	11	17	46727	622	75	0.041	0.008	0.0022	0.0002	0.0006	0.00003	12.2	0.5
E2R-	Mnz04	11	18	38965	539	72	0.045	0.009	0.0022	0.0002	0.00061	0.00003	12.4	0.5
E2R-	Mnz04	11	19	7062	327	22	0.020	0.013	0.0022	0.0002	0.00062	0.00003	12.5	0.5
E2R-	Mnz04	11	20	8011	329	24	0.039	0.011	0.0022	0.0002	0.00062	0.00003	12.6	0.5
E2R-	Mnz04	11	21	8226	327	25	0.034	0.013	0.0022	0.0002	0.00063	0.00003	12.7	0.5
E2R-	Mnz04	11	22	8776	330	27	0.045	0.012	0.0023	0.0002	0.00062	0.00003	12.5	0.5
E2R-	Mnz04	11	23	9803	330	30	0.039	0.011	0.0020	0.0002	0.00062	0.00003	12.5	0.5
E2R-	Mnz04	11	24	11039	335	33	0.042	0.012	0.0021	0.0002	0.00061	0.00003	12.4	0.5

Annexe 5-1 EPMA intensity maps

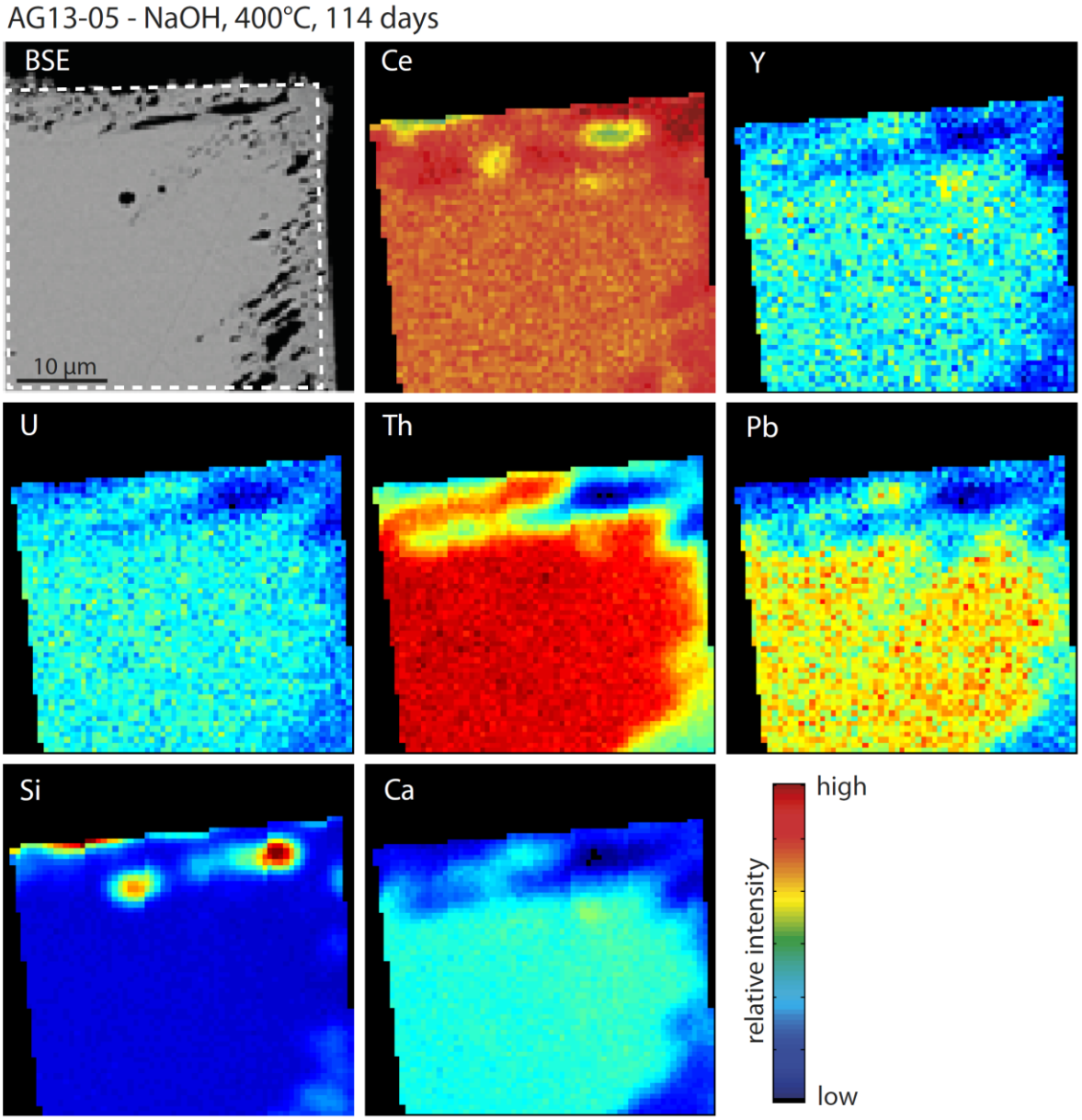

Annexe 5-2 EPMA intensity maps

AG13-03 - NaOH, 500°C, 114 days

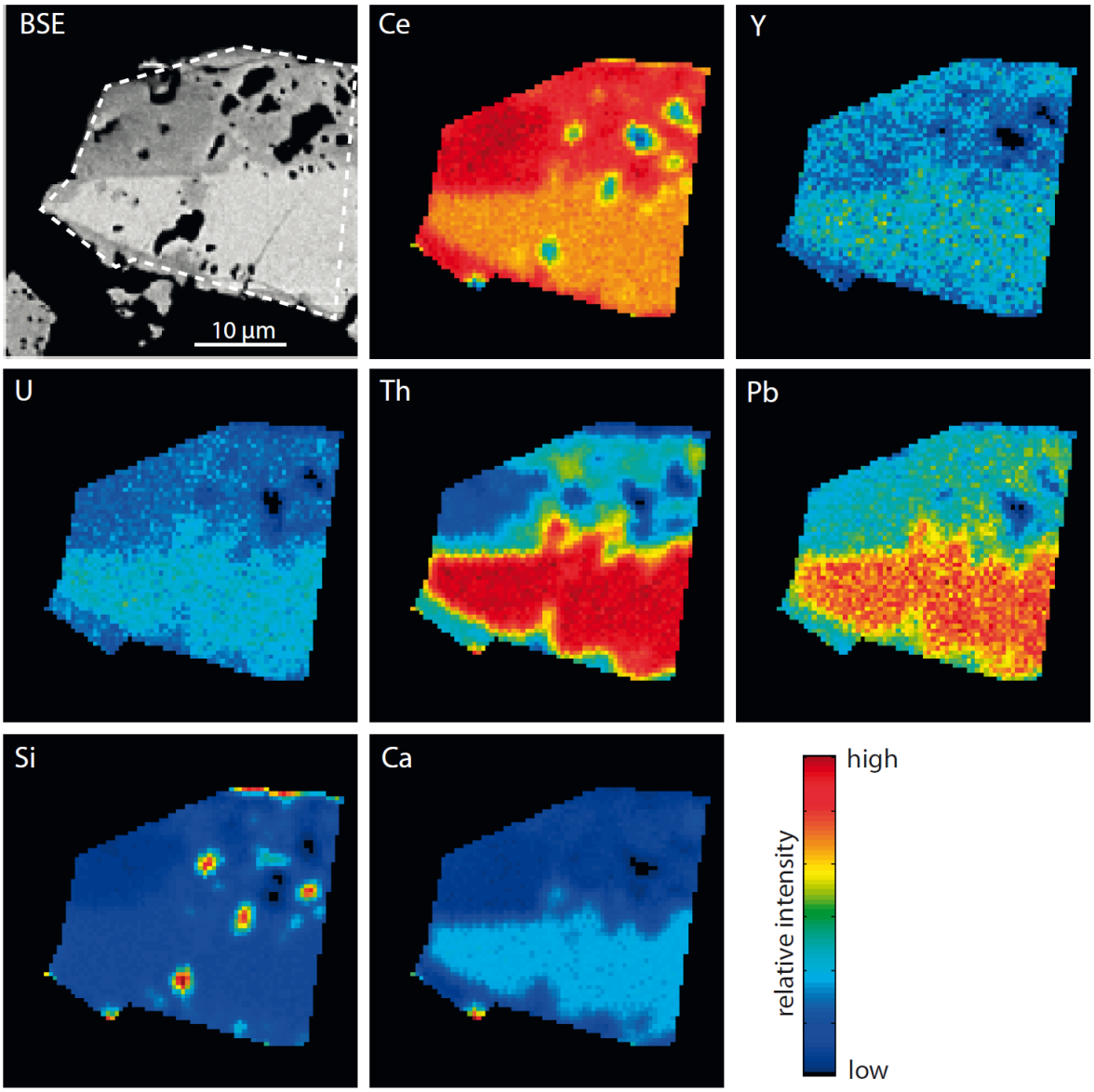

Annexe 5-3 EPMA intensity maps

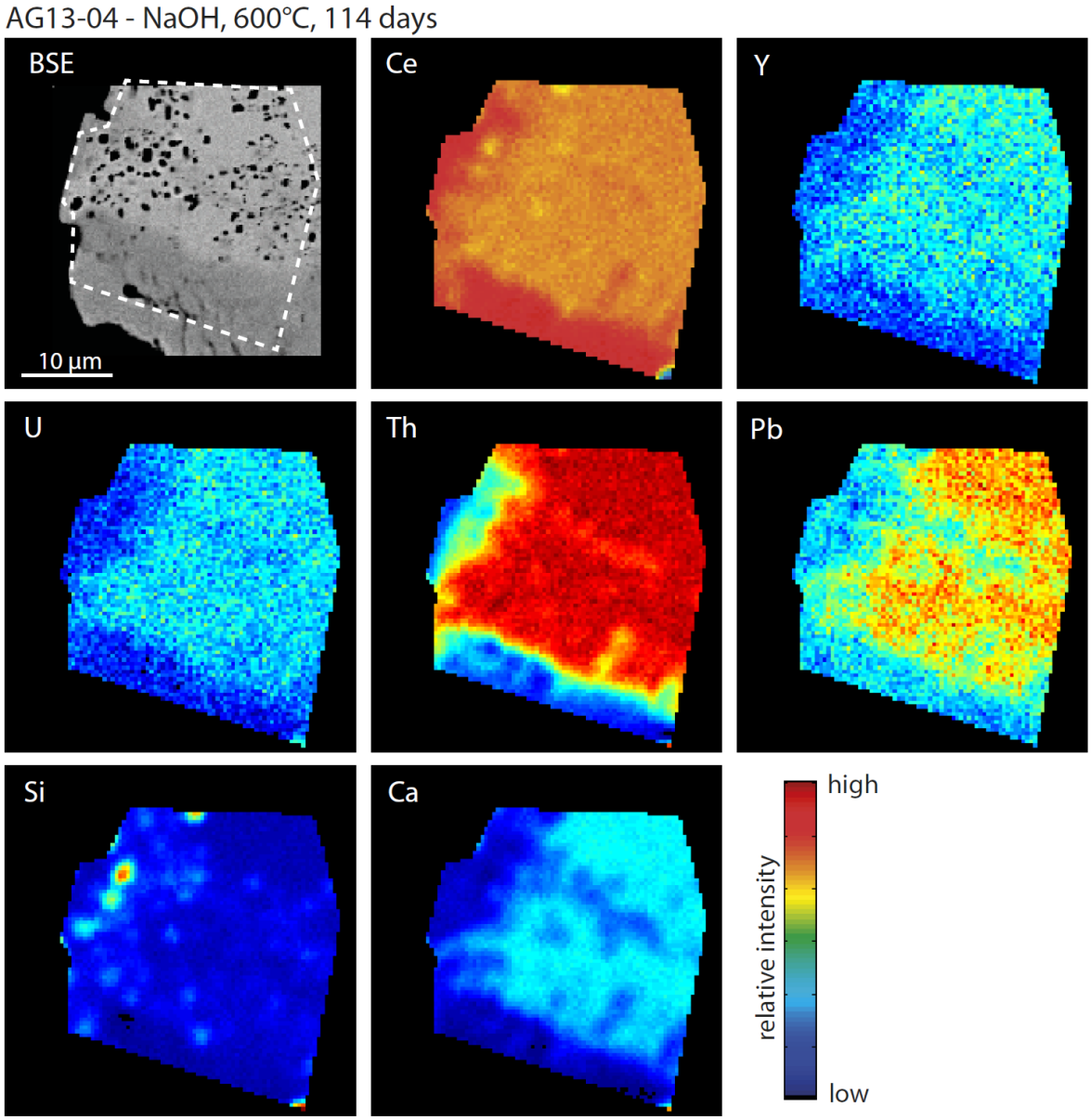

Annexe 5-4 EPMA intensity maps

AG13-04 - NaOH, 600°C, 114 days

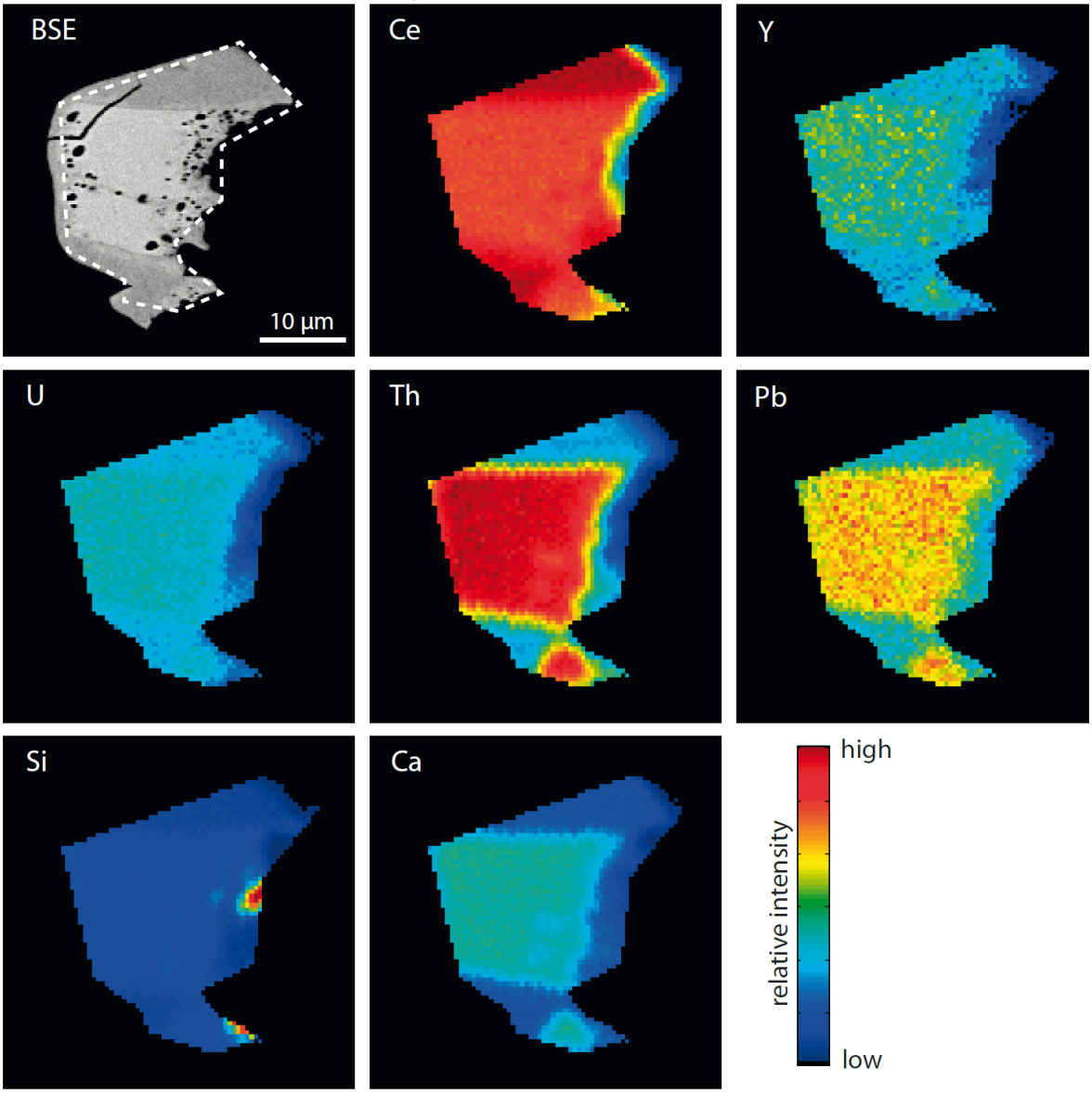

Annexe 5-5 Cartographie Raman en ^{18}O

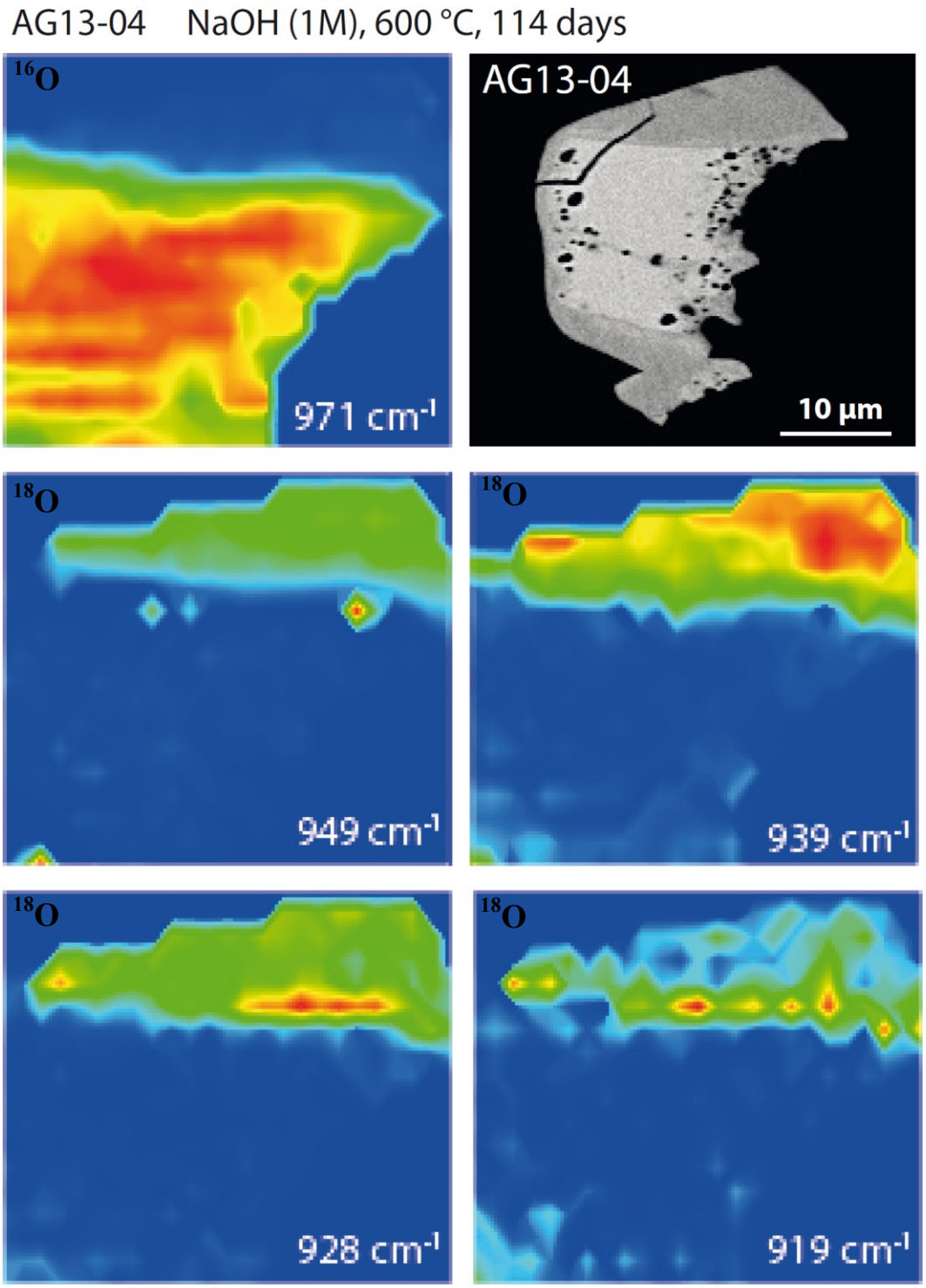

Annexe 5-6 Cartographie Raman en ^{18}O

AG13-02 600°C, NaOH (2M) 14 jours

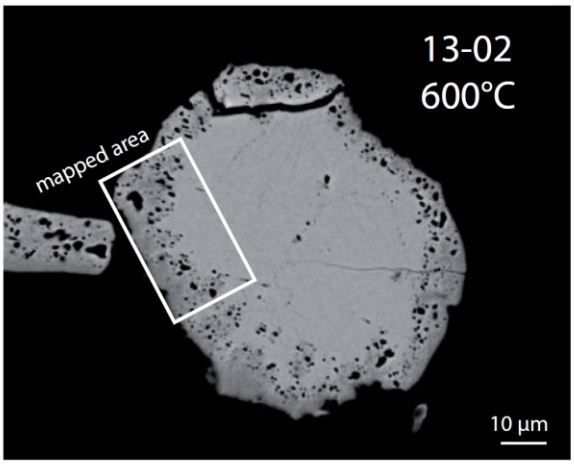

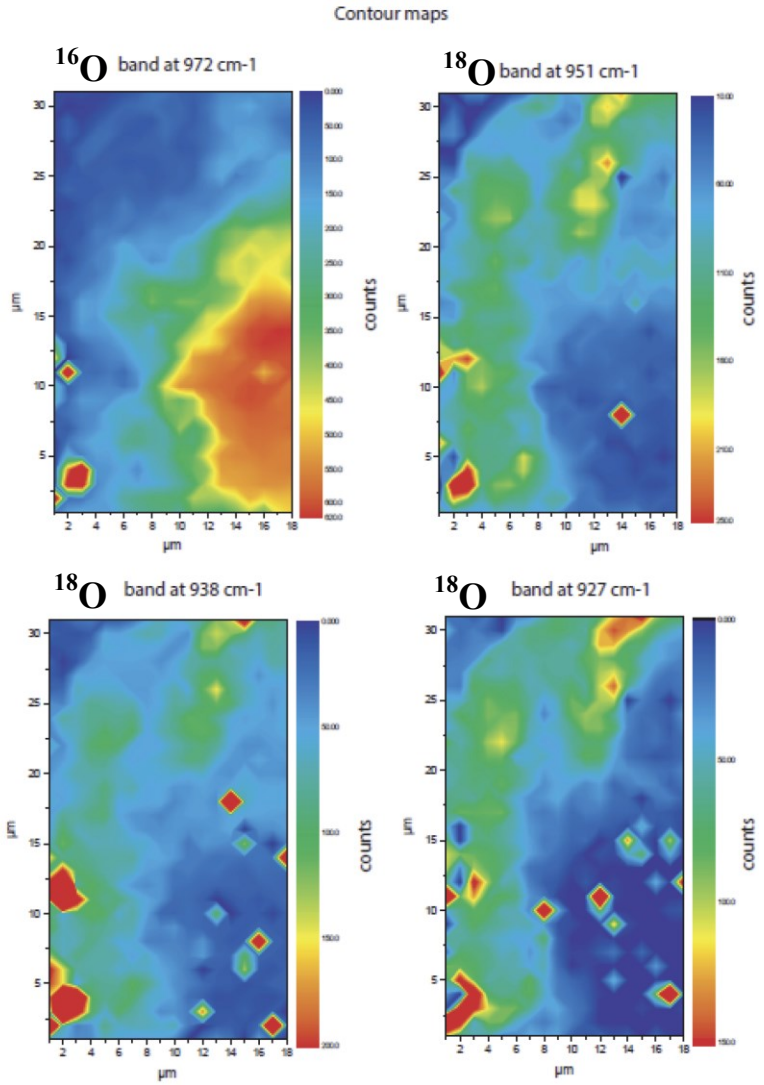

Annexe 5-7 Quartz recristallisés expérimentalement

AG12-02 600 °C-200 MPa-H_2O-40 days

AG12-04 600 °C-200 MPa-$NaOH_{1M}$-40 days

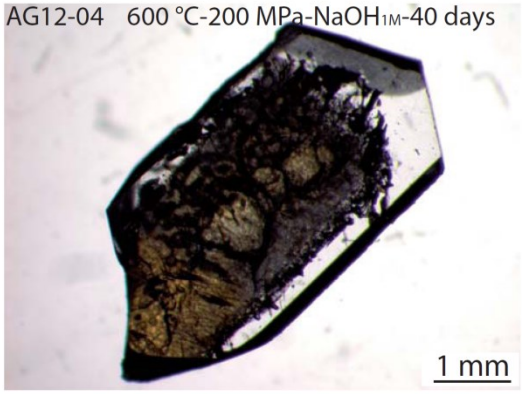

AG13-01 500 °C-200 MPa-$NaOH_{2M}$-21 days

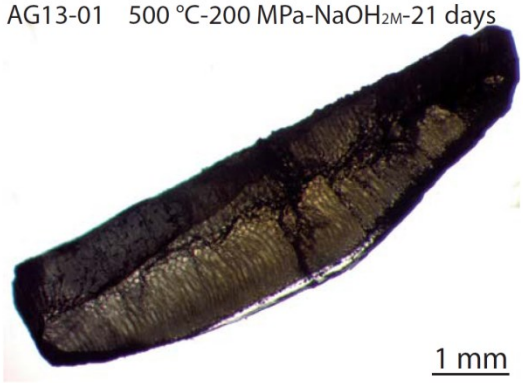

AG13-02 600 °C-200 MPa-$NaOH_{2M}$-14 days

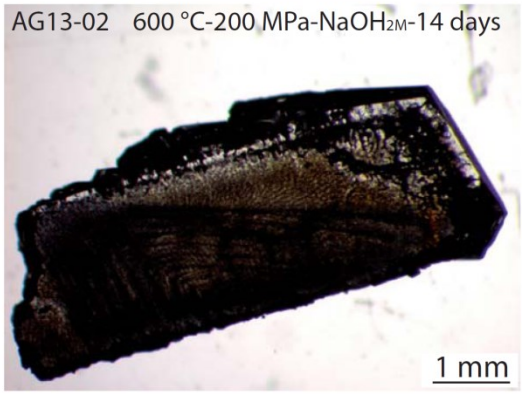

AG13-06 300 °C-200 MPa-$NaOH_{1M}$-114 days

AG13-06 400 °C-200 MPa-$NaOH_{1M}$-114 days

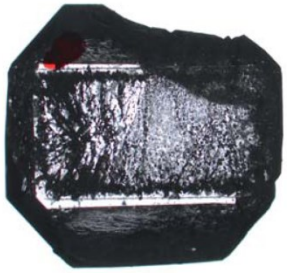

AG13-03 500 °C-200 MPa-$NaOH_{1M}$-114 days

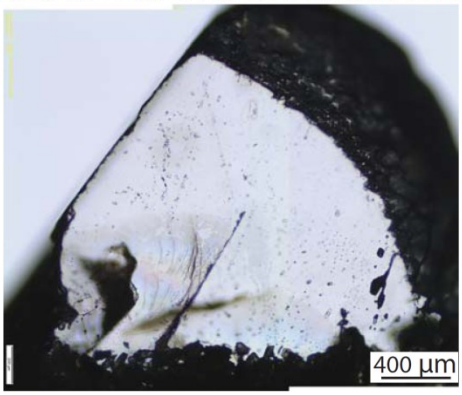

AG13-04 500 °C-200 MPa-$NaOH_{1M}$-114 days

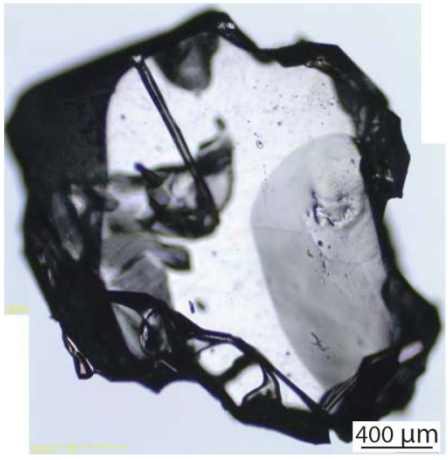

Annexe 5-7 Inclusions fluides synthétiques dans le quartz

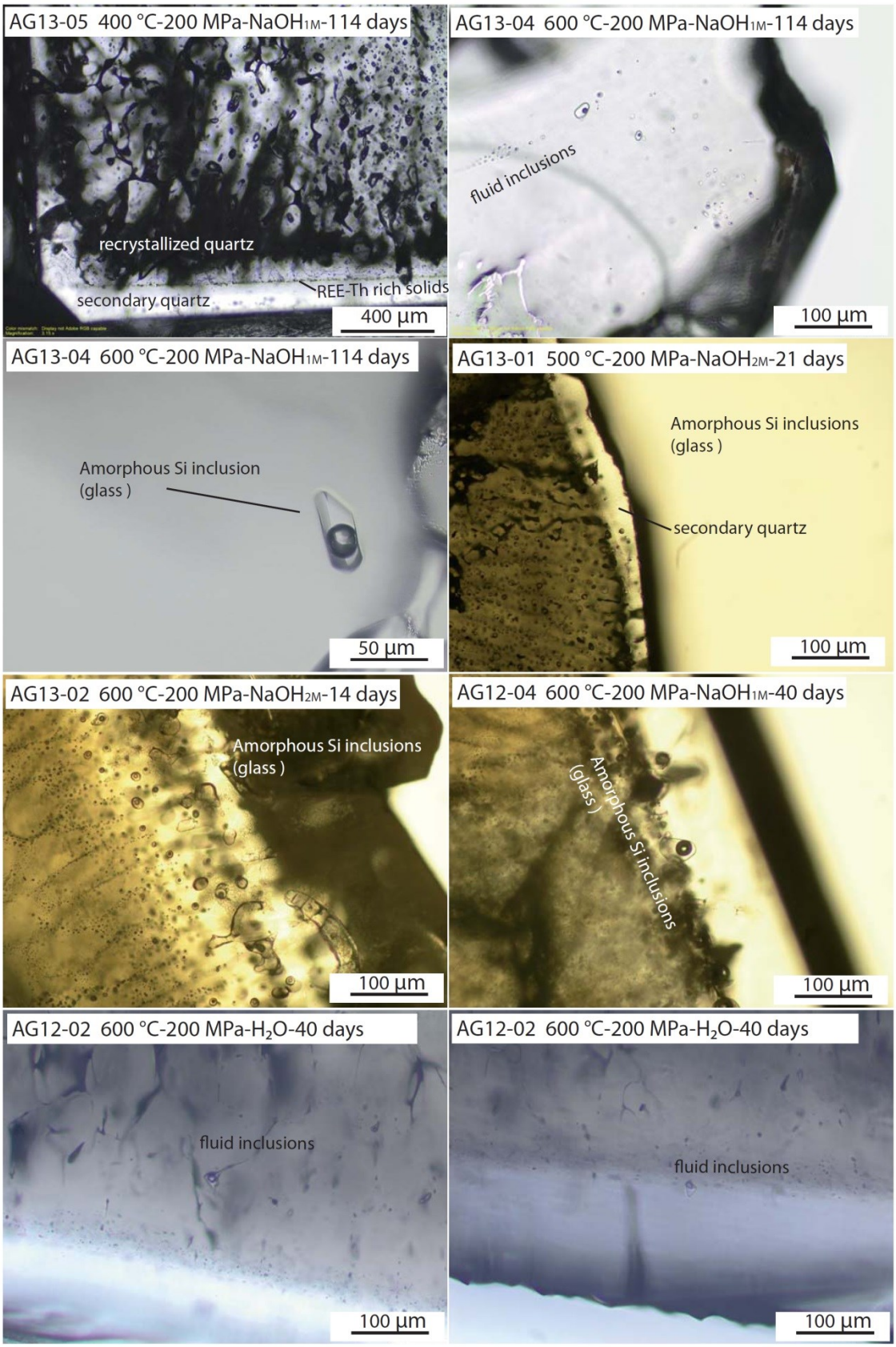

Annexe 6-1 Localisation des analyses LA-ICP-MS

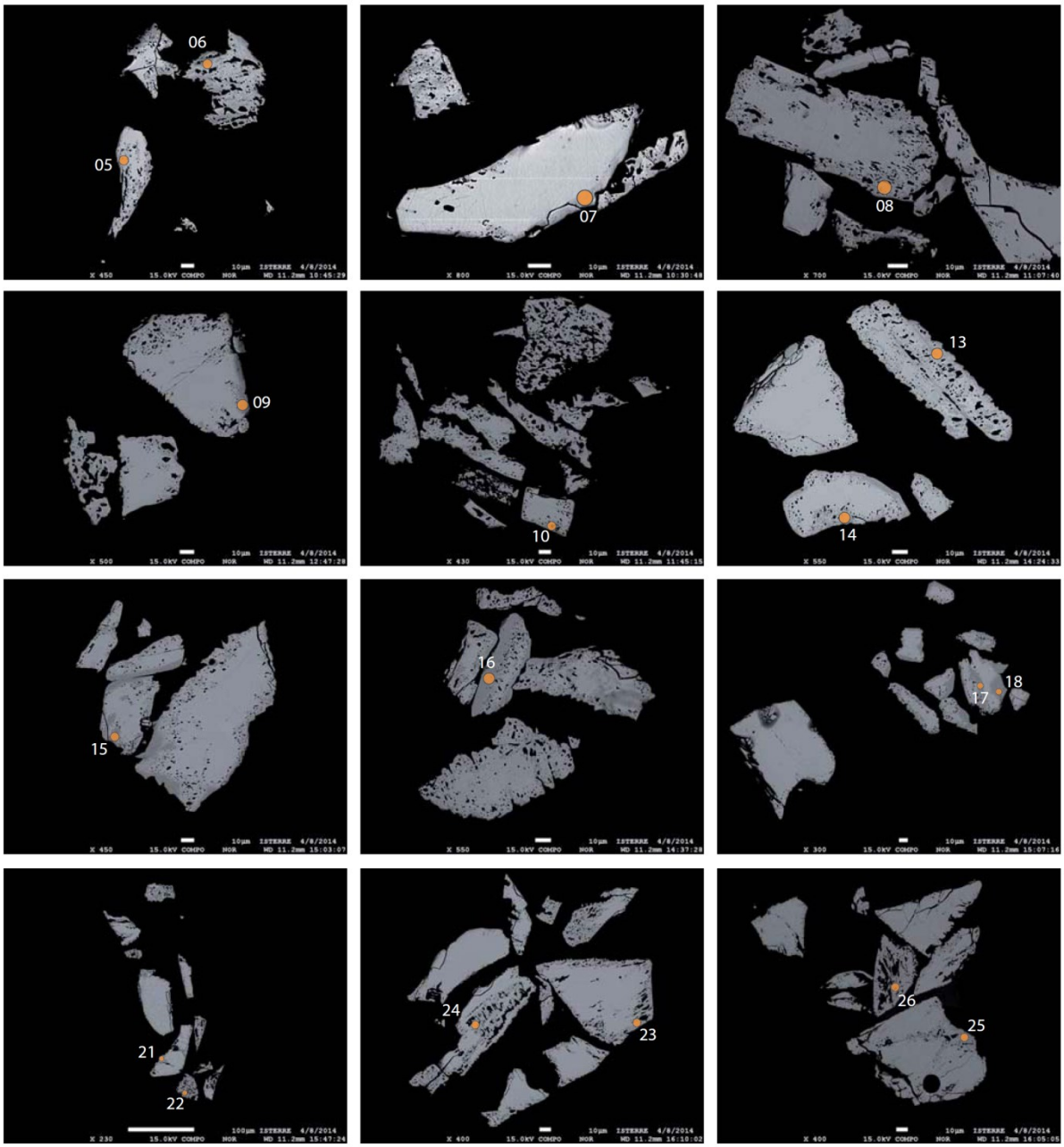

Figure DR1. Localization of LA-ICPMS analyzes on BSE images of reacted monazites

Annexe 6-2 Résultats des analyses LA-ICP-MS

Table DR3 LA-ICPMS analyzes

Analysis #	Run	Concentrations				Isotopic ratios						Ages (Ma)					
		[Th] ppm	[U] ppm	[Pb] ppm	Th/U	$^{207}Pb/^{235}U$	± 2σ	$^{206}Pb/^{238}U$	± 2σ	$^{208}Pb/^{232}Th$	± 2σ	$^{207}Pb/^{235}U$	± 2σ	$^{206}Pb/^{238}U$	± 2σ	$^{208}Pb/^{232}Th$	± 2σ
*27210314d	13-05	93056	2531	2137	37	0.719	0.035	0.0886	0.0033	0.0270	0.0008	550	21	547	20	538	17
*28210314d	13-05	95863	2112	2163	45	0.747	0.038	0.0875	0.0033	0.0267	0.0008	567	22	541	20	532	17
21210314d	13-05	105240	3048	2214	35	0.702	0.035	0.0833	0.0031	0.0246	0.0008	540	21	516	19	492	15
22210314d	13-05	55786	236	123	236	0.477	0.109	0.0557	0.0031	0.0026	0.0001	396	75	350	19	52	2
23210314d	13-05	34512	300	170	115	0.519	0.140	0.0587	0.0041	0.0058	0.0002	424	93	368	25	117	4
24210314d	13-05	73041	1153	1078	63	0.701	0.053	0.0838	0.0033	0.0174	0.0005	539	32	519	20	349	11
25210314d	13-05	60787	726	733	84	0.719	0.050	0.0835	0.0032	0.0143	0.0005	550	29	517	19	286	9
26210314d	13-05	109925	2598	2205	42	0.687	0.033	0.0817	0.0031	0.0236	0.0008	531	20	506	18	472	15
05210314d	13-03	79316	2082	1859	38	0.815	0.039	0.0985	0.0037	0.0275	0.0009	605	22	606	21	548	17
06210314d	13-03	73084	1546	1148	47	0.711	0.041	0.0832	0.0032	0.0184	0.0006	545	24	515	19	369	12
07210314d	13-03	44398	863	369	51	0.428	0.048	0.0496	0.0022	0.0097	0.0003	362	34	312	13	196	6
08210314d	13-03	118061	2120	1933	56	0.648	0.041	0.0788	0.0030	0.0193	0.0006	507	25	489	18	387	12
09210314d	13-03	113883	1632	937	70	0.485	0.039	0.0594	0.0024	0.0097	0.0003	402	27	372	15	195	6
10210314d	13-03	123434	2690	2511	46	0.685	0.036	0.0820	0.0031	0.0240	0.0008	530	22	508	18	480	15
13210314d	13-04	114939	3227	2648	36	0.736	0.034	0.0899	0.0033	0.0270	0.0009	560	20	555	20	539	17
14210314d	13-04	115118	3103	2051	37	0.645	0.031	0.0775	0.0029	0.0209	0.0007	505	19	481	17	417	13
15210314d	13-04	105884	2798	2170	38	0.710	0.037	0.0843	0.0032	0.0240	0.0008	545	22	522	19	480	15
16210314d	13-04	74058	590	352	126	0.563	0.057	0.0639	0.0027	0.0056	0.0002	453	37	399	16	112	4
17210314d	13-04	117501	3537	2694	33	0.739	0.035	0.0882	0.0033	0.0268	0.0008	562	20	545	19	535	17
18210314d	13-04	101747	906	546	112	0.563	0.062	0.0663	0.0029	0.0063	0.0002	453	40	414	18	127	4

*: analyzes on grain core (Mnz1)

Annexe 6-3 Résultats des analyses U-Th-Pb microsonde (1/3)

Table DR4 U-Th-Pb EPMA analysis and chemical ages (2σ uncertainty) of hydrothermal experiment products

Analysis	UO_2	ThO_2	PbO	Age (Ma)
Mnz1 domain				
1202-1	0.18	12.60	0.32	569 ± 24
1202-2	0.17	12.31	0.31	574 ± 24
1202-3	0.15	11.69	0.28	540 ± 24
1202-4	0.17	12.80	0.32	564 ± 26
1202-5	0.18	12.66	0.32	572 ± 24
1202-6	0.18	13.14	0.33	564 ± 24
1204-1	0.18	13.37	0.33	557 ± 23
1204-4	0.18	12.94	0.33	569 ± 25
1204-7	0.18	12.79	0.33	579 ± 26
1204-8	0.18	13.39	0.32	545 ± 23
1204-9	0.18	13.55	0.33	549 ± 24
1204-12	0.17	12.84	0.32	559 ± 24
1204-13	0.17	12.76	0.32	568 ± 24
1207-6	0.19	14.03	0.35	555 ± 22
1207-7	0.19	13.91	0.34	555 ± 23
1207-11	0.16	12.28	0.32	578 ± 25
1208-1	0.15	12.78	0.33	579 ± 24
1208-2	0.15	12.87	0.32	568 ± 25
1208-3	0.15	13.11	0.33	570 ± 24
1208-7	0.15	13.29	0.32	542 ± 24
1208-8	0.14	12.88	0.31	549 ± 24
1208-12	0.15	12.55	0.32	568 ± 25
1208-13	0.16	12.34	0.31	564 ± 24
1208-2b	0.14	12.79	0.32	561 ± 25
1301-1	0.17	13.00	0.33	569 ± 24
1301-2	0.17	13.14	0.31	533 ± 24
1301-3	0.17	12.73	0.32	565 ± 25
1301-4	0.21	12.59	0.32	561 ± 24
1301-5	0.19	12.58	0.32	564 ± 25
1301-7	0.19	12.73	0.31	546 ± 25
1301-8	0.17	12.60	0.31	547 ± 25
1302-1	0.12	12.65	0.32	578 ± 25
1302-2	0.12	12.52	0.31	555 ± 26
1302-6	0.18	12.68	0.32	566 ± 25
1302-7	0.17	12.46	0.32	569 ± 24
1302-14	0.14	12.82	0.30	539 ± 24
1302-15	0.15	13.09	0.32	547 ± 24
1303-1	0.13	12.97	0.31	535 ± 25
1303-2	0.13	13.21	0.31	533 ± 23
1303-7	0.14	13.40	0.31	523 ± 23
1303-9	0.13	12.97	0.31	545 ± 24
1303-17	0.18	11.74	0.30	564 ± 25
1304-5	0.18	13.64	0.32	525 ± 21
1304-13	0.17	12.92	0.31	540 ± 23
1305-1	0.14	12.52	0.31	556 ± 25

Annexe 6-3 Résultats des analyses U-Th-Pb microsonde (2/3)

Table DR4 U-Th-Pb EPMA analysis and chemical ages (2σ uncertainty) of hydrothermal experiment products

Analysis	UO_2	ThO_2	PbO	Age (Ma)
1305-5	0.18	14.66	0.36	561 ± 20
1305-10	0.13	12.98	0.32	562 ± 22
1305-17	0.18	13.58	0.32	524 ± 22
1306-1	0.14	12.93	0.30	518 ± 23
1306-2	0.18	13.18	0.30	516 ± 23
1306-5	0.16	13.13	0.33	567 ± 23
Average				**554 ± 11**
400°C				
1305-2	0.05	6.25	0.07	258 ± 41
1305-3	0.05	6.68	0.08	266 ± 44
1305-4	0.04	4.98	0.05	219 ± 63
1305-6	0.06	7.85	0.03	91 ± 24
1305-7	0.05	8.20	0.08	234 ± 37
1305-11	0.03	7.49	0.06	187 ± 38
1305-12	0.09	10.27	0.11	251 ± 27
1305-13	0.05	7.99	0.08	224 ± 31
1305-14	0.05	9.25	0.06	149 ± 22
1305-15	0.02	5.57	0.02	102 ± 54
1305-16	0.05	8.13	0.10	288 ± 42
1305-18	0.06	8.21	0.11	298 ± 32
1305-19	0.15	12.02	0.26	487 ± 24
1305-20	0.03	6.16	0.05	194 ± 40
1305-23	0.05	9.96	0.03	77 ± 25
1305-61	0.05	7.95	0.04	125 ± 21
1305-62	0.03	7.06	0.03	111 ± 24
Average				**198 ± 61**
500°C				
1207-5	0.08	8.97	0.04	102 ± 17
1207-10	0.04	7.24	0.07	222 ± 21
1303-3	0.08	10.04	0.16	368 ± 31
1303-4	0.07	9.91	0.13	302 ± 28
1303-5	0.10	10.95	0.21	440 ± 28
1303-6	0.02	5.73	0.02	97 ± 48
1303-8	0.04	8.54	0.06	167 ± 37
1303-10	0.08	11.14	0.17	352 ± 25
1303-11	0.06	10.42	0.06	145 ± 26
1303-12	0.03	8.58	0.06	171 ± 30
1303-13	0.04	9.22	0.10	261 ± 32
1303-16	0.02	6.10	0.03	124 ± 38
1303-20	0.11	13.52	0.08	131 ± 23
1303-21	0.08	11.64	0.04	75 ± 16
1303-22	0.08	11.96	0.13	250 ± 27
1303-23	0.04	9.00	0.02	40 ± 17

Annexe 6-3 Résultats des analyses U-Th-Pb microsonde (3/3)

Table DR4 U-Th-Pb EPMA analysis and chemical ages (2σ uncertainty) of hydrothermal experiment products

Analysis	UO_2	ThO_2	PbO	Age (Ma)
1303-24	0.06	9.05	0.04	94 ± 26
1303-32	0.08	9.79	0.05	120 ± 15
Average				**163 ± 54**
600°C				
1204-10	0.11	9.41	0.02	61 ± 17
1204-11	0.08	8.83	0.01	28 ± 19
1208-9	0.08	9.62	0.07	164 ± 16
1304-2	0.03	6.63	0.02	64 ± 21
1304-6	0.02	5.58	0.02	87 ± 49
1304-7	0.04	6.83	0.01	47 ± 44
1304-8	0.03	4.95	0.03	137 ± 47
1304-14	0.04	9.18	0.02	50 ± 21
1304-22	0.03	8.70	0.01	35 ± 17
1304-23	0.04	8.87	0.02	63 ± 36
1304-24	0.03	7.07	0.05	162 ± 37
1304-26	0.05	6.83	0.03	88 ± 38
1304-27	0.06	9.64	0.04	89 ± 29
1304-29	0.02	4.79	0.03	138 ± 52
1304-30	0.02	4.68	0.03	156 ± 97
1304-61	0.01	3.56	0.02	105 ± 47
1304-63	0.01	3.55	*bdl*	0 ± -
Average				**71 ± 27**

bdl : below detection limit

9. RÉFÉRENCES BIBLIOGRAPHIQUES

A

Agard P, Monié P, Jolivet L, Goffé B (2002) Exhumation of the Schistes Lustrés complex: in situ laser probe 40Ar/39Ar constraints and implications for the Western Alps. J Metamorph Geol 20:599–618.

Allaz J, Selleck B, Williams ML, Jercinovic MJ (2013) Microprobe analysis and dating of monazite from the Potsdam Formation, New York: A progressive record of chemical reaction and fluid interaction. Am Mineral 98:1106–1119

Andrehs G, Heinrich W (1998) Experimental determination of REE distributions between monazite and xenotime: potential for temperature-calibrated geochronology. Chem Geol 149:83–96.

Ayers J, Watson E (1991) Solubility of apatite, monazite, zircon, and rutile in supercritical aqueous fluids with implications for subduction zone geochemistry. Philos Trans R Soc Lond Ser -Math Phys Eng Sci 335:365–375

Ayers JC, Miller C, Gorisch B, Milleman J (1999) Textural development of monazite during high-grade metamorphism; hydrothermal growth kinetics, with implications for U, Th-Pb geochronology. Am Mineral 84:1766–1780.

B

Baietto A, Perello P, Cadoppi P, Martinotti G (2009) Alpine tectonic evolution and thermal water circulations of the Argentera Massif (South-Western Alps). Swiss J Geosci 102:223–245

Barféty, J.C., Blaise, J., Fourneaux, J.C., Meloux, J., 1984. Carte géologique de la France au 1/50000, feuille 750 (la Rochette) [Geological map of France 1/50 000, map 750 (la Rochette)]. BRGM editions, Orléans.

Bea F (1996) Residence of REE, Y, Th and U in granites and crustal protoliths; Implications for the chemistry of crustal melts. J Petrol 37:521–552

Bellanger M, Augier R, Bellahsen N, Jolivet L, Monié P, Baudin T, Beyssac O (2015) Shortening of the European Dauphinois margin (Oisans Massif, Western Alps): New insights from RSCM maximum temperature estimates and 40Ar/39Ar in situ dating. J Geodyn 83:37–64

Berger A, Gnos E, Janots E, Fernandez A, Giese J (2008) Formation and composition of rhabdophane, bastnäsite and hydrated thorium minerals during alteration: Implications for geochronology and low-temperature processes. Chem Geol 254:238–248.

Berger A, Gnos E, Janots E, Whitehouse M, Soom M, Frei R, Waight TE (2013) Dating brittle tectonic movements with cleft monazite: Fluid-rock interaction and formation of REE minerals: dating tectonics with cleft monazite. Tectonics 32:1176–1189

Bergemann C, Gnos E, Berger A, et al. Th-Pb ion probe dating of zoned cleft monazite: Implications for shear zone activity in the Grimsel area, Switzerland. Submitted to Tectonics

Bernet M, Garver JI (2005) Fission-track analysis of detrital zircon. Low-Temp Thermochronology Tech Interpret Appl 58:205–237

Bernet M (2009) A field-based estimate of the zircon fission-track closure temperature. Chem Geol 259:181–189

Bertrand JM, Ailleres L, Gasquet D, Macaudiere J (1996) The Pennine front zone in Savoie (western Alps), a review and new interpretations from the zone Houillere Brianconnaise. Eclogae Geol Helvetiae 89:297–320.

Beucher R (2009) Évolution Néogène de l'Arc Alpin sud-occidental. Approches sismotectonique et thermochronologique. PhD, Université Joseph Fourier (France)

Beucher R, van der Beek P, Braun J, Batt GE (2012) Exhumation and relief development in the Pelvoux and Dora-Maira massifs (western Alps) assessed by spectral analysis and inversion of thermochronological age transects. J Geophys Res.

Bigot-Cormier F, Sosson M, Poupeau G, Stephan J-F, Labrin E (2006) The denudation history of the Argentera Alpine External Crystalline Massif (Western Alps, France-Italy): an overview from the analysis of fission tracks in apatites and zircons. Geodin Acta 19:455–473

Bingen B, Demaiffe D, Hertogen J (1996) Redistribution of rare earth elements, thorium, and uranium over accessory minerals in the course of amphibolite to granulite facies metamorphism: the role of apatite. Geochim. Cosmochim. Acta 60:1341–1354.

Bingen B, van Breemen O (1998) U-Pb monazite ages in amphibolite-to granulite-facies orthogneiss reflect hydrous mineral breakdown reactions: Sveconorwegian Province of SW Norway. Contrib Mineral Petrol 132:336–353.

Boatner LA, Beall GW, Abraham MM, Finch CB, Huray PG, Rappaz M. (1980) Monazite and other lanthanide orthophosphates as alternate actinide waste forms. In: Northrup Jr CJM, editor. Scientific basis for nuclear waste management, vol. 2. New York: Plenum Publishing Corporation; p. 289–96.

Boatner LA (2002) Synthesis, structure, and properties of monazite, pretulite, and xenotime. In: Kohn MJ, Rakovan J, Hughes JM (eds) Phosphates: Geochemical, Geobiological, and Materials Importance. pp 87–121

Bodnar R (1993) Revised equation and table for determining the freezing-point depression. Geochim Cosmochim Acta 57:683–684

Bodnar R.J. (1994) Philosophy of fluid inclusion analysis. *In* Fluid Inclusions in Minerals, Methods and Applications (B. De Vivo & M. L. Frezzotti, eds.) Virginia Tech, Blacksburg, VA, p. 1-6.

Bodnar, R.J., (2003b) Introduction to fluid inclusions. In: Samson, I., Anderson, A., Marshall, D. (Eds.), Fluid inclusions: Analysis and Interpretation. Mineral. Assoc. Can., Short Course Ser., 32, pp. 1–8.

Bogdanoff S, Michard A, Mansour M, Poupeau G (2000) Apatite fission track analysis in the Argentera massif: evidence of contrasting denudation rates in the External Crystalline Massifs of the Western Alps. Terra Nova 12:117–125.

Bollinger L, Janots E (2006) Evidence for Mio-Pliocene retrograde monazite in the Lesser Himalaya, far western Nepal. Eur. J. Mineral. 18:289–297.

Bonin B, et al (1993) Late Variscan magmatic evolution of the Alpine basement, in Pre-Mesozoic Geology in the Alps, edited by J. F. von Raumer and F. Neubauer, Springer, Heidelberg

Bordet P. and Bordet C. (1963) Belledonne-Grandes Rousses et Aiguilles Rouges-Mont Blanc: quelques données nouvelles sur leurs rapports structuraux. In: « Livre à la mémoire du Professeur P. Fallot ». Mém. h.s. Soc. géol. Fr., II, 309-320.

Bosse V, Boulvais P, Gautier P, Tiepolo M, Ruffet G, Devidal JL, Cherneva Z, Gerdjikov I, Paquette JL (2009) Fluid-induced disturbance of the monazite Th-Pb chronometer: In situ dating and element mapping in pegmatites from the Rhodope (Greece, Bulgaria). Chem Geol 261:286–302

Breecker DO, Sharp ZD (2007) A monazite oxygen isotope thermometer. Am Mineral 92:1561–1572

Broska I, Williams CT, Janák M, Nagy G (2005) Alteration and breakdown of xenotime-(Y) and monazite-(Ce) in granitic rocks of the Western Carpathians, Slovakia. Lithos 82:71-83.

Bucher S, Schmid SM, Bousquet R, Fügenschuh B (2003) Late-stage deformation in a collisional orogen (Western Alps): nappe refolding, back-thrusting or normal faulting? Terra Nova 15:109–117.

Budzyń B, Hetherington CJ, Williams ML, Jercinovic MJ, Michalik M (2010) Fluid–mineral interactions and constraints on monazite alteration during metamorphism. Mineral Mag 74:659–681

Budzyn B, Harlov DE, Williams ML, Jercinovic MJ (2011) Experimental determination of stability relations between monazite, fluorapatite, allanite, and REE-epidote as a function of pressure, temperature, and fluid composition. Am Mineral 96:1547–1567

Budzyn B, Koinecny P, Kozub-Budzyn GA (2015) Stability of monazite and disturbance of the Th-U-Pb system under experimental conditions of 250-350 degrees C AND 200-400 MPa. Ann Soc Geol Pol 85:405–424.

Bussy F, Von Raumer JF (1994) U-Pb geochronology of Palaeozoic magmatic events in the Mont Blanc crystalline Massif, Western Alps, Schweiz Mineral Petrogr Mitt. 74:514–515

C

Cabella R, Lucchetti G, Marescotti P (2001) Authigenic monazite and xenotime from pelitic metacherts in pumpellyite–actinolite-facies conditions, Sestri–Voltaggio Zone, central Liguria, Italy. Can Mineral 39:717–727.

Cabral AR, Zeh A, Galbiatti HF, Lehmann B (2015) Late Cambrian Au-Pd mineralization and Fe enrichment in the Itabira district, Minas Gerais, Brazil, at 496 Ma: constraints from U-Pb monazite dating of a Jacutinga lode. Econ Geol 110:263–272.

Campani M, Mancktelow N, Seward D, Rolland Y, Müller W, Guerra I (2010) Geochronological evidence for continuous exhumation through the ductile-brittle transition along a crustal-scale low-angle normal fault: Simplon Fault Zone, central Alps: Exhumation on a low-angle normal fault. Tectonics 29

Carpena J (1992) Fission-track dating of zircon - zircons from Mont-Blanc granite (french-italian Alps). J Geol 100:411–421.

Catlos EJ, Gilley LD, Harrison TM (2002) Interpretation of monazite ages obtained via in situ analysis. Chem Geol 188:193–215.

Catlos EJ (2013) Versatile Monazite: resolving geological records and solving challenges in materials science: Generalizations about monazite: Implications for geochronologic studies. Am Mineral 98:819–832

Cenki-Tok B, Darling JR, Rolland Y, Dhuime B, Storey CD (2014) Direct dating of mid-crustal shear zones with synkinematic allanite: new in situ U-Th-Pb geochronological approaches applied to the Mont Blanc massif. Terra Nova 26:29–37

Ceriani S, Fugenschuh B, Schmid S (2001) Multi-stage thrusting at the "Penninic Front" in the Western Alps between Mont Blanc and Pelvoux massifs. Int J Earth Sci 90:685–702

Cetiner ZS, Wood SA, Gammons CH (2005) The aqueous geochemistry of the rare earth elements. Part XIV. The solubility of rare earth element phosphates from 23 to 150 °C. Chem Geol 217:147–169

Challandes N, Marquer D, Villa IM (2008) P-T-t modelling, fluid circulation, and 39Ar-40Ar and Rb-Sr mica ages in the Aar Massif shear zones (Swiss Alps). Swiss J Geosci 101:269–288

Cherniak DJ (2006) Pb and rare earth element diffusion in xenotime. Lithos 88:1–14

Cherniak DJ (2010) Diffusion in Accessory Minerals: Zircon, Titanite, Apatite, Monazite and Xenotime. Rev Mineral Geochem 72:827–869

Cherniak DJ, Pyle JM (2008) Th diffusion in monazite. Chem Geol 256:52–61

Cherniak DJ, Watson EB, Grove M, Harrison TM (2004) Pb diffusion in monazite: A combined RBS/SIMS study. Geochim Cosmochim Acta 68:829–840

Clavier N, Podor R, Dacheux N (2011) Crystal chemistry of the monazite structure. J Eur Ceram Soc 31:941–976

Cocherie A, Mezeme EB, Legendre O, Fanning CM, Faure M, Rossi P (2005) Electron-microprobe dating as a tool for determining the closure of Th-U-Pb systems in migmatitic monazites. Am Mineral 90:607–618

Corfu F (1988) Differential response of u-pb systems in coexisting accessory minerals, winnipeg river subprovince, canadian shield - implications for archean crustal growth and stabilization. Contrib Mineral Petrol 98:312–325

Corfu F (2013) A century of U-Pb geochronology: The long quest towards concordance. Geol Soc Am Bull 125:33–47

Corsini M, Ruffet G, Caby R (2004) Alpine and late-hercynian geochronological constraints in the Argentera Massif (Western Alps). Eclogae Geol Helvetiae 97:3–15

Cottle J M, Kylander-Clark AR, Vrijmoed JC (2012) U–Th/Pb geochronology of detrital zircon and monazite by single shot laser ablation inductively coupled plasma mass spectrometry (SS-LA-ICPMS). Chem Geol 332-333:136–147.

Crerar DA, Anderson GM (1971) Solubility and solvation reactions of quartz in dilute hydrothermal solutions. Chem Geol 8:107 – 122

Crespo-Blanc A, Masson H, Sharp Z, Cosca M, Hunziker J (1995) A stable and 40Ar/39Ar isotope study of a major thrust in the Helvetic nappes (Swiss Alps): evidence for fluid flow and constraints on nappe kinematics. Geol Soc Am Bull 107:1129–1144.

Crouzet C, Ménard G, Rochette P (2001) Cooling history of the Dauphinoise Zone (Western Alps, France) deduced from the thermopaleomagnetic record: geodynamic implications. Tectonophysics 340:79–93.

Cruz MJ, Cunha JC, Merlet C, et al (1996) Dataçaõ pontual das monazitas da regiaõ de Itambé, Bahia, através da microssonda electrônica. XXXIX Congresso Brasileiro de Geologia, vol. 2. Sociedade Brasileira de Geologià-Núcleo, Bahià-Segipe. pp. 206– 209

Cuney M, Mathieu R (2000) Extreme light rare earth element mobilization by diagenetic fluids in the geological environment of the Oklo natural reactor zones, Franceville basin, Gabon. Geology 28:743–746.

D

Debelmas J, Caby R, Desmons J, et al (1991) Geological map and explanatory text of the sheet n◦728 Sainte-Foy-Tarentaise, scale: 1: 50000. ed. BRGM.

Debon F., Guerrot C., Ménot R.-P., Vivier G. & Cocherie A. (1998). Late Variscan granites of the Belledonne massif (French western Alps): an early Visean magnesian plutonism. Schweiz. Mineral. Petrogr. Mitt., 78, 67-85.

Dempster TJ (1986) Isotope systematics in minerals - Biotite rejuvenation and exchange during alpine metamorphism. Earth Planet Sci Lett 78:355–367

Deschanels X, Seydoux-Guillaume AM, Magnin V, Mesbah A, Tribet M, Moloney MP, Serruys Y, Peuget S (2014) Swelling induced by alpha decay in monazite and zirconolite ceramics: A XRD and TEM comparative study. J Nucl Mater 448:184–194

Devidal J.-L., Gibert F., Kieffer B., Pin C., Montel J.-M. (1998) "A new method for solubility measurement: application to NdPO4 system in H2O-NaCl-HCl hydrothermal fluids." Mineralogical Magazine 62A: 375-376.

Didier A (2013) Comportement géochimique du chronomètre U-Th-Pb dans la monazite : approche par analyses in-situ au LA-ICP-MS. Phd, Université Blaise Pascal (France)

Debelmas J., (1989) Carte géol. France (1/50000), feuille Moûtiers (751). BRGM, Orléans

Didier A, Bosse V, Boulvais P, Bouloton J, Paquette J-L, Montel J-M, Devidal J-L (2013) Disturbance versus preservation of U–Th–Pb ages in monazite during fluid–rock interaction: textural, chemical

and isotopic in situ study in microgranites (Velay Dome, France). Contrib Mineral Petrol 165:1051–1072

Didier A, Bosse V, Cherneva Z, Gautier P, Georgieva M, Paquette JL, Gerdjikov I (2014) Syn-deformation fluid-assisted growth of monazite during renewed high-grade metamorphism in metapelites of the Central Rhodope (Bulgaria, Greece). Chem Geol 381:206–222

Didier A, Bosse V, Bouloton J, Mostefaoui S, Viala M, Paquette JL, Devidal JL, Duhamel R (2015) NanoSIMS mapping and LA-ICP-MS chemical and U–Th–Pb data in monazite from a xenolith enclosed in andesite (Central Slovakia Volcanic Field). Contrib Mineral Petrol. 170:45

Dodson MH (1973) Closure temperature in cooling geochronological and petrological systems. Contrib. Miner. Petrol. 40:259–274.

Duchene S, BlichertToft J, Luais B, Telouk P, Lardeaux JM, Albarede F (1997) The Lu-Hf dating of garnets and the ages of the Alpine high-pressure metamorphism. Nature 387:586–589.

Dumont T, Champagnac J-D, Crouzet C, Rochat P (2008) Multistage shortening in the Dauphiné zone (French Alps): the record of Alpine collision and implications for pre-Alpine restoration. Swiss J Geosci 101:89–110

Dunkel KG, Putnis A (2014) Replacement and ion exchange reactions of scolecite in a high pH aqueous solution. Eur J Mineral 26:61–69

E

Evans J, Zalasiewicz J (1996) U-Pb, Pb-Pb and Sm-Nd dating of authigenic monazite: Implications for the diagenetic evolution of the Welsh Basin. Earth Planet Sci Lett 144:421–433

Evans J, Zalasiewicz J, Fletcher I, Rasmussen B, Pearce NJG (2002) Dating diagenetic monazite in mudrocks: constraining the oil window? J.Geol. Soc. 159:619-22.

F

Fabre J (1961) Contribution à l'étude de la Zone Houillère Briançonnaise en Maurienne et en Tarentaise (Alpes de Savoie). Mém. Bur. Rech. Géol. Min. 2, 315 pp

Fabre C., Boiron M.C., Dubessy J., Cathelineau M., Banks D.A. (2002). Paleofluid chemistry of a single fluid event: a bulk and in-situ multi-technique analysis (LIBS, Raman spectroscopy) of an Alpine fluid (Mont-Blanc). Chem. Geol., 182, 249-264

Faure-Muret A (1955) Études géologiques sur le massif de l'Argentera-Mercantour et ses enveloppes sédimentaires. Mém. Soc. Géol. France, 336 pp

Ferry JM (2000) Patterns of mineral occurrence in metamorphic rocks. Am Mineral 85:1573–1588.

Finger F, Broska I, Roberts MP, Schermaier A (1998) Replacement of primary monazite by apatite-allanite-epidote coronas in an amphibolite facies granite gneiss from the eastern Alps. Am Mineral 83:248–258.

Finger F, Krenn E (2007) Three metamorphic monazite generations in a high-pressure rock from the Bohemian Massif and the potentially important role of apatite in stimulating polyphase monazite growth along a PT loop. Lithos 95:103–115.

Forster HJ (1998a) The chemical composition of REE-Y-Th-U-rich accessory minerals in peraluminous granites of the Erzgebirge-Fichtelgebirge region, Germany, Part I: The monazite-(Ce)-brabantite solid solution series. Am Mineral 83:259–272.

Forster HJ (1998b) The chemical composition of REE-Y-Th-U-rich accessory minerals in peraluminous granites of the Erzgebirge-Fichtelgebirge region, Germany. Part II: Xenotime. Am Mineral 83:1302–1315.

Fletcher IR, McNaughton NJ, Davis WJ, Rasmussen B (2010) Matrix effects and calibration limitations in ion probe U-Pb and Th-Pb dating of monazite. Chem Geol 270:31–44

Franz G, Andrehs G, Rhede D (1996) Crystal chemistry of monazite and xenotime from Saxothuringian-Moldanubian metapelites , NE Bavaria , Germany. Eur. J. Mineral. 8, 1097–1118.

Freeman SR, Butler RWH, Cliff RA, Inger S, Barnicoat AC (1998) Deformation migration in an orogen-scale shear zone array: an example from the basal Briançonnais thrust, internal Franco-Italian Alps. Geol Mag 135:349–367.

Freeman SR, Inger S, Butler RWH, Cliff RA (1997) Dating deformation using Rb-Sr in white mica: Greenschist facies deformation ages from the Entrelor shear zone, Italian Alps. Tectonics 16:57–76

Fudral S, Deville E, Nicoud G, et al (1994) Geological map and explanatory text of the sheet n◦776 Lanslebourg-Mont-d'Ambin, scale: 1: 50000. ed. BRGM.

Fügenschuh B, Loprieno A, Ceriani S, Schmid SM (1999) Structural analysis of the Subbriançonnais and Valais units in the area of Moûtiers (Savoy, Western Alps): paleogeographic and tectonic consequences. Int J Earth Sci 88:201–218.

Fügenschuh B, Schmid SM (2003) Late stages of deformation and exhumation of an orogen constrained by fission-track data: a case study in the Western Alps. Geol Soc Am Bull 115:1425–1440.

G

Gallagher K, Brown R, Johnson C (1998) Fission track analysis and its applications to geological problems. Annu Rev Earth Planet Sci 26:519–572.

Ganne J (2003) Les domes de socles HP-BT dans le domaine Pennique des Alpes nord-occidentales (massifs d'Ambin et de Vanoise Sud): modalities de leur exhumation. PhD, Université de Savoie (France)

Ganne J, Bertrand J-M, Fudral S, Marquer D, Vidal O (2007) Structural and metamorphic evolution of the Ambin massif (western Alps): toward a new alternative exhumation model for the Brianconnais domain. Bull Soc Geol Fr 178:437–458

Gardés E, Jaoul O, Montel J-M, Seydoux-Guillaume A-M, Wirth R (2006) Pb diffusion in monazite: An experimental study of interdiffusion. Geochim Cosmochim Acta 70:2325–2336

Gardés E, Montel J-M, Seydoux-Guillaume A-M, Wirth R (2007) Pb diffusion in monazite: New constraints from the experimental study of interdiffusion. Geochim Cosmochim Acta 71:4036–4043

Gasquet D (1979) Etude pétrologique, géochimique et structurale des terrains cristallins de Belledonne et du Grand Chatelard traversés par les galeries EDF Arc-Isère, Alpes françaises.PhD, Université de Grenoble (France)

Gasquet D, Bertrand J-M, Paquette J-L, Lehmann J, Ratzov G, Guedes RDA, Tiepolo M, Boullier A-M, Scaillet S, Nomade S (2010) Miocene to Messinian deformation and hydrothermal activity in a pre-Alpine basement massif of the French western Alps: new U-Th-Pb and argon ages from the Lauzière massif. Bull Société Géologique Fr 181:227–241.

Gasser D, Bruand E, Rubatto D, Stüwe K (2012) The behaviour of monazite from greenschist facies phyllites to anatectic gneisses: An example from the Chugach Metamorphic Complex, southern Alaska. Lithos, 134-135:108–122.

Gély, J.P. (1989) Sratigraphie, tectonique et métamorphisme comparés de part et d'autre du front pennique en Tarentaise (Alpes de Savoie, France). Premières applications cristallochimiques, géochimiques et isotopiques dans les reconstitutions paléogéographiques et géodynamiques régionales. Thèse de Doctorat, Université de Savoie, 342p.

Gerber W (2008) Evolution tectono-métamorphique du Briançonnais interne: comportement du socle et de sa couverture dans un contexte de subduction continentale profonde. PhD, Université Pierre et Marie Curie (France)

Gibert F., Montel J.-M. (1996) "Étude expérimentale de la solubilité de la monazite dans des fluides à H2O-CO2". In Réunion des Sciences de la Terre 16. Orléans.

Gibert F, Guillaume D, Laporte D (1998) Importance of fluid immiscibility in the H 2 O-NaCl-CO 2 system and selective CO 2 entrapment in granulites; experimental phase diagram at 5-7 kbar, 900 degrees C and wetting textures. Eur J Mineral 10:1109–1123.

Gibson H, Carr S, Brown R, Hamilton M (2004) Correlations between chemical and age domains in monazite, and metamorphic reactions involving major pelitic phases: an integration of ID-TIMS and SHRIMP geochronology with Y-Th-U X-ray mapping. Chem Geol 211:237–260

Glotzbach C, Reinecker J, Danišík M, Rahn M, Frisch W, Spiegel C (2010) Thermal history of the central Gotthard and Aar massifs, European Alps: Evidence for steady state, long-term exhumation. J Geophys Res.

Glotzbach C, van der Beek PA, Spiegel C (2011) Episodic exhumation and relief growth in the Mont Blanc massif, Western Alps from numerical modelling of thermochronology data. Earth Planet Sci Lett 304:417–430

Gnos E, Janots E, Berger A, Whitehouse M, Walter F, Pettke T, Bergemann C (2015) Age of cleft monazites in the eastern Tauern Window: constraints on crystallization conditions of hydrothermal monazite. Swiss J Geosci.

Goldfarb RJ, Groves DI, Gardoll S (2001) Orogenic gold and geologic time: a global synthesis. Ore Geol Rev 18:1–75

Goldsmith, J.R., Laves, F., 1954. The microcline–sanidine stability relations. Geochim. Cosmochim. Acta 5, 1–19

Goldstein R.H., Reynolds, T.J. (1994) Systematics of fluid inclusions in diagenetic minerals: Society for Sedimentary Geology Short Course 31, 199 pp.

Goncalves P, Williams ML, Jercinovic MJ (2005) Electron-microprobe age mapping of monazite. Am. Mineral. 90:578-585.

Gratz R, Heinrich W (1997) Monazite-xenotime thermobarometry: Experimental calibration of the miscibility gap in the binary system CePO4-YPO4. Am Mineral 82:772–780.

H

Hall D, Sterner S, Bodnar R (1988) Freezing-point depression of NaCl-KCl-H_2O solutions. Econ Geol 83:197–202.

Harlov DE, Wirth R, Hetherington CJ (2007) The relative stability of monazite and huttonite at 300 900 C and 200 1000 MPa: Metasomatism and the propagation of metastable mineral phases. Am Mineral 92:1652–1664

Harlov DE, Hetherington CJ (2010) Partial high-grade alteration of monazite using alkali-bearing fluids: Experiment and nature. Am Mineral 95:1105–1108

Harlov D (2011) Petrological and experimental application of REE- and actinide-bearing accessory minerals to the study of Precambrian high-grade gneiss terranes. In: Geological Society of America Memoirs. Geological Society of America, pp 13–24

Harlov DE, Wirth R, Hetherington CJ (2011) Fluid-mediated partial alteration in monazite: the role of coupled dissolution–reprecipitation in element redistribution and mass transfer. Contrib Mineral Petrol 162:329–348

Harrison, T.M., Ryerson, F.J., Le Fort, P., Yin, A., Lovera, O.M., Catlos, E.J., (1997) A late Miocene–Pliocene origin for the Central Himalayan inverted metamorphism: Earth and Planetary Science Letters, v. 146, p. E1–E8.

Hawkins DP, Bowring SA (1997) U-Pb systematics of monazite and xenotime: case studies from the Paleoproterozoic of the Grand Canyon, Arizona. Contrib Mineral Petrol 127:87–103.

Hawkins DP, Bowring SA (1999) U-Pb monazite, xenotime, and titanite geochronological constraints on the prograde to post-peak metamorphic thermal history of Paleoproterozoic migmatites from the Grand Canyon, Arizona. Contrib. Mineral Petrol 134:150-169.

Heinrich W, Rehs G, Franz G (1997) Monazite–xenotime miscibility gap thermometry. I. An empirical calibration. J Metamorph Geol 15:3–16

Hetherington CJ, Harlov DE (2008) Metasomatic thorite and uraninite inclusions in xenotime and monazite from granitic pegmatites, Hidra anorthosite massif, southwestern Norway: Mechanics and fluid chemistry. Am Mineral 93:806–820

Hetherington CJ, Harlov DE, Budzyń B (2010) Experimental metasomatism of monazite and xenotime: mineral stability, REE mobility and fluid composition. Mineral Petrol 99:165–184

Hietpas J, Samson S, Moecher D, Schmitt AK (2010) Recovering tectonic events from the sedimentary record: Detrital monazite plays in high fidelity. Geology 38:167–170.

Hovelmann J, Putnis A, Geisler T, Schmidt BC, Golla-Schindler U (2010) The replacement of plagioclase feldspars by albite: observations from hydrothermal experiments. Contrib Mineral Petrol 159:43–59

J

Jackson SE, Pearson NJ, Griffin WL, Belousova EA (2004) The application of laser ablation-inductively coupled plasma-mass spectrometry to in situ U-Pb zircon geochronology. Chem Geol 211:47–69

Jamtveit B, Putnis CV, Malthe-Sorenssen A (2009) Reaction induced fracturing during replacement processes. Contrib Mineral Petrol 157:127–133

Janots E, Brunet F, Goffé B, Poinssot C, Burchard M, Cemič L (2007) Thermochemistry of monazite-(La) and dissakisite-(La): implications for monazite and allanite stability in metapelites. Contrib Mineral Petrol 154:1–14

Janots E, Engi M, Berger A, Allaz J, Schwarz J-O, Spandler C (2008) Prograde metamorphic sequence of REE minerals in pelitic rocks of the Central Alps: implications for allanite–monazite–xenotime phase relations from 250 to 610 °C. J Metamorph Geol 26:509–526

Janots E, Engi M, Rubatto D, Berger A, Gregory C, Rahn M (2009) Metamorphic rates in collisional orogeny from in situ allanite and monazite dating. Geology 37:11–14.

Janots E, Berger A, Engi M (2011) Physico-chemical control on the REE minerals in chloritoid-grade metasediments from a single outcrop (Central Alps, Switzerland). Lithos 121:1–11

Janots E, Berger A, Gnos E, Whitehouse M, Lewin E, Pettke T (2012) Constraints on fluid evolution during metamorphism from U–Th–Pb systematics in Alpine hydrothermal monazite. Chem Geol 326-327:61–71

Janots E, Rubatto D (2014) U–Th–Pb dating of collision in the external Alpine domains (Urseren zone, Switzerland) using low temperature allanite and monazite. Lithos 184-187:155–166

Janssen A, Putnis A, Geisler T, Putnis CV (2010) The experimental replacement of ilmenite by rutile in HCl solutions. Mineral Mag 74:633–644

Jercinovic MJ (2005) Analytical perils (and progress) in electron microprobe trace element analysis applied to geochronology: Background acquisition, interferences, and beam irradiation effects. Am Mineral 90:526–546

Jonas L, John T, King HE, Geisler T, Putnis A (2014) The role of grain boundaries and transient porosity in rocks as fluid pathways for reaction front propagation. Earth Planet Sci Lett 386:64–74

K

Kamenetsky VS, Kamenetsky MB (2010) Magmatic fluids immiscible with silicate melts: examples from inclusions in phenocrysts and glasses, and implications for magma evolution and metal transport. Geofluids 10:293–311

Kasioptas A, Geisler T, Perdikouri C, Trepmann C, Gussone N, Putnis A (2011) Polycrystalline apatite synthesized by hydrothermal replacement of calcium carbonates. Geochim Cosmochim Acta 75:3486–3500

Kelly NM, Harley SL, Möller A (2012) Complexity in the behavior and recrystallization of monazite during high-T metamorphism and fluid infiltration. Chem Geol 322-323:192–208

Kempe U, Lehmann B, Wolf D, Rodionov N, Bombach K, Schwengfelder U, Dietrich A (2008) U–Pb SHRIMP geochronology of Th-poor, hydrothermal monazite: An example from the Llallagua tin-porphyry deposit, Bolivia. Geochim Cosmochim Acta 72:4352–4366

Kingsbury J, Miller C, Wooden J, Harrison T (1993) Monazite paragenesis and U-PB systematics in rocks of the eastern mojave desert, california, USA - implications for thermochronometry. Chem Geol 110:147–167

Kirschner DL, Masson H, Cosca MA (2003) An 40 Ar/ 39 Ar, Rb/Sr, and stable isotope study of micas in low-grade fold-and-thrust belt: an example from the Swiss Helvetic Alps. Contrib Mineral Petrol 145:460–480

Kositcin N, McNaughton NJ, Griffin BJ, Fletcher IR, Groves DI, Rasmussen B (2003) Textural and geochemical discrimination between xenotime of different origin in the Archaean Witwatersrand Basin, South Africa. Geochim Cosmochim Acta 67:709–731

Kralik M, Clauer N, Holnsteiner R, Huemer H, Kappel F (1992) Recurrent fault activity in the Grimsel test site (GTS, Switzerland) - revealed by RB-SR, K-AR AND tritium isotope techniques. J Geol Soc 149:293–301

Krenn E, Finger F (2004) Metamorphic formation of Sr–apatite and Sr-bearing monazite in a high-pressure rock from the Bohemian Massif. American Mineralogist 89:1323–1329.

Krenn E, Finger F (2007) Formation of monazite and rhabdophane at the expense of allanite during Alpine low temperature retrogression of metapelitic basement rocks from Crete, Greece: Microprobe data and geochronological implications. Lithos, 95: 130–147.

Krenn E, Ustaszewski K, Finger F (2008) Detrital and newly formed metamorphic monazite in amphibolite-facies metapelites from the Motajica Massif, Bosnia. Chem. Geol. 254: 164–174.

Krenn, E. and Finger, F. (2010) Unusually Y-rich monazite-(Ce) with 6-14 wt% Y2O3 in a granulite from the Bohemian Massif: Implications for high-temperature monazite growth from the monazite-xenotime miscibility gap thermometry. Mineralogical Magazine, 74, 217–225.

Krenn E, Putz H, Finger F, Paar WH (2011) Sulfur-rich monazite with high common Pb in ore-bearing schists from the Schellgaden mining district (Tauern Window, Eastern Alps). Mineral Petrol 102:51–62

L

Lach P, Mercadier J, Dubessy J, Boiron M-C, Cuney M (2013) In Situ Quantitative Measurement of Rare Earth Elements in Uranium Oxides by Laser Ablation-Inductively Coupled Plasma-Mass Spectrometry. Geostand Geoanalytical Res 37:277–296

Lanari P, Guillot S, Schwartz S, Vidal O, Tricart P, Riel N, Beyssac O (2012) Diachronous evolution of the alpine continental subduction wedge: Evidence from P–T estimates in the Briançonnais Zone houillère (France – Western Alps). J Geodyn 56-57:39–54

Lanari P, Rolland Y, Schwartz S, Vidal O, Guillot S, Tricart P, Dumont T (2014) P-T-t estimation of deformation in low-grade quartz-feldspar-bearing rocks using thermodynamic modelling and 40 Ar/ 39 Ar dating techniques: example of the Plan-de-Phasy shear zone unit (Briançonnais Zone, Western Alps). Terra Nova 26:130–138

Lan Z-W, Chen Z-Q, Li X-H, Li B, Adams D (2013) Hydrothermal origin of the Paleoproterozoic xenotime from the King Leopold Sandstone of the Kimberley Group, Kimberley, NW Australia: Implications for a ca 1.7 Ga far-field hydrothermal event. Aust J Earth Sci 60:497–508

Leisen M, Dubessy J, Boiron M-C, Lach P (2012) Improvement of the determination of element concentrations in quartz-hosted fluid inclusions by LA-ICP-MS and Pitzer thermodynamic modeling of ice melting temperature. Geochim Cosmochim Acta 90:110–125

Lelarge L (1993) Thermochronologie par la méthode des traces de fission d'une marge passive (Dôme de Ponta Grossa, SE Brésil) et au sein d'une chaîne de collision (zone externe de l'arc alpin, France), PhD, Université Joseph Fourier (France)

Leloup PH, Arnaud N, Sobel ER, Lacassin R (2005) Alpine thermal and structural evolution of the highest external crystalline massif: The Mont Blanc: Exhumation of the Mont Blanc massif. Tectonics 24

Leutwein F, Poty B, Sonet J, Zimmerman JL (1970) Age des cavités à cristaux du granite du Mont Blanc. CR Acad. Sci. Paris 271:156-158

Liu XW, Byrne RH (1997) Rare earth and yttrium phosphate solubilities in aqueous solution. Geochim Cosmochim Acta 61:1625–1633

Longerich HP, Jackson SE, Gunther D (1996) Laser ablation inductively coupled plasma mass spectrometric transient signal data acquisition and analyte concentration calculation. J Anal At Spectrom 11:899–904

Ludwig KR (2001) Isoplot/Ex rev. 2.49- A Geochronological Toolkit for Microsoft Excel. Berkeley Geochronology center. Special publication, No.1a

M

Malusà MG, Polino R, Zattin M, Bigazzi G, Martin S, Piana F (2005) Miocene to Present differential exhumation in the Western Alps: Insights from fission track thermochronology: Exhumation in the western alps. Tectonics 24

Malusà MG, Philippot P, Zattin M, Martin S (2006) Late stages of exhumation constrained by structural, fluid inclusion and fission track analyses (Sesia–Lanzo unit, Western European Alps). Earth Planet Sci Lett 243:565–580

Malusà MG, Vezzoli G (2006) Interplay between erosion and tectonics in the Western Alps: Interplay between erosion and tectonics. Terra Nova 18:104–108

Marquer D, Calcagno P, Barfety J-C, Baudin T (2006) 3D modeling and kinematics of the external zone of the French Western Alps (Belledonne and Grand Châtelard Massifs, Maurienne Valley, Savoie). Eclogae Geol Helvetiae 99:211–222.

Marshall D, Pfeifer HR, Hunziker JC, Kirschner D (1998) A pressure-temperature-time path for the NE Mont-Blanc massif; fluid-inclusion, isotopic and thermobarometric evidence. Eur J Mineral 10:1227–1240.

Mathieu R, Zetterström L, Cuney M, Gauthier-Lafaye F, Hidaka H (2001) Alteration of monazite and zircon and lead migration as geochemical tracers of fluid paleocirculations around the Oklo–Okélobondo and Bangombé natural nuclear reaction zones (Franceville basin, Gabon). Chem Geol 171:147–171.

McDonough, W.F., Sun, S.S., 1995. The Composition of the Earth. Chemical Geology, 120: 223-253.

Meldrum A, Boatner LA, Wang LM, Ewing RC (1997) Displacive irradiation effects in the monazite- and zircon- structure orthophosphates. Physical Review B56, 13805-13814.

Michalski I, Soom M (1990) The Alpine thermo-tectonic evolution of the Aar and Gotthard massifs, central Switzerland: Fission track ages on zircon and apatite and K-Ar mica ages. Schweiz Miner Petrogr Mitt 70:373–387.

Montel JM (1993) A model for monazite/melt equilibrium and application to the generation of granitic magmas, Chem Geol 110:127-146.

Montel J-M, Foret S, Veschambre M, Nicollet C, Provost A (1996) Electron microprobe dating of monazite. Chem Geol 131:37–53.

Montel JM, Devidal JL, Avignant D (2002) X-ray diffraction study of brabantite-monazite solid solutions. Chem Geol 191:89–104

Mullis J, Dubessy J, Poty B, ONeil J (1994) Fluid regimes during late stages of a continental collision - physical, chemical, and stable-isotope measurements of fluid inclusions in fissure quartz from a geotraverse through the Central Alps, Switzerland. Geochim Cosmochim Acta 58:2239–2267

Mullis J (1996) P-T-t path of quartz formation in extensional veins of the Central Alps. Schweiz Mineral Petrogr Mitteilungen 76:159–164.

N

Nakano N, Osanai Y, Owada M, Satish-Kumar M, Adachi T, Jargalan S, Yoshimoto A, Syeryekhan K, Boldbaatar C (2015) Multiple growth of garnet, sillimanite/kyanite and monazite during amphibolite facies metamorphism: implications for the P-T-t and tectonic evolution of the western Altai Range, Mongolia. J Metamorph Geol 33:937–958

Ni Y, Hughes JM, Mariano AN (1995) Crystal chemistry of the monazite and xenotime structures. Am. Mineral. 80: 21-26.

Nziengui JJ (1993) Excès d'argon radiogénique dans les quartz des fissures tectoniques: implications pour la datation des séries métamorphiques. L'exemple de la coupe de la Romanche, Alpes Occidentales françaises, PhD, Univ Joseph Fourier (France)

O

O'Neil, J.R., Taylor, H.P.J., (1967) The oxygen isotope and cation exchange chemistry of feldspars. Am. Mineral. 52, 1414–1437

Oelkers EH, Poitrasson F (2002) An experimental study of the dissolution stoichiometry and rates of a natural monazite as a function of temperature from 50 to 230 C and pH from 1.5 to 10. Chem Geol 191:73–87.

Oelkers EH, Montel J-M (2008) Phosphates and nuclear waste storage. Elements 4:113–116

Ondrejka M, Uher P, Putiš M, Broska I, Bačík P, Konečný P, Schmiedt I (2012) Two-stage breakdown of monazite by postmagmatic and metamorphic fluids: An example from the Veporic orthogneiss, Western Carpathians, Slovakia. Lithos, 142-143:245–255.

Overstreet WC (1964) The geological occurrence of monazite. US Geological Survey Professional Paper, 530.

P

Paquette JL, Nedelec A, Moine B, Rakotondrazafy M (1994) U-Pb, single zircon Pb-Evaporation, AND Sm-Nd isotopic study of a granulite domain in SE Madagascar. J Geol 102:523–538.

Paquette JL, Tiepolo M (2007) High resolution (5 μm) U–Th–Pb isotope dating of monazite with excimer laser ablation (ELA)-ICPMS. Chem Geol 240:222–237

Parrish RR (1990) U-PB dating of monazite and its application to geological problems. Can J Earth Sci 27:1431–1450

Pearce NJG, Perkins WT, Westgate JA, Gorton MP, Jackson SE, Neal CR, Chenery SP (1997) A compilation of new and published major and trace element data for NIST SRM 610 and NIST SRM 612 glass reference materials. Geostand Newsl- J Geostand Geoanalysis 21:115–144

Perdikouri C, Kasioptas A, Geisler T, Schmidt BC, Putnis A (2011) Experimental study of the aragonite to calcite transition in aqueous solution. Geochim Cosmochim Acta 75:6211–6224

Petrik I, Konecny P (2009) Metasomatic replacement of inherited metamorphic monazite in a biotite-garnet granite from the Nizke Tatry Mountains, Western Carpathians, Slovakia: Chemical dating and evidence for disequilibrium melting. Am Mineral 94:957–974

Pettke T, Diamond LW, Villa IM (1999) Mesothermal gold veins and metamorphic devolatilization in the northwestern Alps: The temporal link. Geology 27:641–644

Picot V, Deschanels X, Peuget S, Glorieux B, Seydoux-Guillaume AM, Wirth R (2008) Ion beam radiation effects in monazite. J Nucl Mater 381:290–296

Plumper O, Royne A, Magraso A, Jamtveit B (2012) The interface-scale mechanism of reaction-induced fracturing during serpentinization. Geology 40:1103–1106

Poitrasson F, Chenery S, Bland DJ (1996) Contrasted monazite hydrothermal alteration mechanisms and their geochemical implications. Earth Planet Sci Lett 145:79–96.

Poitrasson F, Chenery S, Shepherd TJ (2000) Electron microprobe and LA-ICP-MS study of monazite hydrothermal alteration:: Implications for U-Th-Pb geochronology and nuclear ceramics. Geochim Cosmochim Acta 64:3283–3297.

Poitrasson F, Oelkers E, Schott J, Montel J-M (2004) Experimental determination of synthetic NdPO4 monazite end-member solubility in water from 21°C to 300°C: implications for rare earth element mobility in crustal fluids. Geochim Cosmochim Acta 68:2207–2221

Pollok K, Putnis CV, Putnis A (2011) Mineral replacement reactions in solid solution-aqueous solution systems: volume changes, reactions paths and end-points using the example of model salt systems. Am J Sci 311:211–236

Poncerry E. (1981). – Contribution à l'étude des granitoïdes de Vallorcine, Beaufort, Lauzière, de leur encaissant et des minéralisations uranifères associées, Alpes françaises. – Thèse 3ème cycle, Université de Grenoble, 319 p.

Poty B. (1969). – La croissance des cristaux de quartz dans les filons sur l'exemple du filon de La Gardette (Bourg d'Oisans) et des filons

Poty B, Stadler HA, Weisbrod AM (1974) Fluid inclusions studies in quartz from fissures of the western and Central Alps. Schweiz Mineral Petrogr Mitt. 54:717-752

Poujol M, Boulvais P, Kosler J (2010) In-situ LA-ICP-MS U–Th–Pb dating of metasomaticfluid circulation: evidence of regional-scale albitization in the Pyrénées. J Geol Soc Lond 167:751–767.

Pourtier E, Devidal J-L, Gibert F (2010) Solubility measurements of synthetic neodymium monazite as a function of temperature at 2kbars, and aqueous neodymium speciation in equilibrium with monazite. Geochim Cosmochim Acta 74:1872–1891

Putnis A (2002) Mineral replacement reactions: from macroscopic observations to microscopic mechanisms. Mineral Mag 66:689–708

Putnis CV, Geisler T, Schmid-Beurmann P, Stephan T, Giampaolo C (2007) An experimental study of the replacement of leucite by analcime. Am Mineral 92:19–26

Putnis A (2009) Mineral replacement reactions. Rev Mineral Geochem 70:87–124.

Putnis A, Austrheim H (2010) Fluid-induced processes: metasomatism and metamorphism. Geofluids. 10:254-269

Putnis A, Putnis CV (2007) The mechanism of reequilibration of solids in the presence of a fluid phase. J Solid State Chem 180:1783–1786

Pyle JM, Spear FS, Rudnick RL, McDonough WF (2001) Monazite-xenotime-garnet equilibrium in metapelites and a new monazite-garnet thermometer. J Petrol 42: 2083-2107.

Pyle JM, Spear FS (2003) Four generations of accessory-phase growth in low-pressure migmatites from SW New Hampshire. Am Mineral 88:338–351.

Pyle JM (2005) Contributions to precision and accuracy of monazite microprobe ages. Am Mineral 90:547–577

Pyle JM (2006) Temperature-time paths from phosphate accessory phase paragenesis in the Honey Brook Upland and associated cover sequence, SE Pennsylvania, USA. Lithos 88:201–232

R

Rapp RP, Watson EB (1986) Monazite solubility and dissolution kinetics: implications for the thorium and light rare earth chemistry of felsic magmas. Contrib Mineral Petrol 94:304–316.

Rasmussen B, Fletcher IR, McNaughton NJ (2001) Dating low-grade metamorphic events by SHRIMP U-Pb analysis of monazite in shales. Geology 29:963–966

Rasmussen B (2005) Radiometric dating of sedimentary rocks: the application of diagenetic xenotime geochronology. Earth-Sci Rev 68:197–243

Rasmussen B, Fletcher IR, Muhling JR, Mueller AG, Hall GC (2007a) Bushveld-aged fluid flow, peak metamorphism, and gold mobilization in the Witwatersrand basin, South Africa: Constraints from in situ SHRIMP U-Pb dating of monazite and xenotime. Geology 35:931–934.

Rasmussen B, Fletcher IR, Muhling JR, Thorne WS, Broadbent GC (2007b) Prolonged history of episodic fluid flow in giant hematite ore bodies: Evidence from in situ U–Pb geochronology of hydrothermal xenotime. Earth Planet Sci Lett 258:249–259

Rasmussen B, Muhling JR (2007) Monazite begets monazite: evidence for dissolution of detrital monazite and reprecipitation of syntectonic monazite during low-grade regional metamorphism. Contrib Mineral Petrol 154:675–689

Rasmussen B, Muhling JR (2009) Reactions destroying detrital monazite in greenschist-facies sandstones from the Witwatersrand basin, South Africa. Chem Geol 264:311–327

Raufaste C, Jamtveit B, John T, Meakin P, Dysthe DK (2011) The mechanism of porosity formation during solvent-mediated phase transformations. Proc R Soc Math Phys Eng Sci 467:1408–1426

Reiners PW (2005) Zircon (U-Th)/He thermochronometry. Low-Temp Thermochronology Tech Interpret Appl 58:151–179

Richard A, Montel J-M, Leborgne R, Peiffert C, Cuney M, Cathelineau M (2015) Monazite Alteration in H2O ± HCl ± NaCl ± CaCl2 Fluids at 150 oC and psat: Implications for Uranium Deposits. Minerals 5:693–706

Roedder, E. (1984) Fluid inclusion, reviews in mineralogy. Mineralogical Society of America 12, 644.

Roger F, Teyssier C, Respaut J-P, Rey PF, Jolivet M, Whitney DL, Paquette J-L, Brunel M (2015) Timing of formation and exhumation of the Montagne Noire double dome, French Massif Central. Tectonophysics 640-641:53–69

Rolland Y, Cox S, Boullier A-M, Pennacchioni G, Mancktelow N (2003) Rare earth and trace element mobility in mid-crustal shear zones: insights from the Mont Blanc Massif (Western Alps). Earth Planet Sci Lett 214:203–219

Rolland Y, Cox SF, Corsini M (2009) Constraining deformation stages in brittle–ductile shear zones from combined field mapping and 40Ar/39Ar dating: The structural evolution of the Grimsel Pass area (Aar Massif, Swiss Alps). J Struct Geol 31:1377–1394

Rolland Y, Rossi M, Cox SF, Corsini M, Mancktelow N, Pennacchioni G, Fornari M, Boullier AM (2008) 40Ar/39Ar dating of synkinematic white mica: insights from fluid-rock reaction in low-grade shear zones (Mont Blanc Massif) and constraints on timing of deformation in the NW external Alps. Geol Soc Lond Spec Publ 299:293–315

Rossi M, Rolland Y (2014) Stable isotope and Ar/Ar evidence of prolonged multiscale fluid flow during exhumation of orogenic crust: Example from the Mont Blanc and Aar Massifs (NW Alps): Multi-scale fluid flow in the Alps. Tectonics 33:1681–1709

Rossi M, Rolland Y, Vidal O, Cox SF (2005) Geochemical variations and element transfer during shear-zone development and related episyenites at middle crust depths: insights from the Mont Blanc granite (French—Italian Alps). Geol Soc Lond Spec Publ 245:373–396.

Rubatto D, Gebauer D, Compagnoni R (1999) Dating of eclogite-facies zircons: the age of Alpine metamorphism in the Sesia-Lanzo Zone (Western Alps). Earth Planet Sci Lett 167:141–158

Rubatto D, Williams IS, Buick IS (2001) Zircon and monazite response to prograde metamorphism in the Reynolds Range, central Australia. Contrib Mineral Petrol 140:458–468.

Ruiz-Agudo E, Putnis CV, Putnis A (2014) Coupled dissolution and precipitation at mineral-fluid interfaces. Chem Geol 383:132–146

S

Sabil N (1995) La datation par traces de fission: aspects méthodologiques et applications thermochronologiques en contexte Alpin et de Marge Continentale. PhD, Univ Joseph Fourier (France)

Sanchez G, Rolland Y, Jolivet M, Brichau S, Corsini M, Carter A (2011a) Exhumation controlled by transcurrent tectonics: the Argentera-Mercantour massif (SW Alps) Terra Nova 23:116-126

Sanchez G, Rolland Y, Schneider J, Corsini M, Oliot E, Goncalves P, Verati C, Lardeaux J-M, Marquer D (2011b) Dating low-temperature deformation by 40Ar/39Ar on white mica, insights from the Argentera-Mercantour Massif (SW Alps). Lithos 125:521–536

Schandl ES, Gorton MP (2004) A textural and geochemical guide to the identification of hydrothermal monazite: criteria for selection of samples for dating epigenetic hydrothermal ore deposits. Econ Geol 99:1027–1035.

Scharer U (1984) The effect of initial TH-230 disequilibrium on young U-PB ages - the Makalu case, Himalaya. Earth Planet Sci Lett 67:191–204

Scherrer NC, Engi M, Gnos E, Jakob V, Liechti A (2000) Monazite analysis; from sample preparation to microprobe age dating and REE quantification. Schweiz Mineral Petrogr Mitteilungen 80:93–105.

Schlenz H, Heuser J, Neumann A, Schmitz S, Bosbach D (2013) Monazite as a suitable actinide waste form. Z Für Krist - Cryst Mater 228:113–123

Schmid SM, Kissling E (2000) The arc of the western Alps in the light of geophysical data on deep crustal structure. Tectonics 19:62–85

Schmidt C, Rickers K, Bilderback DH, Huang R (2007) In situ synchrotron-radiation XRF study of REE phosphate dissolution in aqueous fluids to 800 °C. Lithos 95:87–102

Schoene B (2014) 4.10 - U–Th–Pb Geochronology. In: Turekian HDHK (ed) Treatise on Geochemistry (Second Edition), Second Edition. Elsevier, Oxford, pp 341 – 378

Schwartz S (2000) La zone piémontaise des Alpes occidentales: un paléo-complexe de subduction. Arguments métamorphiques, géochronologiques et structuraux. PhD, Université Claude Bernard (France)

Schwartz S, Lardeaux JM, Tricart P, Guillot S, Labrin E (2007) Diachronous exhumation of HP?LT metamorphic rocks from south-western Alps: evidence from fission-track analysis. Terra Nova 19:133–140

Seward D, Mancktelow NS (1994) Neogene kinematics of the central and western Alps: evidence from fission-track dating. Geology 22:803–806.

Seward D, Ford M, Bürgisser J, et al (1999) Preliminary results of fission track analyses in the Southern Pelvoux area, SE France. 3rd Workshop on Alpine Geological Studies. Mem Sci Geo Padova, 51:25-31

Seydoux-Guillaume A-M, Paquette J-L, Wiedenbeck M, Montel J-M, Heinrich W (2002a) Experimental resetting of the U–Th–Pb systems in monazite. Chem Geol 191:165–181.

Seydoux-Guillaume A-M, Wirth R, Heinrich W, Montel J-M (2002b) Experimental determination of Thorium partitioning between monazite and xenotime using analytical electron microscopy and X-ray diffraction Rietveld analysis. Eur J Mineral 14:869–878

Seydoux-Guillaume AM, Wirth R, Nasdala L, Gottschalk M, Montel JM, Heinrich W (2002c) An XRD, TEM and Raman study of experimentally annealed natural monazite. Phys Chem Miner 29:240–253.

Seydoux-Guillaume A-M, Goncalves P, Wirth R, Deutsch A (2003) Transmission electron microscope study of polyphase and discordant monazites: Site-specific specimen preparation using the focused ion beam technique. Geology 31:973–976.

Seydoux-Guillaume A-M, Wirth R, Deutsch A, Schärer U (2004) Microstructure of 24-1928 Ma concordant monazites; implications for geochronology and nuclear waste deposits. Geochim Cosmochim Acta 68:2517–2527

Seydoux-Guillaume A-M, Montel J-M, Bingen B, Bosse V, de Parseval P, Paquette J-L, Janots E, Wirth R (2012) Low-temperature alteration of monazite: Fluid mediated coupled dissolution–precipitation, irradiation damage, and disturbance of the U–Pb and Th–Pb chronometers. Chem Geol 330-331:140–158

Shazia JR, Harlov DE, Suzuki K, Kim SW, Girish-Kumar M, Hayasaka Y, Ishwar-Kumar C, Windley BF, Sajeev K (2015) Linking monazite geochronology with fluid infiltration and metamorphic histories: Nature and experiment. Lithos 236-237:1–15

Shepherd, T., Rankin, A.H., and Alderton, D.H.M. (1985) A practical guide to fluid inclusion studies. Blackie, London, 239 p.

Simon-Labric T, Rolland Y, Dumont T, Heymes T, Authemayou C, Corsini M, Fornari M (2009) 40 Ar/ 39 Ar dating of Penninic Front tectonic displacement (W Alps) during the Lower Oligocene (31-34 Ma). Terra Nova 21:127–136

Smith HA, Barreiro B (1990) Monazite U-Pb dating of staurolite grade metamorphism in pelitic schists. Contrib. Mineral. Petrol. 105: 602-615.

Smith MP, Henderson P, Campbell LS (2000) Fractionation of the REE during hydrothermal processes: constraints from the Bayan Obo Fe-REE-Nb deposit, Inner Mongolia, China. Geochim Cosmochim Acta 64:3141–3160.

Soom, M. (1986), Geologie und petrographie von Ausserberg (VS). Kluftmineralisation am Südrand des Aarmassivs, 129 pp., Lizenziat-Arbeit Univ. Bern, Bern.

Soom MA (1990) Abkühlungs- und Hebungsgeschichte der Externmassive und der Penninischen decken beidseits der Simplon-Rhone-Linie seit dem Oligozan: Spaltspurdatierungen an apatit/zirkon und K/Ar-datierungen an biotit/muskowit (westliche zentralalpen), PhD, Univ of Bern (Switzerland)

Spear FS (2010) Monazite–allanite phase relations in metapelites. Chem Geol. 279:55-62.

Spear FS, Pyle JM (2010) Theoretical modeling of monazite growth in a low-Ca metapelite. Chem Geol 273:111–119

Steele-MacInnis M, Lecumberri-Sanchez P, Bodnar RJ (2012) HokieFlincs_H2O-NaCl: A Microsoft Excel spreadsheet for interpreting microthermometric data from fluid inclusions based on the PVTX properties of H2O–NaCl. Comput Geosci 49:334–337

Strzerzynski P, Guillot S, Leloup PH, Arnaud N, Vidal O, Ledru P, Courrioux G, Darmendrail X (2012) Tectono-metamorphic evolution of the Briançonnais zone (Modane-Aussois and Southern Vanoise units, Lyon Turin transect, Western Alps). J Geodyn 56-57:55–75

Sterner S, Bodnar R (1984) Synthetic fluid inclusions in natural quartz .1. Compositional types synthesized and applications to experimental geochemistry. Geochim Cosmochim Acta 48:2659–2668

Suzuki K, Adachi M (1991) Precambrian provenance and Silurian metamorphism of the Tsubonosawa paragneiss in the south Kitakami terrane, northeast Japan, revealed by the chemical TH-U-total PB isochron ages of monazite, zircon and xenotime. Geochem J 25:357–376.

Suzuki K, Adachi M, Kajizuka I (1994) Electron microprobe observations of Pb diffusion in metamorphosed detrital monazites. Earth. Planet Sci Lett. 128 : 391-405.

T

Tartese R, Boulvais P, Poujol M, Chevalier T, Paquette J-L, Ireland TR, Deloule E (2012) Mylonites of the South Armorican Shear Zone: Insights for crustal-scale fluid flow and water-rock interaction processes. J Geodyn 56-57:86–107

Tera, F., and Wasserburg, G.J (1972) U-Th-Pb systematics in three Apollo 14 basalts and the problem of initial Pb in lunar rocks: Earth and Planetary Science Letters, v. 14, p. 281–304

Terry MP, Robinson P, Hamilton MA, Jercinovic MJ (2000) Monazite geochronology of UHP and HP metamorphism, deformation, and exhumation, Nordoyane, Western Gneiss Region, Norway. Am. Mineral. 85:1651-64.

Teufel S, Heinrich W (1997) Partial resetting of the U・ Pb isotope system in monazite through hydrothermal experiments: An SEM and U・ Pb isotope study. Chem Geol 137:273–281.

Thiébaud E, Dzikowski M, Gasquet D, Renac C (2010) Reconstruction of groundwater flows and chemical water evolution in an amagmatic hydrothermal system (La Léchère, French Alps). J Hydrol 381:189–202

Townsend KJ, Miller CF, D'Andrea JL, Ayers JC, Harrison TM, Coath CD (2001) Low temperature replacement of monazite in the Ireteba granite, Southern Nevada: geochronological implications. Chem Geol 172:95–112

Tricart P, Van Der Beek P, Schwartz S, Labrin E (2007) Diachronous late-stage exhumation across the western Alpine arc: constraints from apatite fission-track thermochronology between the Pelvoux and Dora-Maira Massifs. J Geol Soc 164:163–174.

Tropper P, Manning CE, Harlov DE (2011) Solubility of CePO4 monazite and YPO4 xenotime in H2O and H2O–NaCl at 800°C and 1GPa: Implications for REE and Y transport during high-grade metamorphism. Chem Geol 282:58–66

Tropper P, Manning CE, Harlov DE (2013) Experimental determination of CePO 4 and YPO 4 solubilities in H 2 O-NaF at 800°C and 1 GPa: implications for rare earth element transport in high-grade metamorphic fluids. Geofluids 13:372–380

V

Vallini DA, Cannon WF, Schulz KJ (2006) Age constraints for Paleoproterozoic glaciation in the Lake Superior Region: detrital zircon and hydrothermal xenotime ages for the Chocolay Group, Marquette Range Supergroup. Can J Earth Sci 43:571–591

Van Achterbergh E, Ryan CG, Jackson SE, Griffin W (2001) Data reduction software for LA-ICP-MS. In: Sylvester P (ed) Laser ablation-ICP-MS in the Earth Science. Mineralogical Association of Canada 29:239–243

Vance J (1999) Zircon fission track evidence for a Jurassic (Tethyan) thermal event in the Western Alps. Memorie di Scienze Geologiche, Padova, 51:473-476

VanEmden B, Thornber MR, Graham J, Lincoln FJ (1997) The incorporation of actinides in monazite and xenotime from placer deposits in Western Australia. Can Mineral 35:95–104.

Villa IM (2010) Disequilibrium textures versus equilibrium modelling: geochronology at the crossroads. Geol Soc Lond Spec Publ 332:1–15.

Villa IM, Bucher S, Bousquet R, Kleinhanns IC, Schmid SM (2014) Dating Polygenetic Metamorphic Assemblages along a Transect across the Western Alps. J Petrol 55:803–830

W

Wall, F. and Mariano, A.N. (1996) Rare earth minerals in carbonatites: a discussion centred on the Kangankunde Carbonatite, Malawi. In: Rare Earth Minerals': Chemistry, Origin and Ore Deposits. (A.P. Jones, F. Wall and C.T. Williams, eds.). Mineralogical Society Series, 7. Chapman and Hall, London, 193 225

Wawrzenitz N, Krohe A, Rhede D, Romer RL (2012) Dating rock deformation with monazite: The impact of dissolution precipitation creep. Lithos 134-135:52–74

Wetherill GW (1956) Discordant Uranium-Lead ages. Trans. AGU. 37:320-336.

Weber WJ, Ewing RC, Catlow CRA, De La Rubia TD, Hobbs LW, Kinoshita C, Matzke H, Motta AT, Nastasi M, Salje EKH, others (1998) Radiation effects in crystalline ceramics for the immobilization of high-level nuclear waste and plutonium. J Mater Res 13:1434–1484.

Williams ML, Jercinovic MJ, Harlov DE, Budzyń B, Hetherington CJ (2011) Resetting monazite ages during fluid-related alteration. Chem Geol 283:218–225

Williams ML, Jercinovic MJ, Hetherington CJ (2007) Microprobe Monazite Geochronology: Understanding Geologic Processes by Integrating Composition and Chronology. Annu Rev Earth Planet Sci 35:137–175

Wing BA, Ferry JM, Harrison TM (2003) Prograde destruction and formation of monazite and allanite during contact and regional metamorphism of pelites: petrology and geochronology. Contrib Mineral Petrol 145:228–250

Y-Z

Yamada R, Tagami T, Nishimura S, Ito H (1995) Annealing kinetics of fission tracks in zircon - an experimental-study. Chem Geol 122:249–258

Zhu, X.K., and O'Nions, R.K. (1999a) Zonation of monazite in metamorphic rocks and its implications for high temperature thermochronology: A case study from the Lewisian terrain. Earth and Planetary Science Letters, 171, 209–220

Zhu XK, O'Nions RK (1999b) Monazite chemical composition: some implications for monazite geochronology. Contrib Mineral Petrol 137:351–363.

Zi J-W, Rasmussen B, Muhling JR, Fletcher IR, Thorne AM, Johnson SP, Cutten HN, Dunkley DJ, Korhonen FJ (2015) In situ U–Pb geochronology of xenotime and monazite from the Abra polymetallic deposit in the Capricorn Orogen, Australia: Dating hydrothermal mineralization and fluid flow in a long-lived crustal structure. Precambrian Res 260:91–112